Award Number:
W81XWH-10-1-0969

TITLE:
Micellar Drug Delivery and Proteomics Analysis for Effective Treatment of Resistant Prostate Cancer

PRINCIPAL INVESTIGATOR:
Ram I. Mahato, Ph.D.

CONTRACTING ORGANIZATION:
University of Nebraska Medical Center
Omaha, Nebraska, 68198

REPORT DATE: December 2015

TYPE OF REPORT: Addendum to Final

PREPARED FOR:
U.S. Army Medical Research and Materiel Command
Fort Detrick, Maryland 21702-5012

REPORT DOCUMENTATION PAGE		Form Approved OMB No. 0704-0188
Public reporting burden for this collection of information is estimated to average 1 hour per response, including the time for reviewing instructions, searching existing data sources, gathering and maintaining the data needed, and completing and reviewing this collection of information. Send comments regarding this burden estimate or any other aspect of this collection of information, including suggestions for reducing this burden to Department of Defense, Washington Headquarters Services, Directorate for Information Operations and Reports (0704-0188), 1215 Jefferson Davis Highway, Suite 1204, Arlington, VA 22202-4302. Respondents should be aware that notwithstanding any other provision of law, no person shall be subject to any penalty for failing to comply with a collection of information if it does not display a currently valid OMB control number. **PLEASE DO NOT RETURN YOUR FORM TO THE ABOVE ADDRESS.**		
1. REPORT DATE: December 2015	**REPORT TYPE: Final Addendum**	**3. DATES COVERED** ***15Sep2014 - 14Sep2015***
4. TITLE AND SUBTITLE Micellar Drug Delivery and Proteomics Analysis for Effective Treatment of Resistant Prostate cancer.		**5a. CONTRACT NUMBER** **5b. GRANT NUMBER** W81XWH-10-1-0969 **5c. PROGRAM ELEMENT NUMBER**
6. AUTHOR(S) Ram I. Mahato E-Mail: ram.mahato@unmc.edu		**5d. PROJECT NUMBER** **5e. TASK NUMBER** **5f. WORK UNIT NUMBER**
7. PERFORMING ORGANIZATION NAME(S) AND ADDRESS(ES) University of Nebraska Medical Center Department of Pharmaceutical Sciences Lab DRC II, Room 6028 986025 Nebraska Medical Center Omaha, NE 68198-6025		**8. PERFORMING ORGANIZATION REPORT NUMBER**
9. SPONSORING / MONITORING AGENCY NAME(S) AND ADDRESS(ES) US Army Medical Research and Materiel Command Fort Detrick, Maryland 21702-5012		**10. SPONSOR/MONITOR'S ACRONYM(S)** **11. SPONSOR/MONITOR'S NUMBER(S)**
12. DISTRIBUTION / AVAILABILITY STATEMENT Approved for public release; distribution unlimited		
13. SUPPLEMENTARY NOTES		

14. ABSTRACT

We found good synergy between XIAP inhibitor embelin and anti-androgen such as bicalutamide and its analog CBD-IV 17 in killing prostate cancer cells. Since antiandrogens and XIAP inhibitor were highly hydrophobic, they were solubilized in polymeric micelles prepared using our newly synthesized copolymer, polyethylene glycol-b-poly (carbonate-co-lactide) (PEG-b-p(CB-co-PLA). Following *in vitro* characterization in terms of particle size and drug loading, these formulations were tested in prostate tumor bearing mice. Sequential administration of bicalutamide followed by embelin was more potent in regressing prostate tumor growth in mouse xenografts compared to monotherapy. Micelles usually are not very stable and tend to disintegrate upon dilution in the blood stream. To address this issue, we formulated micelles using the newly synthesized cross-linkable copolymers. We demonstrated that cross-linked micelles are more stable towards extensive aqueous dilution and in the presence of serum and are non-toxic towards the cell growth even at a high concentration. Using FACS, we demonstrated existence of a higher side population in chemoresistant cells in comparison to the chemo-sensitive cells. We have also found miR-200c, miR-34a and miR-29b highly downregulated and miR-10b, miR-155 upregulated in the chemoresistant cells and in prostate tumor tissues which play a key role in maintaining cancer stem cells (CSCs), inducing chemoresistance and metastasis in the prostate cancer. To achieve site-specific drug delivery to prostate tumor after systemic administration we attached LHRH peptide to the copolymer and synthesized LHRH-PEG-b-p(CB-co-LA). LHRH conjugation enhanced cellular uptake of micelles without adversely affecting CMC, CBDIV17 loading, and drug release profile. CBDIV17 loaded LHRH-PEG-b-p(CB-co-LA) showed higher caspase-3 activity upon treatment compared to free drug and drug loaded by non-conjugated micelles. Further, CBDIV17 loaded LHRH-PEG-b-p (CB-co-LA) micelles significantly inhibited prostate tumor growth compared to CBDIV17 loaded HOOC-PEG-b-p(CB-co-LA) and control groups.

15. SUBJECT TERMS
Prostate cancer, micelles, co-polymer, XIAP inhibitor, anti-androgen

16. SECURITY CLASSIFICATION OF:			**17. LIMITATION OF ABSTRACT**	**18. NUMBER OF PAGES**	**19a. NAME OF RESPONSIBLE PERSON** USAMRMC
a. REPORT	**b. ABSTRACT**	**c. THIS PAGE**			**19b. TELEPHONE NUMBER** *(include area code)*
U	U	U	UU	127	

TABLE OF CONTENTS

Page

INTRODUCTION

Anti-androgen therapy has been a standard line of treatment for prostate cancer. Nevertheless, in majority of the cases recurrence of the prostate cancers has been observed after the initial response to androgen ablation therapy,[1, 2] therefore, in this research project our **focus** was to investigate the therapeutic efficacy and elucidate the underlying mechanism of a novel antiandrogen and XIAP inhibitor based combination therapy for treatment of androgen-dependent prostate cancer as well as androgen-independent prostate cancer growth and metastases. Since the small molecule antiandrogens used for our studies (*e.g*., bicalutamide or CBDIV17) and XIAP inhibitors (*e.g*., embelin or embelin-6g) are highly hydrophobic, we synthesized novel biodegradable LHRH-PEG-b-p(CB-co-LA) co-polymers for preparing micelles for enhanced solubility and loading of these hydrophobic drugs and site specific delivery of the drug-loaded micelles to prostate cancer cells by active targeting. The **scope** of this project was limited to two lines of scientific investigation: (i) whether and how combination of antiandrogen and XIAP inhibitor can result in synergistic inhibition of prostate cancer growth. This objective of the study has been achieved as bicalutamide and embelin combination showed highly synergistic cytotoxicity *in vitro* and *in vivo* in athymic nude mice bearing LNCaP xenografts.[3] To further gain an in depth insight into the molecular mechanisms involved in this synergism, we carried out detailed proteomic profiling of the *in vivo* tumor samples and (ii) Site-specific delivery of bicalutamide and embelin (or their analogs) using polymeric nano-carrier for testing in orthotopic tumor bearing mice (either as combined or sequential administration) to determine tumor regression.

Keywords

- Anti-androgen
- Co-polymer
- Luteinizing hormone-releasing hormone
- Micelles,
- Prostate cancer
- XIAP inhibitor

BODY

Task 1. Can combination of bicalutamide and embelin synergistically inhibit prostate cancer growth?

Combination of embelin and embelin-6g with CBD-IV 17 (bicalutamide analog) resulted in a three-fold decrease in cell proliferation compared to either of these drugs alone. Furthermore, combination of CBD-IV 17 and embelin or embelin-6g was seen to be synergistic in the normalized IC_{50} isobologram.[4] Since CBD-IV17 and embelin combination therapy effectively inhibited prostate cancer growth *in vitro*, we determined the effect of this combination approach in athymic nude mice bearing LNCaP xenografts. CBD-IV 17 and embelin were formulated using PEG-b-p(CB-co-LA) micelles and intratumoral injection of 20 mg/kg CBD-IV17 and 10 mg/kg embelin-loaded micelles was administered on days 0, 3 and 7. CBD-IV17 and embelin combination significantly inhibited tumor growth compared to the mice treated with blank micelles.[3] To understand the mechanism responsible for causing this reduction, we studied AR and PSA expression in the tumor groups treated with combination therapy and it was seen that AR expression was marginally decreased in treated samples compared to control. However, there were obvious morphological differences between the control and treated tumor samples. In contrast, PSA-staining showed significant decrease in PSA expression in treated tissues compared to control and was consistent with differences in tumor size.[3] Based on these results, it was concluded that bicalutamide and embelin combination showed synergistic antitumor activity.

<u>Task 2</u>. Can micelles conjugated with LHRH analog facilitate site-specific delivery to prostate tumor?

To ensure site specific delivery of drug-loaded micelles to prostate cancer cells by active targeting, we conjugated synthetic LHRH analog onto the copolymer since LHRH receptors are overexpressed by prostate cancer cells.[5] Briefly, HOOC-PEG-b-p(CB-co-LA) with the was synthesized using of HOOC-PEG-OH, lactide and base monomer in the presence of 1, 8-diazabicyclo[5.4.0]undec-7-ene (DBU) as a catalyst. Purified HOOC-PEG-b-P(CB-co-LA) copolymer and LHRH-NH_2 peptide (PYR-His-Trp-Ser-Tyr-^{D}Lys-Leu-Arg-Pro-Gly-$CONH_2$) were conjugated using 1-Ethyl-3-(3-dimethylaminopropyl) carbodiimide·HCl (EDC·HCl) and 4-dimethylaminopyridine reaction mixture. The LHRH conjugated polymer was purified by dialysis using 3,500 MWCO Dialysis and characterized by ^{1}HNMR recorded on a Varian (500 MHz, T=25°C) using DMSO-d_6 as a solvent.[6]

CBDIV17 was encapsulated into micelles core using the film hydration method as reported earlier with minor change.[7] CBDIV17 loading and encapsulation efficiency was measured was found to be 4.59±0.01 and 91.80±0.20 for HOOC-PEG-b-p(CB-co-LA) respectively. Drug loading and encapsulation efficiency was found to be 4.54±0.17 and 90.80±3.40 for LHRH-PEG-b-p(CB-co-LA) respectively. The mean micelle size before drug loading was found to be 75.60±2.25 nm and 72.64±1.15 nm for HOOC-PEG-b-p(CB-co-LA) and LHRH-PEG-b-p(CB-co-LA) micelles, respectively. The mean micelle size after drug loading was found to be 82.33±3.93 nm and 84.59±3.29 nm for HOOC-PEG-b-p(CB-co-LA) and LHRH-PEG-b-p(CB-co-LA) micelles, respectively. Our results showed that no significant difference was observed in the mean particles size of the copolymer before and after conjugating LHRH. Fluorescence spectroscopy method was used to estimate the critical micelle concentration (CMC) of HOOC-PEG-b-P(CB-co-LA) and LHRH-PEG-b-P(CB-co-LA) copolymer using pyrene as a hydrophobic fluorescent probe The value of the CMC was obtained as the point of intersection of two tangents drawn to the curve at high and low concentrations, respectively. Results showed that no significant difference was observed in the CMC values of the copolymer before and after conjugating LHRH. We checked LHRH receptor expression in prostate cancer cells by quantitative real-time RT-PCR. Our result showed that LNCaP and C4-2 cancer cells overexpressed LHRH receptor by at least two folds compared to poorly LHRH-expressing RWPE-1 cells. We performed cellular uptake study to demonstrate the effect of LHRH conjugation on cellular uptake. LHRH conjugation onto HOOC-PEG-b-p(CB-co-LA) polymer significantly increase cellular uptake.

We evaluated the cytotoxic effect of CBDIV17 loaded micelles in C4-2 and LNCaP Cells. Drug-loaded micelles were more cytotoxic than free drug (Fig. 4 a & b). IC_{50} value of free CBDIV17, CBDIV17 loaded HOOC-PEG-b-p (CB-co-LA), and CBDIV17 loaded LHRH-PEG-b-p(CB-co-LA) micelles was 25.2, 21.9, and 12.8 μM respectively in LNCaP cells. In C4-2 cells, it was 37.1, 30.9, and 19.8 μM respectively for free CBDIV17, CBDIV17 loaded HOOC-PEG-b-p(CB-co-LA), and CBDIV17 loaded LHRH-PEG-b-p(CB-co-LA) micelles. Additionally, drug loaded LHRH-PEG-b-p(CB-co-LA) micelles exhibited dramatic cell killing efficacy than drug loaded HOOC-PEG-b-p(CB-co-LA) micelles, indicating LHRH conjugation facilitate cellular delivery of CBDIV17 compared

to non-targeting micelles. Further, we determined the transcriptional activity of AR and prostate specific antigen (PSA) by Western blot. CBDIV17 loaded LHRH-PEG-b-p (CB-co-LA) micelles significantly downregulated PSA protein expression, but the effect on AR expression was not significant. We next examined the effect of CBDIV17 loaded micelles on Caspase 3. Our result indicated that CBDIV17 loaded LHRH-PEG-b-p (CB-co-LA) micelles induced more apoptosis than CBDIV17 loaded COOH-PEG-b-p (CB-co-LA) micelles and free drug.

Since CBDIV17 loaded LHRH-PEG-b-p(CB-co-LA) micelles showed a greater anti-cancer effect in vitro than CBDIV17 loaded COOH-PEG-b-p(CB-co-LA) micelles and free CBDIV17, we further evaluated in-vivo tumor growth inhibition efficacy of CBDIV17 loaded micelles in C4-2 ectopic tumor-bearing athymic mice. ~2 x 10^6 C4-2 cells were suspended in 1:1 serum free media and Matrigel and injected subcutaneously in 6-8 weeks old athymic nude mice. When tumor size reached to 150 mm^3, mice were randomly sorted into three groups (n=5) before treatment. Both CBDIV17 loaded HOOC-PEG-b-p(CB-co-LA) and LHRH-PEG-b-p(CB-co-LA) micelles were significantly inhibited tumor growth. CBDIV17 loaded LHRH-PEG-b-p(CB-co-LA) micelles were more effective in inhibiting tumor growth compared to CBDIV17 loaded HOOC-PEG-b-p(CB-co-LA) micelles. On day 17, the tumors from these three groups were excised, and slides were prepared for Ki-67 and apoptosis (caspase 3) immunostaining and for analyzing tumor architecture by Hematoxylin & Eosin for detection. Ki-67 positive cells in tumor tissues from the mice injected with CBDIV17 loaded LHRH-PEG-b-p(CB-co-LA) micelles were significantly lower than the control group and mice that received CBDIV17 loaded HOOC-PEG-b-p(CB-co-LA). Furthermore, CBDIV17 loaded LHRH-PEG-b-p(CB-co-LA) micelles enhanced Caspase-3 expression compared to control group and mice that received CBDIV17 loaded HOOC-PEG-b-p(CB-co-LA). The prostate cancer treatment was evaluated by PSA level.

To establish orthotopic prostate cancer model, we stably transfected C4-2 cells with lentiviral particles (LP) encoding luciferase and GFP gene. Cells were selected using puromycin (1-5 µg/mL). Luciferase and GFP expression from stably transfected cells were confirmed by in vivo IVIS and epifluorescence microscopy respectively. Finally, C4-2-Luc-GFP cells were sorted to obtain luciferase and GFP reporter gene expressing cells population using fluorescence-activated cell sorting (FACS). We then generated orthotopic prostate cancer mice model using these cells in athymic nude mice. Subsequently, 20µL suspensions of 10^6 C4-2-Luc-GFP prostate cancer cells were injected in the dorsal prostate lobe using a 30-gauge needle and a 50 µL glass syringe. After three weeks of surgery, 3mg D-luciferin was administered to each animal via intraperitoneal route (i.p.) and bioluminescent was measured using a Xenogen-IVIS-cooled CCD optical system. Our preliminary result showed that we have successfully developed orthotopic prostate tumor model.

Task 3. Determine the molecular mechanisms by which bicalutamide/embelin inhibit prostate cancer growth?

To elucidate the molecular mechanism underlying the chemotherapeutic effect of embelin and bicalutamide and their analogs, we conducted in vitro cell culture studies where we incubated the cells with these drugs for a predefined period and thereafter studied the expression of molecular markers which play a significant role in prostate cancer. We reported earlier that treatment of C4-2 cells with embelin and embelin-6g (5 μM) resulted in considerable suppression of cyclin D1 and ICAM1 expression which have been implicated in cell proliferation and tumor metastasis, respectively. Also, both the drugs repressed mRNA and protein expression levels of XIAP, AR, and PSA significantly as compared to control.[3]

Embelin monotherapy

We prepared micelles containing embelin with and without targeting molecule LHRH. As we can see from the results, LHRH conjugation does not affect the size, and drug loading capacity of the micelles.

Embelin formulation	Size	PDI	Drug loading	Encapsulation Efficiency
HOOC-PEG-b-p(CB-co-LA)	94.45±4.39	0.231±0.012	2.90±0.41	58.00%±8.20%
LHRH-PEG-b-p(CB-co-LA)	95.72±3.13	0.222±0.017	2.82±0.33	55.40%±6.60%

Further, *in vitro* release profiles of these micelles were studied by a dialysis method. Embelin released from HOOH-PEG-b—p(CB-co-LA) or LHRH-PEG-b—p(CB-co-LA) micelles was continuously monitored for eight days. As illustrated in the figure, we found the slow release of drug from micelles with no significant difference between targeted vs. non-targeted micelles**.** From this study, we can conclude that LHRH conjugation does not negatively affect the micelles properties. And this drug delivery system could minimize the exposure of healthy tissues and enhance the accumulation of anticancer drugs in tumor regions.

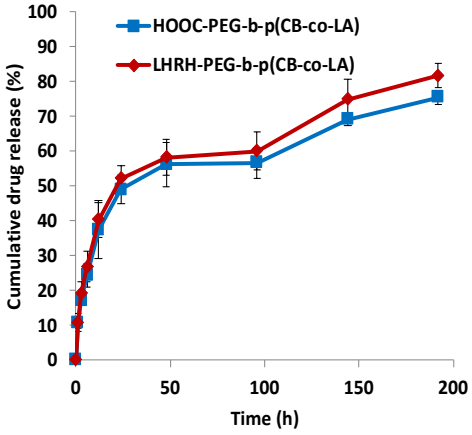

Figure 1. In vitro embelin release profiles of the embelin-loaded co-polymer micelles, and embelin-loaded LHRH conjugated co-polymer micelles.

Micelles Stability:

To estimate the in vivo stability of polymeric micelles, time-dependent Fluorescence Resonance Energy Transfer (FRET) was used to determine the stability of copolymer micelles in the presence of serum proteins, such as alpha beta and gamma globulins.[8] Both lipophilic fluorescent energy donor (DiO) and a lipophilic acceptor (DiI) were loaded into micelles. Emission fluorescence spectra ranging from 490 to 590 nm was obtained at Ex: 488 nm. FRET ratio was calculated as $I_A/ (I_D+I_A)$, where I_A and I_D are peak fluorescence intensities for DiI and DiO at 565 nm and 501 nm, respectively. The decrease of FRET ratio indicated the loss of micelle integrity. Also, the change in particle size and turbidity was measured to determine potential aggregation of micelles in the presence of serum proteins. We observed the similar stability of our LHRH-PEG-b-p(CB-co-LA) micelles compared to commercially available PEG-DSPE and PEG-PLA.

Cytotoxicity and XIAP expression level

We then determined cytotoxicity of free embelin, non-targeted micelles containing embelin and LHRH targeted micelles against LNCaP and C4-2 cells. As can be seen in Figure 2, micelles formulations were more effective in cell killing compared to the free drug. Furthermore, cells treated with LHRH micelles showed the highest toxicity, probably due to higher cellular uptake and LHRH mediated cytotoxicity.

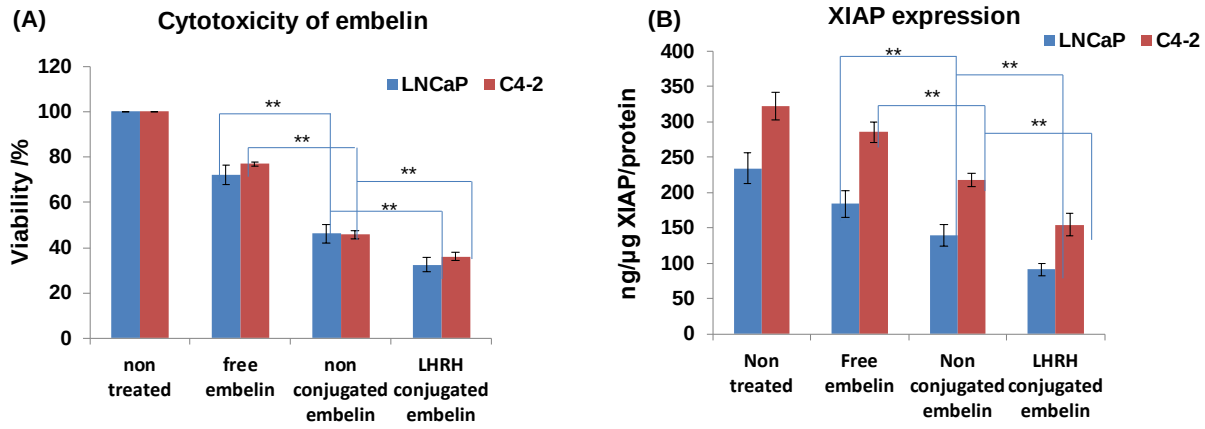

Figure 2. Cytotoxicity and expression levels of XIAP protein. **(A)** cytotoxicity of embeline free drug, encapsulated in non-targeted and LHRH targeted micelles against LNCaP and C4-2 cells at the same drug concentration. **(B)** Effect of free embelin, encapsulated in non-targeted and LHRH targeted micelles on XIAP expression in LNCaP and C4-2 cells. Embelin containing LHRH conjugated micelles decreased the level of apoptosis inhibitor XIAP mRNA.

Androgen ablation therapy

Androgens stimulate prostate cancer cells to grow. Malignant prostate cancer cells initially rely on androgen stimulation via androgen receptors for growth and proliferation and androgen ablation causes a retardation of prostate cell growth.[9] We determined the effect of androgen ablation therapy in androgen-dependent LNCaP cells and androgen-independent C4-2 cells. Cells were seeded in regular medium for three days and then steroid-starved for 48 h in an SR medium, i.e., phenol red-free RPMI 1640 medium containing 5% charcoal/dextran-treated FBS (v/v), 2 mM glutamine, and

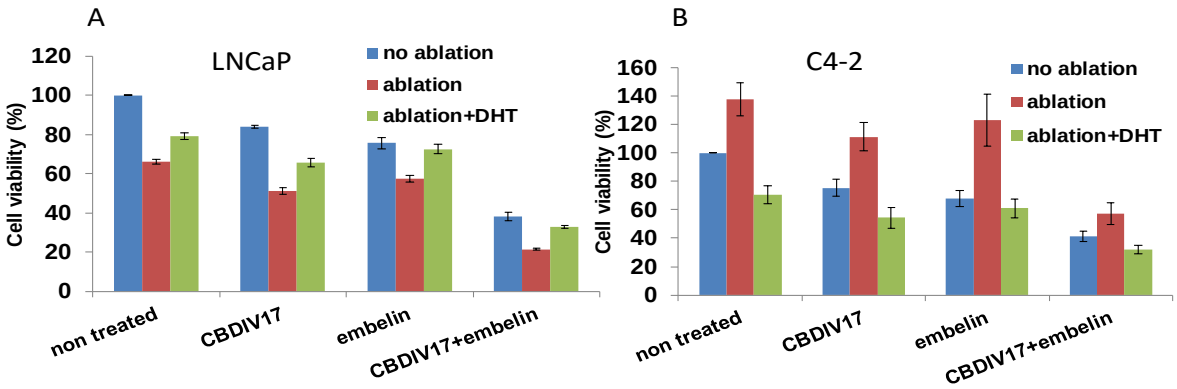

Figure 3. Androgen ablation therapy. (A) effect of androgen ablation in LNCaP cells and in (B) C4-2 cells.

50 mg/ml gentamicin.

As can be seen in Figure 3, androgen ablation decreaseed proliferation of LNCaP cells and inverse was observed by androgen agonist dihydrotestosterone (DHT) treatment. On the other hand, androgen independent C4-2 cells showed increase proliferation upon androgen starvation as compared to control and DHT decreased their proliferation.

KEY RESEARCH ACCOMPLISHMENTS

Task 1: *Can combination of bicalutamide and embelin synergistically inhibit prostate cancer growth?*

In this task, the synergistic and additive effects of bicalutamide and embelin and their analogs were studied after simultaneous and sequential incubation of LNCaP and C4-2 cells. Antitumor efficacy of the combination was also studied in prostate xenograft tumor bearing mice.

- Embelin was more potent than bicalutamide in killing prostate cancer cells irrespective of their androgen status. Micellar formulation of CBDIV17 and embelin combination inhibited tumor growth more potently as compared to the mice treated with blank micelles or monotherapy. Combination therapy significantly reduced the tumor doubling time compared to monotherapy, suggesting that the combination of bicalutamide analog with embelin holds a better potential of treating the prostate tumor.
- CBD-IV 17 (analog of bicalutamide) was more potent than bicalutamide itself in killing prostate cancer cells, especially in C4-2 cells which mimic advanced prostate cancer.
- CBD-IV 17 and bicalutamide induced apoptosis and alter cell cycle of LNCaP and C4-2 cells.
- Embelin-6g exhibited similar cytotoxic activities in prostate cancer cells as embelin.
- Embelin-6g (embelin derivative) was also more potent than bicalutamide and CBD-IV 17 in inhibiting prostate cancer cell proliferation.
- The combination of bicalutamide and embelin was synergistic in killing prostate cancer cells. Furthermore, CBD-IV 17 based combination was more potent than bicalutamide-based combination in inhibiting prostate cancer cell proliferation regardless of XIAP inhibitor used (embelin versus embelin-6g). CBD-IV 17 and embelin effectively inhibited tumor growth in xenograft mice (C4-2 cells).
- Marked decrease in the PSA expression was observed in the in vivo tumor samples after treatment with the combination of CBD-IV 17 and embelin as compared to the control group. Based on these results, it was concluded that the combination of bicalutamide analog CBD-IV 17 and embelin synergistically inhibited prostate cancer growth.

Task 2: *Can micelles conjugated with LHRH analog facilitate site-specific delivery to prostate tumor?* To ensure site specific delivery of the drug-loaded micelles to prostate cancer cells by active targeting, we conjugated synthetic LHRH analogue onto the copolymer since LHRH receptors have been shown to be overexpressed in prostate cancer cells. LHRH conjugated copolymer was synthesized and evaluated for its ability to enable site-specific delivery of the combination of CBDIV 17 and embelin-6g drugs to subcutaneous tumor model and will also be tested in orthotopic tumor mode.

- Designed and synthesized a series of novel amphiphilic lipopolymer, poly(ethylene glycol)-*block*-poly(2-methyl-2-carboxyl-propylene carbonate-graft-dodecanol) (PEG-PCD) for enhanced embelin (XIAP inhibitor) loading and micellar stability. CMC of

PEG-PCD micelles was found to be around 10^{-8} M and decreased with increasing the length of hydrophobic block, indicating good thermodynamic stability. Embelin-loaded PEG-PCD micelles showed significant inhibition of C4-2 prostate cancer cell proliferation in a dose-dependent manner, while no obvious cellular toxicity was observed with blank micelles *per se*.

- To enhance the in vivo stability of our system and sustain the drug release, we synthesized lactic acid- and carbonate-based biodegradable core- and core-corona cross-linkable mPEG-b-P(CB-co-LA-co-MAC) and mPEG-b-PMAC-b-P(CB-co-LA) copolymers by ring opening polymerization of LA, CB and MAC using mPEG as an macroinitiator and 1,8-diazabicycloundec-7-ene (DBU) as a catalyst. Successful cross-linking was confirmed by ^{1}H NMR and IR spectroscopy while light scattering and TEM were used to determine micelle size and morphology. In our preliminary studies, the mean micelle size was found to be 118±1.7 nm and 122±0.81 for core cross-linked and interface cross-linked micelles, respectively. Further, we observed an encapsulation efficiency of 64.08% and drug loading 3.21% w/w for bicalutamide in core cross-linked micelles. We demonstrated that both non-cross-linked micelles (NCM) and cross-linked micelles (CM) remained intact up to a dilution of 2 µg/ml micelle concentration, indicating that these micelles are thermodynamically stable. However, NCM dissociated when micelle concentration was further reduced to 0.20 µg/ml while CM maintained the integrity of their nanostructure. NCM underwent aggregation with time when incubated in BSA (45 mg/ml), as indicated by an increase in particle size while CM showed no signs of aggregation and retained their original size. We evaluated the efficacy of these multiple drugs-loaded cross-linked micelles in inhibiting tumors after systemic administration. For our preliminary *in vivo* studies, xenograft flank tumors were induced in athymic nude mice by subcutaneous injection of 3 million C4-2 cells suspended in 1:1 media and Matrigel. When the tumor volume reached~50 mm, CBDIV17 and embelin loaded micelles prepared using PEG-b-p(CB-co-PLA) copolymer were injected intratumorally at a dose of 10 mg/kg each on days 0, 3 and 7.

- *In vitro* studies indicated that LHRH-PEG-b-p (CB-co-LA) copolymer provided an effective targeting to LHRH receptors that are overexpressed by prostate cancer cells and reduced nonspecific toxicity. LHRH conjugation did not affect CMC, CBDIV17 loading, and drug release profile. Cellular uptake was significantly enhanced by LHRH-PEG-b-p (CB-co-LA) copolymer in LHRH receptor overexpressed cell lines. CBDIV17 loaded LHRH-PEG-b-p(CB-co-LA) micelles showed higher Caspase 3 activity upon treatment compared to free drug and drug loaded by non-conjugated micelles. Our result showed that AR protein expression was not influenced by CBDIV17 loaded LHRH-PEG-b-p(CB-co-LA) micelles while PSA expression was inhibited significantly. In vivo studies indicated that CBDIV17 loaded LHRH-PEG-b-p(CB-co-LA) micelles was significantly inhibited prostate tumor growth compared to CBDIV17 loaded HOOC-PEG-b-p(CB-co-LA) and control groups. CBDIV17 loaded LHRH-PEG-b-p(CB-co-LA) micelles exhibited significant in vivo antitumor efficacy by reducing cancer cells proliferation and enhancing Caspase 3 expression level.

CHANGES TOWARDS NEW DIRECTION

Recent evidence has established that many prostate cancers relapse due to the presence of prostate cancer stem cells (CSCs) which are resistant to most chemotherapeutic agents. CSCs are regulated by miRNAs, and their drug resistant phenotype may be conferred by miRNA dysregulation. Recently, miR-34a has been identified as the key negative regulator of $CD44^+$ prostate cancer stem cells in xenograft and primary tumors and overexpression of miR-34a inhibited tumor regeneration and metastasis, suggesting its importance as a novel therapeutic agent against prostate CSCs.[10] miRNAs regulate cancer stem cells cycle and help stem cells in maintaining their pluripotency by bypassing G1/S checkpoint, thereby maintaining tumorigenic potential.[11] We have recently shown that there is higher gene expression of cancer stem cell marker CD133 and stem cell pluripotency marker OCT4 in a drug-resistant, metastatic prostate cancer cell line. To know the molecular mechanism chemoresistance in prostate cancer, we have determined miRNA profiling in PTX resistant DU145-TXR and PC3-TXR cell lines and clinical prostate tissues. To distinguish the presence of cancer stem cell-like side populations (SP), Hoechst 33342 flow cytometry method was used. Side population analysis of prostate cancer cell line DU145 exhibited a much lower level of side population in comparison to paclitaxel (PTX) resistant cell line DU145-TXR (0.2% vs. 3.2%) After cell sorting, cell cycle analysis showed that in case of non-SP cells, 62% were in the G0-G1 and 30 % in S phase in contrast to 71.5% and 21% for SP cells, respectively ($p< 0.05$). PTX resistant DU145-TXR cells showed higher gene expression of GLI-1 (Hh-pathway marker), OCT-4 (pluripotency/stem cell marker) and CD133 (cancer stem cell marker when compared to PTX sensitive DU145 cells ($p<0.05$). We analyzed the MicroRNA profile in DU145-TXR and PC3-TXR cells and prostate cancer tissue from the patients showed that several miRNAs such as 138, 29b, 200c, 34a and 126 were downregulated while 193b, 30c, 155, 146a, 10b, 10a, 17, 125b and 23b were upregulated. Among these, miRs 155 and 23b were highly upregulated in DU145-TXR cells (~ 230 and 247 fold respectively), while miRs 200c and 29b were highly downregulated (~ 26 and 7 fold, respectively) in these cells with respect to DU145 cells. miRNA profiling studies on the prostate cancer tissues revealed that miRs 17, let7, 31a, 193b, 29b, 155, let 7d, 9, 125b and 30 as being upregulated while miRs 145, 205, 34a, 126, 200c, 27b, 99a and 152 are downregulated in prostate cancer tissue. Dysregulated miRNAs common to tissue and cell arrays viz. miRs 155, 29b, 34a, 200c, 193b and 17 were identified. We shall use these dysregulated miRNAs along with drug delivery to restore chemosensitivity to drug-resistant cancer cells and prevent relapse due to the generation of CSCs in tumors.[12]

REPORTABLE OUTCOMES

Research Papers

1. Wen, D, Chitkara, D., Wu, H., Danquah, M., Patil, R., Miller, D.D., & Mahato, R.I. LHRH-conjugated micelles for targeted delivery of antiandrogen to treat advanced prostate cancer. *Pharm Res* **31**, 2784-95 (2014).
2. Singh, S. *et al*. Chemoresistance in prostate cancer cells is regulated by miRNAs and Hedgehog pathway. *PLoS One* **7**, e40021 (2012).
3. Danquah, M., Duke, C. B.,3rd, Patil, R., Miller, D. D. & Mahato, R. I. Combination therapy of antiandrogen and XIAP inhibitor for treating advanced prostate cancer. *Pharm. Res.* **29**, 2079-2091 (2012).
4. Li, F., Danquah, M., Mahato R.I. Synthesis and Characterization of Amphiphilic Lipopolymers for Micellar Drug Delivery. *Biomacromolecules***. 11**, 2610–20 (2010)**.**
5. Danquah, M., Fujiwara, T. & Mahato, R. I. Self-assembling methoxy poly(ethylene glycol)-b-poly(carbonate-co-L-lactide) block copolymers for drug delivery. *Biomaterials* **31**, 2358-2370 (2010).
6. Danquah, M., Li, F., Duke, C. B.,3rd, Miller, D. D. & Mahato, R. I. Micellar delivery of bicalutamide and embelin for treating prostate cancer. *Pharm. Res.* **26**, 2081-2092 (2009).

Review Articles

1. Li, F., & Mahato, R.I. MicroRNAs and drug resistance in prostate cancers. *Mol Pharm* **4**, 2539-52 (2014).
2. Danquah M, Zhang X, Mahato R. I. Extravasation of polymeric nanomedicines across tumor vasculature. *Adv Drug Deliv Rev.* **8**, 623-39 (2011).

Journal Theme Issue Editor

Li, F., & Mahato, R.I. miRNAs as targets for cancer treatment: Therapeutics design and delivery. *Adv Drug Deliv Rev.* (2015).

Book Editor

Mahato RI and Narang AS (2011), Pharmaceutical Dosage Forms and Drug Delivery, 2nd Edition, CRC Press, Inc., FL

Abstracts

1. Roles of Chemoresistance, Cancer Stem Cells and miRNA in treating Cancer using Polymeric Nanomedicines, Center for Drug Delivery and Nanomedicine, University of Nebraska Medical Center, April 19, 2012

Presentations/Invited Speaker

1. Polymeric Nanomedicines of Antiandrogen and XIAP Inhibitors for Treating Prostate Cancer, Prostate Cancer Focus Group, University of Nebraska Medical Center, October 16, 2014.
2. Polymeric Nanomedicines of Small Molecules and miRNA for Treating Advanced Pancreatic and Prostate Cancers, 6th Mayo Clinic Angiogenesis Symposium, Rochester, MN August 22, 2014.
3. Roles of Chemoresistance, Cancer Stem Cells and miRNA in treating Cancer using Polymeric Nanomedicines, Fudan University, Shanghai, China, September 10, 2013.
4. Nanomedicines Targeting Chemoresistance, Cancer Stem Cells and miRNA for effective treatment of Prostate and Pancreatic Cancer, China Pharmaceutical University, Nanjing, China, September 11, 2013.
5. Roles of Chemoresistance, Cancer Stem Cells and miRNA in treating Cancer using Polymeric Nanomedicines, Department of Pharmaceutical Sciences, Mercer University, Atlanta, GA, September 6, 2013.

Degrees Issued

Michael Danquah (Ph.D. in Pharmaceutical Sciences, 2012).

CONCLUSIONS

We have demonstrated the synergy between anti-androgen and XIAP-inhibitor for improved prostate cancer cell killing in vitro and tumor regression in vivo. We analyzed the miRNA profile in DU145-TXR and PC3-TXR cells and prostate cancer tissue from the patients showed decreased expression of tumor suppressor miRNAs such as miR34a and miR200c. We have demonstrated that LHRH peptide conjugated LHRH-PEG-b-p (CB-co-LA) copolymer provided an effective targeting to LHRH receptors that are overexpressed in prostate cancer cells and facilitated site-specific drug delivery to prostate tumor after systemic administration. We also demonstrated that CBDIV17 loaded LHRH-PEG-b-p(CB-co-LA) micelles was significantly inhibited prostate tumor growth compared to CBDIV17 loaded HOOC-PEG-b-p(CB-co-LA) and control groups. CBDIV17 loaded LHRH-PEG-b-p(CB-co-LA) micelles exhibited significant in vivo antitumor efficacy by reducing cancer cells proliferation and enhancing Caspase 3 expression level.

References

1. Damber, J. E. & Aus, G. Prostate cancer. *Lancet* **371**, 1710-1721 (2008).

2. Yoshida, T. *et al*. Antiandrogen bicalutamide promotes tumor growth in a novel androgen-dependent prostate cancer xenograft model derived from a bicalutamide-treated patient. *Cancer Res.* **65**, 9611-9616 (2005).

3. Danquah, M., Duke, C. B.,3rd, Patil, R., Miller, D. D. & Mahato, R. I. Combination therapy of antiandrogen and XIAP inhibitor for treating advanced prostate cancer. *Pharm. Res.* **29**, 2079-2091 (2012).

4. Danquah, M., Li, F., Duke, C. B.,3rd, Miller, D. D. & Mahato, R. I. Micellar delivery of bicalutamide and embelin for treating prostate cancer. *Pharm. Res.* **26**, 2081-2092 (2009).

5. Dharap, S. S. *et al*. Tumor-specific targeting of an anticancer drug delivery system by LHRH peptide. *Proc. Natl. Acad. Sci. U. S. A.* **102**, 12962-12967 (2005).

6. Wen, D. *et al*. LHRH-conjugated micelles for targeted delivery of antiandrogen to treat advanced prostate cancer. *Pharm. Res.* **31**, 2784-2795 (2014).

7. Danquah, M., Fujiwara, T. & Mahato, R. I. Self-assembling methoxy poly(ethylene glycol)-b-poly(carbonate-co-L-lactide) block copolymers for drug delivery. *Biomaterials* **31**, 2358-2370 (2010).

8. Lu, J., Owen, S. C. & Shoichet, M. S. Stability of Self-Assembled Polymeric Micelles in Serum. *Macromolecules* **44**, 6002-6008 (2011).

9. Horoszewicz, J. S. *et al*. LNCaP model of human prostatic carcinoma. *Cancer Res.* **43**, 1809-1818 (1983).

10. Liu, C. *et al*. The microRNA miR-34a inhibits prostate cancer stem cells and metastasis by directly repressing CD44. *Nat. Med.* **17**, 211-215 (2011).

11. Croce, C. M. & Calin, G. A. miRNAs, cancer, and stem cell division. *Cell* **122**, 6-7 (2005).

12. Singh, S. *et al*. Chemoresistance in prostate cancer cells is regulated by miRNAs and Hedgehog pathway. *PLoS One* **7**, e40021 (2012).

Appendix

1. Wen, D, Chitkara, D., Wu, H., Danquah, M., Patil, R., Miller, D.D., & Mahato, R.I. LHRH-conjugated micelles for targeted delivery of antiandrogen to treat advanced prostate cancer. *Pharm Res* **31**, 2784-95 (2014).
2. Li F. and Mahato R.I. microRNAs and drug resistance in prostate cancers. Mol. Pharmaceutics. **11**, 2539−52 (2014).
3. Singh, S. *et al*. Chemoresistance in prostate cancer cells is regulated by miRNAs and Hedgehog pathway. *PLoS One* **7**, e40021 (2012).
4. Danquah, M., Duke, C. B.,3rd, Patil, R., Miller, D. D. & Mahato, R. I. Combination therapy of antiandrogen and XIAP inhibitor for treating advanced prostate cancer. *Pharm. Res.* **29**, 2079-2091 (2012).
5. Danquah M, Zhang X, Mahato R. I. Extravasation of polymeric nanomedicines across tumor vasculature. Adv Drug Deliv Rev. **8**, 623-39 (2011).
6. Li, F., Danquah, M., Mahato R.I. Synthesis and Characterization of Amphiphilic Lipopolymers for Micellar Drug Delivery. *Biomacromolecules***. 11**, 2610–20 (2010)**.**
7. Danquah, M., Fujiwara, T. & Mahato, R. I. Self-assembling methoxy poly(ethylene glycol)-b-poly(carbonate-co-L-lactide) block copolymers for drug delivery. *Biomaterials* **31**, 2358-2370 (2010).
8. Danquah, M., Li, F., Duke, C. B.,3rd, Miller, D. D. & Mahato, R. I. Micellar delivery of bicalutamide and embelin for treating prostate cancer. *Pharm. Res.* **26**, 2081-2092 (2009).

LIST OF PERSONS RECEIVED PAY FROM THE RESEARCH EFFORT

1	Name	Michael Danquah
	Project Role	Graduate student
	Researcher Identifier	0000-0001-7408-3951
	Nearest person month worked	24
	Contribution to project	
	Funding support	
2	Name	Feng Li
	Project Role	Graduate Student
	Researcher Identifier	
	Nearest person month worked	12
	Contribution to project	Synthesized and characterized lipopolymer micelles for embelin delivery
	Funding support	
3	Name	Saurabh Singh
	Project Role	Post-Doctoral Fellow
	Researcher Identifier	
	Nearest person month worked	12
	Contribution to project	Analyzed the role of miRNAs and side population in chemoresistance
	Funding support	
4	Name	Di Wen
	Project Role	Graduate student
	Researcher Identifier	0000-0002-9547-481X

	Nearest person month worked	12
	Contribution to project	Synthesized and characterized LHRH modified micelles.
	Funding support	

Pharm Res (2014) 31:2784–2795
DOI 10.1007/s11095-014-1375-6

RESEARCH PAPER

LHRH-Conjugated Micelles for Targeted Delivery of Antiandrogen to Treat Advanced Prostate Cancer

Di Wen • Deepak Chitkara • Hao Wu • Michael Danquah • Renukadevi Patil • Duane D. Miller • Ram I. Mahato

Received: 10 February 2014 / Accepted: 21 March 2014 / Published online: 2 May 2014

ABSTRACT

Purpose Our objective was to synthesize LHRH-conjugated amphiphilic copolymer for micellar delivery of CBDIV17, a novel antiandrogen for treating prostate cancer.

Methods LHRH-PEG-b-p(CB-co-LA) was synthesized by opening polymerization of carbonate (CB), lactide (LA), and HOOC-PEG-OH followed by conjugation with LHRH analogue. Bicalutamide analogue CBIDV17 loaded micelles were formulated by film hydration method, and characterized for critical micelle concentration (CMC), drug loading and *in vitro* drug release. Formulations were tested on LNCaP and C4-2 cells for cellular uptake, induction of apoptosis, viability and dowregulation of androgen receptor (AR). *In vivo* studies were performed in ectopic tumor bearing athymic nude mice after tail vein injection at a dose of 10 mg/kg. Tumor volume and body weight were measured for 25 days followed by immunohistochemistry (IHC) of tumor samples for Ki-67, caspase-3, and prostate specific antigen (PSA).

Results HOOC-PEG-b-p(CB-co-LA) and LHRH-PEG-b-p(CB-co-LA) were characterized by ^{1}HNMR and used for preparing micelles, which had a mean particle size of 75.60 ± 2.25 and 72.64 ± 1.15 nm, respectively and CBDIV17 loading of 4.6% w/w. LHRH conjugated micelles showed higher cellular uptake, cytotoxicity, and apoptosis in LNCaP and C4-2 cells compared to non-targeted micelles. CBDIV17 loaded LHRH micelles more efficiently inhibited the proliferation and induced apoptosis of tumor cells according to Ki-67, caspase-3, and PSA expression. There was significant inhibition of tumor growth with the treatment of CBDIV17 loaded LHRH-conjugated micelles.

Conclusion These results demonstrated that LHRH-b-PEG-p (CB-co-LA) micelles have the potential for targeted delivery of CBDIV17 to treat advanced prostate cancer.

KEY WORDS antiandrogen · bicalutamide · LHRH · micelles · prostate cancer

INTRODUCTION

Androgen ablation or blockade of androgen receptor (AR) is the cornerstone of treating early stage prostate cancer. Among various antiandrogens for chemotherapy, bicalutamide has long half-life and tolerable side effects, leading to its wide clinical application for treating early stage prostate cancer (1). However, prolonged treatment with bicalutamide leads to AR proliferation and mutation, which converts bicalutamide from an AR antagonist into an AR agonist. To overcome this issue, we previously synthesized bicalutamide analog CBDIV17, which was more potent than bicalutamide in inhibiting the proliferation of prostate cancer cells and suppressing tumor growth *in vivo* (2). Despite its high efficacy, poor aqueous solubility of CBDIV17 (less than 50 mg/L) results in low and variable drug absorption.

Polymeric micelles are nanosized and have spherical structures with a hydrophobic core, which is able to improve the solubility and stability of hydrophobic anticancer drugs. To enhance the solubility of CBDIV17, we synthesized polyethylene glycol-b-poly (carbonate-co-lactide) (PEG-b-p(CB-co-LA)) copolymer (2–5) to prepare micelles, which successfully encapsulated bicalutamide, embelin, and some other drugs. In our previous results (2), CBDIV17 loaded micelles showed high antitumor efficacy and successfully suppressed tumor growth *in vivo*. However, intratumoral injection of these micelles limited its clinical application to prostate cancer.

D. Wen • D. Chitkara • R. I. Mahato
College of Pharmacy, University of Nebraska Medical Center, Omaha Nebraska 68198, USA

H. Wu • M. Danquah • R. Patil • D. D. Miller
Department of Pharmaceutical Sciences, University of Tennessee Health Science Center, Memphis, Tennessee 38163, USA

R. I. Mahato (✉)
Department of Pharmaceutical Sciences, University of Nebraska Medical Center, 986025 Nebraska Medical Center, Omaha Nebraska 68198-6025, USA
e-mail: ram.mahato@unmc.edu
URL: http://www.unmc.edu/pharmacy/mahato

Traditional chemotherapy usually employs high dose of anti-cancer drugs, which usually cause severe toxicity to healthy organs. Passive targeting tumors *in vivo* mainly utilized enhanced permeability and retention (EPR) effect (6,7) causing preferential accumulation of macromolecules at the tumor site. However, EPR effect is only efficient for targeting solid tumors and is not used for spreading tumors and metastases (8). Active targeting can be used to make micelles site-specific by coupling a target moiety for receptors overexpressed on cancer cells. Furthermore, targeting cancer cells can diminish the cytotoxicity towards other tissues and the drugs loaded micelles accumulate selectively to tumor site (9,10). For targeted delivery of anti-cancer drugs, several receptors, which are overexpressed by cancer cells, are selected as targets for polymer binding, such as prostate specific membrane antigen (PSMA) (11), epidermal growth factor receptor (EGFR) (12), and luteinizing-hormone-releasing hormone (LHRH) receptor (13).

LHRH is a 10 amino acid peptide hormone secreted by hypothalamus and regulates gametogenesis (14). Overexpressed LHRH receptors are detected in prostate (86%), ovarian (80%), and breast (50%) cancers and have low expression in healthy organs (7,15–17). In recent years, LHRH and its analogs have been employed in the clinical trial in the management of prostate cancer. We expect active targeting by LHRH to be safe and efficient after systemic administration. Due to the short half-life of natural LHRH, synthetic LHRH analogue with improved bioactivity has been widely used for targeting LHRH-R (18,19). Therefore, we conjugated LHRH analog to our previously synthesized HOOC-PEG-b-p(CB-co-LA) copolymer and hypothesize that LHRH conjugated micelles would improve the efficacy of antitumor drug *in vitro* and *in vivo* and provide targeted drug delivery to suppress tumor growth. In this study, HOOC-PEG-b-p(CB-co-LA) and LHRH-PEG-b-p(CB-co-LA) were synthesized, characterized, and used for preparing micelles for targeted delivery of CBDIV17. We evaluated the drug therapeutic efficacy of LHRH-conjugated micelles carrying CBDIV17 in an ectopic athymic mouse model of prostate cancer.

MATERIALS AND METHODS

Materials

2, 2-Bis(hydroxymethyl) propionic acid and benzyl bromide were purchased from Sigma Aldrich (St. Louis, MO). Hydroxyl poly(ethylene glycol) carboxyl (HOOC-PEG-OH, M_n = 5000) was purchased from Jenkem Technology (Allen, TX). SYBR Green, real-time RT-PCR master mix, and reverse transcription reagents were purchased from Roche (Indianapolis, IN). LHRH analog peptide, PYR-His-Trp-Ser-Tyr-^{D}Lys-Leu-Arg-Pro-Gly-$CONH_2$, was purchased from Hanhong Group (Shanghai, China). CBDIV17 was synthesized as reported earlier (2). All other chemicals were of analytical grade and used as received.

Synthesis of LHRH-PEG-b-p(CB-co-LA)

5-Methyl-5-benzyloxycarbonyl-1, 3-dioxane-2-one (MBC) and HOOC-PEG-b-p(CB-co-LA) were synthesized as described earlier (20). Briefly, 2, 2-bis(hydroxymethyl)propionic acid (26.8 g, 0.2 mol) and potassium hydroxide (12.72 g, 0.2 mol) were dissolved in 150 mL of dimethylformamide (DMF) and allowed to heat at 100°C for 1 h. Benzyl bromide (41.5 g, 0.243 mol) was then added dropwise and continuously stirred at 100°C for 15 h. DMF was evaporated under vacuum and the crude product was dissolved in ethyl acetate (150 mL), hexanes (150 mL), and water (100 mL). The organic layer was separated, washed with water, and dried with Na_2SO_4. The final solution was evaporated to obtain benzyl 2, 2-bis(methylol)propionate (23.8 g, 56.64%), which was subsequently recrystallized using toluene.

To synthesize 5-methyl-5-benzyloxycarbonyl-1,3-dioxane-2-one (MBC) (base monomer), benzyl 2, 2-bis (methylol)propionate (22.4 g, 0.1 mol) dissolved in pyridine (50 mL) and CH_2Cl_2 (200 mL), and chilled to −78°C over dry ice. A solution of triphosgene (50 mmol, 14.8 g) dissolved in CH_2Cl_2 was added dropwise to the above solution and allowed to stir for 1 h at −78°C and for additional 2 h at room temperature. The solution was quenched with saturated aqueous NH_4Cl. Organic layer was washed with 1 M HCl, saturated aqueous $NaHCO_3$ and then dried with Na_2SO_4. The pure MBC (19.7 g, 88.3%) was obtained by evaporating the organic solvent under vacuum and recrystalized using ice-cold ethyl acetate.

To synthesize HOOC-PEG-b-p(CB-co-LA) with the molecular weight of 10000, 1, 8-diazabicyclo[5.4.0]undec-7-ene (DBU) (40 μL) as a catalyst was added to the mixture of HOOC-PEG-OH (1 g), lactide (0.6 g) and base monomer (0.4 g) dissolved in 10 mL of anhydrous CH_2Cl_2 and allowed to react for 3 h under stirring at room temperature. At the end of the reaction, benzoic acid (60 mg) was added and the solvent was removed under vacuum. Crude polymer was purified by dissolving in chloroform, and precipitate in large amount of isopropanol and diethyl ether, followed by drying under vacuum for 48 h.

Purified copolymer (100 mg, 0.01 mmol) and LHRH-NH_2 (27 mg, 0.02 mmol) were dissolved in a mixture of anhydrous DMSO (3 mL) and anhydrous CH_2Cl_2 (12 mL). The mixture was allowed to stir for 30 min following which 1-Ethyl-3-(3-dimethylaminopropyl)carbodiimide · HCl (EDC · HCl) (3.0 mg, 0.0134 mM) and 4-dimethylaminopyridine (1.0 mg, 0.008 mM) were added. After 48 h, CH_2Cl_2 was removed under vacuum and the mixture was purified by dialysis

(molecular mass cutoff, 3,500 Da) using water as a solvent. Purified LHRH conjugated polymer was dried by lyophilization.

Polymers were characterized using ^{1}HNMR recorded on a Varian (500 MHz, T = 25°C) using DMSO-d_6 as a solvent. The chemical shifts were calibrated using tetramethylsilane as an internal reference and reported as parts per million.

Critical Micelle Concentration

Fluorescence spectroscopy was used to estimate the critical micelle concentration (CMC) of HOOC-PEG-b-p(CB-co-LA) and LHRH-PEG-b-p(CB-co-LA) copolymer using pyrene as a hydrophobic fluorescent probe. Sixteen samples of HOOC-PEG-b-p(CB-co-LA) or LHRH-PEG-b-p(CB-co-LA) dissolved in water with concentrations ranging from 1.0×10^{-8} to 1 g/L were prepared and allowed to equilibrate with a constant pyrene concentration of 6.0×10^{-7} M overnight at room temperature while shaking at 200 rpm. The fluorescent spectra of pyrene were recorded at an excitation wavelength of 335 nm and emission wavelength of 373 nm (I_1) and 384 nm (I_3) using spectrofluorometer (Sunnyvale, CA). Peak height intensity ratio (I_3/I_1) was plotted against the logarithm of polymer concentration. Value of the CMC was obtained as the point of intersection of two tangents drawn to the curve at high and low concentrations, respectively.

Formulation and Characterization of Drug-loaded Micelles

CBDIV17 loaded micelles were prepared using the film hydration method as previously described with slight modifications (21). Briefly, 5 mg of CBDIV17 and 95 mg of HOOC-PEG-b-p(CB-co-LA) or LHRH-PEG-b-p(CB-co-LA) were dissolved in 5 mL chloroform. Solvent was evaporated under vacuum and resulting film was hydrated in 10 mL of phosphate buffered saline (PBS), and sonicated for 10 min using a Misonix ultrasonic liquid processor (Farmingdale, NY) with an amplitude of 60. Free drug was removed by centrifugation at 5,000 rpm for 5 min and filtration using a 0.22 μm nylon filter. Drug loaded micelles were concentrated by Amicon Ultra-15 Centrifugal Filter Unit (3,000 Da) and stored at 4°C. For further characterization, mean particle size and size distribution of drug-loaded micelles were measured by dynamic light scattering using a Malvern Zetasizer (Worcestershire, UK).

Drug Loading and Encapsulation Efficiency

To determine the drug loading and encapsulation efficiency, drug loaded micelles were dissolved in acetonitrile (ACN). Concentration of CBDIV17 was measured by reverse phase high performance liquid chromatography (RP-HPLC, Waters, Milford, MA) with a UV detector at 290 nm using a reverse phase C18 Column (250 mm × 4.6 mm, Inertsil ODS). The mobile phase was composed of 60:40 V/V of acetonitrile and water. CBDIV17 concentration was calculated according to the peak area using the following standard calibration equation: A = 703400X-59.22 (R^2 = 0.999). Drug loading content and encapsulation efficiency were determined using following equations:

$$\text{Drug loading density} = \frac{\text{weight of drug in micelles}}{\text{weight of micelles}} \times 100\% \quad (1)$$

$$\text{Drug encapsulation efficiency} = \frac{\text{weight of drug in micelles}}{\text{weight of drug originally fed}} \times 100\% \quad (2)$$

In Vitro Drug Release Study

Drug release from HOOC-PEG-b-p(CB-co-LA) and LHRH-PEG-b-p(CB-co-LA) micelles was determined after dialysis (3,500 Da cut off) against 25 mL PBS containing 0.1% Tween 80 (pH = 7.2) in a thermo-controlled shaker with a speed of 100 rpm (5). 1 mL samples were taken at specific time points (1, 3, 6, 12, 24, 48, 96, 144, 192 h) and replaced with fresh PBS containing 0.1% tween 80. Drug concentration was measured using RP-HPLC as described for drug loading. Cumulative amount of drug released was evaluated as the percentage of total drug release to the initial amount. All experiments were performed in triplicate and the data reported as the mean of three individual experiments.

Cell Culture and Maintenance

Human prostate cancer cells C4-2 and lymph node prostate adenocarcinoma (LNCaP) were purchased from American Type Culture Collection (ATCC, Manassas, VA). LNCaP and C4-2 cells were cultured in RPMI 1640 media containing 10% fetal bovine serum, 1% antibiotic-antimycotic, and 1% sodium pyruvate at 37°C in humidified environment with 5% CO_2. RWPE-1 cell line was kindly provided by Dr. Ming-Fong Lin (University of Nebraska Medical Center, Omaha, NE).

Cellular Uptake of Targeted Micelles

Cellular uptake study was performed as described by Zou (22) and Kutty (23) with minor modification. LNCaP and C4-2 cells were seeded at a density of 1×10^5 cells/well in 96 well plates. After reaching confluence, medium was replaced by

coumarin-6 loaded micelles suspensions with concentration of 0.3 mg/ml. After 2 h incubation, the micelles solution was removed and cells were washed twice with 1 × PBS. The cells were examined using inverted fluorescent microscope after DAPI staining. For quantitative study, the cells were immersed in 0.5% Triton X-100 in 0.2 N NaOH solutions and concentration of coumarin-6 was measured at excitation wavelength of 430 nm, and emission wavelength of 485 nm. The reading of wells with the cells alone represented the background intensity and was set up as a negative control. The reading of the wells with coumarin-6 loaded micelles (0.3 mg/mL) was used as a positive control. The efficiency of cellular uptake was calculated as (*I*: fluorescence intensity):

$$\text{Uptake efficiency } \% = \frac{I_{sample} - I_{negative}}{I_{positive} - I_{negative}} \times 100\%$$

Cell Viability Assay

Cells were seeded in 96-well plate at a density of 5,000 cells/well to determine cytotoxicity of free, HOOC-PEG-b-p(CB-CO-LA) or LHRH-PEG-b-p(CB-CO-LA) micelles loaded with CBDIV17 at the concentration of 10, 25, 50 μmol/L for 48 h. The cellular toxicity of the two polymers was also determined in these two cell lines. At the end of the treatment, the original medium was replaced by fresh medium with 0.5 mg/mL MTT (3-(4,5-dimethylthiazol-2-yl)-2,5-diphenyltetrazolium bromide) and incubated for another two hours. The supernatant was removed carefully and MTT crystals were dissolved in 200 μl DMSO and analyzed at a wavelength of 560 nm. Cell viability was calculated as a percentage of control using the following formula:

$$\text{Cell viability } (\%) = \frac{absorbance\ \ of\ \ test\ \ sample}{absorbance\ \ of\ \ control} \times 100\%$$

Real-Time RT-PCR

Expression of LHRH receptor was determined by quantitative real-time RT-PCR. Briefly, LNCaP and C4-2 cells were seeded in 24-well plate at the density of 5×10^5cells/well overnight. Total mRNA was isolated from cultured cells using RNeasy mini isolation kit (Qiagen, Valencia, CA) and the concentration was determined by Nanodrop 2000 (Thermo Scientific, Wilmington, DE). 170 ng of total mRNA was converted to cDNA using TaqMan Reverse Transcription Reagents (Life Technologies, Grand Island, NY). cDNA was used as a template and analyzed by SYBR Green universal PCR master mix (Life Technologies, Grand Island, NY) on Roche Real-time PCR instrument. S19 was used as an internal control. All samples were run in triplicate. The primer sequences were as follows: human LHRH receptor (Type 1) (forward): 5′-GACCTTGTCTGGAAAGATCC-3′, (reverse) 5′-CAGGCTGATCACCACCATCA-3′; human S19 (forward): 5′- GGAGCTCTATCCTCTCTCTATT-3′, (reverse): 5′-CCCAGCATGGTTTGTTCTAATG-3′.

Western Blot Analysis

C4-2 (2×10^6/well) cells seeded in 6-well plate were treated with CBDIV17 loaded LHRH-PEG-b-p(CB-co-LA) with the drug concentration of 25 μmol/L for 48 h. Subsequently, cells were lysed with RIPA buffer (Sigma-Aldrich, St. Louis, MO) and protein concentration was measured with micro BCA protein assay kit (Thermo Scientific, Wilmington, DE). The lysate was then mixed with 6 × Laemmli Buffer (Bioworld, Dublin, OH) and boiled for 5 min. The samples were loaded to 4–15% SDS-PAGE for electrophoresis and subsequently transferred to immobilon polyvinylidene fluoride (PVDF) membrane. Membranes were blocked with 5% bovine serum albumin (BSA) in tris buffered saline at room temperature for 1 h and further incubated with primary antibody at 4°C overnight, followed by incubation with secondary antibody conjugated with infrared dyes (IRDye) at room temperature for 1 h. After washing with tris buffered saline and tween 20 for 3 times, the signal of target protein was detected using Li-COR Odyssey infrared imaging system (Li-COR, Lincoln, NE).

Caspase 3 Activity

Caspase 3 activity was analyzed with Caspase-Glo 3 assay kit as per manufacturer's protocol. To a single cell suspension generated by 0.25% Trypsin-EDTA digestion, 100 μL of Caspase-Glo was added with the concentration of 10^4 cells/well in 96 well plate and incubated at room temperature for 1 h. The solution was then transferred to culture tubes to determine luminescence by a luminometer (Berthold, Bad Wildbad, Germany).

In Vivo Efficacy of Drug Loaded LHRH Conjugated Micelles in Ectopic Tumor Bearing Mice

All experiments were performed following the NIH animal use guidelines and the protocol was approved by the Animal Care and Use Committee (ACUC) at the University of Nebraska Medical Center. Ectopic flank tumors were induced in 6 weeks old male athymic nude mice (Jackson Laboratory, Bar Harbor, ME) by subcutaneous injection of 2 million C4-2 cells suspended in 1:1 serum free media and Matrigel. The mice were randomized into the following three groups when the tumor size reached to 150 mm^3: i) untreated control, ii) CBDIV17 loaded non-conjugated micelles, iii) CBDIV17

loaded LHRH conjugated micelles. Formulations were injected intravenously *via* tail vein at the concentration of 10 mg/kg at 3 day intervals for 25 days. Animal body weight and tumor volume were monitored three times a week. Tumors were measured with a caliper prior to each injection, and their volumes calculated using the formula as follows:

$$\text{Volumes} = \left(\text{width}^2 \times \text{length}\right)/2 \quad (3)$$

To determine apoptosis and proliferation of tumor cells, tumors from mice were excised and fixed in 10% buffered formalin, followed by routinely proceeding to paraffin. For embedding histology, 5 μm thick sections were stained with Hematoxylin & Eosin for detection of tumor architecture. Cell proliferation and apoptosis were determined using an antibody against Ki-67 and caspase-3, respectively. The prostate cancer treatment was evaluated by PSA level.

Statistical Analysis

Statistical significance of difference between two groups was determined by unpaired *t* test.

RESULTS

Synthesis and Characterization of HOOC-PEG-b-p (CB-co-LA) and LHRH-PEG-b-p(CB-co-LA)

HOOC-PEG-b-p(CB-co-LA) copolymer was synthesized by ring opening polymerization of L-lactide and 5-methyl-5-benzyloxycarbonyl-1,3-dioxane-2-one using HOOC-PEG as the macroinitiator and DBU as a catalyst. The peak (Fig. 1a) at δ: 10.64 ppm demonstrated the carboxyl group and the multiplet peak at δ: 4–4.5 ppm confirms the successful ring opening polymerization. The following NMR peaks of copolymers were observed of the copolymers at δ: 1.25 (CH_3 in CB unit, s, 3H); δ: 1.60 (CH_3 in LA unit, s, 3H); δ: 3.51 (CH_2 in PEG, m, 4H); δ: 4.15–4.35 (CH_2 in CB main chain, m, 4H); δ: 5.10–5.16 (CH in LA unit q, 1H and CH_2 in CB side group, s, 2H); δ 7.36 (phenyl, m, 5H).

LHRH-PEG-b-p(CB-co-LA) was synthesized by conjugating NH_2 group of DLys in LHRH peptide to COOH group of HOOC-PEG-b-P(CB-co-LA). Conjugation was confirmed by ^{1}HNMR. The peak (Fig. 1c) at δ: 10.64 disappeared and new peaks were observed at δ: 6.80, δ: 6.94, δ: 7.18, δ: 7.82, δ: 8.18, δ: 8.31, δ: 8.64, δ: 8.85, and δ: 9.63 (Fig. 1f), which demonstrated the successful conjugation of LHRH peptide.

Preparation and Characterization of HOOC-PEG-b-p (CB-co-LA) and LHRH-PEG-b-p(CB-co-LA) Copolymer Micelles

We used film sonication method to formulate micelles of HOOC-PEG-b-p(CB-co-LA) and LHRH-PEG-b-p(CB-co-LA) copolymers. Mean particle size of blank and drug loaded micelles was in the range of 72.64-98.91 nm as determined by dynamic light scattering (Table I). Our result showed that the particle size was not influenced by LHRH conjugation. Micelles were further characterized by critical micelle concentration (CMC). Similar CMC values of HOOC-PEG-b-p (CB-co-LA) and LHRH-PEG-b-p(CB-co-LA) suggest that the conjugation of LHRH does not influence the self-assembly of the polymer (Fig. 2a).

In vitro Drug Loading and Drug Release from Micelles

The amount of CBDIV17 loaded into micelles was calculated using Eq. (1) based on 5% theoretical drug loading. According to our result (Table I), CBDIV17 loading were not influenced by LHRH conjugation. CBDIV17 loading was 4.59 ± 0.01%. There was 50% of CBDIV17 released from both micelles after 24 h. LHRH conjugation did not affect the *in vitro* release of CBDIV17 (Fig. 2b).

In Vitro Cellular Uptake

To demonstrate the effect of LHRH conjugation on cellular uptake, we first determined LHRH receptor expression on LNCaP and C4-2 cancer cells and found to be overexpressed by at least two folds as determined by real time RT-PCR (Fig. 3a), while LHRH receptor was poorly expressed on RWPE-1 cells. We then determined the cellular uptake of coumarin-6 loaded micelles. Figure 3b and c show fluorescent microscope image of LNCaP and C4-2 cells after 2 h incubation with coumarin-6 loaded non-conjugated or LHRH conjugated micelles. The nucleus stained by DAPI was circumvented by green fluorescence of coumarin-6, suggesting that the micelles were internalized in the cytoplasm. Both cell lines incubated with coumarin-6 loaded LHRH-PEG-b-p (CB-co-LA) micelles exhibited brighter fluorescence. Figure 3d and e shows fluorescent intensity reading of the two micelles in LNCaP and C4-2 cell lines. The uptake efficiency of non-conjugated micelles was 22.7% for LNCaP and 28.3% for C4-2. The uptake efficiency of LHRH-PEG-b-p(CB-co-LA) micelles was 33.1% for LNCaP and 35.3% for C4-2. There was no significant difference in the fluorescent intensity between HOOC-PEG-b-p(CB-co-LA) and LHRH-PEG-b-p(CB-co-LA) (data not shown). It can be seen that the uptake of micelles in both cell lines, which has overexpressed LHRH receptor, significantly increased with LHRH conjugation. However, LHRH conjugation did not influence cellular

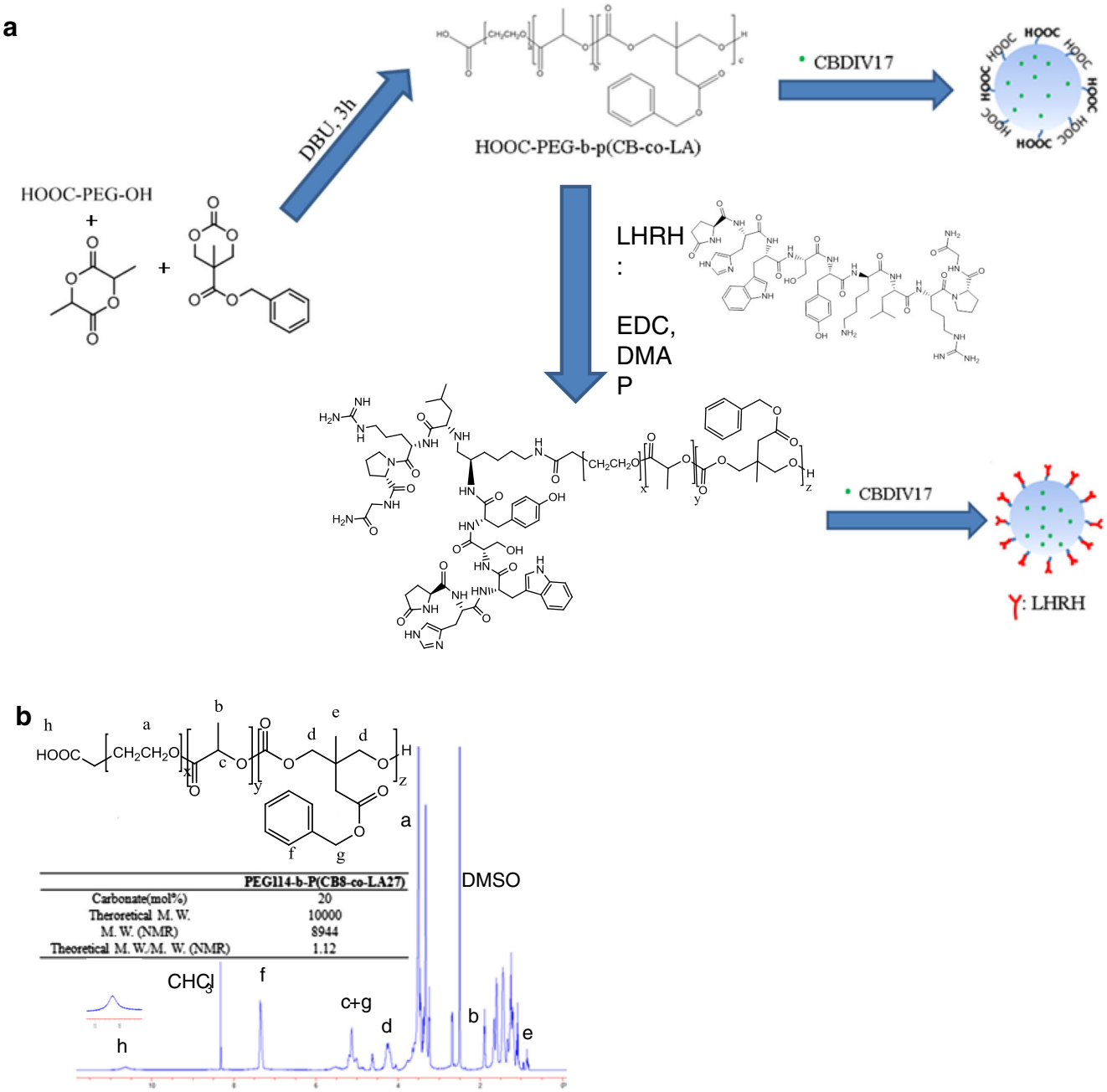

Fig. 1 Synthesis and characterization of LHRH-PEG-b-p(CB-co-LA) copolymer. (**a**) Outline of synthesis and formulation, (**b**) NMR of HOOC-PEG-b-p(CB-co-LA), (**c**) NMR of LHRH peptide and (**d**) NMR of LHRH-PEG-b-p(CB-co-LA), (**e**) Structure and NMR of LHRH peptide (ppm 6–9), (**f**) NMR of LHRH-PEG-b-p (CB-co-LA) (ppm 6–9).

uptake of micelles for RWPE-1 cells, which does not have detectable LHRH receptor, according to both fluorescent image and reading (Data not shown).

Effect of CBDIV17 Loaded LHRH-PEG-b-p(CB-co-LA) and HOOC-PEG-b-p(CB-co-LA) on LNCaP and C4-2 Growth

We determined the anticancer activity of CBDIV17 loaded micelles in LNCaP and C4-2 cells. As shown in Fig. 4a and b, CBDIV17 exhibited dose dependent anti-cancer activity in both the cell lines. Drug loaded micelles were more cytotoxic than free drug. IC50 of free CBDIV17, CBDIV17 loaded HOOC-PEG-b-p(CB-co-LA), and CBDIV17 loaded LHRH-PEG-b-p(CB-co-LA) was 25.2, 21.9, and 12.8 μM respectively in LNCaP cells. In C4-2 cells, it was 37.1, 30.9, and 19.8 μM respectively for free CBDIV17, CBDIV17 loaded HOOC-PEG-b-p(CB-co-LA), and CBDIV17 loaded LHRH-PEG-b-p(CB-co-LA) micelles. Additionally, there was a dramatic increase in the inhibition of prostate cancer cell growth

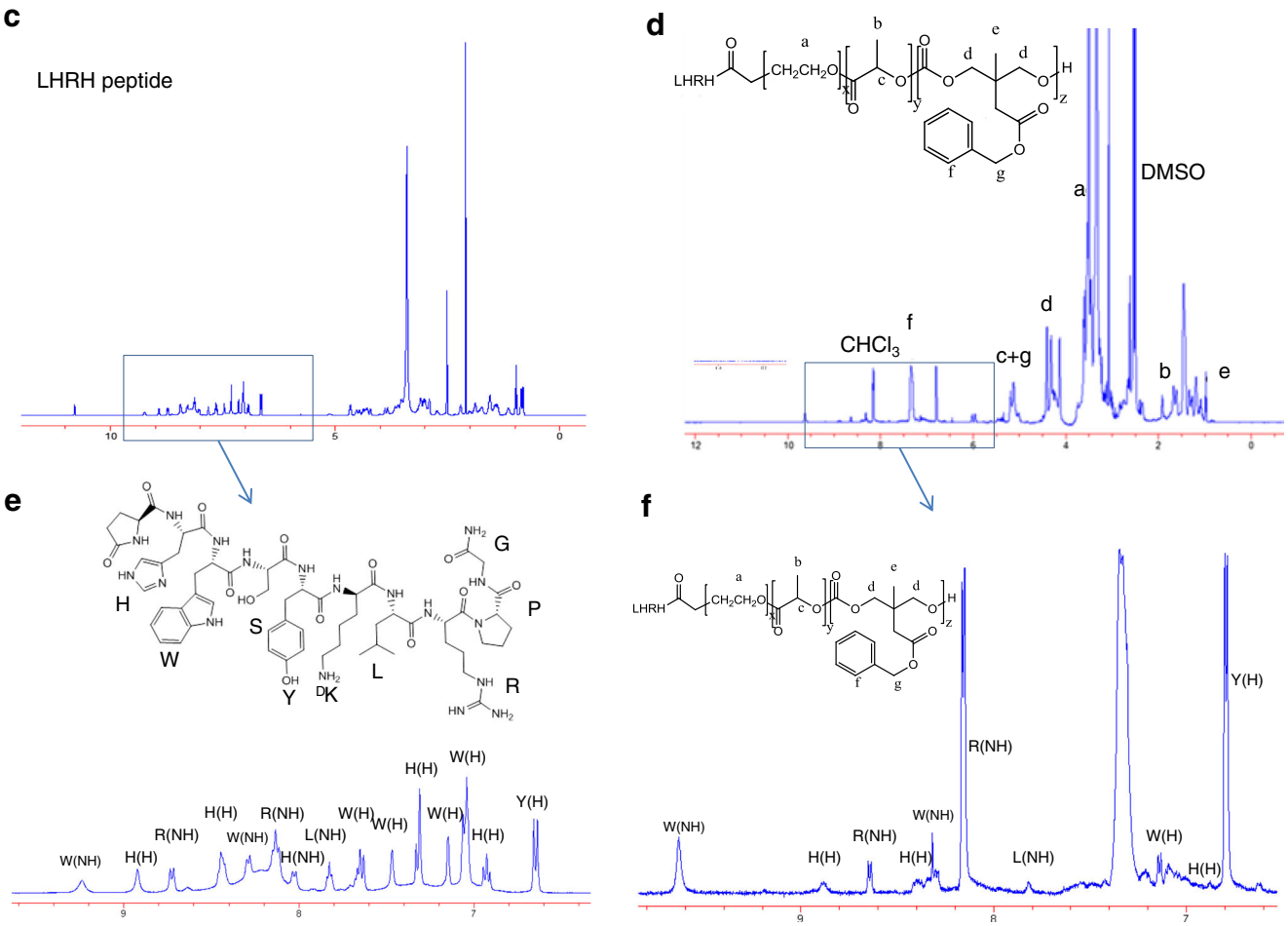

Fig. 1 (continued)

for drug loaded LHRH-PEG-b-p(CB-co-LA) micelles compared to drug loaded HOOC-PEG-b-p(CB-co-LA) micelles, suggesting LHRH conjugated micelles increased cellular uptake of CBDIV17 compared to non-conjugated micelles.

Caspase 3 and AR Activity

We next examined the influence of CBDIV loaded micelles on Caspase 3. Drug loaded micelles, especially LHRH conjugated micelles, induced more cell apoptosis than free drug according to Caspase 3 activity (Fig. 4c).

Furthermore, we determined the effect of drug loaded micelles on the transcriptional activity of AR by measuring protein expression of AR and prostate specific antigen (PSA) after treating LNCaP and C4-2 cells with 25 μmol/L LHRH-PEG-b-p(CB-co-LA) for 48 h. As shown in Fig. 4d, PSA protein expression was significantly downregulated with CBDIV17 loaded LHRH-PEG-b-p(CB-co-LA) micelles treated, while there was little effect on AR expression.

Table I Particle Size and CBDIV17 Loading (%) of HOOC-b-p(CB-co-LA) and LHRH-PEG-bp(CB-co-LA) Micelles

	Size (nm)	PDI	Drug loading (%)	Encapsulation Efficiency (%)
Before drug loading				
HOOC-PEG-b-p(CB-co-LA)	75.60 ± 2.25	0.242 ± 0.01	–	–
LHRH-PEG-b-p(CB-co-LA)	72.64 ± 1.15	0.195 ± 0.01	–	–
After CBDIV17 loading				
HOOC-PEG-b-p(CB-co-LA)	82.33 ± 3.93	0.237 ± 0.02	4.59 ± 0.01	91.80 ± 0.20
LHRH-PEG-b-p(CB-co-LA)	84.59 ± 3.29	0.197 ± 0.02	4.54 ± 0.17	90.80 ± 3.40

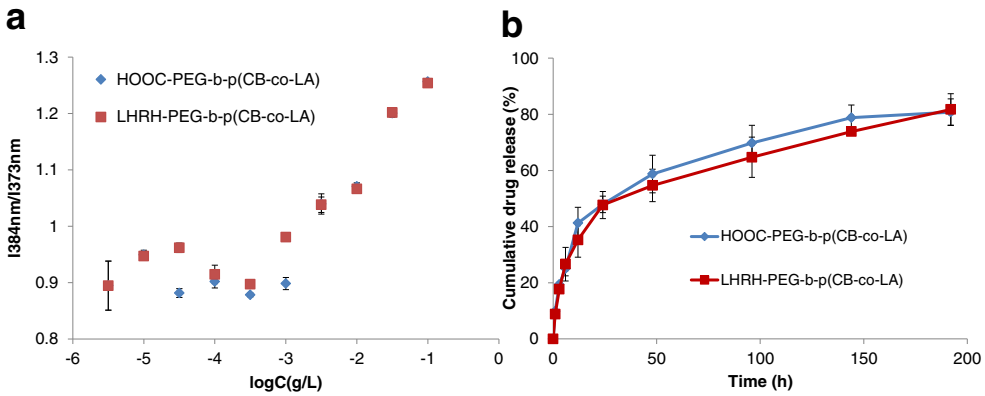

Fig. 2 Characterization of HOOC-PEG-b-p(CB-co-LA) and LHRH-PEG-b-p(CB-co-LA). (**a**) Plots of intensity ratio I_1(373 nm)/I_3(384 nm) from pyrene fluorescence emission spectra *versus* log concentration (g/L) of HOOC-PEG-b-p(CB-co-LA) and LHRH-PEG-b-p(CB-co-LA); (**b**) CBDIV17 release from HOOC-PEG-b-p(CB-co-LA) and LHRH-PEG-b-p(CB-co-LA) micelles. Release experiments were performed in triplicates. Data presented as the mean ± S.D. ($n = 3$).

In Vivo Efficacy of CBDIV17 Loaded Micelles

Since LHRH-PEG-b-p(CB-co-LA) significantly enhanced the effect of CBDIV17 *in vitro*, we further determined the effect of CBDIV17 loaded micelles in C4-2 ectopic tumor bearing athymic mice. CBDIV17 were formulated to HOOC-PEG-b-p(CB-co-LA) and LHRH-PEG-b-p(CB-co-LA) with the concentration of 2 mg/mL. The formulation was injected intravenously 4 times at the dose of 10 mg/kg at 3 day intervals. Changes in the relative tumor volume and body weight are shown in Fig. 5. Tumor growth was significantly inhibited by both CBDIV17 loaded HOOC-PEG-b-p(CB-co-LA) and LHRH-PEG-b-p(CB-co-LA) micelles. CBDIV17 loaded LHRH-PEG-b-p(CB-co-LA) micelles were more

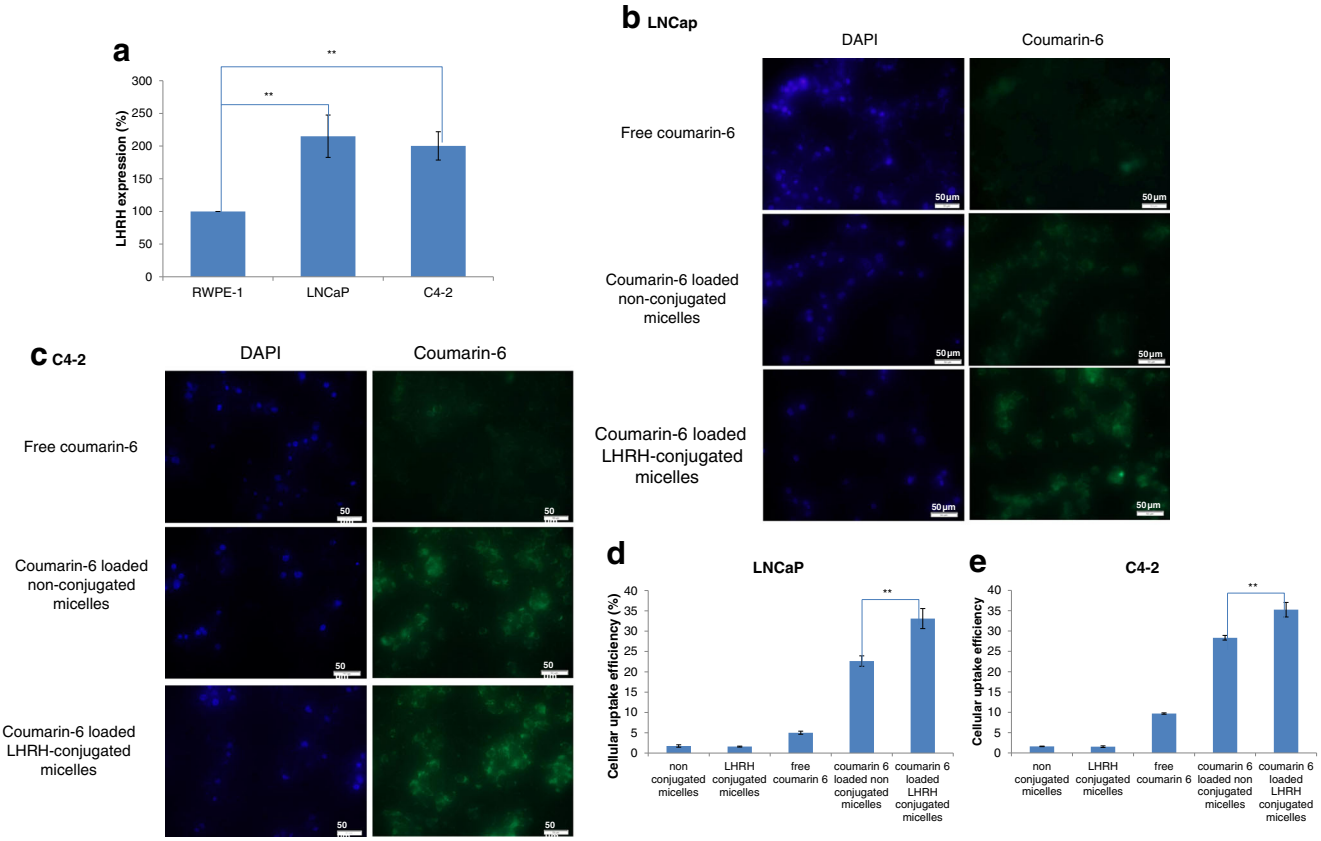

Fig. 3 Effect of LHRH conjugated micelles on the cellular uptake of antiandrogen CBDIV17. (**a**) LHRH expression by prostate cancer cells as determined by RT-PCR; (**b** and c) Fluorescent microscopy of coumarin-6 loaded LHRH-conjugated and non-conjugated micelles after incubation in LNCaP and C4-2 cells; (**d** and **e**) Cellular uptake of CBDIV17 after encapsulation into LHRH-conjugated and non-conjugated micelles. Data presented as the mean ± S.D. ($n = 3$).

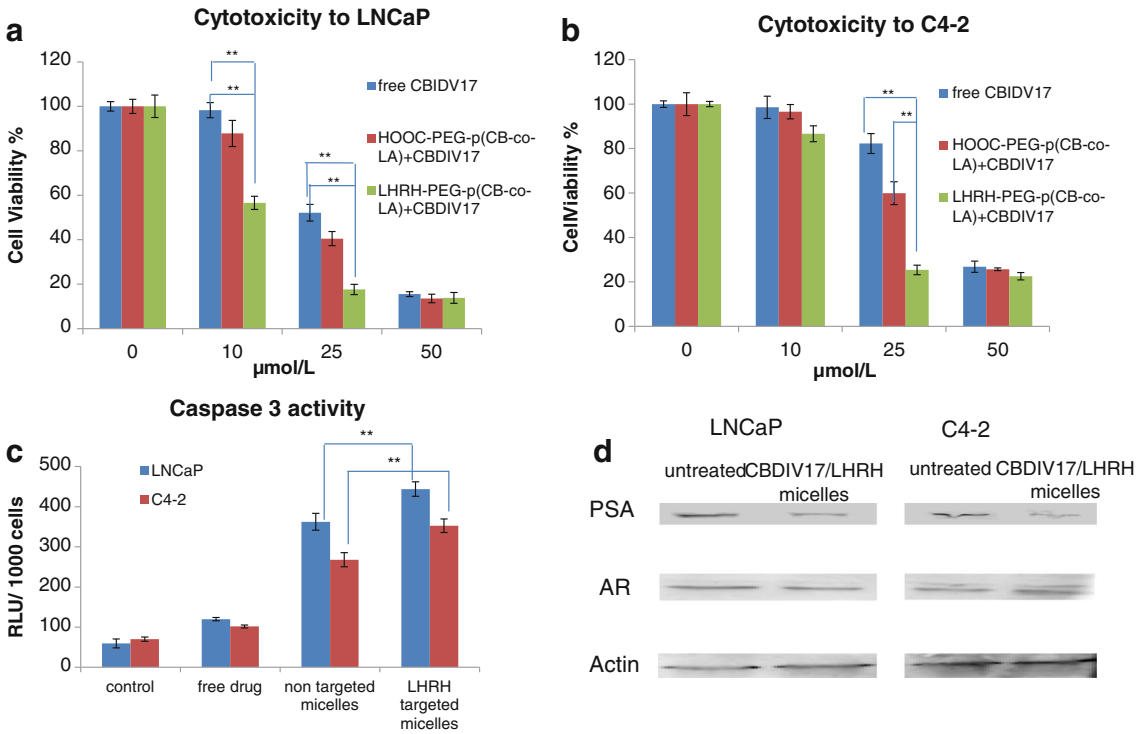

Fig. 4 Effect of HOOC-PEG-b-p(CB-co-LA) and LHRH-PEG-b-p(CB-co-LA) micellar formulation of CBDIV17 on inhibition of LNCaP and C4-2 cell proliferation. MTT assay was used for cell viability estimation. All experiments were performed in triplicates. (**a**) Cytotoxicity of CBDIV17 loaded micelles to LNCaP cells. (**b**) Cytotoxicity of CBDIV17 loaded micelles to C4-2 cells. (**c**) Caspase 3 activity after treating with 25 μmol/L CBDIV17 for 48 h. (**d**) Western blot of PSA and AR after 25 μmol/L CBDIV17 loaded micelles treated for 48 h.

effective in inhibiting tumor growth compared to CBDIV17 loaded HOOC-PEG-b-p(CB-co-LA) micelles. No significant loss in body weight was observed in the whole study, suggesting acceptable toxicity of the treatment (Fig. 5b).

On day 17, the tumors from these three groups were excised and incubated with Ki-67 and Caspase-3 antibodies to elucidate the mechanism of tumor suppression (Fig. 6). The number of cell proliferation marker Ki-67 positive cells in the control group was significantly higher compared to the mice that received CBDIV17 loaded HOOC-PEG-b-p(CB-co-LA) and LHRH-PEG-B-P(CB-CO-LA) micelles, indicating that micellar delivery of CBDIV17 efficiently suppressed tumor growth. There were only minor Ki-67 positive cells in tumor tissues from the mice injected with CBDIV17 loaded LHRH-PEG-b-p(CB-co-LA) micelles. CBDIV17 loaded LHRH-PEG-b-p(CB-co-LA) micelles were the most efficient in inducing cell apoptosis to the tumor tissues, leading to high Caspase-3 expression. Furthermore, nucleus intensity of

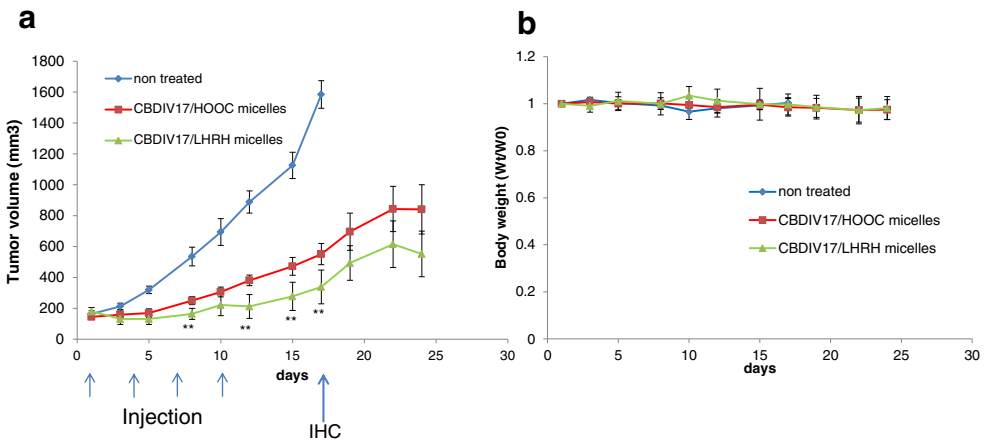

Fig. 5 Effects of CBDIV17/HOOC-PEG-b-p(CB-co-LA) and CBDIV17/LHRH-PEG-b-p(CB-co-LA) micelles on tumor growth *in vivo* (**a**) Tumor growth curve (**b**) Body weight. The number of mice use per group was 5.

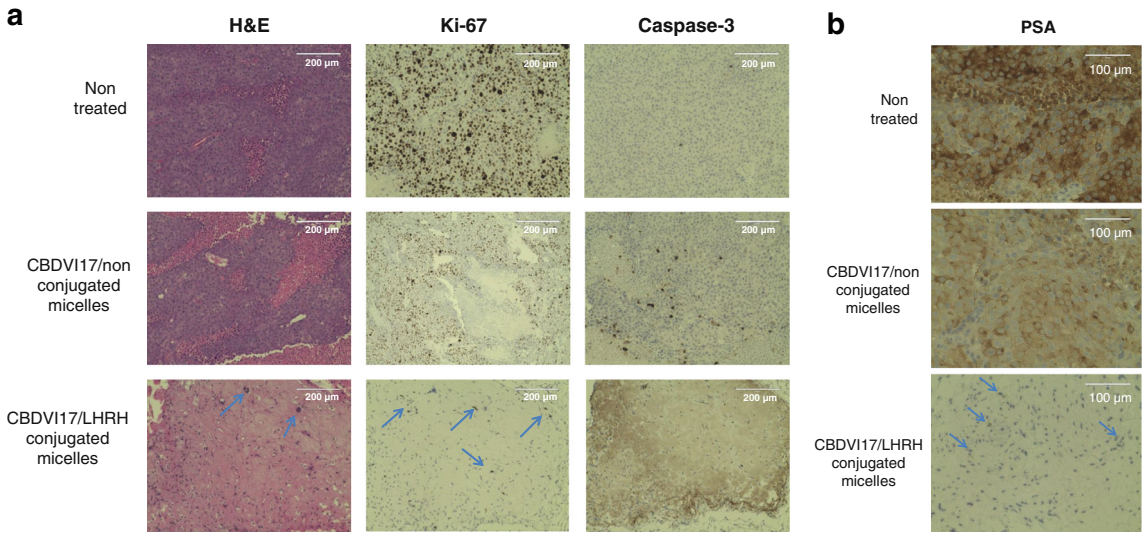

Fig. 6 Effects of CBDIV17 loaded HOOC-PEG-b-p(CB-co-LA) and LHRH-PEG-b-p(CB-co-LA) micelles on Ki-67, Caspase-3, and PSA expression in tumor.

CBDIV17/LHRH-PEG-b-p(CB-co-LA) group was obviously less other two groups, suggesting tumor growth has been successfully suppressed. Enhanced Caspase-3 expression was also observed in CBDIV17 loaded HOOC-PEG-b-p(CB-co-LA) treated tumor compared to control group, which proved antitumor efficacy of non-target delivery of CBDIV17.

DISCUSSION

Androgen inhibition is the first choice for treating early stage prostate cancer. However, AR mutation and drug resistance after prolonged treatment makes this approach less effective. Thus, more potent drugs to block androgen activity are necessary to treat advanced prostate cancer. We have previously shown that CBDIV17 was more potent than bicalutamide in inhibiting the proliferation of LNCaP and C4-2 cells (2). However, the poor solubility of CBDIV17 (less than 50 mg/L) limits its potential applications. To solve this issue, we thereby have formulated polymeric micelles, which solubilize the drugs with their hydrophobic core. Furthermore, polymeric micelles exhibit passive targeting due to the enhanced permeability and retention (EPR) effect causing preferential accumulation in tumors and inflammation sites. For targeted delivery of drug loaded micelles to the tumors, LHRH peptide was conjugated to HOOC-PEG-b-p (CB-co-LA) copolymer for targeting delivery of CBDIV17 to tumor site after systemic administration. LHRH peptide provides an effective targeting ligand to LHRH receptors overexpressed in prostate cancer cells and limited drug accumulation in normal organs, where LHRH receptors are not expressed detectably. Due to the wide application of LHRH analog, such as leuprolide, buserelin and histrelin, in the clinical trials, active targeting by LHRH analog are expected to be safe and efficient.

A modified synthetic analog of LHRH, which has free amine group to be linked with polymer without affecting its function, was used as a targeting moiety to LHRH receptors. Therefore, the choice of conjugation with –COOH or –NHS was offered (24,25). According to our NMR spectra and cytotoxicity results, the conjugation of LHRH with HOOC-PEG-b-p(CB-co-LA) was successful and there was significant difference in cytotoxicity when LHRH was conjugated to the micelles. Our results suggest that—COOH is efficient to be connected with LHRH for targeting LNCaP and C4-2 cells. LHRH conjugation did not affect the release profile of CBDIV17 (Fig. 2b). After LHRH conjugation, cellular uptake was significantly enhanced in LHRH receptor overexpressed cell lines (Fig. 3).

LHRH has been an effective systemic treatment for prostate cancer for the past 7 decades (26). Thus, we first demonstrated the non-cytotoxicity of free LHRH analog, HOOC-PEG-b-p(CB-co-LA), and LHRH-PEG-b-p(CB-co-LA) (data not shown). We observed significant cytotoxicity caused by LHRH conjugated micelles with 10 μM of CBDIV17 in LNCaP cells and 25 μM in C4-2 cells after incubating for 48 h (Fig. 4a and b). Significantly lower IC 50 demonstrated higher efficacy and cellular uptake of CBDIV17 after coating with LHRH-PEG-b-p(CB-co-LA). Blockage of androgen activity did not show high efficiency in C4-2 cells, which is androgen independent. Significantly higher Caspase 3 activity was also observed upon treatment with CBDIV17 loaded LHRH-PEG-b-p(CB-co-LA) micelles as compared to free drug and drug loaded by non-conjugated micelles, suggesting higher cell apoptosis.

PSA, which is a pivotal downstream target gene of androgen receptor (27), is always elevated in the presence of prostate

cancer and other prostate disorders. Blocking AR would reduce the transcription activity of AR, which reduces the expression of PSA. Our data (Fig. 4d) showed that AR protein expression was not influenced by CBDIV17 loaded LHRH-PEG-b-p(CB-co-LA) micelles while PSA expression was significantly inhibited. These results were similar to previously published results of bicalutamide (28,29). It means CBDIV17 does not downregulate AR expression but binds to AR and prevent AR activation, which is same as the mechanism of bicalutamide.

Following *in vitro* characterization, CBDIV17 were formulated and concentrated to HOOC-PEG-b-p(CB-co-LA) or LHRH-PEG-b-p(CB-co-LA) to evaluate tumor suppression efficacy in mice bearing C4-2 xenografts. Consistent with *in vitro* data, CBDIV17loaded LHRH-PEG-b-p(CB-co-LA) micelles was more potent in repressing prostate tumor growth compared to CBDIV17 loaded HOOC-PEG-b-p(CB-co-LA) and control groups. To further determine the mechanism of antitumor effect, we evaluated the expression of cell proliferation marker Ki-67 and apoptosis marker Caspase-3 to elucidate cell proliferation and apoptosis level in tumor tissue. Few Ki-67 positive cells and high Caspase-3 expression level demonstrated significant *in vivo* antitumor efficacy of CBDIV17 loaded LHRH-PEG-b-p(CB-co-LA). We also observed similar but less effect of CBDIV17 loaded HOOC-PEG-b-p(CB-co-LA) and tumor growth suppression after CBDIV17 loaded HOOC-PEG-b-p(CB-co-LA) treatment, which is probably caused by EPR effect.

In conclusion, we have successfully conjugated LHRH peptide to HOOC-PEG-b-p(CB-co-LA) and demonstrated that LHRH conjugation did not affect CMC, CBDIV17 loading, and drug release profile. We also revealed the mechanism of CBDIV17 as an androgen receptor antagonist. Finally, CBDIV17 loaded LHRH-PEG-b-p(CB-co-LA) showed significant potential to suppress tumor cell growth *in vitro* and *in vivo*.

ACKNOWLEDGMENTS AND DISCLOSURES

This work is supported by an Idea Award (W81XWH-10-1-0969) from the Department of Defense Prostate Cancer Research Program. We would like to thank Dr. Ming-Fong Lin of the Department of Biochemistry and Molecular Biology, University of Nebraska Medical Center for his help in analyzing IHC figures.

REFERENCES

1. Blackledge G. Casodex–mechanisms of action and opportunities for usage. Cancer. 1993;72(12 Suppl):3830–3.
2. Danquah M, Duke 3rd CB, Patil R, Miller DD, Mahato RI. Combination therapy of antiandrogen and XIAP inhibitor for treating advanced prostate cancer. Pharm Res. 2012;29(8):2079–91.
3. Chitkara D, Singh S, Kumar V, Danquah M, Behrman SW, Kumar N, *et al.* Micellar delivery of Cyclopamine and Gefitinib for treating pancreatic cancer. Mol Pharm. 2012;9:2350–7.
4. Kumar V, Mundra V, Mahato RI. Nanomedicines of Hedgehog Inhibitor and PPAR-gamma Agonist for treating liver fibrosis. Pharm Res 2013 Nov 19.
5. Mundra V, Lu Y, Danquah M, Li W, Miller DD, Mahato RI. Formulation and characterization of polyester/polycarbonate nanoparticles for delivery of a novel microtubule destabilizing agent. Pharm Res. 2012;29(11):3064–74.
6. Greish K, Fang J, Inutsuka T, Nagamitsu A, Maeda H. Macromolecular therapeutics: advantages and prospects with special emphasis on solid tumour targeting. Clin Pharmacokinet. 2003;42(13):1089–105.
7. Grundker C, Gunthert AR, Millar RP, Emons G. Expression of gonadotropin-releasing hormone II (GnRH-II) receptor in human endometrial and ovarian cancer cells and effects of GnRH-II on tumor cell proliferation. J Clin Endocrinol Metab. 2002;87(3):1427–30.
8. Chandna P, Saad M, Wang Y, Ber E, Khandare J, Vetcher AA, *et al.* Targeted proapoptotic anticancer drug delivery system. Mol Pharm. 2007;4(5):668–78.
9. Minko T. Drug targeting to the colon with lectins and neoglycoconjugates. Adv Drug Deliv Rev. 2004;56(4):491–509.
10. Minko T, Dharap SS, Pakunlu RI, Wang Y. Molecular targeting of drug delivery systems to cancer. Curr Drug Targets. 2004;5(4):389–406.
11. Chen Z, Penet MF, Nimmagadda S, Li C, Banerjee SR, Winnard Jr PT, *et al.* PSMA-targeted theranostic nanoplex for prostate cancer therapy. ACS Nano. 2012;6(9):7752–62.
12. Yip WL, Weyergang A, Berg K, Tonnesen HH, Selbo PK. Targeted delivery and enhanced cytotoxicity of cetuximab-saporin by photochemical internalization in EGFR-positive cancer cells. Mol Pharm. 2007;4(2):241–51.
13. Taratula O, Kuzmov A, Shah M, Garbuzenko OB, Minko T. Nanostructured lipid carriers as multifunctional nanomedicine platform for pulmonary co-delivery of anticancer drugs and siRNA. J Control Release. 2013;171(3):349–57.
14. Delves PJ, Lund T, Roitt IM. Antifertility vaccines. Trends Immunol. 2002;23(4):213–9.
15. Dharap SS, Qiu B, Williams GC, Sinko P, Stein S, Minko T. Molecular targeting of drug delivery systems to ovarian cancer by BH3 and LHRH peptides. J Control Release. 2003;91(1–2):61–73.
16. Dharap SS, Minko T. Targeted proapoptotic LHRH-BH3 peptide. Pharm Res. 2003;20(6):889–96.
17. Engel J, Emons G, Pinski J, Schally AV. AEZS-108: a targeted cytotoxic analog of LHRH for the treatment of cancers positive for LHRH receptors. Expert Opin Investig Drugs. 2012;21(6):891–9.
18. Pu C, Chang S, Sun J, Zhu S, Liu H, Zhu Y, *et al.* Ultrasound-mediated destruction of LHRHa-targeted and paclitaxel-loaded lipid microbubbles for the treatment of Intraperitoneal ovarian cancer xenografts. Mol Pharm. 2014;11(1):49–58.
19. Dharap SS, Wang Y, Chandna P, Khandare JJ, Qiu B, Gunaseelan S, *et al.* Tumor-specific targeting of an anticancer drug delivery system by LHRH peptide. Proc Natl Acad Sci U S A. 2005;102(36):12962–7.
20. Danquah M, Fujiwara T, Mahato RI. Lactic acid- and carbonate-based crosslinked polymeric micelles for drug delivery. J Polym Sci A Polym Chem. 2013;51(2):347–62.
21. Danquah M, Fujiwara T, Mahato RI. Self-assembling methoxypoly (ethylene glycol)-b-poly(carbonate-co-L-lactide) block copolymers for drug delivery. Biomaterials. 2010;31(8):2358–70.

22. Zou T, Gu L. TPGS emulsified zein nanoparticles enhanced oral bioavailability of daidzin: in vitro characteristics and in vivo performance. Mol Pharm. 2013;10(5):2062–70.
23. Kutty RV, Feng SS. Cetuximab conjugated vitamin E TPGS micelles for targeted delivery of docetaxel for treatment of triple negative breast cancers. Biomaterials. 2013;34(38):10160–71.
24. Taratula O, Garbuzenko OB, Kirkpatrick P, Pandya I, Savla R, Pozharov VP, *et al.* Surface-engineered targeted PPI dendrimer for efficient intracellular and intratumoral siRNA delivery. J Control Release. 2009;140(3):284–93.
25. Jiang X, Sha X, Xin H, Chen L, Gao X, Wang X, *et al.* Self-aggregated pegylated poly (trimethylene carbonate) nanoparticles decorated with c(RGDyK) peptide for targeted paclitaxel delivery to integrin-rich tumors. Biomaterials. 2011;32(35):9457–69.
26. Huggins C, Hodges CV. Studies on prostatic cancer: I. The effect of castration, of estrogen and of androgen injection on serum phosphatases in metastatic carcinoma of the prostate. 1941. J Urol. 2002;168(1):9–12.
27. Saxena P, Trerotola M, Wang T, Li J, Sayeed A, Vanoudenhove J, *et al.* PSA regulates androgen receptor expression in prostate cancer cells. Prostate. 2012;72(7):769–76.
28. Wang Y, Mikhailova M, Bose S, Pan CX, deVere White RW, Ghosh PM. Regulation of androgen receptor transcriptional activity by rapamycin in prostate cancer cell proliferation and survival. Oncogene. 2008;27(56):7106–17.
29. Colquhoun AJ, Venier NA, Vandersluis AD, Besla R, Sugar LM, Kiss A, *et al.* Metformin enhances the antiproliferative and apoptotic effect of bicalutamide in prostate cancer. Prostate Cancer Prostatic Dis. 2012;15(4):346–52.

molecular pharmaceutics

Review

pubs.acs.org/molecularpharmaceutics

MicroRNAs and Drug Resistance in Prostate Cancers

Feng Li*,† and Ram I. Mahato*,‡

†Department of Pharmaceutical Sciences, School of Pharmacy, Hampton University, Hampton, Virginia 23668, United States

‡Department of Pharmaceutical Sciences, University of Nebraska Medical Center, Omaha, Nebraska 68198, United States

ABSTRACT: Prostate cancer is the second leading cause of cancer related death in American men. Androgen deprivation therapy (ADT) is used to treat patients with aggressive prostate cancers. After androgen deprivation therapy, prostate cancers slowly progress to an androgen-independent status. Taxanes (e.g., docetaxel) are used as standard treatments for androgen-independent prostate cancers. However, these chemotherapeutic agents will eventually become ineffective due to the development of drug resistance. A microRNA (miRNA) is a small noncoding RNA molecule, which can regulate gene expression at the post-transcription level. miRNAs elicit their effects by binding to the 3′-untranslated region (3′-UTR) of their target mRNAs, leading to the inhibition of translation or the degradation of the mRNAs. miRNAs have received increasing attention as targets for cancer therapy, as they can target multiple signaling pathways related to tumor progression, metastasis, invasion, and chemoresistance. Emerging evidence suggests that aberrant expression of miRNAs can lead to the development of resistant prostate cancers. Here, we discuss the roles of miRNAs in the development of resistant prostate cancers and their involvement in various drug resistant mechanisms including androgen signaling, apoptosis avoidance, multiple drug resistance (MDR) transporters, epithelialmesenchymal transition (EMT), and cancer stem cells (CSCs). In addition, we also discuss strategies for treating resistant prostate cancers by targeting specific miRNAs. Different delivery strategies are also discussed with focus on those that have been successfully used in human clinical trials.

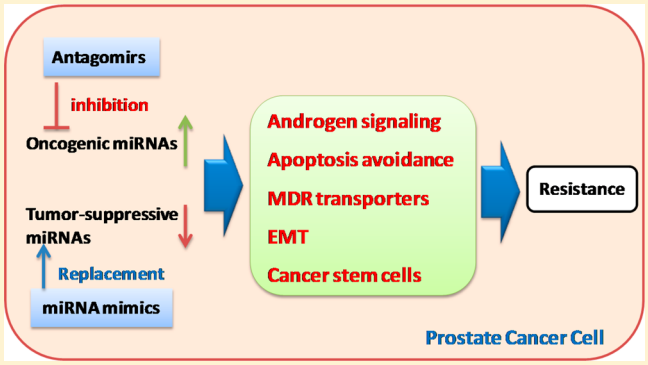

KEYWORDS: *miRNA, prostate cancers, chemoresistance, cancer stem cells, epithelial−mesenchymal transition (EMT), androgen resistance, apoptosis, MDR transporters, delivery systems*

1. INTRODUCTION

Prostate cancer is the second leading cause of cancer related death in men in the United States. It is estimated that 238,590 new cases of prostate cancer were diagnosed in 2013 and that approximately 29,720 men died from this disease in 2013.[1,2] Although a localized prostate cancer can be effectively treated with less difficulty, the treatment of aggressive and metastatic forms of prostate cancer is a significant challenge. Currently, androgen deprivation therapy (ADT) is used to treat patients with aggressive prostate cancers. Despite temporary response, most patients relapse and eventually progress to androgen-independent prostate cancers (AIPCs).[3,4] AIPCs are developed because of the perturbation of androgen receptor (AR) signaling. Taxanes (e.g., docetaxel) are used as standard treatments for AIPCs.[5] However, only half of the patients respond to docetaxel therapy. Even those who initially respond to docetaxel treatment will eventually become resistant.[6−9]

MicroRNAs (miRNAs) were first discovered in 1993 as endogenous small noncoding RNA molecules in *Caenorhabditis elegans*.[10] miRNAs can regulate gene expression at the post-transcription level. Mature miRNAs of 18−22 nucleotides in length recognize and bind to the 3′-untranslated region (3′-UTR) of target mRNAs, leading to the degradation of target mRNAs or the inhibition of translation. miRNAs are being implicated in a range of physiological processes (e.g., development, cell differentiation, cell cycle control, and metabolism) as well as the pathogenesis of several human diseases, including prostate cancers.[11,12] Deregulated miRNAs are involved in initiation, progression, and metastasis of prostate cancers. These miRNAs can be classified as oncogenic miRNAs, which can promote cancer progression, and tumor suppressor miRNAs, which can inhibit the progression of prostate cancers. Because of the significant role of miRNAs in prostate cancers, they have been extensively investigated as therapeutic targets for cancer treatment as well as biomarkers for diagnosis. The unique advantage of using miRNAs as targets for cancer therapy lies in the fact that a single miRNA can regulate multiple target genes in the same signaling pathway or even multiple signaling pathways and therefore can be more effective in treating cancers that are inherently heterogeneous and are resulted from the deregulation of multiple genes.

Special Issue: Drug Delivery and Reversal of MDR

Received: February 1, 2014
Revised: April 11, 2014
Accepted: April 17, 2014
Published: April 17, 2014

   dx.doi.org/10.1021/mp500099g | *Mol. Pharmaceutics* 2014, 11, 2539−2552

An increasing number of miRNAs has been discovered in prostate cancer cell lines as well as human tissue samples, indicating the significant functional roles of miRNAs in prostate cancers. Emerging evidence suggests that miRNAs are involved in the development of resistant prostate cancers through the regulation of androgen signaling pathway, apoptosis, drug transporters, epithelialmesenchymal transition (EMT), and cancer stem cells (CSCs) (Figure 1). Here, we discuss the

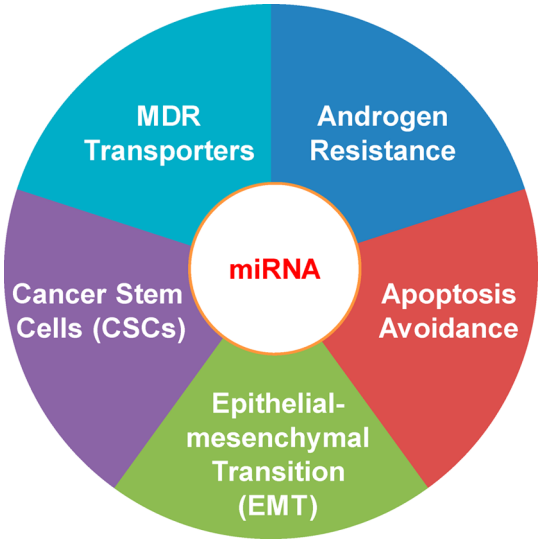

Figure 1. miRNAs regulate prostate cancer drug-resistance through different mechanisms.

regulatory roles of miRNAs in the above cellular processes and their involvement in the development of resistant prostate cancers. The use of these miRNAs as potential therapeutic targets for treating resistant prostate cancers and the design of appropriate therapeutic approaches are also discussed. Different delivery strategies are also discussed with focus on those that have been successfully used in human clinical trials.

2. ROLE OF MIRNAS IN DIFFERENT DRUG RESISTANCE MECHANISMS

2.1. Androgen Signaling. Early stage localized prostate cancers need androgen for proliferation. Therefore, androgen ablation is a standard treatment for recurred prostate cancers after radiation therapy. However, most prostate cancers eventually obtain the capacities to survive without androgens and develop resistance to hormone therapy. At this stage, prostate cancers are defined as AIPCs or hormone refractory prostate cancers (HRPCs). AR, which is a nuclear hormone receptor, plays a significant role in the development of AIPCs. The role of AR signaling in the progression of prostate cancers to androgen independence has been previously discussed.[13] Many studies have investigated the interaction between AR signaling and miRNAs as well as the involvement of miRNAs in the progression of AIPCs. Evidence indicates that miRNAs are critical modulators of androgen signaling (Table 1).

2.1.1. Up-Regulation of miRNAs in AIPCs. miR-125b is overexpressed in AIPCs. The overexpression of miR-125b confers the resistance of LNCaP prostate cancer cells to androgen withdrawal. Prostate cancer cells can be sensitized to chemotherapy through the inhibition of miR-125b. The target genes regulated by miR-125b include p53, Puma, and Bak1.[14−16] Genome-wide expression profile studies showed

Table 1. Deregulated miRNAs in AIPCs

miRNA	targets	refs
Up-Regulated		
miR-125b	P53, Puma, BAK1	14−16
miR-221/-222	P27/Kip1, HECTD2, RAB1A	17−19
miR-32	BTG2	22
miR-21	PDCD4, maspin	20,22
miR-148a	PIK3IP1	22
miR-616	TFPI-2	23
miR-375 378 141		24
Down-Regulated		
miR-146a	ROCK1, EGFR, MMP2	22,23
let-7c	AR	24,25
miR-124	AR, p53	29
miR-34a,c	AR, PSA, Notch-1	27,28
miR-148a	MSK1	32
miR-31	AR, E2F1, E2F2, EXO1, FOXM1, MCM2	33
miR-200b-3p		34
miR-185	AR, CDC6	35
miR-205	AR, PSA	36

that miR-221/-222 were also up-regulated in AIPCs as well as bone metastatic tumor specimens.[17] The analysis of human tumor specimens indicated that 90% of the AIPCs had up-regulated miR-221/-222 expression.[18] The overexpression of miR-221/-222 in AIPCs (e.g., LNCaP and LAPC-4) could promote androgen-independent cell growth.[17] miR-221 also promotes androgen resistance through the down-regulation of HECTD2 and Ras-related protein Rab-1A (RAB1A).[19] miR-21 is also overexpressed in AIPCs.[20−22] A microarray analysis showed that miR-21 was an AR responsive miRNA. AR regulates the transcription of miR-21 by binding to its promoter. Overexpression of miR-21 in AIPCs could make them resistant to androgen ablation. In addition, the reduction of miR-21 could inhibit androgen-induced prostate cancer growth.[20,21] miR-616 induces androgen-independent growth of prostate cancers by suppressing the expression of tissue factor pathway inhibitor (TFPI-2).[23] Circulating miRNAs are also associated with the progression of AIPCs. A recent study showed that serum samples from a patient with AIPCs had high levels of miR-375, miR-378*, and miR-141, indicating their roles in the development of AIPCs. These signature circulating miRNAs have the potential to be used as biomarkers for prostate cancer diagnosis.[24]

2.1.2. Down-Regulation of miRNAs in AIPCs. Several tumor suppressive miRNAs are down-regulated in AIPCs, including miR-146a,[25,26] *let-7C*,[27,28] miR-124,[29] miR-34a, miR-34c,[30,31] miR-148a,[32] miR-31,[33] miR-200b-3p,[34] miR-185,[35] and miR-205.[36] Down-regulation of these tumor suppressive miRNAs in prostate cancer may lead to cancer progression, increased aggressiveness, and resistance to androgen deprivation therapy. For example, down-regulation of miR-205 is also correlated with the poor therapeutic outcome of prostate cancer patients.[36] Restoration of these miRNAs in AIPCs can inhibit cell growth, reduce cell invasion, and prevent metastasis. AR is negatively regulated by several miRNAs including *let-7C*, miR-124, miR-34a, miR-34c, miR-31, miR-183, and miR-205. Down-regulation of these miRNAs results in the overexpression of AR, which is an important risk factor for androgen independence.[13] These miRNAs also regulate other targets in AIPCs. The targets of miR-146a include Rho-associated, coiled-coil containing protein kinase 1 (ROCK1), epidermal growth factor

receptor (EGFR), and matrix metalloproteinase-2 (MMP2). Down-regulation of miR-146a is critical for the overexpression of EGFR in AIPCs.[25,26] miR-124 can increase p53 levels.[29] miR-34a can inhibit prostate-specific antigen (PSA) and Notch-1, thus preventing cell proliferation and decreasing the self-renewal capacity of prostate cancers.[30,31] miR-148a can inhibit mitogen and stress-activated protein kinase (MSK1).[32] miR-31 can inhibit cell-cycle regulators such as E2F1, E2F2, EXO1, FOXM1, and MCM2.[33] These miRNAs (e.g., miR-124 and miR-34a) are down-regulated due to the hypermethylation of their promoters.[29,30] In addition, *let-7C* is negatively regulated by Lin28.[27,28] miR-200b-3p expression level is correlated with that of p73 protein, which is related to p53 protein and is considered as a tumor suppressor. The interaction between miR-200b-3p and p73 can also promote the proliferation of AIPCs.[34]

2.2. Apoptosis Avoidance. Apoptosis is a process of programed cell death with defined unique morphology and biochemical changes of cells in response to apoptotic signals including death ligands, DNA damage, irradiation, and chemotherapy drugs. The ability to avoid apoptosis is developed during the tumorigenesis and is a hallmark of cancers.[37] There are two major apoptotic pathways: extrinsic pathway and intrinsic pathways.[38,39] These two pathways have considerable cross-talk and may proceed concurrently. The apoptosis defect and dysregulation of apoptotic mediators is an important mechanism leading to the chemoresistance of prostate cancers. Recent evidence has indicated the roles of miRNAs in the regulation of apoptosis and their association with the development of resistant prostate cancers (Table 2 and Figure 2).

Table 2. miRNAs Involved in Apoptosis Avoidance

miRNA	targets	refs
Up-Regulated		
miR-21	PDCD4, TPM1, MARCKS, PTEN	53−57
miR-32	BCL2L11 (Bim)	46
miR-106b	E2F1, p21/WAF1	46
miR-125b	P14(ARF), mdm2, p53, BAK1, Puma	14−16,47
miR-19b,23b,26a,92a	PTEN, PI3K/Akt, Cyclin D1	52
miR-20a	E2F1	51
Down-Regulated		
miR-15a/16-1	BCL2, CCND1, WNT3A	43
miR-31	E2F6	44
miR-205	BCL2	42,44
miR-34a	BCL2, SIRT1	40
miR-34c	BCL2, E2F3	41
miR-574-3p	BCl-XL	45

Bcl-2 family proteins are important regulators of apoptosis. Overexpression of antiapoptotic proteins (e.g., Bcl-2 and Bcl-XL) or underexpression of pro-apoptotic proteins [e.g., BAX, Puma (p53 up-regulated modulator of apoptosis), and Bim (Bcl-2-interacting mediator of cell death)] has contributed to the resistance of prostate cancers to chemotherapy. Recent studies have demonstrated the role of miRNAs in the regulation of Bcl-2 family proteins. These studies showed that Bcl-2 was regulated by miR-34a,[40] miR-34c,[41] miR-205,[42] and miR-15a/miR-16-1.[43] Bcl2L2 was regulated by miR-205;[44] and Bcl-XL was regulated by miR-574-3p.[45] Underexpression of these miRNAs results in the overexpression of pro-survival Bcl-2 family proteins. In contrast, miR-32 and 125b regulate pro-

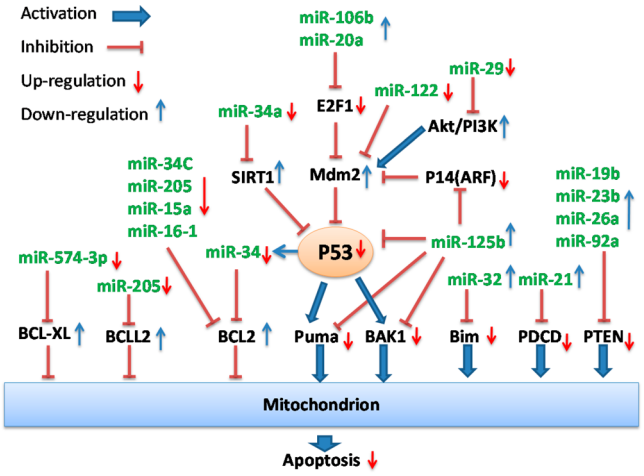

Figure 2. Aberrant expression of miRNAs targeting apoptotic pathways in prostate cancer leads to avoidance of apoptosis.

apoptotic Bcl-2 family proteins such as *Bcl2L11/Bim*, Puma/BBC3, and Bak1.[15,16,46] Overexpression of miR-32 or 125b causes down-regulation of above pro-apoptotic proteins. Either overexpression of pro-apoptotic proteins or down-regulation of antiapoptotic proteins can promote cell apoptosis.

P53 is a tumor suppressor protein and a critical mediator of cell cycle and apoptosis in response to different stress signals, including hypoxia, DNA damage, and free radical formation. It initiates apoptosis by activating pro-apoptotic proteins and inhibiting anti-apoptotic proteins. Several miRNAs are involved in the regulation of p53. The up-regulation of miR-125b can inhibit p53 through the up-regulation of mouse double minute 2 homologue (MDM2), which is a negative regulator of p53.[16,47] miR-29 can up-regulate p53 through the PI3K-AKT-MDM2 pathway. miR-122 activates p53 through the inhibition of cylclin G1/pp2A-MDM2 pathway.[48] At the same time, p53 also regulates certain miRNAs (e.g., miR-145, miR-34, miR-192, and miR-215) to affect cell survival and proliferation.[48] For example, the expression of miR-34a is transcriptionally regulated p53. miR-34a is regulating genes controlling cell cycle and apoptosis. The overexpression of miR-34a can inhibit cell growth, induce apoptosis, and sensitize resistant cells to camptothecin, indicating miR-34a as a potential target for p53-defective prostate cancer treatment.[49] Similar studies were reported by Lodygin et al., who showed that miR-34a was a target of p53. In their studies, miR-34a overexpression in prostate cancers induced cell senescence and cell cycle arrest though targeting cyclin-dependent kinase 6 (CDK6).[50]

miRNAs also regulate apoptosis by targeting E2F transcription factors. E2F6 is a target of miR-31. The overexpression of miR-31 can increase the level of E2F6 and induce apoptosis.[44] E2F1 are regulated by miR-106b[46] and miR-20a.[51] Up-regulation of miR-106b or miR-20a may lead to down-expression of E2F1 transcription factors and thus reduce apoptosis.

Several other pro-apoptotic proteins are also inhibited by miRNAs. Phosphatase and tensin homologue (PTEN) can be inhibited by miR-19b, miR-23b, miR-26a, miR-92a, or miR-21.[52,53] Programmed cell death 4 (PDCD4) is a target of miR-21.[53−57] miR-21 can inhibit PDCD4 and results in the resistance of PC3 prostate cancer cells to docetaxel.[56] Antisense oligonucleotide mediated inhibition of miR-21 in DU145 and

dx.doi.org/10.1021/mp500099g | *Mol. Pharmaceutics* 2014, 11, 2539−2552

PC3 prostate cancer cells has increased their sensitivity to apoptosis.[54]

2.3. MDR Transporters. Overexpression of multiple drug resistance (MDR) transporters, such as P-glycoprotein (Pgp), breast cancer resistance protein (BCRP), and multiple drug resistance proteins (MRPs), is an important reason for chemoresistance.[58−68] These transporters function as drug efflux pumps, which reduce intracellular accumulation of chemotherapeutic agents. The overexpression of MDR transporters correlates negatively with the sensitivity of prostate cancers to chemotherapy drugs.[59] For example, Pgp and other MDR transporters were up-regulated in two paclitaxel-resistant cell lines (DU145-TXR and PC3-TXR), leading to the resistance of these cells to paclitaxel and other chemotherapeutic agents.[61] Many studies have demonstrated the regulatory roles of miRNAs on various MDR transporters.

Pgp/MDR1 is one of the most important MDR transporters. MDR1 is responsible for the resistance to various chemotherapy drugs including taxol, doxorubicin, etoposide, and vinblastine. The regulation of MDR1 by miRNAs has been demonstrated in multiple studies. miR-9 is involved in the Pgp expression and drug resistance. Inhibition of miR-9 with anti-miR-9 could sensitize brain cancer cells to Temozolomide.[69] miR-381 and miR-495 are also down-regulated in resistant cancer cells with up-regulated MDR1.[70] Down-regulation of *let-7* family is associated with the resistance of cancer cells to taxol. *Let-7* enhances cell resistance through the up-regulation of its target IGF2 mRNA-binding protein 1 (IMP-1), which, in turn, can stabilize MDR1.[71] miR-122 can sensitize hepatocellular carcinoma to chemotherapy by the down-regulation of MDR1, MRP, and Bcl-w.[72]

The role of miR-27a and miR-451 on the modulation of Pgp has been reported in several papers with conflicting results.[73−77] Some studies indicated that these two miRNAs were down-regulated in resistant cancer cells and were negative regulators of Pgp.[73−75] Kocalchuk et al. reported that miR-451 was a negative regulator of Pgp. Doxorubicin resistant cells could be sensitized by the transfection of miR-451.[73] Similarly, Feng et al. reported that miR-27a and miR-331-5p were down-regulated in leukemia cell lines. Their down-regulation was associated with Pgp overexpression in these cells.[74] Chen et al. also reported that miR-27a was down-regulated in resistant hepatocellular carcinoma cells.[75] In contrast, several other studies showed that both miR-27a and miR-451 were overexpressed in resistant cells and caused the overexpression of Pgp.[76,77] Zhu et al. showed that both miR-451 and miR-27a were up-regulated in MDR cancer cell lines, such as A2780DX5 and KB-V1. The overexpression of these two miRNAs resulted in a high level of Pgp.[76] Li et al. also showed that both miR-27a and Pgp were up-regulated in drug resistant ovarian cancer cells.[77] These studies were carried out on different cell lines, indicating the importance of cellular context for miRNA functions. It is worthwhile to further investigate the role of miR-451 and miR-27a in regulating Pgp expression and their effects on drug resistance.

BCRP/ABCG2 is negatively regulated by miR-328 and miR-519.[78,79] Overexpression of miR-328 could down-regulate BCRP in breast cancer cells and thus increase their sensitivity to mitoxantrone.[78] However, the expression of BCRP is significantly up-regulated when the miRNA binding site at the 3′-UTR of BCRP mRNA is missing.[80]

MRP1/ABCC1 is up-regulated in VP-16-resistant breast cancer cells (MCF-7/VP).[81] MRP-1 is negatively regulated by miR-326. The down-regulation of miR-326 has been observed in resistant cancer cells with MRP-1 overexpression. MRP4/ABCC4 is another drug efflux transporter that is negatively regulated by miR-124a and miR-506.[82]

2.4. Epithelial−Mesenchymal Transition. Epithelial−mesenchymal transition (EMT) is a process in which epithelial cells assume a mesenchymal phenotype. During the EMT process, cells demonstrate elongated fibroblast morphology. Cell adhesions between epithelial cells are lost. Actin cytoskeleton is reorganized. Epithelial markers (e.g., E-cadherin) are down-regulated, while mesenchymal markers and matrix metalloproteinases (MMPs) are up-regulated. The EMT process is regulated by multiple transcription factors including N-cadherin, Snail, zinc-finger E-box binding homeobox 1 (ZEB1), ZEB2, and Slug. EMT process is activated in the initiation of cancer metastasis and during the development of chemoresistance.[83−88] EMT is associated with the resistance of several different cancers including gemcitabine-resistant pancreatic cancers,[89] lapatinib-resistant gastric cancers,[90] and taxol-resistant ovarian cancers.[91,92] Emerging evidence suggests that miRNAs play critical roles in the regulation of EMT process (Table 3).[93−96]

Table 3. miRNAs Regulate EMT in Prostate Cancers

miRNA[a]	functions	refs
miR-143	enhance E-cadherin; reduce fibronectin	97
miR-145	enhance E-cadherin; reduce fibronectin; inhibit HEF1	97,98
miR-29b	enhance E-cadherin; reduce N-cadherin, Twist, and Snail	99
miR-34b	enhance E-cadherin; reduce vimentin, ZO1, N-cadherin, and Snail	100
miR-200c, 205	enhance E-cadherin; reduce ZEB1, ZEB2, and vimentin	101
miR-200	enhance E-cadherin; reduce N-cadherin, Snail, ZEB1, ZEB2, Slug	102,103
miR-203	reduce N-cadherin and vimentin; modulate Wnt signaling pathway	104
miR-23b/27b	reduce E-cadherin; inhibit Rac1 activity	105

[a]These miRNAs are down-regulated during EMT.

The following miRNAs are down-regulated in prostate cancers and are associated with the EMT process: miR-143,[97] miR-145,[97,98] miR-29b,[99] miR-34b,[100] miR-200 family,[101−103] miR-205,[101] miR-203,[104] and miR-23b/27b.[105] The down-regulation of these miRNAs results in high levels of mesenchymal markers and low levels of epithelial markers, which can promote EMT process and increase the aggressiveness of prostate cancers. For example, the down-regulation of miR-143 and miR-145 has contributed to the bone metastasis of prostate cancers.[97] These miRNAs regulate EMT through the modulation of their targets. miR-145 suppresses EMT through the inhibition of its direct target HEF1.[98] miR-29b increases E-cadherin expression, while reducing N-cadherin, Twist, and Snail expression.[99] miR-34b inhibits EMT by reducing mesenchymal markers including vimentin, ZO1, N-cadherin, and Snail, while increasing epithelial markers such as E-cadherin.[100] The levels of miR-200C and miR-205 are reduced in docetaxel-resistant prostate cancer cells. These cells are undergoing EMT with decreased E-cadherin and increased

mesenchymal markers. Restoration of miR-200C and miR-205 through transfection can result in the re-expression of E-cadherin.[101] miR-1, miR-200, and Slug form a regulatory loop. Slug is a direct repressor of these two miRNAs.[106] The targets for miR-200 family include ZEB1 and ZEB2. Overexpression of miR-200 reverses EMT in PC3 PDGF-D cells through the down-regulation of ZEB1, ZEB2, and Snail.[103] The treatment with erismodegib (a smoothened inhibitor) could regulate miR-200 and reverse EMT through the inhibition of transcription factors such as Snail, Slug, and ZEB1.[102] miR-203 reduces cancer cell invasion and metastasis through the inhibition of Wnt signaling pathway.[104] miR-23b/27b cluster is down-regulated in metastatic, castration-resistant cancer. They could inhibit Ras-related C3 botulinum toxin substrate 1 (Rac1) activity and increase the level of E-cadherin. The ectopic expression of miR-23B/27B could suppress metastasis of castration-resistant prostate cancers.[105]

2.5. Cancer Stem Cells. Cancer stem cells (CSCs), also known as tumor-initiating cells, are a subgroup of less differentiated cancer cells. Although only a small percentage of CSCs are present in tumors, CSCs are critical for cancer progression, metastasis, and chemoresistance. CSCs can self-renew, differentiate, and drive the expansion of cancers. They can be isolated from bulk tumor cells based on characteristic cell surface markers. CD44 has been used as a marker either alone or in combination with other CSCs markers.[107−109] $CD44^+$ prostate cancer cells demonstrated CSC-like properties such as increased clonogenic potential, tumorigenecity, and metastasis. Most current therapeutic agents are targeting at bulk tumor cells but not at CSCs. The use of these agents can effectively kill bulk tumor cells but are ineffective in the elimination of CSCs. The spared CSCs may cause cancer recurrence and drug resistance. The exact mechanism accounting for the development of drug resistant properties in CSCs is still unclear. The differentiation of CSCs under the selection pressure of chemotherapy drugs may generate drug resistant daughter cells and thus acquire drug resistance. Some CSCs have a high level of expression of MDR drug efflux transporters. For example, MRP1/ABCC1 overexpression in prostate cancers has resulted in the resistance of these cells to arsenic treatment.[110] In another study, prostate CSCs showed resistance to several chemotherapeutic agents including cisplatin, doxorubicin, paclitaxel, and methotrexate.[111]

miRNAs have a pivotal role in the regulation of CSCs. For example, miR-34a is down-regulated in $CD44^+$, $CD133^+$, or $\alpha2\beta1^+$ prostate CSCs sorted from prostate cancer xenograft and prostate tumor patient tissues. Overexpression of miR-34a in prostate cancer cells or isolated $CD44^+$ CSCs cells can significantly reduce tumor growth and metastasis. miR-34a inhibits prostate CSCs through the inhibition of CD44. Down-regulation of miR-34 in $CD44^-$ prostate cancer cells enhances the aggressiveness of tumors. miR-34a is a negative regulator of $CD44^+$ prostate CSCs.[112,113] Similar studies showed multiple miRNAs were down-regulated in prostate CSCs (e.g., miR-34a, *let-7b*, miR-106a, and miR-141), while other miRNAs were up-regulated (e.g., miR-301 and miR-452). The overexpression of *let-7* could inhibit the prostate cancer growth through their effects on CSCs.[114] miR-320 has been identified as a negative regulator of $CD44^+$ prostate CSCs. miR-320 inhibits β-catenin expression and suppresses prostate CSCs through the inhibition of the Wnt/beta-catenin signaling pathway. Down-regulation of miR-320 enhances CSC properties such as tumor sphere formation, chemoresistance, and tumorigenicity. These CSC properties could be inhibited by the overexpression of miR-320.[115] Enhancer of zeste homologue 2 (EZH2) is involved in CSC proliferation and differentiation. It is up-regulated in $CD44^+/CD133^+$ prostate CSCs and is negatively regulated by miR-101.[116]

2.6. Interrelationship between EMT, CSCs, Chemo-resistance, and miRNAs. Growing evidence suggests the connections among EMT, CSCs, chemoresistance, and miRNAs.[117−119] EMT cells have CSC-like properties such as self-renewal and mammosphere formation, while CSCs have mesenchymal-like features. EMT cells and CSCs have demonstrated chemo-resistance phenotypes, while a higher percentage of EMT cells and CSCs are identified in drug resistant prostate cancers. In addition, EMT and CSC development shares common signaling pathways, including Wnt, Notch, and hedgehog (Hh) pathways.[120] EMT process is in parallel with the acquisition of "stemness". Drug resistant cancers are usually developed through EMT. miRNAs play a pivotal role in the regulation of both EMT process and the CSC proliferation. miRNAs are the common thread connecting EMT, CSCs, and drug resistance (Figure 3). Therefore,

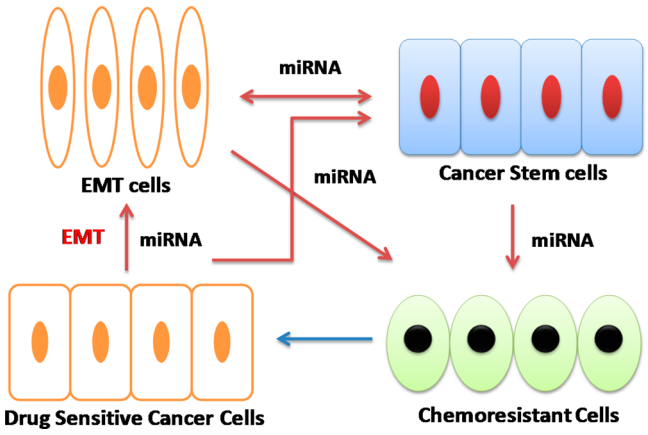

Figure 3. Interrelationship between epithelial−mesenchymal transition (EMT), cancer stem cells (CSCs), chemoresistance, and miRNAs. EMT cells, CSCs, and chemoresistant prostate cancer cells are connected and regulated by miRNAs (ref 125).

targeting specific miRNAs involved in EMT or CSCs will be a promising cancer therapy approach, which could effectively eliminate CSCs and EMT cells and overcome drug resistance.

In a recent study, erismodegib (a smoothened inhibitor) demonstrated the ability to inhibit EMT as well as CSC growth. The treatment with erismodegib may lead to the change of several miRNAs (miR-21, miR-128, and miR-200 family). Erismodegib can increase the levels of PDCD4 and promote apoptosis through the inhibition of miR-21. Erismodegib can also inhibit Bmi-1 through the up-regulation of miR-128. Bmi-1 plays an important role in CSCs. The inhibition of Bmi-1 as well as several other proteins is associated with the inhibition of prostate CSCs. In addition, erismodegib inhibits EMT through the miR-200 family, which can up-regulate E-cadherin and down-regulate N-cadherin, Snail, Slug, and ZEB1.[102] In another study, miR-203 was suppressed during the EMT process through the methylation of the promoter. The deregulation of miR-203 not only promoted EMT but also enhanced stemness of the cancer cells. miR-203 inhibited the invasion and metastasis of cancers by inhibiting the Wnt signaling pathway.[104] Docetaxel-resistant prostate cancer cells are undergoing

EMT and have increased CSC populations. miR-200C and miR-205 are key regulators of EMT and CSCs. These two miRNAs are reduced in the above resistant cells. Reintroduction of these miRNAs can reverse EMT. This study has demonstrated the role of EMT and CSCs in docetaxel resistance and their regulation by miR-200C and miR-205.[101]

3. THERAPEUTIC STRATEGIES

Many miRNAs are aberrantly expressed in resistant prostate cancer cells and cause the resistance of cancer cells through the modulation of their targets. Because of their important roles in the development of chemoresistance, these miRNAs can be used as potential therapeutic targets for overcoming drug resistance. Here, we discuss different therapeutic agents that can be used to target miRNAs for treating resistant prostate cancers.

3.1. Macromolecule Therapeutics. Two categories of macromolecule therapeutics can be utilized to correct the miRNA expression levels in resistant cancers. Antagomirs (also known as anti-miRs)[121] and miRNA sponges (mRNAs with multiple targeting sites for a specific miRNA)[122,123] are usually used to reduce oncogenic miRNAs that are up-regulated in resistant cancers. An antagomir is a chemically modified synthetic RNA that is complementary to a specific miRNA target and used to silence endogenous miRNAs. The chemical modifications of antagomir are usually used to increase its resistance to nuclease degradation. Tumor suppressive miRNAs are down-regulated in resistant cancers. The levels of tumor suppressive miRNAs can be restored by using synthetic miRNAs (miRNA mimics) or genetic precursors (vector based miRNAs).[124] The restoration of down-regulated tumor suppressive miRNAs is also called miRNA replacement therapy. Although a variety of therapeutic strategies have been developed and demonstrated therapeutic efficacies, anti-miRs and miRNA mimics are the two most advanced approaches to enter clinical trials.

3.2. Small Molecule Drugs. A growing body of studies have discovered the activities of small molecule drugs in the regulation of miRNAs and demonstrated their potential for overcoming drug resistance in prostate cancers. In our study, we have used the combination of paclitaxel and Hh pathway inhibitor cyclopamine to treat paclitaxel resistant prostate cancers. The combination therapy has successfully restored the expression of miR-220C and miR-34a in prostate cancer cells, thus effectively reversing chemoresistance and eliminating CSC side population. This study has demonstrated the feasibility of using small molecule agents to overcome drug resistance through the modulation of miRNA expression.[125] Several chemicals derived from natural products have also been utilized to sensitize cancers by targeting miRNAs.[126−128] For example, the treatment with 3,3′-diindolylmethane (DIM) and isoflavone increased the expression of miR-200 and *let*-7, which, in turn, reversed EMT process and increased the sensitivity of cancer cells to gemcitabine.[126] A curcumin analogue, EF24, can effectively induce apoptosis in DU145 prostate cancer cells. It works through the inhibition of miR-21, thus enhancing the expression of miR-21 target genes such as PDCD4 and PTEN.[129] Similarly, resveratrol can also reduce prostate cancer growth and metastasis by targeting miR-21.[21] Genistein, a soy isoflavone, has shown anticancer effects on prostate cancer cells through the up-regulation of miR-34a.[130] The advantages of small molecule drugs are their favorable in vivo stabilities and pharmacokinetics (PK) profiles, thus having less challenge in drug delivery.

3.3. Combination Therapy. The correction of aberrant miRNAs in resistant prostate cancers has been demonstrated to be an effective approach for sensitizing resistant prostate cancer to chemotherapy. For example, the transfection of miR-148 or miR-34a can sensitize paclitaxel resistant PC3 cells to paclitaxel treatment.[32,40,49] The overexpression of miR-143 has also shown the ability to enhance the sensitivity of prostate cancer cells to docetaxel.[131] Therefore, the combination of small molecule chemotherapeutic agents and miRNA therapeutics can be a promising strategy for treating resistant prostate cancers. The rationale of this combination therapy is that the correction of aberrant miRNA levels can sensitize resistant prostate cancer cells to small molecule drugs. A delivery system that could simultaneously deliver miRNA and small molecule drugs will be of great interest. In the past few years, many delivery systems were investigated for the codelivery of small molecule drugs and gene medicines (including miRNA, siRNA, and DNA) for cancer therapy.[132−137]

4. DELIVERY STRATEGIES FOR MIRNA THERAPEUTICS

Despite promising results in the development of miRNA therapeutics and successes on in vitro cell based studies, very limited progress has been made at in vivo studies or clinical trials. The major obstacle for miRNA-based therapy is the in vivo delivery of miRNA therapeutics.[138] Significant efforts have been made for the delivery and targeting of miRNA therapeutics. Various delivery strategies have been successfully developed for miRNA therapeutics. There is still only a limited success with miRNA delivery and targeting and will continue being a great challenge. Although a variety of miRNA therapeutics have been studied, many of them are not suitable for human use. For example, vector-based systems rely on plasmids or viral vectors to deliver and express miRNA in cells. The safety concerns restrict their application in human as a drug candidate even though they can be very useful systems for in vitro cell-based studies. miRNA mimic (a double-strand RNA) is the most promising miRNA therapeutic, which has advanced to clinical trials. For example, MRX34 is the first miRNA mimic that has entered phase I clinical trial as a miRNA replacement therapy to treat liver cancers.[139] miRNA inhibitory short single-strand oligonucleotide (e.g., antagomir) is another promising approach, which achieves therapeutic effects through the down-regulation of target miRNA. Therefore, in this section, we will discuss the most promising delivery strategies that have advanced into clinical trials. miRNA therapeutics have large molecular weight and are hydrophilic. They have very poor ability to cross cell membranes, which are composed of lipophilic phospholipids bilayers. In addition, they are unstable when exposed to nucleases in the blood. A successful in vivo delivery approach should be able to (1) protect miRNA therapeutics against serum nucleases, avoid renal clearance, prolong circulation time, and minimize the nonspecific interaction with nontarget cells or organs; (2) enhance the accumulation of miRNA therapeutics in target tissues and facilitate their uptake by target cells and their release inside the cells. Here, we discuss miRNA delivery strategies including (1) chemical modification, (2) lipid-based particles, (3) cyclodextrin polymer nanoparticle, and (4) bioconjugates. All of these approaches have been successfully used for in vivo delivery of siRNAs. Because of the similarity between siRNAs

and miRNA mimics (both are double-strand RNA), these delivery strategies can be transferred for miRNA delivery.

4.1. Chemical Modification. To increase the stability in serum, a variety of methods have been developed for the chemical modification of RNAs (Figure 4). Both phosphodiester and ribose can be potentially modified. The nonbridging oxygen in the phosphodiester can be replaced with sulfur (phosphorothioate), boron (boranophosphate), or methyl (methylphosphonate) groups. The 2′-position of the ribose can also be modified to 2′-fluoro (2′-F), 2′-O-methyl (2′-OMe), 2′-O-(2-methoxyethyl) (MOE), 2′-O-fluoro-β-D-arabinonucleotide (FANA), and locked nucleic acid (LNA). Optimized chemical modifications can increase the resistance to serum nuclease, avoid the activation of innate immune system, and reduce off-target effects.[140] Miravirsen is a good example of a chemically modified miRNA inhibitor, which was developed by Santaris Pharma A/S. Miravirsen is composed of locked nucleic acid (LNAs) RNA interspaced throughout a phosphorothioate oligonucleotide. It is complementary to the 5′-end of miR-122 and can thus hybridize to miR-122. It inhibits Hepatitis C virus (HCV) by blocking the interaction between HCV RNA and miR-122. The chemical modifications in miravirsen can provide nuclease resistance and enhance its affinity to its target. Miravirsen is the first miRNA targeting drug that enters clinical trials and is currently in phase 2 trials for treating patients with HCV.[141,142] The same platform has also been used by miRagen Therapeutic in the development of three drugs including MGN-9103 (targeting miR-208), MGN-1374 (targeting miR-15 and miR-195), and MGN-4893 (targeting miR-451).[143] These drugs are being developed in collaboration with Santaris Pharma A/S and are still at the preclinical stage. Chemical modification has also been widely used for siRNAs. For example, siRNA targeting Hepatitis B virus (HBV) has been chemically modified to improve its stability.[144,145] Although chemical modification can increase the stability of siRNAs or miRNA mimics, a synthetic carrier is usually needed for their in vivo delivery and targeting.[144,145]

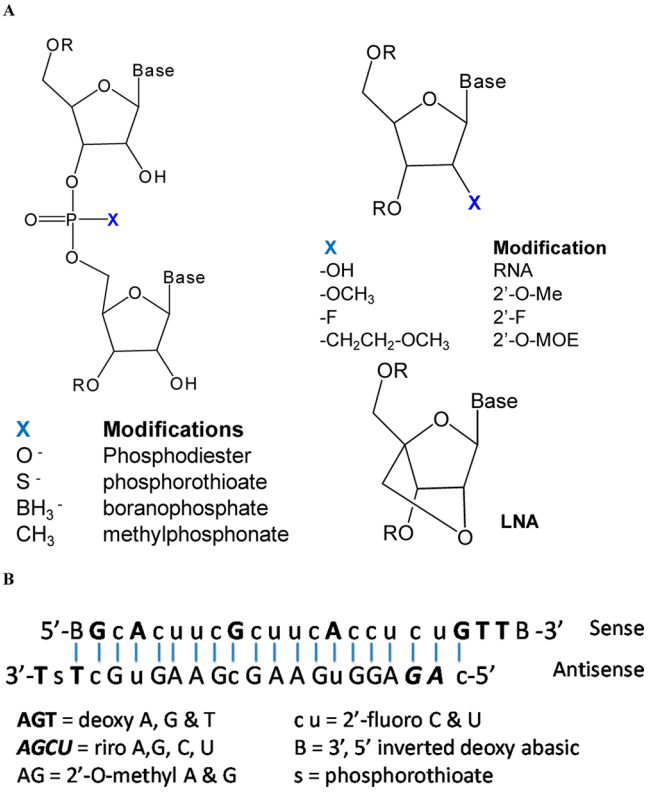

Figure 4. (A) RNA molecules can be modified by changing the nonbridging oxygen in the phosphodiester (left) or 2′-position of the ribose (right). (B) The use of a combination of different modifications to improve the in vivo stability of a siRNA (ref 150).

4.2. Lipid-Based Particles. Lipid-based particles (or liposomes) have been used for decades for the delivery of gene medicines including plasmids, antisense oligonucleotides, and siRNAs. A number of lipid-based particle systems have been developed for delivery of siRNAs or miRNA mimics and used in clinical trials (Figure 5A).[146,147]

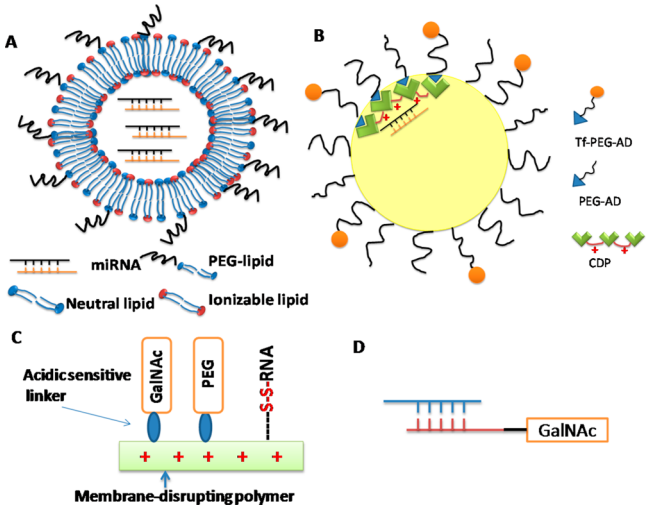

Figure 5. Types of miRNA delivery systems: (A) lipid particles; (B) cyclodextrin polymer nanoparticles (CDP); (C) dynamic polyconjugate (DPC); and (D) GalNAc-siRNA.

Stable nucleic acid−lipid particle (SNALP) is the most popular siRNA delivery system, which was originally developed by Tekira, and has been used as the delivery system for several products in human clinical trials (e.g., TKM-PLK1 and ALN-TTR02).[148,149] A typical SNALP formulation includes ionizable lipids, shielding lipids, cholesterols, and targeting ligands. (1) Ionizable lipids in SNALP formulation are quite similar to those in Smarticles. The ionization status and thus the charge of the lipids are pH dependent. The positive charge at acidic pH can enhance encapsulation of RNA in the liposome, enhance cellular uptake, and facilitate endosomal escape. These lipids are unionized and neutral at physiological pH, thus avoiding nonspecific interaction and preventing rapid elimination of lipid particles. DLinDMA (1,2-dilinoleyloxy-*N*,*N*-dimethyl-3-aminopropane) is the first generation ionizable lipid used in SNALP.[150] The second generation of ionizable lipids including Dlin-KC2-DMA and Dlin-MC3-DMA were discovered through extensive structure−activity relationship (SAR) studies.[151] The pK_a of the lipids is critical for siRNA delivery. Optimization of the pK_a of the ionizable lipid head groups could enhance their membrane fusion and endosomal escape properties. In addition, the delivery efficiency is also affected by the structure of lipids including amine head groups, linkers, and hydrophobic tails.[152] ReLNP (rapid eliminated LNP) developed by Alnylam is the third generation of SNALP, which uses degradable lipids derived from Dlin-MC3-DMA. The use of biodegradable lipids can reduce toxicity and improve biocompatibility.[153] (2)

dx.doi.org/10.1021/mp500099g | Mol. Pharmaceutics 2014, 11, 2539−2552

Shielding lipids are PEG-lipid conjugates used to make stealth liposomes. Because of the steric effect of PEG coating, the PEGylation of lipid particles can reduce nonspecific interaction with serum components, avoid uptake by the cells of reticuloendothelial system (RES), minimize the kidney elimination, and increase the circulation time. However, shielding lipids can reduce the cellular uptake of particles in target cells and negatively affect the endosomal release of siRNAs, for PEG can sterically block the interaction of liposomes with cell membranes or endosome membranes. This issue can be addressed by using acid-sensitive shielding lipids, which can be detached from lipid particles inside the endosome, which has an acidic pH environment.[154,155] (3) Both endogenous and exogenous targeting ligands can be utilized to enhance the delivery of liposomes into target cells or organs. Neutral liposomes often bind to serum proteins and thus are directed by the coated serum proteins to their target cells. For example, lipoprotein Apo-E has been used as a targeting ligand to enhance the uptake of liposomes in hepatocytes.[156,157] Exogenous ligands can also be used to enhance the delivery of liposomes into target cells. These targeting ligands include antibodies, peptides, and small molecules.

Smarticles is a proprietary liposomal delivery system from Marina Biotech (Bothell, WA) and has been used for delivery of MRX34, which is the first miRNA mimic that entered clinical trials.[146] MRX34 is a double-strand RNA to treat liver cancers. The ionizable lipid is a key component for enhancing the in vivo delivery of miRNA mimics or siRNAs. Because of the presence of ionizable lipid, smarticles is anionic at normal physiological pH but becomes cationic at lower pH. This pH-dependent change of surface charge is critical for minimizing nonspecific interaction during circulation in the blood but has efficient cellular uptake and endosomal escape ability in target cells. Smarticles is also used for delivery of PNR2258, which is an anti-Bcl-2 cancer drug developed by ProRNAi Therapeutics and is currently in phase II clinical trials.[147]

4.3. Cyclodextrin Polymer Nanoparticle (CDP). RONDEL (RNAi/oligonucleotide nanoparticle delivery) is the delivery platform for Arrowhead Research's CALAA-01. It is the first targeted delivery of siRNA entering the human trials. RONDEL delivery system has three major components: (1) a water-soluble positive charged cyclodextrin-containing polymer (CDP); (2) a PEG-adamantane conjugate (PEG-AD); and (3) a transferrin decorated PEG-AD (Tf-PEG-AD) (Figure 5B). When the siRNA solution is mixed with RONDEL before, targeted nanoparticles with a size of 50−70 nm are formed through self-assembly.[158] The RONDEL delivery system has several advantages including the simple formulation preparation process, optimal particle size for enhanced permeability, and retention (EPR) effect, and inclusion of tumor targeting ligands (transferrin) for active tumor targeting. However, adverse events were observed among some patients during the phase I studies. Arrowhead Research has decided not to advance the CALAA-01 into phase II trials.[159]

4.4. Bioconjugates. Dynamic polyconjugate (DPCs) is a multiple component conjugate composed of an amphiphilic endosomolytic polymer, PEG, targeting ligand (GalNac), and siRNA (Figure 5C).[160] In the first generation of DPC, polymer poly(butyl amino vinyl either) (PBAVE) is selected as the amphiphilic endosomolytic polymer. Both PEG and targeting ligand (GalNac) are conjugated to the polymer through an acid-sensitive linker. GalNac can enhance the targeting and cellular uptake of DPC by hepatocytes. Membrane distrusting PBAVE is masked by attached shielding PEGs during the circulation. After cellular uptake, PEGs are released and the exposed PBAVE can promote endosomal escape. Double-strand RNAs are attached to PBAVE polymer via a degradable disulfide linker, which can be cleaved in the reducing environment of cytoplasm to release RNAs. The small size of DPC (5−20 nm) is also helpful for tumor targeting. A new generation of DPC polymer has also been synthesized through an improved polymerization process to produce homogeneous polymers. In a recent study, siRNA−cholesterol conjugates were coinjected with DPC instead of using siRNA−DPC conjugates. The coinjection approach has also shown effective gene silencing in the liver.[161] The coinjection approach is currently used by Arrowhead Research in their flagship pipeline, ARC-520, which is in phase I trials for the treatment of HBV. For ARC-520, a melittin-like peptide is used, which is similar to PBAVE and also has reversibly masked endosomolytic activities.[162]

GalNAc−siRNA is a liver-targeted conjugate delivery platform used by Alnylam in several drug candidates (ALN-TTRsc, ALN-AT3, and ALN-PCSsc).[163] In this delivery system, three targeting ligands (GalNAc) are attached to the 3′-terminus of the passenger strand of siRNA via a triantennary spacer. GalNAc can bind to the asialoglycoprotein receptor (ASGPR) overexpressed in hepatocytes and facilitate the cellular uptake through endocytosis (Figure 5D).

In summary, the delivery systems discussed above have all demonstrated in vivo delivery efficacy and have been used in human clinical trials. They are diverse in the working mechanism and have different design features including size, chemical structure, and preparation method. "All roads lead to Rome" is a good summary of the current status of RNA therapeutics delivery approaches. At the same time, we also notice that a successful delivery system usually includes multiple functional elements to overcome various barriers to their in vivo delivery and has a good biocompatibility and safety profile for human use.

5. CONCLUSIONS AND PERSPECTIVES

miRNAs play significant roles in the development of resistant prostate cancers by targeting multiple signaling pathways or mechanisms. Deregulated miRNAs are associated with the occurrence of chemoresistant prostate cancers. Therefore, correction of aberrant miRNAs could be a strategy to overcome resistance in prostate cancer therapy. Many miRNAs related to drug resistance have been discovered, and additional ones are expected to be identified in the future. We are expecting to have a better understanding regarding the mechanisms of drug resistance in prostate cancers. The identification of the most critical miRNA(s) that are associated with drug resistance will be the cornerstone for the design of therapeutics. It is also noticed that, although many miRNAs have differential expression between normal cells and cancer cells, not all these miRNAs are the cause of cancer development and thus cannot be used as therapeutic targets. In addition, most current miRNA targets are discovered in prostate cell lines because they are more accessible than human prostate cancer tissues. These miRNA targets need to be further validated with translational research or clinical studies before they can become clinically useful therapeutic targets. More miRNA targets will be discovered from human prostate cancer tissues, which will be clinically relevant and more valid.

Antagomirs and miRNA mimics are the two most promising miRNA-based therapeutics. miRNA mimics have demonstrated their great potential for treating cancers, especially drug-resistant cancers, by its ability to simultaneously inhibit multiple oncogenes or signaling pathways. Since the development of cancers and their resistance to treatments are usually caused by the aberrant expression of multiple genes and signaling pathways, the use of siRNAs or small molecule inhibitors targeting a single mRNA (or other intracellular target) can merely induce a modest therapeutic response. However, miRNA mimics can restore the level of an underexpressed miRNA, repress multiple oncogenes and pathways regulated by these miRNA, and thus effectively treat resistant cancers. At the same time, we also need to be cautious about the broad effects of miRNA mimics. Since multiple targets or complex signaling networks are regulated by a single miRNA mimic, a nontraditional approach must be used to evaluate their therapeutic effects by monitoring a broad gene expression profile rather than focusing on a single gene or protein. The prediction of side effects might also be a challenge due to the broad inhibition effects of miRNAs.

Off-target effects are side effects caused during the use of RNAi due to the unintended interactions between RNAi molecules and cellular components. Off-target effects can be divided into two categories based on their mechanisms: (1) specific off-target effects (caused by limited degree of complementarity between siRNA and nontargeting mRNAs); and (2) nonspecific off-target effects (toxicities caused by the activation of Toll-like receptor mediated innate immune response or due to the saturation of cellular RNAi machinery).[164] As we discussed before, miRNA inhibition and miRNA replacement are two major approaches of miRNA-based therapeutics. Antagomirs can be designed to reduce the aberrantly up-regulated oncogenic miRNAs by being perfectly complementary to the specific miRNA target by mispairing at the cleavage site of Ago2. Antagomir recognizes and irreversibly binds to specific target miRNA. Antagomirs work similar to siRNAs in silencing target mRNAs. Therefore, off-target effects will be an issue for the use of antagomir or other similar miRNA inhibitors because they may bind to nontarget miRNAs or even mRNAs or induce innate immune responses. Approaches for minimizing off-target effects include the optimization of antagomir sequences and chemical modifications of its backbone and structure. MiRNA replacement therapy refers to the use of miRNA mimics to restore the down-regulated tumor suppressor miRNAs in cancer cells. Unlike siRNA, miRNA mimics are usually present in cells and are considered as "endogenous" molecules. A miRNA mimic has the same sequence as an endogenous miRNA and thus will not cause off-target effects. Since the same miRNAs are also present in normal cells, the introduction of miRNA mimics into normal cells will be well-tolerated. However, the use of miRNA mimics may still cause side effects. Since our knowledge about the expression levels of particular miRNAs is still very limited and their intracellular levels vary among different cells and same cell exposed to different environment, the delivery of too much miRNAs may cause side effects while too less will not be able to achieve sufficient therapeutic effects.

Significant progress has been made in the target identification and the design of miRNA based therapeutics because of the availability of bioinformatics tools and high throughput research methods. The identification of miRNA therapeutic targets and design of miRNA therapeutics is no longer a significant bottleneck. However, it is widely accepted that the delivery of miRNA therapeutics is still a challenge because of their poor in vivo stability, large molecular weight, hydrophilicity, and other in vivo delivery obstacles. Delivery systems discussed in this review have all demonstrated in vivo efficacy and have been pursued in human clinical trials. Although they are diverse in design features, all have demonstrated great potentials in addressing the delivery challenge. Liposomal systems are the most advanced formulation with several products in the development pipeline. Bioconjugate is also a promising system, which has precisely controlled structure and function. These delivery platforms will jump-start the clinical development of miRNA therapeutics, and some of them will finally become available as approved medications. Also, more delivery systems will be developed through the efforts from researchers from different scientific disciplines including chemistry, polymer sciences, engineering, pharmaceutical sciences, and biology. However, it is worth mentioning that most of the current miRNA delivery systems in clinical trials are to deliver therapeutic agents to the liver through either using liver targeting ligands or relying on the passive accumulation of delivery systems in the liver. The delivery into the liver is relatively less difficult because liver is a well-perfused tissue and has discontinuous endothelium. However, miRNA delivery to hepatocytes remains a challenge as liposomal and polymeric particualtes carrying miRNA are likely to be taken up by Kuffer cells before reaching the hepatocytes.[165] The delivery to prostate cancer or other less accessible tissues will be more difficult. Additional efforts are needed to modify the current systems to make them more efficient in delivering miRNA therapeutics into prostate cancers. In addition to the general properties needed for siRNA delivery, additional features such as prolonged circulation for EPR effects and prostate cancer targeting ligands for active targeting are needed.

In conclusion, recent research and development in the understanding of miRNAs has demonstrated their great therapeutic potential for resistant prostate cancers. Further clinical or translational research will lead to the identification of miRNA targets and design of effective miRNA-based therapeutics. The recent progress achieved by using several different delivery systems is inspiring; however, delivery still remains a great challenge.

AUTHOR INFORMATION

Corresponding Authors

*(F.L.) Address: Hampton University School of Pharmacy, Kittrell Hall RM 216, Hampton, Virginia 23668, United States. Tel: (757) 727-5585. E-mail: feng.li@hamptonu.edu.

*(R.I.M.) Address: Department of Pharmaceutical Sciences, University of Nebraska Medical Center, 986025 Nebraska Medical Center, Omaha, Nebraska 68198-6025, United States. Tel: (402) 559-5422. E-mail: ram.mahato@unmc.edu.

Notes

The authors declare no competing financial interest.

ACKNOWLEDGMENTS

We thank the following grants for support: Hampton University Faculty Research Award and AACP New Investigator Award (to L.F.); and an Idea Award (W81XWH-10-1-0969) from the Department of Defense Prostate Cancer Research Program (to R.I.M.).

REFERENCES

(1) American Cancer Society. *Cancer Facts and Figures 2013*; American Cancer Society: Atlanta, GA, 2013.

(2) National Cancer Institute. Prostate Cancer. http://www.cancer.gov/cancertopics/types/prostate.

(3) Dillioglugil, O.; Leibman, B. D.; Kattan, M. W.; Seale-Hawkins, C.; Wheeler, T. M.; Scardino, P. T. Hazard rates for progression after radical prostatectomy for clinically localized prostate cancer. *Urology* **1997**, *50* (1), 93−9.

(4) Sharifi, N.; Dahut, W. L.; Steinberg, S. M.; Figg, W. D.; Tarassoff, C.; Arlen, P.; Gulley, J. L. A retrospective study of the time to clinical endpoints for advanced prostate cancer. *BJU Int.* **2005**, *96* (7), 985−9.

(5) Kellokumpu-Lehtinen, P. L.; Harmenberg, U.; Joensuu, T.; McDermott, R.; Hervonen, P.; Ginman, C.; Luukkaa, M.; Nyandoto, P.; Hemminki, A.; Nilsson, S.; McCaffrey, J.; Asola, R.; Turpeenniemi-Hujanen, T.; Laestadius, F.; Tasmuth, T.; Sandberg, K.; Keane, M.; Lehtinen, I.; Luukkaala, T.; Joensuu, H. 2-Weekly versus 3-weekly docetaxel to treat castration-resistant advanced prostate cancer: a randomised, phase 3 trial. *Lancet Oncol.* **2013**, *14* (2), 117−124.

(6) Theyer, G.; Schirmbock, M.; Thalhammer, T.; Sherwood, E. R.; Baumgartner, G.; Hamilton, G. Role of the MDR-1-encoded multiple drug resistance phenotype in prostate cancer cell lines. *J. Urol.* **1993**, *150* (5 Pt 1), 1544−7.

(7) van Brussel, J. P.; Mickisch, G. H. Multidrug resistance in prostate cancer. *Onkologie* **2003**, *26* (2), 175−81.

(8) Hwang, C. Overcoming docetaxel resistance in prostate cancer: a perspective review. *Ther. Adv. Med. Oncol.* **2012**, *4* (6), 329−40.

(9) Petrylak, D. P.; Tangen, C. M.; Hussain, M. H.; Lara, P. N., Jr.; Jones, J. A.; Taplin, M. E.; Burch, P. A.; Berry, D.; Moinpour, C.; Kohli, M.; Benson, M. C.; Small, E. J.; Raghavan, D.; Crawford, E. D. Docetaxel and estramustine compared with mitoxantrone and prednisone for advanced refractory prostate cancer. *N. Engl. J. Med.* **2004**, *351* (15), 1513−20.

(10) Lee, R. C.; Feinbaum, R. L.; Ambros, V. The *C. elegans* heterochronic gene lin-4 encodes small RNAs with antisense complementarity to lin-14. *Cell* **1993**, *75* (5), 843−54.

(11) Ambros, V. The functions of animal microRNAs. *Nature* **2004**, *431* (7006), 350−5.

(12) Kloosterman, W. P.; Plasterk, R. H. The diverse functions of microRNAs in animal development and disease. *Dev. Cell* **2006**, *11* (4), 441−50.

(13) Saraon, P.; Jarvi, K.; Diamandis, E. P. Molecular alterations during progression of prostate cancer to androgen independence. *Clin. Chem.* **2011**, *57* (10), 1366−75.

(14) DeVere White, R. W.; Vinall, R. L.; Tepper, C. G.; Shi, X. B. MicroRNAs and their potential for translation in prostate cancer. *Urol. Oncol.* **2009**, *27* (3), 307−11.

(15) Shi, X. B.; Xue, L.; Yang, J.; Ma, A. H.; Zhao, J.; Xu, M.; Tepper, C. G.; Evans, C. P.; Kung, H. J.; deVere White, R. W. An androgen-regulated miRNA suppresses Bak1 expression and induces androgen-independent growth of prostate cancer cells. *Proc. Natl. Acad. Sci. U.S.A.* **2007**, *104* (50), 19983−8.

(16) Shi, X. B.; Xue, L.; Ma, A. H.; Tepper, C. G.; Kung, H. J.; White, R. W. miR-125b promotes growth of prostate cancer xenograft tumor through targeting pro-apoptotic genes. *Prostate* **2011**, *71* (5), 538−49.

(17) Sun, T.; Wang, Q.; Balk, S.; Brown, M.; Lee, G. S.; Kantoff, P. The role of microRNA-221 and microRNA-222 in androgen-independent prostate cancer cell lines. *Cancer Res.* **2009**, *69* (8), 3356−63.

(18) Sun, T.; Yang, M.; Chen, S.; Balk, S.; Pomerantz, M.; Hsieh, C. L.; Brown, M.; Lee, G. S.; Kantoff, P. W. The altered expression of MiR-221/-222 and MiR-23b/-27b is associated with the development of human castration resistant prostate cancer. *Prostate* **2012**, *72* (10), 1093−103.

(19) Sun, T.; Wang, X.; He, H. H.; Sweeney, C. J.; Liu, S. X.; Brown, M.; Balk, S.; Lee, G. S.; Kantoff, P. W. MiR-221 promotes the development of androgen independence in prostate cancer cells via downregulation of HECTD2 and RAB1A. *Oncogene* **2013**, DOI: 10.1038/onc.2013.230.

(20) Ribas, J.; Ni, X.; Haffner, M.; Wentzel, E. A.; Salmasi, A. H.; Chowdhury, W. H.; Kudrolli, T. A.; Yegnasubramanian, S.; Luo, J.; Rodriguez, R.; Mendell, J. T.; Lupold, S. E. miR-21: an androgen receptor-regulated microRNA that promotes hormone-dependent and hormone-independent prostate cancer growth. *Cancer Res.* **2009**, *69* (18), 7165−9.

(21) Sheth, S.; Jajoo, S.; Kaur, T.; Mukherjea, D.; Sheehan, K.; Rybak, L. P.; Ramkumar, V. Resveratrol reduces prostate cancer growth and metastasis by inhibiting the Akt/MicroRNA-21 pathway. *PLoS One* **2012**, *7* (12), e51655.

(22) Jalava, S. E.; Urbanucci, A.; Latonen, L.; Waltering, K. K.; Sahu, B.; Janne, O. A.; Seppala, J.; Lahdesmaki, H.; Tammela, T. L.; Visakorpi, T. Androgen-regulated miR-32 targets BTG2 and is overexpressed in castration-resistant prostate cancer. *Oncogene* **2012**, *31* (41), 4460−71.

(23) Ma, S.; Chan, Y. P.; Kwan, P. S.; Lee, T. K.; Yan, M.; Tang, K. H.; Ling, M. T.; Vielkind, J. R.; Guan, X. Y.; Chan, K. W. MicroRNA-616 induces androgen-independent growth of prostate cancer cells by suppressing expression of tissue factor pathway inhibitor TFPI-2. *Cancer Res.* **2011**, *71* (2), 583−92.

(24) Nguyen, H. C.; Xie, W.; Yang, M.; Hsieh, C. L.; Drouin, S.; Lee, G. S.; Kantoff, P. W. Expression differences of circulating microRNAs in metastatic castration resistant prostate cancer and low-risk, localized prostate cancer. *Prostate* **2013**, *73* (4), 346−54.

(25) Lin, S. L.; Chiang, A.; Chang, D.; Ying, S. Y. Loss of mir-146a function in hormone-refractory prostate cancer. *RNA* **2008**, *14* (3), 417−24.

(26) Xu, B.; Wang, N.; Wang, X.; Tong, N.; Shao, N.; Tao, J.; Li, P.; Niu, X.; Feng, N.; Zhang, L.; Hua, L.; Wang, Z.; Chen, M. MiR-146a suppresses tumor growth and progression by targeting EGFR pathway and in a p-ERK-dependent manner in castration-resistant prostate cancer. *Prostate* **2012**, *72* (11), 1171−8.

(27) Nadiminty, N.; Tummala, R.; Lou, W.; Zhu, Y.; Shi, X. B.; Zou, J. X.; Chen, H.; Zhang, J.; Chen, X.; Luo, J.; deVere White, R. W.; Kung, H. J.; Evans, C. P.; Gao, A. C. MicroRNA let-7c is downregulated in prostate cancer and suppresses prostate cancer growth. *PLoS One* **2012**, *7* (3), e32832.

(28) Nadiminty, N.; Tummala, R.; Lou, W.; Zhu, Y.; Zhang, J.; Chen, X.; deVere White, R. W.; Kung, H. J.; Evans, C. P.; Gao, A. C. MicroRNA let-7c suppresses androgen receptor expression and activity via regulation of Myc expression in prostate cancer cells. *J. Biol. Chem.* **2012**, *287* (2), 1527−37.

(29) Shi, X. B.; Xue, L.; Ma, A. H.; Tepper, C. G.; Gandour-Edwards, R.; Kung, H. J.; deVere White, R. W. Tumor suppressive miR-124 targets androgen receptor and inhibits proliferation of prostate cancer cells. *Oncogene* **2013**, *32* (35), 4130−8.

(30) Kashat, M.; Azzouz, L.; Sarkar, S. H.; Kong, D.; Li, Y.; Sarkar, F. H. Inactivation of AR and Notch-1 signaling by miR-34a attenuates prostate cancer aggressiveness. *Am. J. Transl. Res.* **2012**, *4* (4), 432−42.

(31) Ostling, P.; Leivonen, S. K.; Aakula, A.; Kohonen, P.; Makela, R.; Hagman, Z.; Edsjo, A.; Kangaspeska, S.; Edgren, H.; Nicorici, D.; Bjartell, A.; Ceder, Y.; Perala, M.; Kallioniemi, O. Systematic analysis of microRNAs targeting the androgen receptor in prostate cancer cells. *Cancer Res.* **2011**, *71* (5), 1956−67.

(32) Fujita, Y.; Kojima, K.; Ohhashi, R.; Hamada, N.; Nozawa, Y.; Kitamoto, A.; Sato, A.; Kondo, S.; Kojima, T.; Deguchi, T.; Ito, M. MiR-148a attenuates paclitaxel resistance of hormone-refractory, drug-resistant prostate cancer PC3 cells by regulating MSK1 expression. *J. Biol. Chem.* **2010**, *285* (25), 19076−84.

(33) Lin, P. C.; Chiu, Y. L.; Banerjee, S.; Park, K.; Mosquera, J. M.; Giannopoulou, E.; Alves, P.; Tewari, A. K.; Gerstein, M. B.; Beltran, H.; Melnick, A. M.; Elemento, O.; Demichelis, F.; Rubin, M. A. Epigenetic repression of miR-31 disrupts androgen receptor homeostasis and contributes to prostate cancer progression. *Cancer Res.* **2013**, *73* (3), 1232−44.

(34) He, M.; Liu, Y.; Deng, X.; Qi, S.; Sun, X.; Liu, G.; Zhao, M. Down-regulation of miR-200b-3p by low p73 contributes to the androgen-independence of prostate cancer cells. *Prostate* **2013**, *73* (10), 1048−56.

(35) Qu, F.; Cui, X.; Hong, Y.; Wang, J.; Li, Y.; Chen, L.; Liu, Y.; Gao, Y.; Xu, D.; Wang, Q. MicroRNA-185 suppresses proliferation, invasion, migration, and tumorigenicity of human prostate cancer cells through targeting androgen receptor. *Mol. Cell. Biochem.* **2013**, *377* (1−2), 121−30.
(36) Hagman, Z.; Haflidadottir, B. S.; Ceder, J. A.; Larne, O.; Bjartell, A.; Lilja, H.; Edsjo, A.; Ceder, Y. miR-205 negatively regulates the androgen receptor and is associated with adverse outcome of prostate cancer patients. *Br. J. Cancer* **2013**, *108* (8), 1668−76.
(37) Hanahan, D.; Weinberg, R. A. The hallmarks of cancer. *Cell* **2000**, *100* (1), 57−70.
(38) Fulda, S.; Debatin, K. M. Extrinsic versus intrinsic apoptosis pathways in anticancer chemotherapy. *Oncogene* **2006**, *25* (34), 4798−811.
(39) Johnstone, R. W.; Ruefli, A. A.; Lowe, S. W. Apoptosis: a link between cancer genetics and chemotherapy. *Cell* **2002**, *108* (2), 153−64.
(40) Kojima, K.; Fujita, Y.; Nozawa, Y.; Deguchi, T.; Ito, M. MiR-34a attenuates paclitaxel-resistance of hormone-refractory prostate cancer PC3 cells through direct and indirect mechanisms. *Prostate* **2010**, *70* (14), 1501−12.
(41) Hagman, Z.; Larne, O.; Edsjo, A.; Bjartell, A.; Ehrnstrom, R. A.; Ulmert, D.; Lilja, H.; Ceder, Y. miR-34c is downregulated in prostate cancer and exerts tumor suppressive functions. *Int. J. Cancer* **2010**, *127* (12), 2768−76.
(42) Verdoodt, B.; Neid, M.; Vogt, M.; Kuhn, V.; Liffers, S. T.; Palisaar, R. J.; Noldus, J.; Tannapfel, A.; Mirmohammadsadegh, A. MicroRNA-205, a novel regulator of the anti-apoptotic protein Bcl2, is downregulated in prostate cancer. *Int. J. Oncol.* **2013**, *43* (1), 307−14.
(43) Bonci, D.; Coppola, V.; Musumeci, M.; Addario, A.; Giuffrida, R.; Memeo, L.; D'Urso, L.; Pagliuca, A.; Biffoni, M.; Labbaye, C.; Bartucci, M.; Muto, G.; Peschle, C.; De Maria, R. The miR-15a-miR-16-1 cluster controls prostate cancer by targeting multiple oncogenic activities. *Nat. Med.* **2008**, *14* (11), 1271−7.
(44) Bhatnagar, N.; Li, X.; Padi, S. K.; Zhang, Q.; Tang, M. S.; Guo, B. Downregulation of miR-205 and miR-31 confers resistance to chemotherapy-induced apoptosis in prostate cancer cells. *Cell Death Dis.* **2010**, *1*, e105.
(45) Chiyomaru, T.; Yamamura, S.; Fukuhara, S.; Hidaka, H.; Majid, S.; Saini, S.; Arora, S.; Deng, G.; Shahryari, V.; Chang, I.; Tanaka, Y.; Tabatabai, Z. L.; Enokida, H.; Seki, N.; Nakagawa, M.; Dahiya, R. Genistein up-regulates tumor suppressor microRNA-574-3p in prostate cancer. *PLoS One* **2013**, *8* (3), e58929.
(46) Ambs, S.; Prueitt, R. L.; Yi, M.; Hudson, R. S.; Howe, T. M.; Petrocca, F.; Wallace, T. A.; Liu, C. G.; Volinia, S.; Calin, G. A.; Yfantis, H. G.; Stephens, R. M.; Croce, C. M. Genomic profiling of microRNA and messenger RNA reveals deregulated microRNA expression in prostate cancer. *Cancer Res.* **2008**, *68* (15), 6162−70.
(47) Amir, S.; Ma, A. H.; Shi, X. B.; Xue, L.; Kung, H. J.; Devere White, R. W. Oncomir miR-125b suppresses p14(ARF) to modulate p53-dependent and p53-independent apoptosis in prostate cancer. *PLoS One* **2013**, *8* (4), e61064.
(48) Feng, Z.; Zhang, C.; Wu, R.; Hu, W. Tumor suppressor p53 meets microRNAs. *J. Mol. Cell Biol.* **2011**, *3* (1), 44−50.
(49) Fujita, Y.; Kojima, K.; Hamada, N.; Ohhashi, R.; Akao, Y.; Nozawa, Y.; Deguchi, T.; Ito, M. Effects of miR-34a on cell growth and chemoresistance in prostate cancer PC3 cells. *Biochem. Biophys. Res. Commun.* **2008**, *377* (1), 114−9.
(50) Lodygin, D.; Tarasov, V.; Epanchintsev, A.; Berking, C.; Knyazeva, T.; Korner, H.; Knyazev, P.; Diebold, J.; Hermeking, H. Inactivation of miR-34a by aberrant CpG methylation in multiple types of cancer. *Cell Cycle* **2008**, *7* (16), 2591−600.
(51) Sylvestre, Y.; De Guire, V.; Querido, E.; Mukhopadhyay, U. K.; Bourdeau, V.; Major, F.; Ferbeyre, G.; Chartrand, P. An E2F/miR-20a autoregulatory feedback loop. *J. Biol. Chem.* **2007**, *282* (4), 2135−43.
(52) Tian, L.; Fang, Y. X.; Xue, J. L.; Chen, J. Z. Four microRNAs promote prostate cell proliferation with regulation of PTEN and its downstream signals in vitro. *PLoS One* **2013**, *8* (9), e75885.
(53) Folini, M.; Gandellini, P.; Longoni, N.; Profumo, V.; Callari, M.; Pennati, M.; Colecchia, M.; Supino, R.; Veneroni, S.; Salvioni, R.; Valdagni, R.; Daidone, M. G.; Zaffaroni, N. miR-21: an oncomir on strike in prostate cancer. *Mol. Cancer* **2010**, *9*, 12.
(54) Li, T.; Li, D.; Sha, J.; Sun, P.; Huang, Y. MicroRNA-21 directly targets MARCKS and promotes apoptosis resistance and invasion in prostate cancer cells. *Biochem. Biophys. Res. Commun.* **2009**, *383* (3), 280−5.
(55) Yang, C. H.; Yue, J.; Fan, M.; Pfeffer, L. M. IFN induces miR-21 through a signal transducer and activator of transcription 3-dependent pathway as a suppressive negative feedback on IFN-induced apoptosis. *Cancer Res.* **2010**, *70* (20), 8108−16.
(56) Shi, G. H.; Ye, D. W.; Yao, X. D.; Zhang, S. L.; Dai, B.; Zhang, H. L.; Shen, Y. J.; Zhu, Y.; Zhu, Y. P.; Xiao, W. J.; Ma, C. G. Involvement of microRNA-21 in mediating chemo-resistance to docetaxel in androgen-independent prostate cancer PC3 cells. *Acta Pharmacol. Sin.* **2010**, *31* (7), 867−73.
(57) Bourguignon, L. Y.; Spevak, C. C.; Wong, G.; Xia, W.; Gilad, E. Hyaluronan-CD44 interaction with protein kinase C(epsilon) promotes oncogenic signaling by the stem cell marker Nanog and the production of microRNA-21, leading to down-regulation of the tumor suppressor protein PDCD4, anti-apoptosis, and chemotherapy resistance in breast tumor cells. *J. Biol. Chem.* **2009**, *284* (39), 26533−46.
(58) Szakacs, G.; Paterson, J. K.; Ludwig, J. A.; Booth-Genthe, C.; Gottesman, M. M. Targeting multidrug resistance in cancer. *Nat. Rev. Drug Discovery* **2006**, *5* (3), 219−34.
(59) Sanchez, C.; Mendoza, P.; Contreras, H. R.; Vergara, J.; McCubrey, J. A.; Huidobro, C.; Castellon, E. A. Expression of multidrug resistance proteins in prostate cancer is related with cell sensitivity to chemotherapeutic drugs. *Prostate* **2009**, *69* (13), 1448−59.
(60) Zalcberg, J.; Hu, X. F.; Slater, A.; Parisot, J.; El-Osta, S.; Kantharidis, P.; Chou, S. T.; Parkin, J. D. MRP1 not MDR1 gene expression is the predominant mechanism of acquired multidrug resistance in two prostate carcinoma cell lines. *Prostate Cancer Prostatic Dis.* **2000**, *3* (2), 66−75.
(61) Takeda, M.; Mizokami, A.; Mamiya, K.; Li, Y. Q.; Zhang, J.; Keller, E. T.; Namiki, M. The establishment of two paclitaxel-resistant prostate cancer cell lines and the mechanisms of paclitaxel resistance with two cell lines. *Prostate* **2007**, *67* (9), 955−67.
(62) Gottesman, M. M.; Fojo, T.; Bates, S. E. Multidrug resistance in cancer: role of ATP-dependent transporters. *Nat. Rev. Cancer* **2002**, *2* (1), 48−58.
(63) Doyle, L.; Ross, D. D. Multidrug resistance mediated by the breast cancer resistance protein BCRP (ABCG2). *Oncogene* **2003**, *22* (47), 7340−58.
(64) Gardner, E. R.; Ahlers, C. M.; Shukla, S.; Sissung, T. M.; Ockers, S. B.; Price, D. K.; Hamada, A.; Robey, R. W.; Steinberg, S. M.; Ambudkar, S. V.; Dahut, W. L.; Figg, W. D. Association of the ABCG2 C421A polymorphism with prostate cancer risk and survival. *BJU Int.* **2008**, *102* (11), 1694−9.
(65) Ding, X. W.; Wu, J. H.; Jiang, C. P. ABCG2: a potential marker of stem cells and novel target in stem cell and cancer therapy. *Life Sci.* **2010**, *86* (17−18), 631−7.
(66) Van Brussel, J. P.; Jan Van Steenbrugge, G.; Van Krimpen, C.; Bogdanowicz, J. F.; Van Der Kwast, T. H.; Schroder, F. H.; Mickisch, G. H. Expression of multidrug resistance related proteins and proliferative activity is increased in advanced clinical prostate cancer. *J. Urol.* **2001**, *165* (1), 130−5.
(67) Munoz, M.; Henderson, M.; Haber, M.; Norris, M. Role of the MRP1/ABCC1 multidrug transporter protein in cancer. *IUBMB Life* **2007**, *59* (12), 752−7.
(68) Grzywacz, M. J.; Yang, J. M.; Hait, W. N. Effect of the multidrug resistance protein on the transport of the antiandrogen flutamide. *Cancer Res.* **2003**, *63* (10), 2492−8.
(69) Munoz, J. L.; Bliss, S. A.; Greco, S. J.; Ramkissoon, S. H.; Ligon, K. L.; Rameshwar, P. Delivery of functional anti-miR-9 by mesenchymal stem cell-derived exosomes to glioblastoma multiforme

cells conferred chemosensitivity. *Mol. Ther. Nucleic Acids* **2013**, *2*, e126.
(70) Xu, Y.; Ohms, S. J.; Li, Z.; Wang, Q.; Gong, G.; Hu, Y.; Mao, Z.; Shannon, M. F.; Fan, J. Y. Changes in the expression of miR-381 and miR-495 are inversely associated with the expression of the MDR1 gene and development of multi-drug resistance. *PLoS One* **2013**, *8* (11), e82062.
(71) Boyerinas, B.; Park, S. M.; Murmann, A. E.; Gwin, K.; Montag, A. G.; Zillhardt, M.; Hua, Y. J.; Lengyel, E.; Peter, M. E. Let-7 modulates acquired resistance of ovarian cancer to Taxanes via IMP-1-mediated stabilization of multidrug resistance 1. *Int. J. Cancer* **2012**, *130* (8), 1787−97.
(72) Xu, Y.; Xia, F.; Ma, L.; Shan, J.; Shen, J.; Yang, Z.; Liu, J.; Cui, Y.; Bian, X.; Bie, P.; Qian, C. MicroRNA-122 sensitizes HCC cancer cells to adriamycin and vincristine through modulating expression of MDR and inducing cell cycle arrest. *Cancer Lett.* **2011**, *310* (2), 160−9.
(73) Kovalchuk, O.; Filkowski, J.; Meservy, J.; Ilnytskyy, Y.; Tryndyak, V. P.; Chekhun, V. F.; Pogribny, I. P. Involvement of microRNA-451 in resistance of the MCF-7 breast cancer cells to chemotherapeutic drug doxorubicin. *Mol. Cancer Ther* **2008**, *7* (7), 2152−9.
(74) Feng, D. D.; Zhang, H.; Zhang, P.; Zheng, Y. S.; Zhang, X. J.; Han, B. W.; Luo, X. Q.; Xu, L.; Zhou, H.; Qu, L. H.; Chen, Y. Q. Down-regulated miR-331-5p and miR-27a are associated with chemotherapy resistance and relapse in leukaemia. *J. Cell Mol. Med.* **2011**, *15* (10), 2164−75.
(75) Chen, Z.; Ma, T.; Huang, C.; Zhang, L.; Lv, X.; Xu, T.; Hu, T.; Li, J. MiR-27a modulates the MDR1/P-glycoprotein expression by inhibiting FZD7/beta-catenin pathway in hepatocellular carcinoma cells. *Cell Signalling* **2013**, *25* (12), 2693−701.
(76) Zhu, H.; Wu, H.; Liu, X.; Evans, B. R.; Medina, D. J.; Liu, C. G.; Yang, J. M. Role of MicroRNA miR-27a and miR-451 in the regulation of MDR1/P-glycoprotein expression in human cancer cells. *Biochem. Pharmacol.* **2008**, *76* (5), 582−8.
(77) Li, Z.; Hu, S.; Wang, J.; Cai, J.; Xiao, L.; Yu, L.; Wang, Z. MiR-27a modulates MDR1/P-glycoprotein expression by targeting HIPK2 in human ovarian cancer cells. *Gynecol Oncol* **2010**, *119* (1), 125−30.
(78) Pan, Y. Z.; Morris, M. E.; Yu, A. M. MicroRNA-328 negatively regulates the expression of breast cancer resistance protein (BCRP/ABCG2) in human cancer cells. *Mol. Pharmacol.* **2009**, *75* (6), 1374−9.
(79) Li, X.; Pan, Y. Z.; Seigel, G. M.; Hu, Z. H.; Huang, M.; Yu, A. M. Breast cancer resistance protein BCRP/ABCG2 regulatory microRNAs (hsa-miR-328, -519c and -520(h) and their differential expression in stem-like ABCG2+ cancer cells. *Biochem. Pharmacol.* **2011**, *81* (6), 783−92.
(80) To, K. K.; Zhan, Z.; Litman, T.; Bates, S. E. Regulation of ABCG2 expression at the 3′ untranslated region of its mRNA through modulation of transcript stability and protein translation by a putative microRNA in the S1 colon cancer cell line. *Mol. Cell. Biol.* **2008**, *28* (17), 5147−61.
(81) Liang, Z.; Wu, H.; Xia, J.; Li, Y.; Zhang, Y.; Huang, K.; Wagar, N.; Yoon, Y.; Cho, H. T.; Scala, S.; Shim, H. Involvement of miR-326 in chemotherapy resistance of breast cancer through modulating expression of multidrug resistance-associated protein 1. *Biochem. Pharmacol.* **2010**, *79* (6), 817−24.
(82) Markova, S. M.; Kroetz, D. L. ABCC4 is Regulated by microRNA-124a and microRNA-506. *Biochem. Pharmacol.* **2013**, *87*, 515−22.
(83) Thiery, J. P.; Acloque, H.; Huang, R. Y.; Nieto, M. A. Epithelial-mesenchymal transitions in development and disease. *Cell* **2009**, *139* (5), 871−90.
(84) Thiery, J. P.; Sleeman, J. P. Complex networks orchestrate epithelial-mesenchymal transitions. *Nat. Rev. Mol. Cell Biol.* **2006**, *7* (2), 131−42.
(85) Arumugam, T.; Ramachandran, V.; Fournier, K. F.; Wang, H.; Marquis, L.; Abbruzzese, J. L.; Gallick, G. E.; Logsdon, C. D.; McConkey, D. J.; Choi, W. Epithelial to mesenchymal transition contributes to drug resistance in pancreatic cancer. *Cancer Res.* **2009**, *69* (14), 5820−8.
(86) Fuchs, B. C.; Fujii, T.; Dorfman, J. D.; Goodwin, J. M.; Zhu, A. X.; Lanuti, M.; Tanabe, K. K. Epithelial-to-mesenchymal transition and integrin-linked kinase mediate sensitivity to epidermal growth factor receptor inhibition in human hepatoma cells. *Cancer Res.* **2008**, *68* (7), 2391−9.
(87) Bandyopadhyay, A.; Wang, L.; Agyin, J.; Tang, Y.; Lin, S.; Yeh, I. T.; De, K.; Sun, L. Z. Doxorubicin in combination with a small TGFbeta inhibitor: a potential novel therapy for metastatic breast cancer in mouse models. *PLoS One* **2010**, *5* (4), e10365.
(88) Sabbah, M.; Emami, S.; Redeuilh, G.; Julien, S.; Prevost, G.; Zimber, A.; Ouelaa, R.; Bracke, M.; De Wever, O.; Gespach, C. Molecular signature and therapeutic perspective of the epithelial-to-mesenchymal transitions in epithelial cancers. *Drug Resist. Update* **2008**, *11* (4−5), 123−51.
(89) Wang, Z.; Li, Y.; Kong, D.; Banerjee, S.; Ahmad, A.; Azmi, A. S.; Ali, S.; Abbruzzese, J. L.; Gallick, G. E.; Sarkar, F. H. Acquisition of epithelial-mesenchymal transition phenotype of gemcitabine-resistant pancreatic cancer cells is linked with activation of the notch signaling pathway. *Cancer Res.* **2009**, *69* (6), 2400−7.
(90) Kim, H. P.; Han, S. W.; Song, S. H.; Jeong, E. G.; Lee, M. Y.; Hwang, D.; Im, S. A.; Bang, Y. J.; Kim, T. Y. Testican-1-mediated epithelial-mesenchymal transition signaling confers acquired resistance to lapatinib in HER2-positive gastric cancer. *Oncogene* **2013**, DOI: 10.1038/onc.2013.285.
(91) Du, F.; Wu, X.; Liu, Y.; Wang, T.; Qi, X.; Mao, Y.; Jiang, L.; Zhu, Y.; Chen, Y.; Zhu, R.; Han, X.; Jin, J.; Ma, X.; Hua, D. Acquisition of paclitaxel resistance via PI3Kdependent epithelialmesenchymal transition in A2780 human ovarian cancer cells. *Oncol. Rep.* **2013**, *30* (3), 1113−8.
(92) Kajiyama, H.; Shibata, K.; Terauchi, M.; Yamashita, M.; Ino, K.; Nawa, A.; Kikkawa, F. Chemoresistance to paclitaxel induces epithelial-mesenchymal transition and enhances metastatic potential for epithelial ovarian carcinoma cells. *Int. J. Oncol.* **2007**, *31* (2), 277−83.
(93) Zeisberg, M.; Neilson, E. G. Biomarkers for epithelial-mesenchymal transitions. *J. Clin. Invest.* **2009**, *119* (6), 1429−37.
(94) Bracken, C. P.; Gregory, P. A.; Khew-Goodall, Y.; Goodall, G. J. The role of microRNAs in metastasis and epithelial-mesenchymal transition. *Cell. Mol. Life Sci.* **2009**, *66* (10), 1682−99.
(95) Zhang, J.; Ma, L. MicroRNA control of epithelial-mesenchymal transition and metastasis. *Cancer Metastasis Rev.* **2012**, *31* (3−4), 653−62.
(96) Bullock, M. D.; Sayan, A. E.; Packham, G. K.; Mirnezami, A. H. MicroRNAs: critical regulators of epithelial to mesenchymal (EMT) and mesenchymal to epithelial transition (MET) in cancer progression. *Biol. Cell* **2012**, *104* (1), 3−12.
(97) Peng, X.; Guo, W.; Liu, T.; Wang, X.; Tu, X.; Xiong, D.; Chen, S.; Lai, Y.; Du, H.; Chen, G.; Liu, G.; Tang, Y.; Huang, S.; Zou, X. Identification of miRs-143 and -145 that is associated with bone metastasis of prostate cancer and involved in the regulation of EMT. *PLoS One* **2011**, *6* (5), e20341.
(98) Guo, W.; Ren, D.; Chen, X.; Tu, X.; Huang, S.; Wang, M.; Song, L.; Zou, X.; Peng, X. HEF1 promotes epithelial mesenchymal transition and bone invasion in prostate cancer under the regulation of microRNA-145. *J. Cell. Biochem.* **2013**, *114* (7), 1606−15.
(99) Ru, P.; Steele, R.; Newhall, P.; Phillips, N. J.; Toth, K.; Ray, R. B. miRNA-29b suppresses prostate cancer metastasis by regulating epithelial-mesenchymal transition signaling. *Mol. Cancer Ther.* **2012**, *11* (5), 1166−73.
(100) Majid, S.; Dar, A. A.; Saini, S.; Shahryari, V.; Arora, S.; Zaman, M. S.; Chang, I.; Yamamura, S.; Tanaka, Y.; Chiyomaru, T.; Deng, G.; Dahiya, R. miRNA-34b inhibits prostate cancer through demethylation, active chromatin modifications, and AKT pathways. *Clin. Cancer Res.* **2013**, *19* (1), 73−84.
(101) Puhr, M.; Hoefer, J.; Schafer, G.; Erb, H. H.; Oh, S. J.; Klocker, H.; Heidegger, I.; Neuwirt, H.; Culig, Z. Epithelial-to-mesenchymal transition leads to docetaxel resistance in prostate cancer and is

mediated by reduced expression of miR-200c and miR-205. *Am. J. Pathol.* **2012**, *181* (6), 2188−201.
(102) Nanta, R.; Kumar, D.; Meeker, D.; Rodova, M.; Van Veldhuizen, P. J.; Shankar, S.; Srivastava, R. K. NVP-LDE-225 (Erismodegib) inhibits epithelial-mesenchymal transition and human prostate cancer stem cell growth in NOD/SCID IL2Rgamma null mice by regulating Bmi-1 and microRNA-128. *Oncogenesis* **2013**, *2*, e42.
(103) Kong, D.; Li, Y.; Wang, Z.; Banerjee, S.; Ahmad, A.; Kim, H. R.; Sarkar, F. H. miR-200 regulates PDGF-D-mediated epithelial-mesenchymal transition, adhesion, and invasion of prostate cancer cells. *Stem Cells* **2009**, *27* (8), 1712−21.
(104) Taube, J. H.; Malouf, G. G.; Lu, E.; Sphyris, N.; Vijay, V.; Ramachandran, P. P.; Ueno, K. R.; Gaur, S.; Nicoloso, M. S.; Rossi, S.; Herschkowitz, J. I.; Rosen, J. M.; Issa, J. P.; Calin, G. A.; Chang, J. T.; Mani, S. A. Epigenetic silencing of microRNA-203 is required for EMT and cancer stem cell properties. *Sci. Rep.* **2013**, *3*, 2687.
(105) Ishteiwy, R. A.; Ward, T. M.; Dykxhoorn, D. M.; Burnstein, K. L. The microRNA -23b/-27b cluster suppresses the metastatic phenotype of castration-resistant prostate cancer cells. *PLoS One* **2012**, *7* (12), e52106.
(106) Liu, Y. N.; Yin, J. J.; Abou-Kheir, W.; Hynes, P. G.; Casey, O. M.; Fang, L.; Yi, M.; Stephens, R. M.; Seng, V.; Sheppard-Tillman, H.; Martin, P.; Kelly, K. MiR-1 and miR-200 inhibit EMT via Slug-dependent and tumorigenesis via Slug-independent mechanisms. *Oncogene* **2013**, *32* (3), 296−306.
(107) Patrawala, L.; Calhoun, T.; Schneider-Broussard, R.; Zhou, J.; Claypool, K.; Tang, D. G. Side population is enriched in tumorigenic, stem-like cancer cells, whereas ABCG2+ and ABCG2- cancer cells are similarly tumorigenic. *Cancer Res.* **2005**, *65* (14), 6207−19.
(108) Patrawala, L.; Calhoun, T.; Schneider-Broussard, R.; Li, H.; Bhatia, B.; Tang, S.; Reilly, J. G.; Chandra, D.; Zhou, J.; Claypool, K.; Coghlan, L.; Tang, D. G. Highly purified CD44+ prostate cancer cells from xenograft human tumors are enriched in tumorigenic and metastatic progenitor cells. *Oncogene* **2006**, *25* (12), 1696−708.
(109) Patrawala, L.; Calhoun-Davis, T.; Schneider-Broussard, R.; Tang, D. G. Hierarchical organization of prostate cancer cells in xenograft tumors: the CD44+alpha2beta1+ cell population is enriched in tumor-initiating cells. *Cancer Res.* **2007**, *67* (14), 6796−805.
(110) Tokar, E. J.; Qu, W.; Liu, J.; Liu, W.; Webber, M. M.; Phang, J. M.; Waalkes, M. P. Arsenic-specific stem cell selection during malignant transformation. *J. Natl. Cancer Inst.* **2010**, *102* (9), 638−49.
(111) Liu, T.; Xu, F.; Du, X.; Lai, D.; Zhao, Y.; Huang, Q.; Jiang, L.; Huang, W.; Cheng, W.; Liu, Z. Establishment and characterization of multi-drug resistant, prostate carcinoma-initiating stem-like cells from human prostate cancer cell lines 22RV1. *Mol. Cell. Biochem.* **2010**, *340* (1−2), 265−73.
(112) Liu, C.; Kelnar, K.; Liu, B.; Chen, X.; Calhoun-Davis, T.; Li, H.; Patrawala, L.; Yan, H.; Jeter, C.; Honorio, S.; Wiggins, J. F.; Bader, A. G.; Fagin, R.; Brown, D.; Tang, D. G. The microRNA miR-34a inhibits prostate cancer stem cells and metastasis by directly repressing CD44. *Nat. Med.* **2011**, *17* (2), 211−5.
(113) Liu, C.; Tang, D. G. MicroRNA regulation of cancer stem cells. *Cancer Res.* **2011**, *71* (18), 5950−4.
(114) Liu, C.; Kelnar, K.; Vlassov, A. V.; Brown, D.; Wang, J.; Tang, D. G. Distinct microRNA expression profiles in prostate cancer stem/progenitor cells and tumor-suppressive functions of let-7. *Cancer Res.* **2012**, *72* (13), 3393−404.
(115) Hsieh, I. S.; Chang, K. C.; Tsai, Y. T.; Ke, J. Y.; Lu, P. J.; Lee, K. H.; Yeh, S. D.; Hong, T. M.; Chen, Y. L. MicroRNA-320 suppresses the stem cell-like characteristics of prostate cancer cells by down-regulating the Wnt/beta-catenin signaling pathway. *Carcinogenesis* **2013**, *34* (3), 530−8.
(116) Li, K.; Liu, C.; Zhou, B.; Bi, L.; Huang, H.; Lin, T.; Xu, K. Role of EZH2 in the growth of prostate cancer stem cells isolated from LNCaP cells. *Int. J. Mol. Sci.* **2013**, *14* (6), 11981−93.
(117) Singh, A.; Settleman, J. EMT, cancer stem cells and drug resistance: an emerging axis of evil in the war on cancer. *Oncogene* **2010**, *29* (34), 4741−51.
(118) Wang, Z.; Li, Y.; Ahmad, A.; Azmi, A. S.; Kong, D.; Banerjee, S.; Sarkar, F. H. Targeting miRNAs involved in cancer stem cell and EMT regulation: An emerging concept in overcoming drug resistance. *Drug Resist. Update* **2010**, *13* (4−5), 109−18.
(119) Danquah, M.; Singh, S.; Behrman, S. W.; Mahato, R. I. Role of miRNA and cancer stem cells in chemoresistance and pancreatic cancer treatment. *Expert Opin. Drug Delivery* **2012**, *9* (12), 1443−7.
(120) Blick, T.; Hugo, H.; Widodo, E.; Waltham, M.; Pinto, C.; Mani, S. A.; Weinberg, R. A.; Neve, R. M.; Lenburg, M. E.; Thompson, E. W. Epithelial mesenchymal transition traits in human breast cancer cell lines parallel the CD44(hi/)CD24 (lo/-) stem cell phenotype in human breast cancer. *J. Mammary Gland Biol. Neoplasia* **2010**, *15* (2), 235−52.
(121) Krutzfeldt, J.; Rajewsky, N.; Braich, R.; Rajeev, K. G.; Tuschl, T.; Manoharan, M.; Stoffel, M. Silencing of microRNAs in vivo with 'antagomirs'. *Nature* **2005**, *438* (7068), 685−9.
(122) Hansen, T. B.; Jensen, T. I.; Clausen, B. H.; Bramsen, J. B.; Finsen, B.; Damgaard, C. K.; Kjems, J. Natural RNA circles function as efficient microRNA sponges. *Nature* **2013**, *495* (7441), 384−8.
(123) Ebert, M. S.; Sharp, P. A. MicroRNA sponges: progress and possibilities. *RNA* **2010**, *16* (11), 2043−50.
(124) Wang, Z. The guideline of the design and validation of MiRNA mimics. *Methods Mol. Biol.* **2011**, *676*, 211−23.
(125) Singh, S.; Chitkara, D.; Mehrazin, R.; Behrman, S. W.; Wake, R. W.; Mahato, R. I. Chemoresistance in prostate cancer cells is regulated by miRNAs and hedgehog pathway. *PLoS One* **2012**, *7* (6), e40021.
(126) Li, Y.; VandenBoom, T. G., II; Kong, D.; Wang, Z.; Ali, S.; Philip, P. A.; Sarkar, F. H. Up-regulation of miR-200 and let-7 by natural agents leads to the reversal of epithelial-to-mesenchymal transition in gemcitabine-resistant pancreatic cancer cells. *Cancer Res.* **2009**, *69* (16), 6704−12.
(127) Sun, M.; Estrov, Z.; Ji, Y.; Coombes, K. R.; Harris, D. H.; Kurzrock, R. Curcumin (diferuloylmethane) alters the expression profiles of microRNAs in human pancreatic cancer cells. *Mol. Cancer Ther.* **2008**, *7* (3), 464−73.
(128) Tsang, W. P.; Kwok, T. T. Epigallocatechin gallate up-regulation of miR-16 and induction of apoptosis in human cancer cells. *J. Nutr. Biochem.* **2010**, *21* (2), 140−6.
(129) Yang, C. H.; Yue, J.; Sims, M.; Pfeffer, L. M. The curcumin analog EF24 targets NF-kappaB and miRNA-21, and has potent anticancer activity in vitro and in vivo. *PLoS One* **2013**, *8* (8), e71130.
(130) Chiyomaru, T.; Yamamura, S.; Fukuhara, S.; Yoshino, H.; Kinoshita, T.; Majid, S.; Saini, S.; Chang, I.; Tanaka, Y.; Enokida, H.; Seki, N.; Nakagawa, M.; Dahiya, R. Genistein inhibits prostate cancer cell growth by targeting miR-34a and oncogenic HOTAIR. *PLoS One* **2013**, *8* (8), e70372.
(131) Xu, B.; Niu, X.; Zhang, X.; Tao, J.; Wu, D.; Wang, Z.; Li, P.; Zhang, W.; Wu, H.; Feng, N.; Hua, L.; Wang, X. miR-143 decreases prostate cancer cells proliferation and migration and enhances their sensitivity to docetaxel through suppression of KRAS. *Mol. Cell. Biochem.* **2011**, *350* (1−2), 207−13.
(132) Kim, C.; Shah, B. P.; Subramaniam, P.; Lee, K. B. Synergistic induction of apoptosis in brain cancer cells by targeted codelivery of siRNA and anticancer drugs. *Mol. Pharmaceutics* **2011**, *8* (5), 1955−61.
(133) Zhi, F.; Dong, H.; Jia, X.; Guo, W.; Lu, H.; Yang, Y.; Ju, H.; Zhang, X.; Hu, Y. Functionalized graphene oxide mediated adriamycin delivery and miR-21 gene silencing to overcome tumor multidrug resistance in vitro. *PLoS One* **2013**, *8* (3), e60034.
(134) Ren, Y.; Kang, C. S.; Yuan, X. B.; Zhou, X.; Xu, P.; Han, L.; Wang, G. X.; Jia, Z.; Zhong, Y.; Yu, S.; Sheng, J.; Pu, P. Y. Co-delivery of as-miR-21 and 5-FU by poly(amidoamine) dendrimer attenuates human glioma cell growth in vitro. *J. Biomater. Sci., Polym. Ed.* **2010**, *21* (3), 303−14.
(135) Wang, Y.; Gao, S.; Ye, W. H.; Yoon, H. S.; Yang, Y. Y. Co-delivery of drugs and DNA from cationic core−shell nanoparticles self-assembled from a biodegradable copolymer. *Nat. Mater.* **2006**, *5* (10), 791−6.

(136) Saad, M.; Garbuzenko, O. B.; Minko, T. Co-delivery of siRNA and an anticancer drug for treatment of multidrug-resistant cancer. *Nanomedicine* **2008**, *3* (6), 761−76.
(137) Chen, A. M.; Zhang, M.; Wei, D.; Stueber, D.; Taratula, O.; Minko, T.; He, H. Co-delivery of doxorubicin and Bcl-2 siRNA by mesoporous silica nanoparticles enhances the efficacy of chemotherapy in multidrug-resistant cancer cells. *Small* **2009**, *5* (23), 2673−7.
(138) Zhang, Y.; Satterlee, A.; Huang, L. In vivo gene delivery by nonviral vectors: overcoming hurdles? *Mol. Ther.* **2012**, *20* (7), 1298−304.
(139) Bouchie, A. First microRNA mimic enters clinic. *Nat. Biotechnol.* **2013**, *31* (7), 577.
(140) Li, F.; Mahato, R. I. RNA interference for improving the outcome of islet transplantation. *Adv. Drug Delivery Rev.* **2011**, *63* (1−2), 47−68.
(141) Wang, S.; Liu, B.; Gu, C.; Song, Y.; Qian, C.; Hu, M.; Chai, L.; Wang, C. Self-similar evolution in a short fiber amplifier through nonlinear pulse preshaping. *Opt. Lett.* **2013**, *38* (3), 296−8.
(142) Yang, T. C.; Chang, C. H.; Liu, Y. T.; Chen, Y. L.; Tu, P. H.; Chen, H. C. Predictors of shunt-dependent chronic hydrocephalus after aneurysmal subarachnoid haemorrhage. *Eur. Neurol.* **2013**, *69* (5), 296−303.
(143) He, D.; Lu, W.; Chang, K.; Liu, Y.; Zhang, J.; Zeng, Z. Vascular endothelial growth factor polymorphisms and risk of Alzheimer's disease: a meta-analysis. *Gene* **2013**, *518* (2), 296−302.
(144) Liu, F.; Zhu, Z. J.; Li, P.; He, Y. L. Creation of a female rabbit model for intrauterine adhesions using mechanical and infectious injury. *J. Surg. Res.* **2013**, *183* (1), 296−303.
(145) Niu, H.; Yuan, R.; Chai, Y.; Mao, L.; Liu, H.; Cao, Y. Highly amplified electrochemiluminescence of peroxydisulfate using bienzyme functionalized palladium nanoparticles as labels for ultrasensitive immunoassay. *Biosens. Bioelectron.* **2013**, *39* (1), 296−9.
(146) Shields, N.; Dodd, K. J.; Abblitt, C. Do children with Down Syndrome perform sufficient physical activity to maintain good health? A pilot study. *Adapt. Phys. Act. Q.* **2009**, *26* (4), 307−20.
(147) Product Pipeline. http://www.pronai.com/pipeline/index.htm.
(148) Pipeline Products. http://www.tekmira.com/pipeline/pipeline-products.php.
(149) Alnylam 5 × 15. http://www.alnylam.com/product-pipeline/alnylam-5x15/.
(150) Morrissey, D. V.; Lockridge, J. A.; Shaw, L.; Blanchard, K.; Jensen, K.; Breen, W.; Hartsough, K.; Machemer, L.; Radka, S.; Jadhav, V.; Vaish, N.; Zinnen, S.; Vargeese, C.; Bowman, K.; Shaffer, C. S.; Jeffs, L. B.; Judge, A.; MacLachlan, I.; Polisky, B. Potent and persistent in vivo anti-HBV activity of chemically modified siRNAs. *Nat. Biotechnol.* **2005**, *23* (8), 1002−7.
(151) Semple, S. C.; Akinc, A.; Chen, J.; Sandhu, A. P.; Mui, B. L.; Cho, C. K.; Sah, D. W.; Stebbing, D.; Crosley, E. J.; Yaworski, E.; Hafez, I. M.; Dorkin, J. R.; Qin, J.; Lam, K.; Rajeev, K. G.; Wong, K. F.; Jeffs, L. B.; Nechev, L.; Eisenhardt, M. L.; Jayaraman, M.; Kazem, M.; Maier, M. A.; Srinivasulu, M.; Weinstein, M. J.; Chen, Q.; Alvarez, R.; Barros, S. A.; De, S.; Klimuk, S. K.; Borland, T.; Kosovrasti, V.; Cantley, W. L.; Tam, Y. K.; Manoharan, M.; Ciufolini, M. A.; Tracy, M. A.; de Fougerolles, A.; MacLachlan, I.; Cullis, P. R.; Madden, T. D.; Hope, M. J. Rational design of cationic lipids for siRNA delivery. *Nat. Biotechnol.* **2010**, *28* (2), 172−6.
(152) Jayaraman, M.; Ansell, S. M.; Mui, B. L.; Tam, Y. K.; Chen, J.; Du, X.; Butler, D.; Eltepu, L.; Matsuda, S.; Narayanannair, J. K.; Rajeev, K. G.; Hafez, I. M.; Akinc, A.; Maier, M. A.; Tracy, M. A.; Cullis, P. R.; Madden, T. D.; Manoharan, M.; Hope, M. J. Maximizing the potency of siRNA lipid nanoparticles for hepatic gene silencing in vivo. *Angew. Chem., Int. Ed.* **2012**, *51* (34), 8529−33.
(153) Maier, M. A.; Jayaraman, M.; Matsuda, S.; Liu, J.; Barros, S.; Querbes, W.; Tam, Y. K.; Ansell, S. M.; Kumar, V.; Qin, J.; Zhang, X.; Wang, Q.; Panesar, S.; Hutabarat, R.; Carioto, M.; Hettinger, J.; Kandasamy, P.; Butler, D.; Rajeev, K. G.; Pang, B.; Charisse, K.; Fitzgerald, K.; Mui, B. L.; Du, X.; Cullis, P.; Madden, T. D.; Hope, M. J.; Manoharan, M.; Akinc, A. Biodegradable lipids enabling rapidly eliminated lipid nanoparticles for systemic delivery of RNAi therapeutics. *Mol. Ther.* **2013**, *21* (8), 1570−8.
(154) Kolli, S.; Wong, S. P.; Harbottle, R.; Johnston, B.; Thanou, M.; Miller, A. D. pH-triggered nanoparticle mediated delivery of siRNA to liver cells in vitro and in vivo. *Bioconjugate Chem.* **2013**, *24* (3), 314−32.
(155) Lin, S. Y.; Zhao, W. Y.; Tsai, H. C.; Hsu, W. H.; Lo, C. L.; Hsiue, G. H. Sterically polymer-based liposomal complexes with dual-shell structure for enhancing the siRNA delivery. *Biomacromolecules* **2012**, *13* (3), 664−75.
(156) Akinc, A.; Querbes, W.; De, S.; Qin, J.; Frank-Kamenetsky, M.; Jayaprakash, K. N.; Jayaraman, M.; Rajeev, K. G.; Cantley, W. L.; Dorkin, J. R.; Butler, J. S.; Qin, L.; Racie, T.; Sprague, A.; Fava, E.; Zeigerer, A.; Hope, M. J.; Zerial, M.; Sah, D. W.; Fitzgerald, K.; Tracy, M. A.; Manoharan, M.; Koteliansky, V.; Fougerolles, A.; Maier, M. A. Targeted delivery of RNAi therapeutics with endogenous and exogenous ligand-based mechanisms. *Mol. Ther.* **2010**, *18* (7), 1357−64.
(157) Bisgaier, C. L.; Siebenkas, M. V.; Williams, K. J. Effects of apolipoproteins A-IV and A-I on the uptake of phospholipid liposomes by hepatocytes. *J. Biol. Chem.* **1989**, *264* (2), 862−6.
(158) Davis, M. E. The first targeted delivery of siRNA in humans via a self-assembling, cyclodextrin polymer-based nanoparticle: from concept to clinic. *Mol. Pharmaceutics* **2009**, *6* (3), 659−68.
(159) With Roche Delivery Tech Advancing, Arrowhead Drops First-Generation Cancer Drug. http://www.genomeweb.com/rnai/roche-delivery-tech-advancing-arrowhead-drops-first-generation-cancer-drug.
(160) Lewis, D. Dynamic Polyconjugates (DPC) Technology: An Elegant Solution to the siRNA Delivery Problem. http://www.arrowheadresearch.com/sites/default/files/udocs/Arrowhead_Research_Corporation-DPC_Technology_White_Paper.pdf.
(161) Wong, S. C.; Klein, J. J.; Hamilton, H. L.; Chu, Q.; Frey, C. L.; Trubetskoy, V. S.; Hegge, J.; Wakefield, D.; Rozema, D. B.; Lewis, D. L. Co-injection of a targeted, reversibly masked endosomolytic polymer dramatically improves the efficacy of cholesterol-conjugated small interfering RNAs in vivo. *Nucleic Acid Ther.* **2012**, *22* (6), 380−90.
(162) Wooddell, C. I.; Rozema, D. B.; Hossbach, M.; John, M.; Hamilton, H. L.; Chu, Q.; Hegge, J. O.; Klein, J. J.; Wakefield, D. H.; Oropeza, C. E.; Deckert, J.; Roehl, I.; Jahn-Hofmann, K.; Hadwiger, P.; Vornlocher, H. P.; McLachlan, A.; Lewis, D. L. Hepatocyte-targeted RNAi therapeutics for the treatment of chronic hepatitis B virus infection. *Mol. Ther.* **2013**, *21* (5), 973−85.
(163) Maier, M. Advances in Systemic Delivery of RNAi Therapeutics. http://www.alnylam.com/Files/Presentations/ALNY-12thUS-Japan%20Symp-on%20DDS-131220.pdf.
(164) Singh, S.; Narang, A. S.; Mahato, R. I. Subcellular fate and off-target effects of siRNA, shRNA, and miRNA. *Pharm. Res.* **2011**, *28* (12), 2996−3015.
(165) Mahato, R. I.; Kawabata, K.; Nomura, T.; Takakura, Y.; Hashida, M. Physicochemical and pharmacokinetic characteristics of plasmid DNA/cationic liposome complexes. *J. Pharm. Sci.* **1995**, *84* (11), 1267−71.

OPEN ACCESS Freely available online

PLoS one

Chemoresistance in Prostate Cancer Cells Is Regulated by miRNAs and Hedgehog Pathway

Saurabh Singh[1], Deepak Chitkara[1,2], Reza Mehrazin[3], Stephen W. Behrman[4], Robert W. Wake[3], Ram I. Mahato[1]*

1 Department of Pharmaceutical Sciences, University of Tennessee Health Science Center, Memphis, Tennessee, United States of America, **2** Department of Pharmaceutics, National Institute of Pharmaceutical Education and Research, SAS Nagar (Mohali), Punjab, India, **3** Department of Urology, University of Tennessee Health Science Center, Memphis, Tennessee, United States of America, **4** Department of Surgery, University of Tennessee Health Science Center, Memphis, Tennessee, United States of America

Abstract

Many prostate cancers relapse due to the generation of chemoresistance rendering first-line treatment drugs like paclitaxel (PTX) ineffective. The present study aims to determine the role of miRNAs and Hedgehog (Hh) pathway in chemoresistant prostate cancer and to evaluate the combination therapy using Hh inhibitor cyclopamine (CYA). Studies were conducted on PTX resistant DU145-TXR and PC3-TXR cell lines and clinical prostate tissues. Drug sensitivity and apoptosis assays showed significantly improved cytotoxicity with combination of PTX and CYA. To distinguish the presence of cancer stem cell like side populations (SP), Hoechst 33342 flow cytometry method was used. PTX resistant DU145 and PC3 cells, as well as human prostate cancer tissue possess a distinct SP fraction. Nearly 75% of the SP cells are in the G0/G1 phase compared to 62% for non-SP cells and have higher expression of stem cell markers as well. SP cell fraction was increased following PTX monotherapy and treatment with CYA or CYA plus PTX effectively reduced their numbers suggesting the effectiveness of combination therapy. SP fraction cells were allowed to differentiate and reanalyzed by Hoechst staining and gene expression analysis. Post differentiation, SP cells constitute 15.8% of total viable cells which decreases to 0.6% on treatment with CYA. The expression levels of P-gp efflux protein were also significantly decreased on treatment with PTX and CYA combination. MicroRNA profiling of DU145-TXR and PC3-TXR cells and prostate cancer tissue from the patients showed decreased expression of tumor suppressor miRNAs such as miR34a and miR200c. Treatment with PTX and CYA combination restored the expression of miR200c and 34a, confirming their role in modulating chemoresistance. We have shown that supplementing mitotic stabilizer drugs such as PTX with Hh-inhibitor CYA can reverse PTX chemoresistance and eliminate SP fraction in androgen independent, metastatic prostate cancer cell lines.

Citation: Singh S, Chitkara D, Mehrazin R, Behrman SW, Wake RW, et al. (2012) Chemoresistance in Prostate Cancer Cells Is Regulated by miRNAs and Hedgehog Pathway. PLoS ONE 7(6): e40021. doi:10.1371/journal.pone.0040021

Editor: Wing-Kin Syn, Institute of Hepatology London, United Kingdom

Received January 26, 2012; **Accepted** May 30, 2012; **Published** June 29, 2012

Funding: This work is supported by an Idea Award (W81XWH-10-1-0969) from the Department of Defense Prostate Cancer Research Program. Financial support by Kosten Foundation (www.kostenfoundation.com) is also gratefully acknowledged. The funders had no role in study design, data collection and analysis, decision to publish, or preparation of the manuscript.

Competing Interests: The authors have declared that no competing interests exist.

* E-mail: rmahato@uthsc.edu

Introduction

Prostate cancer is the second leading cause of cancer related death in men in the United States [1]. While anti-androgen therapy is currently the first line of treatment for patients diagnosed with prostate cancers, most patients will eventually develop the androgen-independent form of prostate cancers which is highly metastatic and has poor prognosis [2]. Microtubule stabilizers such as PTX are effective in treating patients diagnosed with androgen-independent prostate cancer [3]. While clinical trials have proven the initial efficacy of taxanes in increasing survival in prostate cancer patients [4], there are currently few effective approaches for treating chemoresistant prostate cancers.

Most tumors are heterogeneous and are composed of bulk and tumor initiating cells (TICs) with the latter forming a distinct subpopulation in many cancers. TICs are often referred to as cancer stem cells (CSCs) and are responsible for tumor initiation, self-renewal, and chemoresistance [5,6]. Many prostate cancers relapse due to the presence of highly chemoresistant tumor initiating/cancer stem cells [7,8]. Chemoresistance to anticancer drugs including PTX, by these cells may be contributed by drug-efflux pumps which can efficiently remove lipophilic molecules, including hydrophobic anticancer drugs. This inherent property of chemoresistant cells is used for identification and isolation of a side population (SP), which are a type of cancer stem cells. The SP fraction, initially identified by Goodell, is a small subpopulation of cells with enriched stem cell activity and are known to demonstrate distinctively low levels of Hoechst 33342 dye staining [9]. SP fraction cells have been shown to be insensitive to various chemotherapeutic drugs [10] owing to their ability in effluxing chemotherapy drugs (and lipophilic dyes such as Hoechst 33342) due to the high expression of ATP-binding cassette family, such as MDR1 (P-glycoprotein) and ABCG2 [11]. Chemoresistant SP cells will survive and sustain their clonogenicity during initial exposure to cytostatic drugs, thereby allowing disease recurrence when therapy is withdrawn. These subsets of CSCs are thus considered a viable target for improved therapeutic intervention and preventing chemoresistance and cancer relapse.

The development of chemoresistance through an increase in the number of cancer stem like cells, including SP fractions has been

attributed to alterations at the level of microRNAs (miRNAs) in various cancer types. These non-coding RNA molecules can act as oncogenes as well as tumor suppressor [12,13,14]. Dysregulation of miRNAs has been implicated in tumorigenesis and drug resistance as well. Recent work by Cochrane et al. has identified miRNAs involved in modulating chemoresistance in several cancers [15].

In our present study, we hypothesized that chemoresistance to PTX in metastatic prostate cancer cells could be due to the altered miRNA expression in these cells and that the combination of antimitotic drug with another small molecule that inhibits CSCs is likely to be effective in not only reverting chemoresistance by suppressing CSCs but also target miRNAs involved in chemoresistance. Thus, while failure of traditional chemotherapy is due to a failure to destroy CSCs/SP fractions, a combinatorial approach is likely to yield better results since the CSC-inhibitor will kill pluripotent cancer cells and will allow the antimitotic drug (in this case PTX) to attack bulk tumor cells. Towards this end, we have combined PTX with cyclopamine (CYA), a natural steroidal alkaloid which inhibits the Hedgehog (Hh) pathway resulting in decreased proliferation and increased apoptosis [16]. In recent years, the Hh signaling pathway has been implicated in the development and spread of prostate cancer [17,18]. Evidence has also indicated that Hh signaling supports androgen signaling and androgen-independent growth in prostate cancer cells in a low androgen environment [19]. Inhibition of Hh-pathway results in downregulation of genes involved in stem cell self-renewal as well as regression of prostate tumor without relapse [20]. Combination of docetaxel with CYA and epidermal growth factor receptor (EGFR) inhibitor gefitinib induced greater antiproliferative and apoptotic effects on SP cell fractions isolated from metastatic prostate cancer cells than individual drugs [21]. We have recently demonstrated that adding EGFR-inhibitor lapatinib can enhance the effectiveness of PTX in inducing apoptosis in a paclitaxel-resistant, androgen-independent metastatic prostate cancer cells line DU145-TXR, both *in vitro* as well as in xenograft tumors [22].

To understand the phenomenon of chemoresistance, in the present study we have used androgen independent (AI) metastatic prostate cancer cell lines DU145 and PC3 and their PTX-resistant versions, DU145-TXR and PC3-TXR, respectively. We have shown that PTX resistance of prostate cancer cells may be modulated at the level of miRNAs. We further demonstrate that combination therapy with CYA and PTX can effectively reduce cell viability, decrease SP-cell fraction at doses far lower than that used for CYA monotherapy and impact miRNAs putatively involved in modulating chemoresistance. Our data indicates that combination therapy involving supplementation of PTX with Hh-inhibitors can target specific miRNAs and cancer stem-cell like SP cell populations at doses that are effective in combination but not in monotherapy. This approach may represent a better approach in preventing metastasis and relapse in refractory prostate cancer since it is less likely to be toxic and will present with far fewer side effects for the patient, ensuring better compliance and reducing the chances of a recurrence.

Materials and Methods

Materials

PTX and CYA were purchased from LC Labs (Woburn, MA). SYBR Green real-time PCR master mix and reverse transcription reagents were purchased from Applied Biosystems (Foster city, CA). Goat anti-rabbit P-gp antibody and corresponding secondary antibody was purchased from Santa Cruz Biotechnology (Santa Cruz, CA). All other chemicals were obtained from Sigma-Aldrich (St. Louis, MO) and used as received, unless stated otherwise.

Cell lines

The human metastatic prostate cancer cell lines DU145 and PC3 and their PTX resistant versions DU145-TXR and PC3-TXR were a kind gift of Prof. Evan T. Keller (University of Michigan). All cell lines were maintained in RPMI culture media supplemented with 1% penicillin/ streptomycin and 10% fetal bovine serum (FBS) (Gibco) in a humidified incubator containing 5% CO_2 at 37°C as described earlier [22].

Human Prostate Tissue

Human prostate tissue (cancerous and benign) were obtained from the Veterans Affairs (VA) Hospital, Memphis, TN following established protocols and in accordance with the informed consent waiver provided by the Institutional Review Board (IRB) at UTHSC and at the VA Hospital. Prostate tissue was taken using an 18-gauge core needle biopsy gun and a portion of this tissue was rinsed and either flash frozen in liquid nitrogen and then stored at −80°C or placed in cold serum-free RPMI media containing antibiotics for preparing single cell suspensions. Tissues were classified as malignant or benign based on the diagnosis made by a pathologist.

Drug sensitivity and apoptosis assays in DU145-TXRCells

To determine the extent of cellular apoptosis following drug treatments, DU145-TXR cells were plated into 6-well plates (7.5×10^5 cells/well). After 24 h, the media was removed and fresh media containing varying concentrations of PTX, CYA or their combinations were added. The cells were then stained with Annexin-V and Propidium iodide (PI) using the Vybrant Apoptosis Assay Kit as per the manufacturer's protocol (Molecular Probes). Briefly, cells were trypsinized, washed twice with cold PBS and pelleted by centrifugation at 800 rpm for 5 min. The pellets were resuspended in 100 µl of 1X Annexin binding buffer and 5 µl fluorescein isothiocyanate (FITC)-Annexin-V. Propidium iodide (100 µg/ml) was added to each 100 µl of cell suspension. The stained cells were immediately analyzed by flow cytometry.

DU145-TXR cells were also used to determine the cell growth inhibition ability of PTX and CYA. Cells (5×10^3/well) were seeded in 96 well cell culture plates and incubated for 24 h to allow cell attachment. Media was then replaced with fresh media containing PTX (0.5/1 µM) or CYA (10/25 µM) or combination (PTX 0.5 µM and CYA 10µM) and incubated further for 48 h at 37°C/5% CO_2. Cell viability was then assessed by MTT assay. For this, media was removed and cells were washed with PBS and 200 µl of fresh media containing 3-(4,5-dimethyl-thiazol-2-yl)-2, 5-diphenyl tetrazolium bromide (MTT) (0.5 mg/ml) was added followed by incubation at 37°C/5% CO_2 for 4 h. After 4 h, media was removed and formed formazan crystals were dissolved in 200 µl DMSO and absorbance was measured at 560 nm. Cell viability was calculated using the following formula:

$$Cell\ Viability = \frac{Absorbance\ of\ test\ sample}{Absorbance\ of\ control} \times 100$$

DMSO was used to solubilize PTX and CYA and DMSO controls were included in all experiments.

Side Population analysis and cell sorting by FACS

Side population analysis in DU14-TXR and PC3-TXR cell lines was performed using Hoechst 33342 flow cytometry method. In brief, adherent cells were trypsinized and washed with phosphate buffered saline (PBS). Cells (1×10^6 cell/ml) were then suspended in RPMI media supplemented with 2% FBS and 1 mM HEPES buffer with or without drug solutions (Verapamil, PTX or PTX+CYA). Hoechst 33342 (5 µl; 1 mg/ml) dye was then added followed by incubation for 90 min at 37°C. Cells were recovered by centrifugation and washed several times with PBS to remove unbound dye and finally suspended in ice cold PBS containing 2% FBS. SP fraction in clinical samples was analyzed as described above with additional steps. Briefly, freshly resected prostate tissue was rinsed, mechanically minced and digested for 4 h at 37°C with 100 U/ml collagenase IV (Worthington Biologicals) in serum free RPMI. The tissue was frequently pipetted with a 5-ml serological pipette and at the end of incubation the digest was passed through an 18.5- gauge needle, centrifuged briefly and the supernatant sieved through a 100 µm cell strainer to obtain single cell suspension. Diluted single cell suspensions were then passed once through 40 µm mesh filter, their viability assessed by trypan blue staining and kept on ice until analyzed.

Cell Cycle analysis

Flow cytometry was used to determine the percentage of cells in different growth cycles. Cells (5×10^5) obtained after sorting were washed with PBS and fixed with ethanol (70%) at 4°C overnight followed by treatment with RNAse (1 mg/ml) and stained with PI (10 µg/ml). Percentage of cells in different cell cycle phases was then determined.

In vitro differentiation study

Ability of SP cells to differentiate was determined by culturing the pure cell fractions in a 6 well plate for 14 days post sorting. SP-fraction cells from DU145-TXR and PC-TXR (1×10^5/well) were seeded into 6 well plate and allowed to grow in RPMI culture media supplemented with 10% FBS. After 14 days, Hoechst staining and SP analysis was done on treated or untreated cell populations as described above. Gene expression analysis was also carried out on SP and non-SP cells both before and after-differentiation.

Western blot analysis

Following treatment, DU145 TXR cells were lysed using RIPA buffer and total protein concentration was determined using Bio-Rad RC DC protein assay kit (Hercules, CA). SDS-PAGE was then performed to resolve the proteins which were then transferred to Immobilon polyvinylidene fluoride (PVDF) membrane using iBlot dry blotting system (Invitrogen, Carlsbad, CA). Blocking was done using 5% non-fat dry milk in 1X PBST (PBS containing 0.05% Tween-20) for 1 h at room temperature. Membranes were then incubated with primary antibody for 16 h at 4°C. Actin was used as the loading control and target protein was detected by enhanced chemiluminescence (ECL) detection kit (GE Healthcare Life Sciences, PA).

Real time RT-PCR

Total RNA was extracted from sorted and unsorted prostate cancer cells using RNeasy RNA isolation kit (Qiagen, MD), followed by determination of its quality by Nanodrop 2000 instrument. It was then reverse transcribed into cDNA template as described before [23]. cDNA (100 ng) was then amplified by real-time PCR using SYBR Green dye universal master mix on a Light Cycler 480 instrument (Roche, Indianapolis, IN) using the primers for genes of interest for forty cycles Relative amount of mRNA compared to S19 (housekeeping gene) level was calculated using Crossing point (Cp) values and scaled relative to control samples set at a value of 1. Results for gene expression in experimental samples were plotted compared with the control.

MicroRNA (miRNA) profiling and data validation

Total RNA that includes small non-coding miRNA was isolated from untreated and drug-treated DU145-TXR and DU145 cells or PC3 and PC3-TXR cells using miRNEasy RNA isolation kit (Qiagen MD) following manufacturer's instructions. The same reagents were used to isolate total RNA from human prostate tissue. Briefly, flash frozen tissue was suspended in extraction buffer and subjected to careful disintegration using a hand-held electric homogenizer for 30s at a low-to-middle speed setting. The homogenate was centrifuged for 3 minutes at 4°C and the supernatant was used to extract total RNA. Post-isolation, RNA quality was determined using a Nanodrop 2000 instrument.

For miRNA profiling studies, SYBR green based pathway-focused miScript miRNA PCR Array (Qiagen, MD) was used. The cancer pathway array (catalog number 102ZF) allows the simultaneous detection of 84miRNAs previously identified in human cancers, as well as appropriate housekeeping assays and RNA quality controls. The assay was performed according to the manufacturer's protocol. Three hundred nanograms (ng) of total RNA were converted to cDNA using miScript II RT Kit. Diluted cDNA was mixed with universal primer and SYBR Green dye and added to the wells of 96-well plates containing lyophilized primer. The plates were run on a Roche Light Cycler 480®instrument and the expression of individual miRNAs was analyzed using the obtained C_t values. The fold change for each miRNA was calculated by plugging the C_p values into the manufacturer's web-based software. DU145 cells or PC3 cells, as well as benign prostate samples were considered as 'controls' in order to calculate the fold change in DU145-TXR and PC3-TXR cells and cancerous prostate tissue, respectively. Endogenous controls, RT negative and positive controls, and genomic DNA contamination controls were also tested for each array.

Validation of miRNA profiling data was done by real-time PCR estimation of selected miRNAs. For each of the selected miRNA, a miScript PCR primer was purchased from Qiagen. This assay targets only mature miRNAs, not their precursors. As a normalizer, SNORD6 was used as a housekeeping miRNA. Briefly, diluted cDNA used for miRNA profiling was used as a template in the presence of SYBR Green dye, universal primer and miScript primer. The plate was run as described above and fold changes in miRNA expression were calculated using the C_t value of the normalizer control. A similar approach was used to measure expression of miR200c and miR 34a in DU 145-TXR cells treated with 0.5 µM PTX+10 µM CYA. After treatment, total RNA was isolated, reverse transcribed to cDNA and used to measure miRNA expression as described above.

Statistical Analysis

All values in the figures and text were expressed as the mean ± SD. The results were analyzed and individual group means were compared with Student's unpaired *t*-test. A p value of at least 0.05 was considered significant and is indicated by an asterisk (*).

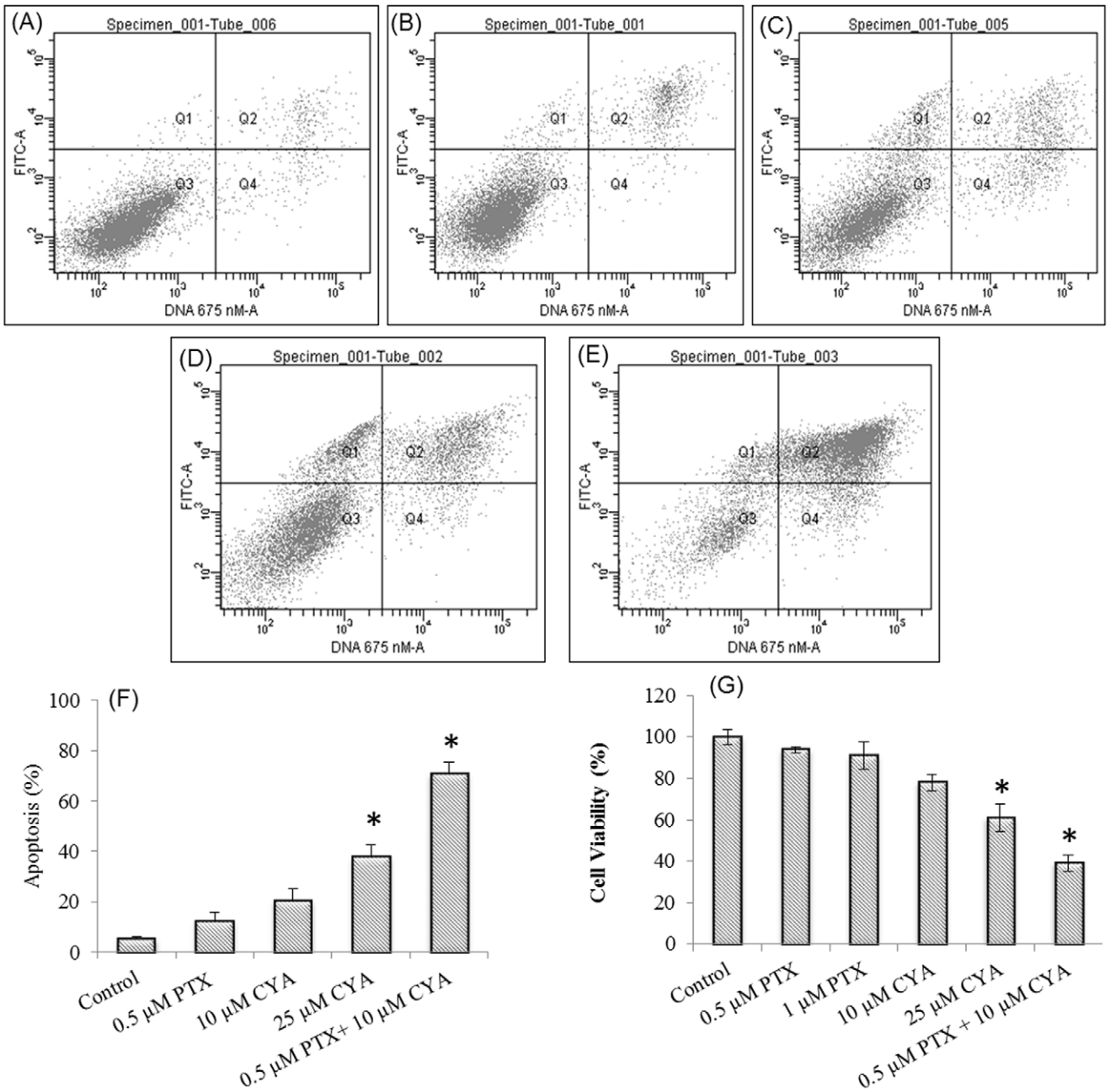

Figure 1. Effect of PTX and CYA combination on viability of PTX resistant DU145-TXR cells. Cells grown in 6-well plates were treated with A) 0.3% DMSO, B) 0.5 μM PTX C) 10 μM CYA, D) 25 μM CYA, E) 0.5 μM PTX +10 μM CYA for 48h and F) in DU145-TXR cells after different drug treatments. Subsequently, cells were trypsinized, washed with PBS and stained with Annexin V-FITC and PI before apoptotic analysis by flow cytometry. A–E are representative plots from three individual experiments. Data in panel F is the quantitation of % cell death and represents mean ± SD (n = 3). *$p<0.05$ vs. control. For MTT assay (Fig. 1G), cells grown in 96 well plate were treated with indicated concentration of drugs for 48 h. Subsequently, MTT reagent in PBS was added and incubation was carried out for another 4 h. The resulting formazan product was solubilized in DMSO and the color intensity was determined using a plate reader. A statistically significant difference (* p value <0.05) was observed when combination of 0.5 μM PTX and 10 μM CYA was used. Cell Viability = $A_{test}/A_{control}$X100. Data are the means±SD (n = 4). PTX, Paclitaxel; CYA, Cyclopamine.

doi:10.1371/journal.pone.0040021.g001

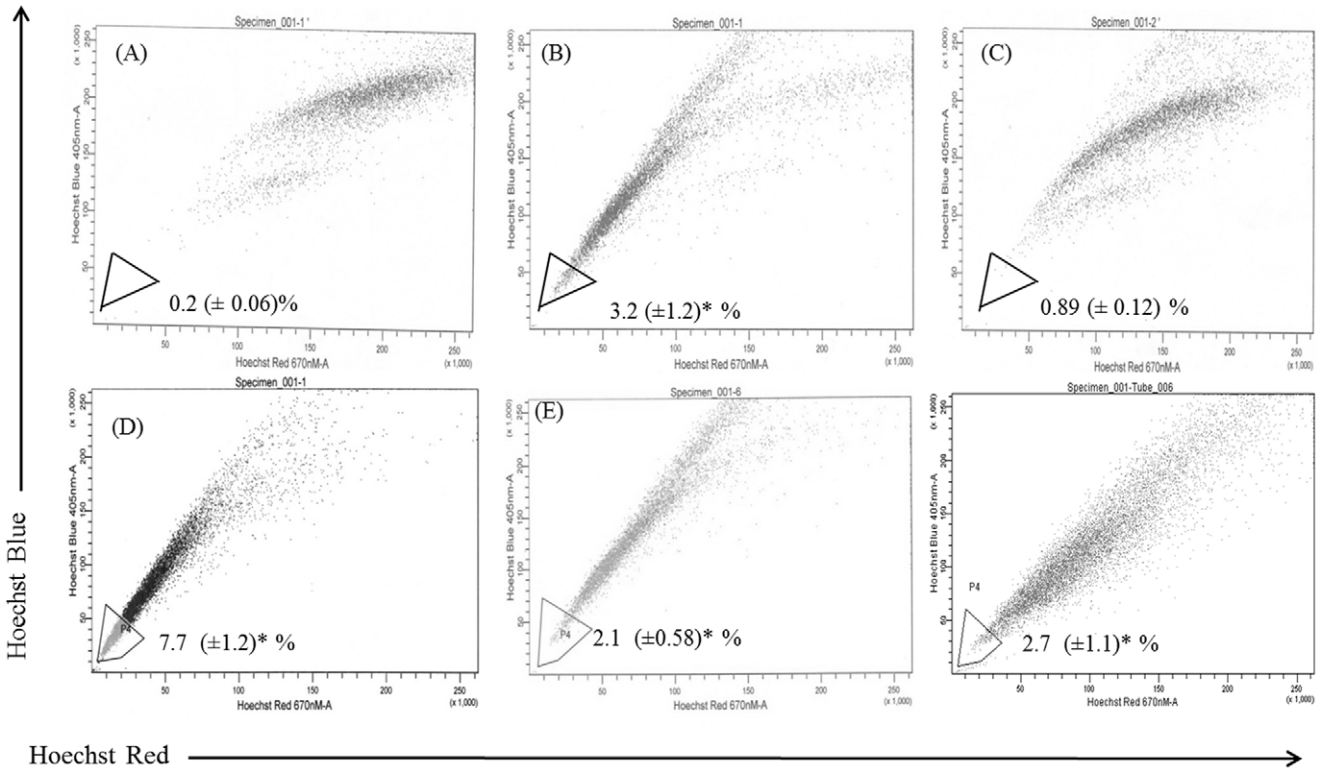

Figure 2. Analysis of side population (SP) fraction in PTX resistant DU145 TXR cells after treatment with PTX and CYA. A) DU145 cells, B) DU145-TXR cells, C) DU145-TXR cells treated with verapamil (10 μM, 90 min), D) DU145-TXR cells treated with PTX (1 μM, 12 h), E) DU145-TXR cells treated with CYA (20 μM, 12 h), F) DU145-TXR cells treated with CYA and PTX (20 μM and 0.5μM, respectively, 12 h). Verapamil was used to gate the SP fraction in all panels and shown as the percentage of the whole viable cell population. Numerical values indicated are the mean±SD of three individual experiments. * $p<0.05$ vs control DU145 cells in (A). PTX, Paclitaxel; CYA, Cyclopamine.
doi:10.1371/journal.pone.0040021.g002

Results

Combination of CYA and PTX reduces cell viability and enhances apoptosis in drug-resistant prostate cancer cells

The ability of combination chemotherapy to inhibit the growth of PTX resistant prostate cancer cell line was assessed by cell viability and apoptosis assay. It was observed that combination of PTX and CYA significantly (p value<0.05) decreases cell viability to 40% as compared to either PTX or CYA alone (Fig. 1, panels A–F). Similar results were obtained in Annexin V cell death assay wherein combination therapy results in a significantly higher cell death as compared to single agent chemotherapy (Fig. 1, G). While a combination of PTX and CYA resulted in nearly 70% of cells dying, the percent cell death observed with PTX or CYA monotherapy was 15% and 25% respectively. However, treatment with 25 μM CYA was significantly more effective than control and resulted in nearly 40% cell death.

Side Population fractions exist in PTX -resistant prostate cancer cells and have unique gene expression

Figures 2 and 3 show the SP analysis of prostate cancer cell lines DU145-TXR and PC3-TXR, respectively as well as the effect of treatment with PTX and CYA. Control DU145 cells have tiny amounts of SP (0.2%, Fig. 2A) while PTX resistant cell line DU145-TXR has ~3.2% of SP cells (Fig. 2B) as indicated by Hoechst staining ($p<0.05$ compared to DU 145 cells). In case of PC3-TXR cells, nearly 2% of viable cells were gated as SP (Fig. 3A). Verapamil, a known suppressor of efflux pumps was used in these studies as a control to set up the gates in the FACS dot plots. As seen in Figures. 2C and 3B, verapamil treatment significantly reduced SP fractions in DU145-TXR cells to 0.89% and to 0.6% in PC3-TXR cells. This data is in agreement with the use of verapamil as a control drug for identifying and gating Hoechst-light cells in various cancer cells, including prostate cancer. While treatment with 1 μM PTX for 12 h increased the SP fraction to 7.8%, treatment with 20 μM CYA, a combination of CYA and PTX 24 h after removal of PTX for a similar time decreased SP fraction to ~ 2% (Fig. 2, panels D, E and F, respectively) ($p<0.05$ in all samples). In PC3-TXR cells, the SP fraction was markedly reduced following treatment with CYA (Fig. 3C) or CYA and PTX combination (Fig. 3D). Real time RT PCR analysis indicates higher expression of pluripotency markers OCT4 and NANOG, and cancer stem cell markers CD133 and ALDH1 in SP fractions compared to non-SP (NSP) fractions in both DU145-TXR and PC3-TXR cells. Post-differentiation fate of SP cells was studied by real time RT-PCR and Hoechst staining after their isolation and re-culturing. These cells differentiated into a mix population comprising SP and NSP fractions which differed in their phenotype (Fig. 4, panels A and B, respectively). Expression analysis of post-differentiation mixed-populations indicates reduced transcripts of the ABC-transporter and cancer stemness marker ABCG2 and higher expression of cell proliferation marker minichromosome maintenance 7 (MCM7) compared to undifferentiated SP-fractions (Fig. 4D). Further treatment of post-differentiation SP populations with 25 μM CYA for 48 h resulted in the SP fraction significantly decreasing from 15.8%

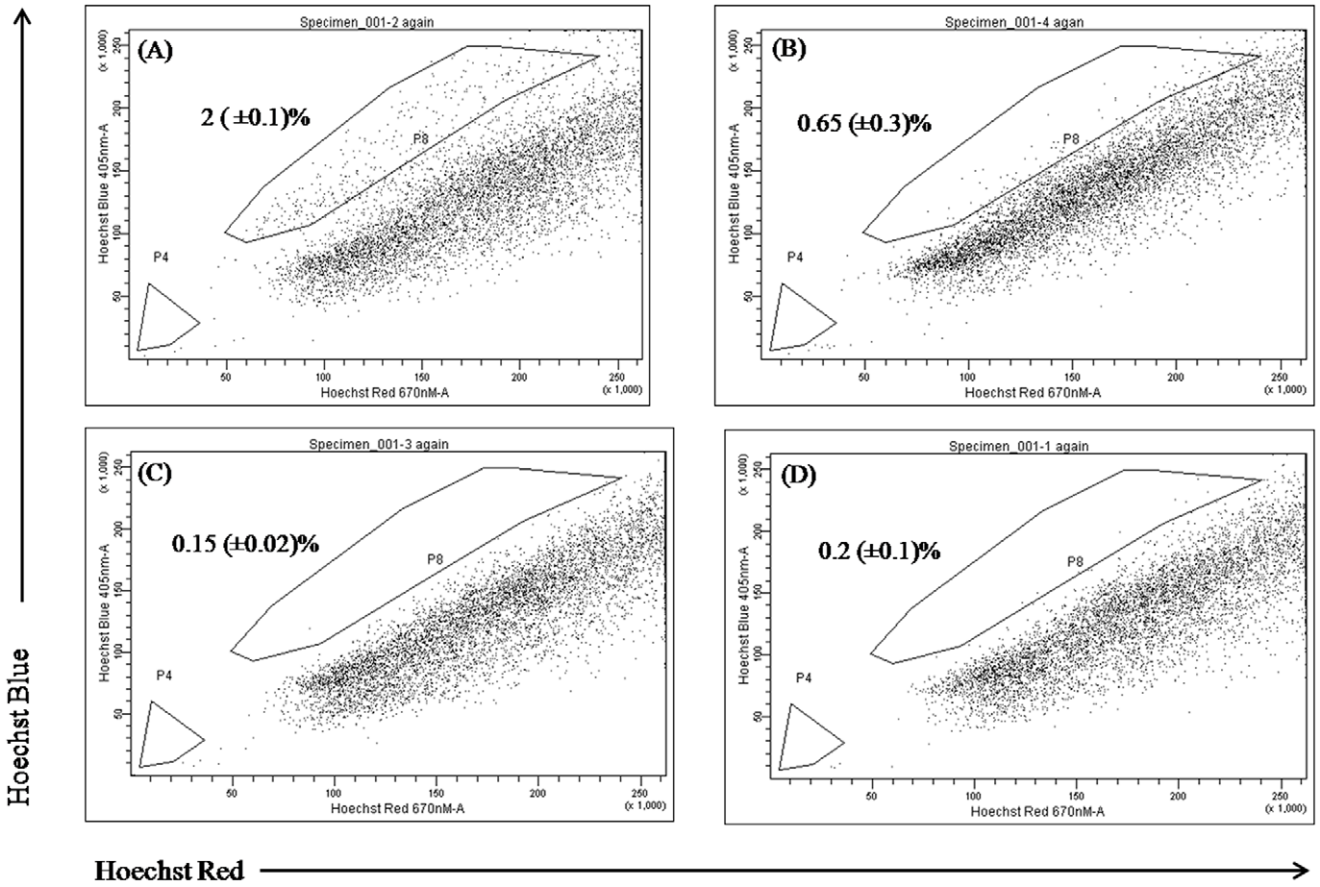

Figure 3. Analysis of side population (SP) fraction in PTX resistant PC3-TXR cells after treatment with PTX and CYA. A) PC3-TXR cells, B) Cells treated with verapamil (10 μM, 90 min), C) PC3-TXR cells treated with CYA (20 μM, 12 h) or, D) CYA and PTX (20 μM and 0.5μM, respectively, 12 h). The SP fraction, which was eliminated by treatment with verapamil, was gated (P8) in all panels and shown as the percentage of the whole viable cell population. Numerical values indicated are the mean±SD of three individual experiments. * $p<0.05$ vs control DU 145 cells (A). PTX, Paclitaxel; CYA, Cyclopamine.
doi:10.1371/journal.pone.0040021.g003

(panel E) to 0.6% (panel F, $p<0.05$). Table 1 shows the cell cycle analysis of the flow sorted SP and NSP cells. It was observed that, 62% NSP cells were in the G0-G1 and 30% in S phase in contrast to 71.5% and 21% for SP cells, respectively ($p<0.05$).

Gene and Protein Expression in DU 145-TXR Cells

Expression of P-glycoprotein (P-gp) was assessed by Western blotting. Proteins were separated by SDS-PAGE and probed with anti-P-gp antibody to determine changes in protein expression following treatments. Figure 5A indicates that treatment with 25 μM CYA or a combination of CYA (10 μM) and PTX (0.5 μM) were equally effective, while treatment with PTX (0.5 μM) alone was ineffective. Expression of GLI-1 (Hh-pathway marker), OCT-4 (pluripotency/stem cell marker) and CD133 (cancer stem cell marker) was assessed using real time RT-PCR method and calculating the fold changes with respect to the Cp values obtained in DU145-TXR cells. Figure 5B show an increased expression of GLI-1, OCT-4 and CD133 ($p<0.05$ for all genes compared to DU 145 cells).

Profiling of Prostate Cancer Cells Identifies miRNAs Altered in Chemoresistance

Recent studies have implicated various miRNAs such as let 7, miR 34a and miR 200c in regulating tumorigenesis and chemoresistance in humans [12,15]. To establish whether chemoresistance to PTX in prostate cancer was regulated at the level of miRNAs, we studied the differential expression of several miRNAs known to be involved in various human cancers. The expression of eighty of the most common cancer-related miRNAs was simultaneously determined by a real time PCR method by adding template cDNA prepared from DU145, DU145-TXR as well as PC3 and PC3-TXR cells to 96-well plates containing miRNA specific primers. A ΔΔCt method was used to calculate fold changes using PTX-sensitive parental cells as controls. Figure 6A and B identifies the miRNAs whose expression is different between PTX-resistant and sensitive prostate cancer cells. As can be seen, several miRNAs such as 1, 18a, 138, 29b, 200c, 34a and 126 were downregulated while 193b, 30c, 155, 146a, 10b, 10a, 17, 125b, 373, 144 and 23b were upregulated in PTX-resistant cells with respect to parental cells. To confirm that our findings using this array methodology were accurate and that we were not reporting false positives, we validated our data by carrying out miScript primer assays on a select few of the differentially expressed miRNAs identified using the PCR array. Figure 6C lists the miRNAs used for data validation. As can be seen, a very high degree of concordance exists between the fold changes obtained through the array data and the validating primer assays. This suggests that our methodology for sample handling

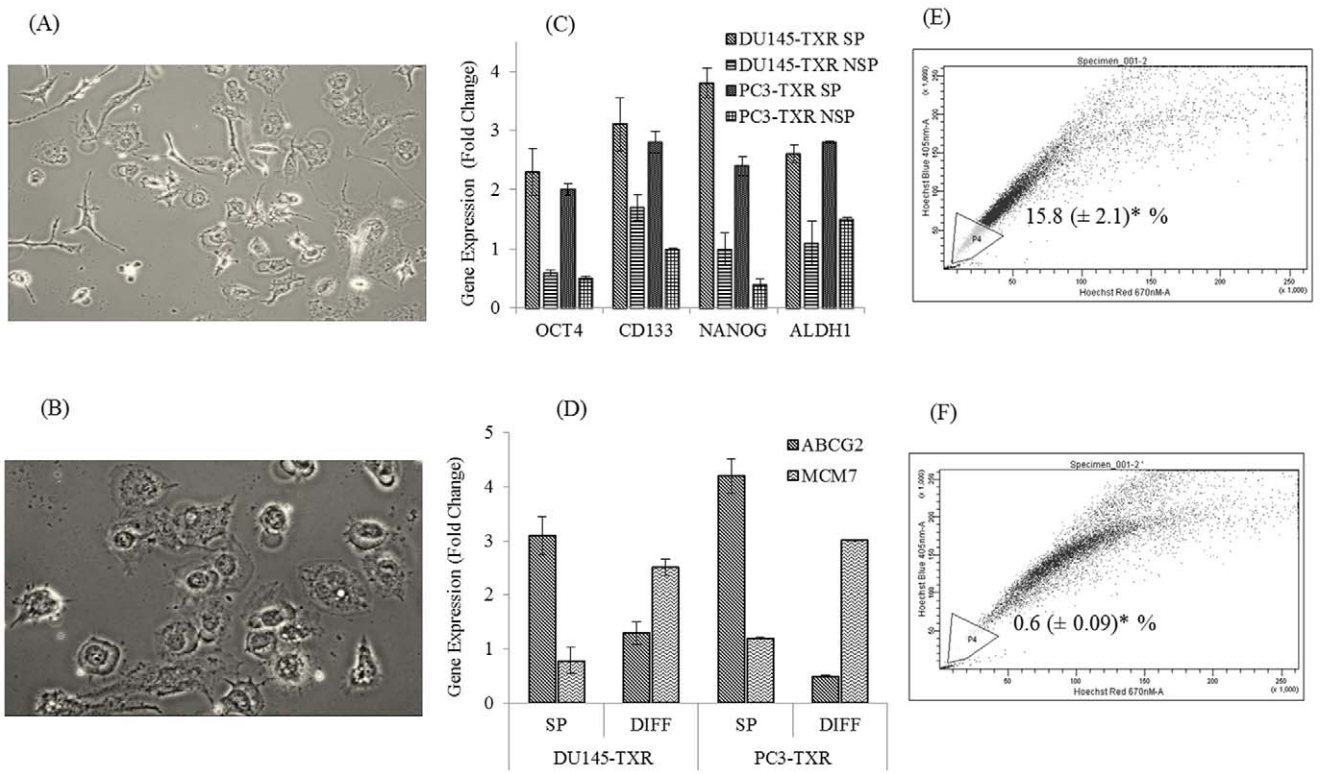

Figure 4. Post differentiation fate of side population fractions from DU145-TXR cells. After flow sorting, pure SP cells were plated and allowed to differentiate for 2-weeks. Representative photomicrographs of SP (A) and NSP cells (B) are shown with more SP cells possessing a fibroblastic, elongated phenotype compared to NSP. Real time RT-PCR was used to confirm higher expression of stem cell markers OCT 4 and NANOG and cancer stem cell markers CD133 and ALDH1 (C). Similar method was used to show higher expression of pluripotency and efflux marker ABCG2 and lower expression of MCM7 transcripts in initial SP cells (SP), compared to mixed populations post-differentiation (DIFF) where decreased ABCG2 and increased MCM7 levels were observed (D). One set of cells was also treated with 25 μM CYA for 48h. Subsequently, cells were trypsinized and re-stained with Hoechst dye and analyzed by flow cytometry. Post-differentiation, cells derived from flow sorted SP cells had higher percentage of SP cell fractions than obtained previously from non-sorted DU145-TXR cells. CYA treatment significantly reduced ($p<0.001$ vs. control) the percentage of SP fraction cells from 15.8 (±2.1) % (Panel E) to 0.6±(0.09) % (Panel F). Representative dot plots from three individual experiments are provided. Data represents mean ± SD (n = 3).
doi:10.1371/journal.pone.0040021.g004

and data processing is correct and this increases our confidence in the validity of our approach.

To confirm that combination therapy is effective in targeting miRNAs involved in modulating chemoresistance, DU145-TXR cells were treated with a combination of PTX (0.5 μM) and CYA (10 μM) for 48 h and expression of miRs 200c and 34a was determined. Figure 6D demonstrates that combination therapy at concentrations effective in reducing cell viability and inducing apoptosis in PTX-resistant prostate cancer cells also upregulated two anticancer miRNAs involved in decreasing the spread of prostate cancer (34a) and increasing sensitivity to drugs like PTX (200c). While expression of miRNA 200c increased approximately 4 fold after treatment, there was nearly a 3-fold increase in miRNA 34a expression ($p<0.05$ compared to untreated control cells).

Table 1. Cell Cycle distribution of SP and non-SP Cells following cell sorting.

DU 145 TXR cells	Cell Cycle Distribution (%)		
	G0-G1	S	G2-M
SP	71.5±1.5*	21±2.4*	7.5±2.7
Non-SP	62.08±2.3	30±1.6	7.92±3.2

SP and non-SP fractions were fixed overnight in ice cold 70% ethanol as indicated in 'Methods'. Subsequently, they were washed with PBS and stained with a solution of propidium iodide (PI) and RNAase A before flow cytometry. A statistically significant difference was observed in the cell cycle distribution.
*$p<0.05$ vs. Non-SP cells.
doi:10.1371/journal.pone.0040021.t001

Expression Analysis of Gene Targets of miRNAs 200c and 34a

Since miRNAs act by either repressing or cleaving their target mRNAs, we carried out gene expression analysis of several known downstream targets of several miRNAs, including miR200c and 34a identified in our cell and tissue miRNA arrays. Figure 7 delineates these target genes and their expression patterns in DU145-TXR cells compared to DU145 cells. As can be seen, there is upregulation of miR 200c target genes like VIMENTIN (2.5 fold), TUBB-3 (5 fold), ZEB 1 (5 fold), and miR 34a targets like CD44 (6 fold) and SIRT1 (2.5 fold) while the expression of another miR200c target E-CADHERIN was downregulated in DU145-TXR cells. In addition, gene targets of several miRNAs differentially expressed in this study were altered in DU145-TXR cells as well. These include DNMT1 (1.5 fold), BAK1 (2.4 fold) and PUMA (2.5 fold) downregulation.

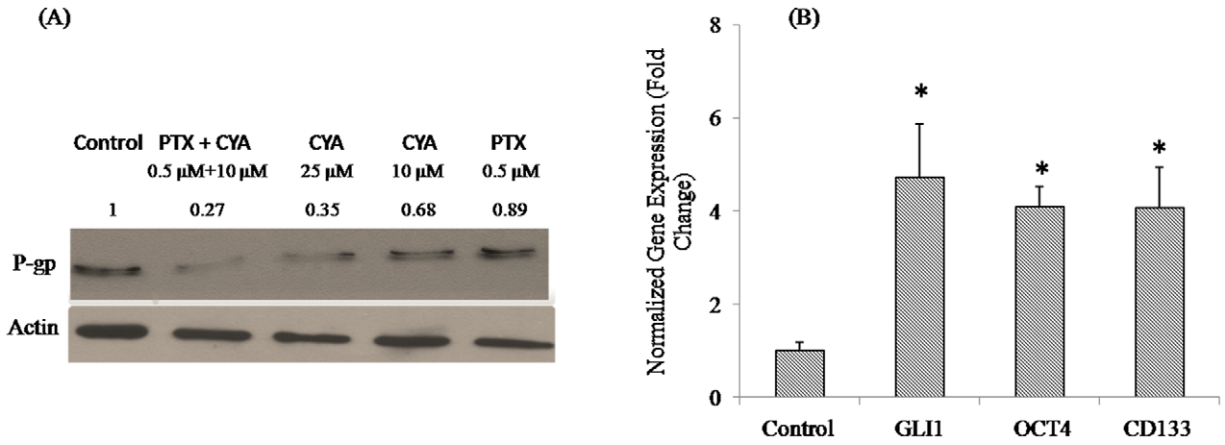

Figure 5. Effect of PTX and CYA on P-gp expression in DU145-TXR cells. Following treatment, with various drugs as described, total protein was extracted and separated by SDS-PAGE before probing with P-gp antibody. Actin was used as a loading control. A combination of 0.5 μM PTX and 10 μM CYA was more effective in downregulating P-gp expression in drug-resistant prostate cancer cells than monotherapy with either CYA or PTX at 10 and 0.5 μM concentration. P-gp downregulation with 25 μM CYA was nearly similar to that obtained by combination therapy. (B) Expression of Hh pathway and stem cell marker genes in DU145-TXR cells. Total RNA was extracted from cells and reverse transcribed to cDNA. Real time RT-PCR was carried out using SYBR Green chemistry and Ct values thus obtained were used to calculate the fold change. Drug resistant DU145-TXR cells have higher expression of all three genes tested. PTX sensitive DU145 cells were used as control and gene expression values for DU145-TXR cells were normalized with respect to the control values. *$p<0.05$ vs. control.
doi:10.1371/journal.pone.0040021.g005

Confirmation of Cell Culture Studies in Clinical Samples

We also carried out SP fraction analysis and cancer miRNA profiling in clinical prostate tissues. SP fraction was analyzed by Hoechst staining as described earlier. Nearly 1% of total viable cells in prostate cancer tissue were SP cells (Fig. 8A), closely mirroring our findings in PTX-resistant prostate cancer cell lines. miRNA profiling of cancer tissue from a second patient was also carried out. For data analysis and subsequent validation, we used benign prostate tissue from a third patient biopsy as a normalization control. Similar to our results described earlier, we were able to identify several miRNAs such as miRs 17, let71, 31a, 193b, 29b, 155, let 7d, 9, 125b and 30 as being upregulated while miRs 145, 205, 34a, 126, 200c, 27b, 99a and 152 were downregulated in prostate cancer tissue (Fig. 8B). Further, there are a number of miRNAs that are common to our tissue and cell arrays in the present study. For example, not only are miRs 155, 29b, 34a, 200c, 193b and 17 differentially expressed in cell line miRNA analysis, their expression patterns too match those seen in the tissue arrays, thereby further validating our data obtained from chemoresistant cancer cells.

Discussion

Advanced prostate cancer is usually treated with drugs like paclitaxel and docetaxel which eradicate the bulk of cells within the tumor. This therapeutic regimen often leads to chemoresistance for which few treatment strategies currently exist. Most tumors are heterogeneous and are composed of bulk cancer cells and a small population of pluripotent stem cells that are capable of self-renewal, are chemoresistant and capable of maintaining the tumor [5,7]. These cancer stem cells (CSCs) are the reason why most chemotherapy drugs eventually lose their efficacy. We have recently shown that combining the antimitotic drug PTX with an Her-2 inhibitor, such as lapatinib can reverse chemoresistance [22]. There is some evidence that lapatinib exerts its anticancer effects in part by targeting the niche population of CSCs [24].

In recent years, inhibitors of Hh pathway such as CYA have been investigated for treating various malignancies as dysregulation of this pathway is a key step in generation and sustainment of cancers [17,19,20]. In prostate cancer too, there is evidence that Hh-pathway is upregulated [25]. Androgen independent prostate cancer cells such as DU145 and PC-3 have higher expression of Hh pathway members than androgen-dependent cells such as LnCaP [26]. Higher Gli-1 gene expression in PTX resistant DU145-TXR cells (Fig. 6) was observed compared to non-resistant parental cells. This prompted us to study the effect of combining CYA with PTX to treat the PTX chemoresistant. Treatment of DU145-TXR cells with 0.5 μM PTX and 10 μM CYA reduced cellular proliferation and cell viability while apoptosis, as measured by AnnexinV-FITC staining, increased significantly after 48 h of treatment (Fig. 1). In accordance with our previous observations [22], 0.5 μM PTX alone was not effective in reducing viability of DU145-TXR cells or inducing significant levels of apoptosis. Even though CYA at 25 μM decreased cell viability significantly, this reduction was still less than that achieved with lower concentration of drugs used in combination therapy. This ability to decrease proliferation of cancer cells while utilizing significantly reduced amounts of highly toxic drugs is a potential advantage for improved chemotherapy.

Many prostate cancers relapse due to multi-drug resistance (MDR) caused by the over-expression of ATP-binding cassette transporter proteins. These transporters actively efflux chemotherapeutic drugs from tumor cells and decrease the intracellular drug concentration [8,27]. Therefore, modulation of MDR transporters is a promising approach to overcome MDR [28,29,30]. We have determined the effect of monotherapy with PTX or CYA, and their combination on the P-gp protein expression which is one of the major efflux pump systems involved in chemoresistance [31,32]. Figure 5 indicates that treatment with a combination of PTX and CYA (0.5 μM and 10 μM, respectively) was able to downregulate P-gp protein expression. Thus, supplementing PTX with CYA can eliminate the chemoresistance of androgen independent prostate cancer cells by possibly suppressing MDR and decreasing P-gp expression.

In addition to the P-gp system, chemoresistance is regulated by various other mechanisms, including cancer stem cells which are

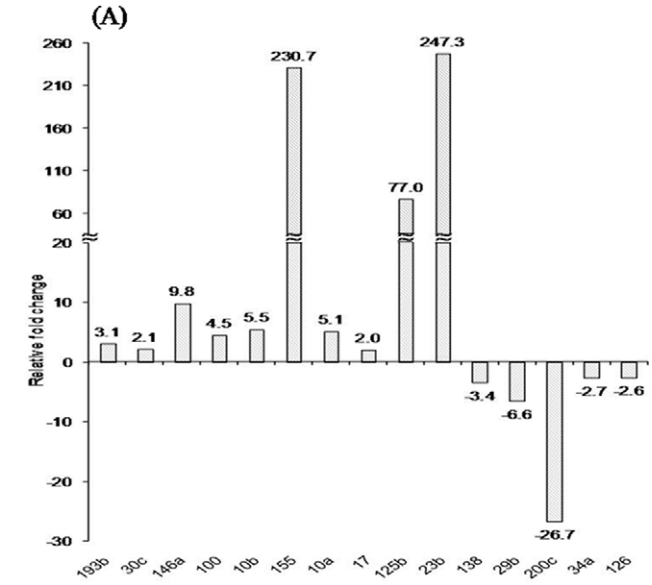

(C)

Validation of miRNA Profiling Data		
miRNA	Fold Change (Primer assay)	Fold change (Array)
miR 29b	-3.7	-6.5
miR 10b	8.5	5.5
miR 155	8.6	230
miR 200c	-22	-23.7
miR 34a	-3	-2.7

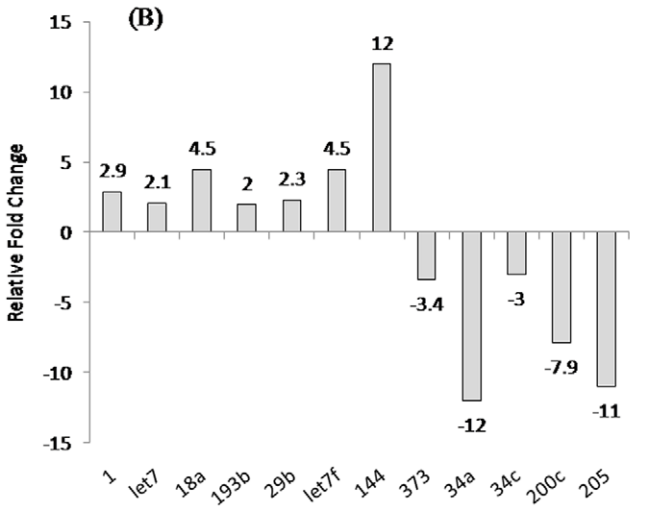

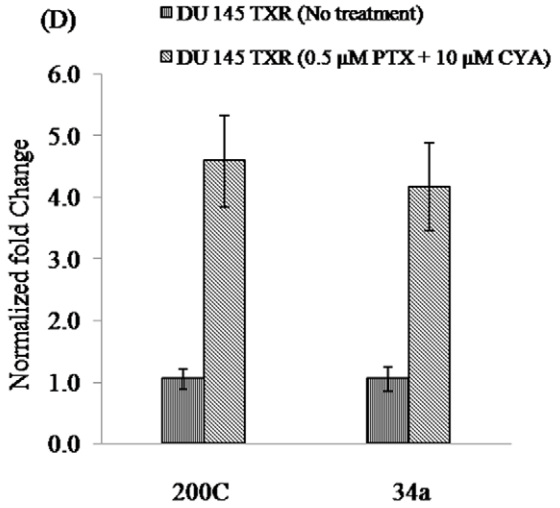

Figure 6. miRNA profiling of prostate cancer cells and effect of combination therapy on miRNA expression. Total RNA including miRNAs was isolated from DU145-TXR and DU145 cells (A) or PC3 and PC3-TXR cells (B) using miRNEasy RNA isolation kit. SYBR Green based pathway-focused miScript miRNA PCR Array (Qiagen, MD) was used for miRNA profiling studies. The plates were run on a Roche Light Cycler 480® instrument and the expression of individual miRNAs was analyzed using the obtained C_p values and the $\Delta\Delta$Ct method. Table in the insert (C) confirms validation of miRNA profiling data by miScript primer assay. Validation of miRNA profiling data was done by a SYBR Green based real time RT-PCR assay of selected miRNAs. As a normalizer, SNORD6 was used as a housekeeping miRNA. (D) Efficacy of combination therapy on restoration of miR 200 c and 34a was determined by treating DU145-TXR cells with PTX (0.5 μM) and CYA (10 μM)combination for 48 h after which total RNA was extracted, converted to cDNA and used as template for miScript primer assay for determining expression of miRNAs 200c and 34a. Untreated DU145-TXR cells were used as control for calculating fold change after a SYBR Green real time RT-PCR assay. Data represents mean ± SD (n = 3). * $p<0.05$ vs. untreated control.

doi:10.1371/journal.pone.0040021.g006

highly chemoresistant due to their ability to efflux chemotherapy drugs. Many current techniques used for characterization of these stem cells rely on the presence of cell surface markers such as CD133 and CD44 which were used to isolate these cells using a flow cytometry approach [5,33]. However, this approach suffers from the fact that during processing, including trypsinization, many of these surface markers are cleaved and therefore not available for antibody binding. Further, CD 133 is not a reliable marker for isolating CSCs as its expression may not be restricted to cancer stem cells and that even CD 133^{-} cells can initiate tumorigenesis [34]. For this reason, the vital dye Hoechst 33242 was used in the present study for separating SP from main population of cancer cells. The SP fractions are a subpopulation of CSCs which were first identified in a hematopoietic stem cell isolation procedure [9]. These cells have a unique fluorescence-activated cell sorting (FACS) signature and can be separated by a flow cytometer with a UV laser as they are distinct from cells that take up the Hoechst 33342 dye. The SP fraction is capable of sustained expansion *ex vivo* and can generate both SP and non-SP progeny. To understand the mechanism of chemoresistance in chemoresistant prostate cancer cells, we hypothesized that these cells are likely to contain a higher percentage of cells that are chemoresistant and therefore have increased ability to efflux chemotherapy drugs like PTX. Staining with Hoechst dye resulted

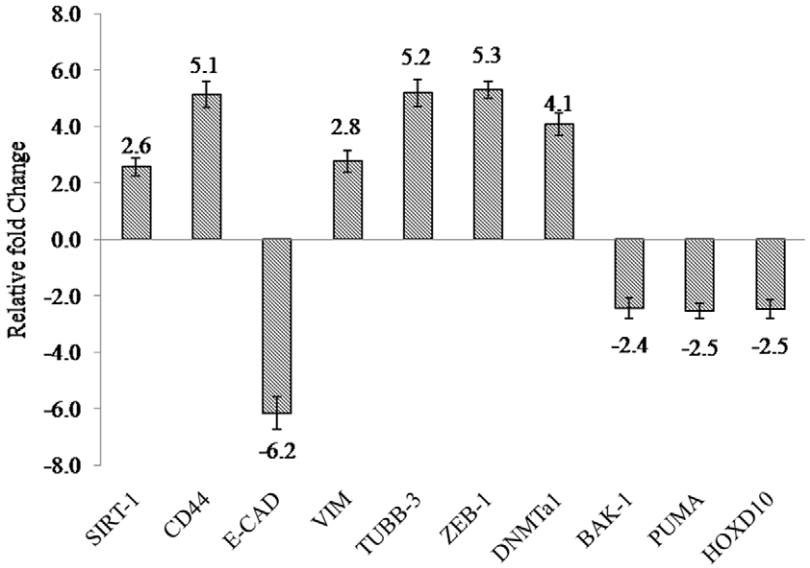

Figure 7. Real time RT-PCR identification of gene targets of miRNA in DU145-TXR Cells. Several genes involved in cancer related biological processes and known targets of differentially expressed miRNAs in our study are altered in PTX resistant DU145 TXR cells. Following RNA extraction and SYBR Green based real time RT-PCR using specific gene primers, Cp values were calculated and resistant DU145 cells were used to normalize the expression of individual genes. Data represents the mean ± SD (n = 3).
doi:10.1371/journal.pone.0040021.g007

in a creation of a typical flow cytometric dot plot profile where P4 gated region in Fig. 3 and P8 gated region in Fig. 4 is lightly stained compared to other cells. These lightly stained cells are the SP fraction which constitutes approximately 2–4% of total viable cells. In contrast, the parental PTX-sensitive DU145 cells had only 0.2% cells in the P4 region, thereby confirming our hypothesis of a distinct cell population with the ability to efflux hydrophobic drugs effectively, thereby inducing chemoresistance. Treatment with verapamil, an inhibitor of calcium gated channels, and known suppressor of cancer stem cells [35] significantly reduced SP fraction thereby confirming that the population being gated is indeed related to CSCs. It is a known fact that in relapsed tumors and metastatic cancers, there are an increased percentage of cancer stem cells and SP fractions. In the present case also, treatment of DU145-TXR cells with 1 μM PTX actually increased SP fraction to nearly twice that observed in untreated samples (7.7% vs 3.4%). These observations are supported by several lines of evidence that indicate the role played by Hh-pathway in maintaining stem cells, including cancer stem cells in various tumors [36,37]. Further, treatment with Hh-inhibitors can reduce or eliminate tumorigenic stem cells [37,38,39]. The present data indicates that there is more expression of OCT 4, a marker for self-renewal and pluripotency and CD133, a general marker for cancer stem cells [5] in DU145-TXR cells. This emphasizes the potential reservoir of CSC like cells mixed with bulk cancer cells in the chemoresistant cell line. From the theory of biogenesis of CSCs, it is clear that SP fraction have the potential for asymmetric differentiation and can give rise to non-SP fractions which will go on to form the bulk tumor cells [5,40]. To verify this theory in prostate cancer cells, pure SP and NSP fractions were isolated by flow sorting recultured and photographed. Fig. 4A and B are representative micrographs of isolated SP cells and NSP fractions. As can be seen, SP fraction has more elongated cells with typical fibroblastic phenotype while NSP cells were more rounded. Further, compared to the non-SP, the SP cells from PTX-resistant versions of both DU 145 and PC3 cells had higher gene expression of pluripotency markers OCT4 and NANOG [41] and increased expressions of cancer stem cell markers ALDH1 and CD133 (Fig. 4C). This is not surprising since CSCs, including SP fractions are capable of self-renewal and can therefore persist in cultures such as those established after flow-sorting. Comparison of expression of ABCG2 and MCM7 transcripts also differed significantly between SP fraction and their progeny mixed populations. While expression of efflux pump ABCG2 was higher in SP cells, proliferation marker MCM7 [42] was highly expressed in post-differentiated cells compared to initial SP cells suggesting the propensity of these cells for reduced proliferation. Even after differentiation, the number of SP-fraction cells was very high (almost 16%) which vanished after treatment with a high concentration of CYA (25 μM) for 48 h suggesting that suppression of Hh-pathway may be playing a role in their persistence and maintenance (Fig. 4E and F, respectively). Isolated SP and NSP fractions were also used to confirm the cell cycle stages. We have shown that more SP cells were in G0/G1 phase than non-SP cells (Table 1). This is in accordance with our gene expression data and studies from other workers who have demonstrated that the inherent stem cell like properties of SP population include a propensity for quiescent phase [21,40]. This may be the reason CSCs can bypass the G1/S checkpoint and thus maintain their ability for self-renewal and remain pluripotent.

Recent studies have demonstrated that dysregulation of various miRNAs is associated with the etiology, metastasis and prognosis of various cancers including prostate cancer [13,14]. So far, nearly 50 miRNAs have been reported to be significantly expressed in human prostate cancer but only a few have been linked directly to the pathology and progression of prostate cancer [43,44]. To confirm the hypothesis that chemoresistance to PTX involves differential expression of miRNAs, a focused profiling of miRNAs known to be involved in various malignancies was carried out in DU145-TXR and PC3-TXR cells (Fig. 6A and B, respectively). Several miRNAs involved in prostate cancer and other malignancies were differentially expressed in chemoresistant prostate cancer cells. Significant among these include miR200c, miR34a and miR29b, all of which are downregulated in DU145-TXR cells.

(A)

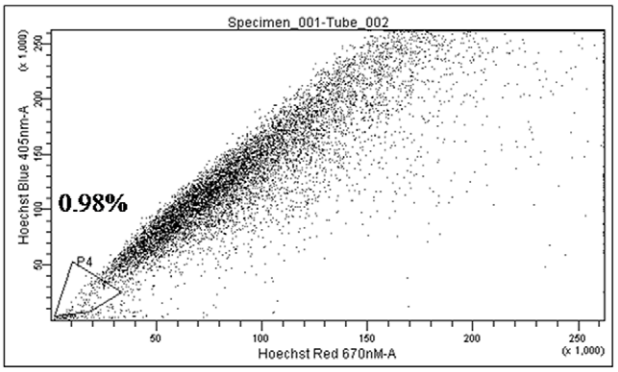

(B)

Validation of miRNA profiling		
miRNA	Fold Change (Primer assay)	Fold change (Array)
miR 200c	-6	-4.6
miR 34a	-21	-26.4
miR 29b	13	8.5

(C)

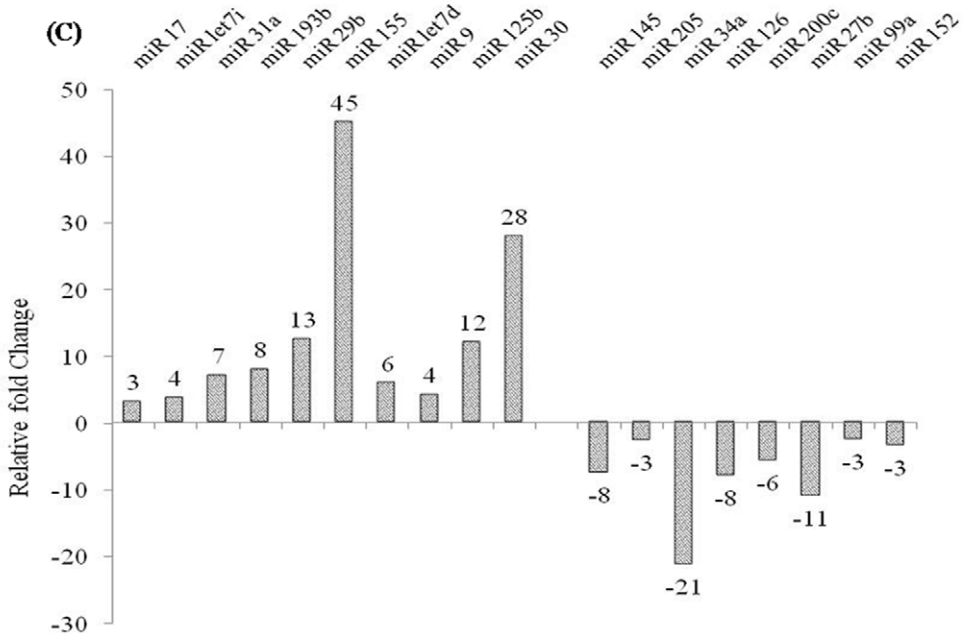

Figure 8. SP fraction analysis and miRNA profiling of clinical prostate tissues. (A) Human prostate cancer tissue was converted to single cell suspensions as described in 'Methods'. Cells were stained with Hoechst dye and analyzed as described previously. Nearly 1% of total viable cell population was gated as the SP fraction. (B) Total RNA was isolated from another set of human prostate tissues (cancer and benign) using miRNEasy RNA isolation kit. SYBR Green based pathway-focused miScript miRNA PCR Array (Qiagen, MD) was used for miRNA profiling studies. The plates were run on a Roche Light Cycler 480® instrument and the expression of individual miRNAs was analyzed using the obtained C_t values and the ΔΔCt method. The fold changes in the tumor tissues were normalized with respect to the benign prostate tissue. (C) Table in the insert confirms validation of miRNA profiling data by miScript primer assay. Validation of miRNA profiling data was done by RT-PCR estimation of selected miRNAs200c, 34a and 29b. SNORD6 was used as a housekeeping miRNA for data normalization.
doi:10.1371/journal.pone.0040021.g008

These data trends are in accordance with studies in literature which shows that miR34 is downregulated in prostate cancer and its experimental replenishment in cultured cells prevents metastasis and invasion [45]. miRNA200c, which is downregulated in DU145-TXR cells, is a tumor-suppressor miRNA known which maintains 'epithelialness' of cancer cells by preventing EMT and the assumption of an aggressive chemoresistant mesenchymal phenotype. A recent study by Cochrane et al. confirmed reduced expression of miR200c as being responsible for chemoresistance to microtubule stabilizers (such as taxanes) in endometrial, breast and ovarian cancer cells. In multi-drug resistant cancer cells, restoration of miR200c levels by transfection of its mimic restored chemosensitivity to PTX [15]. This observation is further supported by evidence that the loss of miR200c expression results in a highly aggressive, mesenchymal and chemoresistant phenotype in lung cancer cells [46]. In view of the findings described above, we decided to confirm the effect of our combination therapy on the expression of miR200c and miR34a (Fig. 6D). After treatment with 0.5 μM PTX and 10 μM CYA for 48 h, the expression of both miRs 200c and 34a were increased significantly, compared to non-treated TXR cells. It is therefore feasible that this increase in the levels of these miRNAs due to the combination therapy is responsible for the increased apoptosis and decreased cell proliferation (Fig. 1).

Expression analysis of select genes which are known targets of differentially expressed miRNAs, including miR200c and 34a was carried out to further support our miRNA data. [47]. Figure 7 details some miRNA target genes which are altered in DU145-TXR cells compared to the parental DU145 cells. SIRT-1 is suppressed by miR34a and is upregulated in prostate cancers following loss or downregulation of miR34a [48]. In wild type cells, downregulation of SIRT-1 by miR34a results in increased

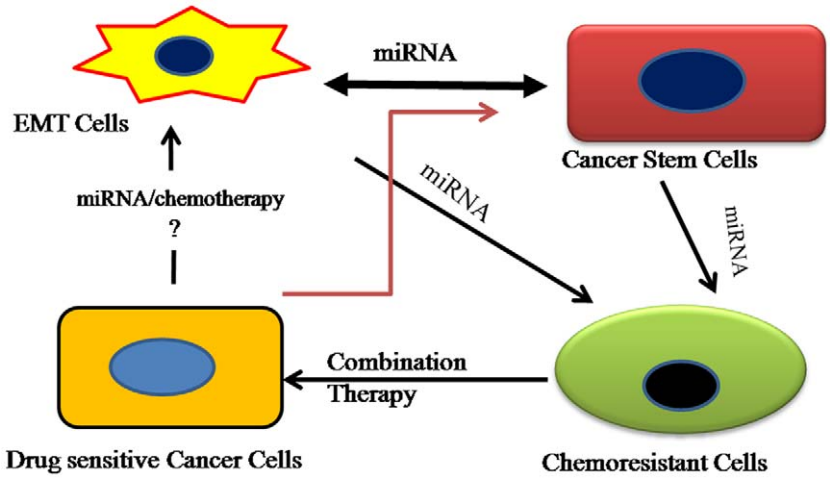

Figure 9. Interrelationship between EMT, cancer stem cells, miRNA and chemoresistance. Significant interrelationship exists between chemoresistance, epithelial to mesenchymal transition and metastasis, which adversely impacts treatment outcomes. Chemoresistance, a key feature of CSCs and cells undergoing EMT, is regulated by the dysregulation of miRNAs. Our proposed combination therapy with PTX and CYA simultaneously targets CSCs and bulk cancer cells, reverses EMT and restores expression of miRNAs altered during generation of chemoresistance and is a viable strategy for treating drug-resistant prostate cancer.
doi:10.1371/journal.pone.0040021.g009

apoptosis [49]. This suggests that the greater resilience of TXR cells may be due this loss of miR34a. CD 44 is also a surface marker for CSCs [5] and it stands to reason that it will be upregulated in a cell line where miR34a is downregulated and where SP fraction cells are found in higher numbers. Downregulation of miRNA200c leads to an EMT transformation which is characterized by a loss of E-CADHERIN (E-CAD) and upregulation of VIMENTIN (VIM) [15]. In aggressively metastatic cell lines from breast, ovarian and endometrial cancers, E-CAD levels are suppressed by ZEB-1 which is upregulated as a result of suppression of miR200c. Downregulation of miR200c also increases the protein and gene levels of TUBB-3. It has been suggested that decreased protein levels of TUBB-3 protein correlate to increased cell death in response to microtubule-targeting agents such as PTX. DNMTa1 which is also upregulated is a target of miR29b and is regulated by global hypomethylation. Loss of miR29b results in upregulation of DNMTa1 at protein and gene levels in aggressive cancer cells [50] such as seen in the present study. Bak-1 which is downregulated in DU145-TXR cells is a target of miR125b, a known oncomir which confers chemoresistance to PTX in breast cancer cells through suppression of Bak-1 gene [51]. Another target of miR125b is PUMA which is a proapoptotic gene and is suppressed when miR125b is overexpressed in cancer cells [52].

Finally, to correlate and extrapolate the above findings to clinical studies, SP fraction analysis (Fig. 8A) and miRNA profiling of prostate cancer tissues (Fig. 8B) was performed. Presence of distinct SP fractions in clinical prostate cancer tissue is supportive of our cell culture data. Further, as several miRNAs which are verifiably altered in PTX-resistant cell lines, such as miR200c and miR34a, are similarly modified in a clinical prostate cancer sample, our hypothesis and the overall approach taken to confirm it are strengthened substantially

Conclusion

We have established that chemoresistance to PTX in DU145-TXR and PC3-TXR cells is possibly regulated by miRNAs which are differentially expressed when the PTX sensitive cell line is transformed to a resistant phenotype. miRNAs are known to regulate cancer stem cells, chemoresistance and EMT since CSCs possess a mesenchymal phenotype that allows them to be invasive. This crosstalk between miRNAs, cancer stem cells and the resulting physiologic processes such as metastasis and chemoresistance is explained in the schematic in Figure 9.

The present study thus suggests a strategy to restore chemosensitivity to drug-resistant cancer cells, thereby ensuring that cancers do not relapse due to generation of CSCs in tumors.

Acknowledgments

The authors would like to thank Mr. Michael Danquah for useful discussions.

Author Contributions

Conceived and designed the experiments: SS RIM SWB RWW. Performed the experiments: SS DC RM. Analyzed the data: SS DC SWB RIM. Contributed reagents/materials/analysis tools: RIM. Wrote the paper: SS DC SWB RIM.

References

1. Jemal A, Siegel R, Ward E, Hao Y, Xu J, et al. (2009) Cancer statistics, 2009. CA Cancer J Clin 59: 225–249.
2. van Brussel JP, Mickisch GH (2003) Multidrug resistance in prostate cancer. Onkologie 26: 175–181.
3. Pazdur R, Kudelka AP, Kavanagh JJ, Cohen PR, Raber MN (1993) The taxoids: paclitaxel (Taxol) and docetaxel (Taxotere). Cancer Treat Rev 19: 351–386.
4. Tannock IF, de Wit R, Berry WR, Horti J, Pluzanska A, et al. (2004) Docetaxel plus prednisone or mitoxantrone plus prednisone for advanced prostate cancer. N Engl J Med 351: 1502–1512.
5. Collins AT, Berry PA, Hyde C, Stower MJ, Maitland NJ (2005) Prospective identification of tumorigenic prostate cancer stem cells. Cancer Res 65: 10946–10951.
6. Ricci-Vitiani L, Lombardi DG, Pilozzi E, Biffoni M, Todaro M, et al. (2007) Identification and expansion of human colon-cancer-initiating cells. Nature 445: 111–115.
7. Liu T, Xu F, Du X, Lai D, Zhao Y, et al. (2010) Establishment and characterization of multi-drug resistant, prostate carcinoma-initiating stem-like cells from human prostate cancer cell lines 22RV1. Mol Cell Biochem 340: 265–273.

8. Szakacs G, Paterson JK, Ludwig JA, Booth-Genthe C, Gottesman MM (2006) Targeting multidrug resistance in cancer. Nat Rev Drug Discov 5: 219–234.
9. Goodell MA, Brose K, Paradis G, Conner AS, Mulligan RC (1996) Isolation and functional properties of murine hematopoietic stem cells that are replicating in vivo. J Exp Med 183: 1797–1806.
10. Hirschmann-Jax C, Foster AE, Wulf GG, Nuchtern JG, Jax TW, et al. (2004) A distinct "side population" of cells with high drug efflux capacity in human tumor cells. Proc Natl Acad Sci U S A 101: 14228–14233.
11. Takubo K, Ohmura M, Azuma M, Nagamatsu G, Yamada W, et al. (2008) Stem cell defects in ATM-deficient undifferentiated spermatogonia through DNA damage-induced cell-cycle arrest. Cell Stem Cell 2: 170–182.
12. Kent OA, Mendell JT (2006) A small piece in the cancer puzzle: microRNAs as tumor suppressors and oncogenes. Oncogene 25: 6188–6196.
13. Yu F, Yao H, Zhu P, Zhang X, Pan Q, et al. (2007) let-7 regulates self renewal and tumorigenicity of breast cancer cells. Cell 131: 1109–1123.
14. Zhang W, Dahlberg JE, Tam W (2007) MicroRNAs in tumorigenesis: a primer. Am J Pathol 171: 728–738.
15. Cochrane DR, Spoelstra NS, Howe EN, Nordeen SK, Richer JK (2009) MicroRNA-200c mitigates invasiveness and restores sensitivity to microtubule-targeting chemotherapeutic agents. Mol Cancer Ther 8: 1055–1066.
16. Bar EE, Chaudhry A, Lin A, Fan X, Schreck K, et al. (2007) Cyclopamine-mediated hedgehog pathway inhibition depletes stem-like cancer cells in glioblastoma. Stem Cells 25: 2524–2533.
17. Chung MK, Kim HJ, Lee YS, Han ME, Yoon S, et al. (2010) Hedgehog signaling regulates proliferation of prostate cancer cells via stathmin1. Clin Exp Med 10: 51–57.
18. Shaw G, Prowse DM (2008) Inhibition of androgen-independent prostate cancer cell growth is enhanced by combination therapy targeting Hedgehog and ErbB signalling. Cancer Cell Int 8: 3.
19. Chen M, Feuerstein MA, Levina E, Baghel PS, Carkner RD, et al. (2010) Hedgehog/Gli supports androgen signaling in androgen deprived and androgen independent prostate cancer cells. Mol Cancer 9: 89.
20. Karhadkar SS, Bova GS, Abdallah N, Dhara S, Gardner D, et al. (2004) Hedgehog signalling in prostate regeneration, neoplasia and metastasis. Nature 431: 707–712.
21. Mimeault M, Johansson SL, Henichart JP, Depreux P, Batra SK (2010) Cytotoxic effects induced by docetaxel, gefitinib, and cyclopamine on side population and nonside population cell fractions from human invasive prostate cancer cells. Mol Cancer Ther 9: 617–630.
22. Li F, Danquah M, Singh S, Wu H, Mahato RI (2011) Paclitaxel- and lapatinib-loaded lipopolymer micelles overcome multidrug resistance in prostate cancer. Drug Deliv and Transl Res 1: 420–428.
23. Danquah M, Li F, III CBD, Miller DD, Mahato RI (2009) Micellar Delivery of Bicalutamide and Embelin for Treating Prostate Cancer. PharmRes 26: 2081–2092.
24. Nguyen NP, Almeida FS, Chi A, Nguyen LM, Cohen D, et al. (2010) Molecular biology of breast cancer stem cells: potential clinical applications. Cancer Treat Rev 36: 485–491.
25. Sanchez P, Hernandez AM, Stecca B, Kahler AJ, DeGueme AM, et al. (2004) Inhibition of prostate cancer proliferation by interference with SONIC HEDGEHOG-GLI1 signaling. Proc Natl Acad Sci U S A 101: 12561–12566.
26. Nadendla SK, Hazan A, Ward M, Harper LJ, Moutasim K, et al. (2011) GLI1 confers profound phenotypic changes upon LNCaP prostate cancer cells that include the acquisition of a hormone independent state. PLoS One 6: e20271.
27. Colabufo NA, Contino M, Berardi F, Perrone R, Panaro MA, et al. (2011) A new generation of MDR modulating agents with dual activity: P-gp inhibitor and iNOS inducer agents. Toxicol In Vitro 25: 222–230.
28. Baumert C, Hilgeroth A (2009) Recent advances in the development of P-gp inhibitors. Anticancer Agents Med Chem 9: 415–436.
29. Coley HM (2010) Overcoming multidrug resistance in cancer: clinical studies of p-glycoprotein inhibitors. Methods Mol Biol 596: 341–358.
30. Shukla S, Ohnuma S, Ambudkar SV (2010) Improving Cancer Chemotherapy with Modulators of ABC Drug Transporters. Curr Drug Targets.
31. Chearwae W, Anuchapreeda S, Nandigama K, Ambudkar SV, Limtrakul P (2004) Biochemical mechanism of modulation of human P-glycoprotein (ABCB1) by curcumin I, II, and III purified from Turmeric powder. Biochem Pharmacol 68: 2043–2052.
32. Limtrakul P, Chearwae W, Shukla S, Phisalphong C, Ambudkar SV (2007) Modulation of function of three ABC drug transporters, P-glycoprotein (ABCB1), mitoxantrone resistance protein (ABCG2) and multidrug resistance protein 1 (ABCC1) by tetrahydrocurcumin, a major metabolite of curcumin. Mol Cell Biochem 296: 85–95.
33. Richardson GD, Robson CN, Lang SH, Neal DE, Maitland NJ, et al. (2004) CD133, a novel marker for human prostatic epithelial stem cells. J Cell Sci 117: 3539–3545.
34. Shmelkov SV, Butler JM, Hooper AT, Hormigo A, Kushner J, et al. (2008) CD133 expression is not restricted to stem cells, and both CD133+ and CD133- metastatic colon cancer cells initiate tumors. J Clin Invest 118: 2111–2120.
35. Komuro H, Saihara R, Shinya M, Takita J, Kaneko S, et al. (2007) Identification of side population cells (stem-like cell population) in pediatric solid tumor cell lines. J Pediatr Surg 42: 2040–2045.
36. Peacock CD, Wang Q, Gesell GS, Corcoran-Schwartz IM, Jones E, et al. (2007) Hedgehog signaling maintains a tumor stem cell compartment in multiple myeloma. Proc Natl Acad Sci U S A 104: 4048–4053.
37. Singh BN, Fu J, Srivastava RK, Shankar S (2011) Hedgehog signaling antagonist GDC-0449 (Vismodegib) inhibits pancreatic cancer stem cell characteristics: molecular mechanisms. PLoS One 6: e27306.
38. Zhou Y, Yang J, Kopecek J (2012) Selective inhibitory effect of HPMA copolymer-cyclopamine conjugate on prostate cancer stem cells. Biomaterials 33: 1863–1872.
39. Ruiz IAA (2011) Hedgehog signaling and the gli code in stem cells, cancer, and metastases. Sci Signal 4: pt9.
40. Yao J, Cai HH, Wei JS, An Y, Ji ZL, et al. (2010) Side population in the pancreatic cancer cell lines SW1990 and CFPAC-1 is enriched with cancer stem-like cells. Oncol Rep 23: 1375–1382.
41. Han J, Zhang F, Yu M, Zhao P, Ji W, et al. (2012) RNA interference-mediated silencing of NANOG reduces cell proliferation and induces G0/G1 cell cycle arrest in breast cancer cells. Cancer Lett.
42. Ho MM, Ng AV, Lam S, Hung JY (2007) Side population in human lung cancer cell lines and tumors is enriched with stem-like cancer cells. Cancer Res 67: 4827–4833.
43. Baranwal S, Alahari SK (2010) miRNA control of tumor cell invasion and metastasis. Int J Cancer 126: 1283–1290.
44. Gandellini P, Folini M, Zaffaroni N (2010) Emerging role of microRNAs in prostate cancer: implications for personalized medicine. Discov Med 9: 212–218.
45. Liu C, Kelnar K, Liu B, Chen X, Calhoun-Davis T, et al. (2011) The microRNA miR-34a inhibits prostate cancer stem cells and metastasis by directly repressing CD44. Nat Med 17: 211–215.
46. Ceppi P, Mudduluru G, Kumarswamy R, Rapa I, Scagliotti GV, et al. (2010) Loss of miR-200c expression induces an aggressive, invasive, and chemoresistant phenotype in non-small cell lung cancer. Mol Cancer Res 8: 1207–1216.
47. Xie X, Lu J, Kulbokas EJ, Golub TR, Mootha V, et al. (2005) Systematic discovery of regulatory motifs in human promoters and 3′ UTRs by comparison of several mammals. Nature 434: 338–345.
48. Fujita Y, Kojima K, Hamada N, Ohhashi R, Akao Y, et al. (2008) Effects of miR-34a on cell growth and chemoresistance in prostate cancer PC3 cells. Biochem Biophys Res Commun 377: 114–119.
49. Yamakuchi M, Ferlito M, Lowenstein CJ (2008) miR-34a repression of SIRT1 regulates apoptosis. Proc Natl Acad Sci U S A 105: 13421–13426.
50. Garzon R, Liu S, Fabbri M, Liu Z, Heaphy CE, et al. (2009) MicroRNA-29b induces global DNA hypomethylation and tumor suppressor gene reexpression in acute myeloid leukemia by targeting directly DNMT3A and 3B and indirectly DNMT1. Blood 113: 6411–6418.
51. Zhou M, Liu Z, Zhao Y, Ding Y, Liu H, et al. (2010) MicroRNA-125b confers the resistance of breast cancer cells to paclitaxel through suppression of pro-apoptotic Bcl-2 antagonist killer 1 (Bak1) expression. J Biol Chem 285: 21496–21507.
52. Shi XB, Xue L, Ma AH, Tepper CG, Kung HJ, et al. (2011) miR-125b promotes growth of prostate cancer xenograft tumor through targeting pro-apoptotic genes. Prostate 71: 538–549.

Pharm Res (2012) 29:2079–2091
DOI 10.1007/s11095-012-0737-1

RESEARCH PAPER

Combination Therapy of Antiandrogen and XIAP Inhibitor for Treating Advanced Prostate Cancer

Michael Danquah • Charles B. Duke III • Renukadevi Patil • Duane D. Miller • Ram I. Mahato

Received: 4 February 2012 / Accepted: 9 March 2012 / Published online: 27 March 2012

ABSTRACT

Purpose Overexpression of the androgen receptor (AR) and anti-apoptotic genes including X-linked inhibitor of apoptosis protein (XIAP) provide tumors with a proliferative advantage. Therefore, our objective was to determine whether novel antiandrogen (CBDIV17) and XIAP inhibitor based combination therapy can treat advanced prostate cancer.

Methods CBDIV17 and embelin-6g were synthesized and their effect on cell proliferation, apoptosis, cell cycle and AR and XIAP gene silencing determined.

Results CBDIV17 was more potent than bicalutamide and inhibited proliferation of C4-2 and LNCaP cells, IC_{50} for CBDIV17 was ~12 μM and ~21 μM in LNCaP and C4-2 cells, respectively, whereas bicalutamide had IC_{50} of ~46 μM in LNCaP cells and minimal effect in C4-2 cells. CBDIV17 induced apoptosis more effectively compared to bicalutamide and significantly inhibited DNA replication. Combination of CBDIV17 and embelin resulted in supra-additive antiproliferative and apoptotic effects. Embelin downregulated AR expression and decreased androgen-mediated AR phosphorylation at Ser^{81}. These hydrophobic drugs were solubilized using micelles prepared with polyethylene glycol-b-poly (carbonate-co-lactide) (PEG-b-p(CB-co-LA)) copolymer. Combination therapy inhibited prostate tumor growth more effectively compared to control or monotherapy *in vivo*.

Conclusions Our results demonstrated that CBDIV17 in combination with embelin can potentially treat advanced prostate cancer.

KEY WORDS androgen receptor · antiandrogen · bicalutamide · embelin · polymeric micelles · prostate cancer · XIAP

Electronic supplementary material The online version of this article (doi:10.1007/s11095-012-0737-1) contains supplementary material, which is available to authorized users.

R. I. Mahato (✉)
University of Tennessee Health Science Center
Department of Pharmaceutical Sciences
19 South Manassas, CRB RM 224
Memphis 38103-3308, Tennessee, USA
e-mail: rmahato@uthsc.edu
URL: http://www.uthsc.edu/pharmacy/rmahato

M. Danquah
University of Tennessee Health Science Center
Department of Pharmaceutical Sciences
19 South Manassas, CRB RM 226
Memphis 38103-3308, Tennessee, USA

C. B. Duke III • R. Patil
University of Tennessee Health Science Center
Department of Pharmaceutical Sciences
327 Johnson Building
Memphis 38163, Tennessee, USA

D. D. Miller
University of Tennessee Health Science Center
Department of Pharmaceutical Sciences
435 Pharmacy Building
Memphis 38163, Tennessee, USA

INTRODUCTION

Prostate Cancer is the most frequently diagnosed neoplasm and the second leading cause of cancer mortality affecting men in the United States (1). Nearly all prostate carcinomas are initially androgen dependent (2). Hence, the disease is classified as hormone-dependent or hormone-refractory depending on the sensitivity of the androgen receptor (AR) to androgens. To date, androgen ablation therapy using antiandrogens remains the gold standard for treating hormone-dependent prostate cancer and is effective in approximately 70 % of patients (3). In spite of its initial efficacy, androgen ablation results in remission lasting two

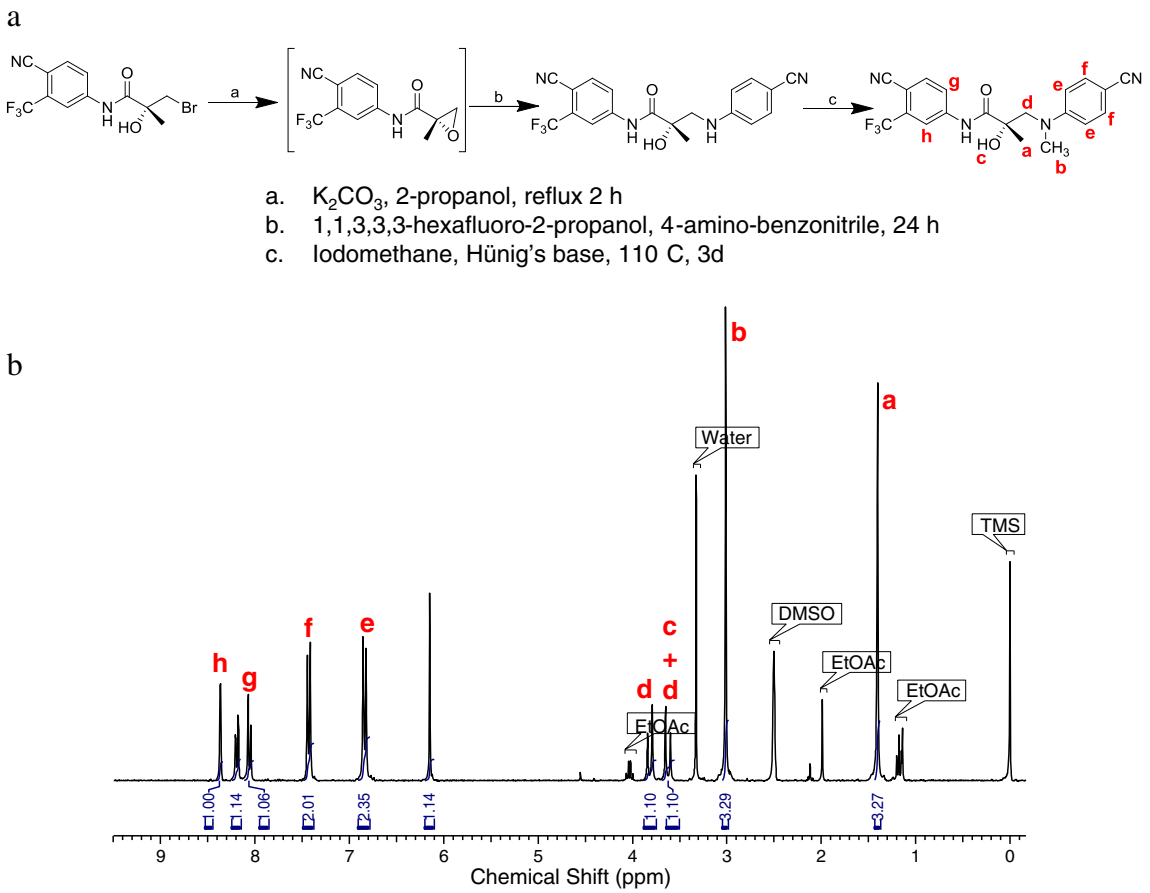

Fig. 1 Synthesis and characterization of (S)-N-(4-cyano-3-(trifluoromethyl)phenyl)-3-((4-cyanophenyl)(methyl)amino)-2-hydroxy-2-methylpropanamide) (CBDIV17). (**a**) Synthesis scheme of CBDIV17. (**b**) ^{1}H NMR spectrum of CBDIV17.

to three years after which the disease recurs in its more aggressive hormone refractory form for which there is no cure (4,5). Consequently, there is an urgent need for novel therapeutic strategies for treating hormone refractory prostate cancer.

We have previously shown that combination therapy targeting AR and XIAP using bicalutamide and embelin is a promising approach to treat prostate cancer (6). However, first generation antiandrogens such as bicalutamide exhibit agonist characteristics upon prolonged treatment due to increased AR gene amplification (7,8). Therefore, we hypothesized new antiandrogens more effective than bicalutamide will be beneficial in treating advanced prostate cancer when combined with XIAP modulation. Hence, our group synthesized a novel antiandrogen ((S)-N-(4-cyano-3-(trifluoromethyl) phenyl)-3-((4-cyanophenyl)(methyl)amino)-2-hydroxy-2-methylpropanamide) (CBDIV17)) using bicalutamide as a starting chemical scaffold due to its relatively high AR binding affinity and selectivity (Fig. 1a).

Systemic delivery of anticancer agents to solid tumors is still a challenge. Aside being toxic, current solubilizing agents such as Cremophor® EL and DMSO contribute to erratic extravasation to tumors leading to sub-optimal therapeutic effects (9). Polymeric micelles are an elegant way to improve the solubility, stability and extravasation of drugs to tumors thereby enhancing therapeutic potential (6,9–12). They self-assemble from amphiphilic diblocks and are typically nanosized, spherical structures with a hydrophobic core which serves as a cargo space for hydrophobic drugs. We recently engineered and synthesized polyethylene glycol-b-poly (carbonate-co-lactide) (PEG-b-p(CB-co-LA)) copolymers with excellent drug loading and stability for optimal delivery of bicalutamide (10) and we will explore the use of this copolymer to formulate CBDIV17 and embelin in this work.

The focus of the present study is three fold. First to demonstrate the superiority of CBDIV17 in treating prostate cancer compared to bicalutamide. Second, to evaluate two XIAP inhibitors: embelin and 2,5-dihydroxy-3-(2-[4-(2-m-tolyl-ethyl)-phenyl]-ethyl)-[1,4] benzoquinone (embelin-6g) to determine the more appropriate compound to combine with CBDIV17. Third, to show that combination of CBDIV17 and chosen XIAP inhibitor is more potent than

control or monotherapy in inhibiting cell growth and inducing apoptosis *in vitro* as well as in regressing prostate cancer tumors in xenograft mouse model.

MATERIALS AND METHODS

Materials

SYBR Green real-time RT-PCR master mix and reverse transcription reagents were purchased from Applied Biosystems (Foster city, CA). Human total XIAP ELISA kit was purchased from R&D Systems (Minneapolis, MN). Primary and secondary antibodies were purchased from Abcam (Cambridge, MA). All other reagents were obtained from Sigma-Aldrich (St. Louis, MO) unless otherwise stated and were used as received.

Synthesis of CBDIV17

CBDIV17 was synthesized by treating 3-Bromo-2-hydroxy-N-(4-isocyano-3-trifluoromethyl-phenyl)-2-methyl-propionamide (bromide N) with K_2CO_3 in 2-propanol at reflux for 2 h before filtering the solution. The reaction mixture was concentrated to a paste, dissolved in EtOAc, and washed with water before drying using Na_2SO_4 and concentrating to a resin. The epoxide intermediate was then treated with 4-aminobenzonitrile in 1, 1, 1, 3, 3, 3-hexafluoro-2-propanol at 100 °C overnight. Flash chromatography on silica gel (EtOAc/Hexanes 20–100 %) afforded (S)-N-(4-cyano-3-(trifluoromethyl)phenyl)-3-((4-cyanophenylamino)-2-hydroxy-2-methylpropanamide), which was treated with MeI and Hünig's base in a pressure vessel for 3 days at 110 °C. Flash chromatography on silica gel (EtOAc/Hexanes 20–100 %) afforded CBDIV17.

In Vitro Cell Viability Assays

LNCaP and C4-2 cells (American Type Culture Collection) were incubated in RPMI 1640 media, 10 % fetal bovine serum and 1 % antibiotic-antimycotic at 37 °C in humidified environment of 5 % CO_2 and subcultured every 3–4 days to maintain exponential growth. Cells were seeded in 96-well plates at a density of 1 x 10^4 viable cells/well and incubated for 48 h. The cells were exposed to antiandrogen or XIAP inhibitor at various concentrations for specified time periods. At the end of treatment, 20 µl of MTT (5 mg/ml) was added to each well, incubated for 3–4 h and analyzed at a test wavelength of 560 nm. Cell viability was expressed as a percentage of the intensity of controls. LNCaP cells are androgen dependent and non-bone metastatic prostate cancer cells with low tumorigenicity. In contrast, C4-2 cells are a subline of LNCaP, but androgen independent and more tumorigenic compared to LNCaP cells. These cells lines were selected as *in vitro* models since they both express the androgen receptor and possess a threonine to alanine mutation of amino acid 877 (T877A) in the androgen receptor (13,14). Furthermore, LNCaP represents hormone dependent prostate cancer whereas C4-2 is a model for advanced prostate cancer.

Real-Time RT-PCR

RNA extraction and real-time RT-PCR was performed as previously described (6). Primers are as follows: AR: forward, 5′-AGC CAT TGA GCC AGG TGT AG-3′; reverse, 5′-CGT GTA AGT TGC GGA AGC C-3′. PSA: forward, 5′-GTG GGT CCC GGT TGT CT-3′; reverse, 5′-AGCCCAGCTCCCTGTCT-3′. XIAP: forward, 5′-TGT TTC AGC ATC AAC ACT GGC ACG-3′; reverse, 5′-GCA TGA CAA CTA AAG CAC CGG AC-3′. Cyclin D1: forward, 5′-GAT GCC AAC CTC CTC AAC GAC-3′; reverse, 5′-CTC CTC GCA CTT CTG TTC CTC-3′.

Western Blot Analysis

Cells were treated with embelin and embelin-6g for 96 h. Subsequently, cells were lysed using RIPA buffer (Sigma-Aldrich, St. Louis, MO) and protein concentration measured with bicinchoninic acid (BCA) protein assay kit (Pierce, Rockford, IL). The lysate was boiled for 5 min, subjected to a 15 % SDS-PAGE and transferred to a PVDF membrane using iBlot™ system (Invitrogen, Carlsbad, CA). Membranes were blocked with 3 % BSA in 1x tris buffered saline (TBS) at room temperature for 1 h and then incubated with primary antibodies at 4 °C overnight, followed by incubation with secondary antibody conjugated with horseradish peroxidase (HRP) at room temperature for 1 h. The signal of target proteins was detected using Immun-Star HRP chemiluminescent kit (BioRad, Hercules, CA) or Li-COR Odyssey® infrared imaging system (Li-COR, Lincoln, NE).

XIAP Detection Using ELISA

C4-2 cells were treated with embelin or embelin-6g for 48 h. Cells were lysed and XIAP concentration detected using Human XIAP ELISA kit as described in the manufacturer's protocol.

Apoptosis and Cell Cycle Analysis

Following treatment with 25 µM antiandrogen for 72 h, cells were trypsinized and fixed in 70 % ice-cold ethanol and washed with PBS. Samples were resuspended in 500 µl of

propidium iodide solution containing RNAse A (BD Pharmingen, San Diego, CA) for 15 min at room temperature. Relative DNA content per cell was acquired by measuring DNA fluorescence using flow cytometry and subsequent analysis performed with Modfit program.

Confocal Microscopy

Confocal microscopy was used to elucidate the effect of XIAP inhibitor on DHT stimulated nuclear translocation of AR. Briefly, LNCaP and C4-2 cells were cultured in chamber slides in RPMI media and treated with XIAP inhibitor (5 μM) or DMSO for 3 h and then incubated with DHT (1 nmol/L) for an additional 3 h. Cells were fixed in methanol at room temperature for 10 min, washed with PBS, and incubated with PBS containing 10 % (*w*/*v*) rabbit serum for 2 h at room temperature. Afterwards, the cells were treated with anti-AR antibody (1:100 in PBS buffer) 4 °C overnight. Cells were then washed with PBS and incubated with FITC-conjugated secondary antibody for 1 h at room temperature followed by counterstaining with DAPI. Slides were examined under a Zeiss LSM-710 confocal microscope at 63× objective lens magnification and data processed using a ZEN 2009 LE software.

Preparation and Characterization of Micelles

The film sonication method was used for loading drug into the core of PEG-b-p(CB-co-LA) micelles at a theoretical drug loading of 5 %. Briefly, 5 mg of drug and 95 mg of PEG-b-p(CB-co-LA) was dissolved in 5 ml methanol. The mixture was allowed to stir for 5 min and the solvent evaporated. The resulting film was hydrated and sonicated for 7 min using a Misonix ultrasonic liquid processor (Farmingdale, NY) with an output power of 25 W. The resultant formulation was then centrifuged at 5,000 rpm for 10 min to separate micelles from residual free drug. Subsequently, the supernatant was filtered using a 0.22 μm nylon filter.

In Vivo Efficacy of CBDIV17 and Embelin-Loaded Micelles in Mouse Xenografts

All animal experiments were performed in a humane manner in accordance with NIH animal use guidelines and the protocol approved by the Animal Care and Use Committee (ACUC) at the University of Tennessee Health Science Center. Xenograft flank tumors were induced in 6 week old male athymic nu/nu mice (Jackson Laboratory, Bar Harbor, ME) by subcutaneous injection of 3 million C4-2 cells suspended in 1:1 media and matrigel. When tumors reached approximately 50 mm^3, mice were randomized into four groups of 7 mice, minimizing weight and tumor size differences. Each group was treated with intratumoral injection of blank micelles or drug-loaded micelles. Tumors were measured with a caliper prior to each injection, and their volumes calculated using the formula of $(width^2 \times length)/2$.

RESULTS

Synthesis and Characterization of CBDIV17

CBDIV17 was synthesized as shown in Fig. 1a and characterized by ESI and high-resolution mass spectrometry (HRMS), ^{1}H NMR (Fig. 1b) and ^{13}C NMR. MS (ESI): calculated for $C_{20}H_{17}F_3N_4O_2$ 402.1, found 400.9 [M - H]. HRMS calculated for $C_{20}H_{17}F_3N_4O_2$ 403.13818 found 403.13696. ^{1}H NMR (300 MHz, *chloroform-d*) 10.42–10.51 (m, 1H), 8.33–8.41 (m, 1H), 8.14–8.24 (m, 1H), 8.06 (d, J=8.54 Hz, 1H), 7.43 (d, J=9.16 Hz, 2H), 6.84 (d, J=9.16 Hz, 2H), 6.15 (s, 1H), 3.81 (d, J=15.26 Hz, 1H), 3.62 (d, J=14.95 Hz, 1H), 3.01 (s, 3H), 1.37–1.43 (m, 3H) ppm (Fig. 1). ^{13}C NMR (101 MHz, DMSO-d_6) δ 175.4, 152.3, 142.9, 136.1, 132.7, 131.3 (q, J=31.5 Hz), 122.8, 122.4 (q, J=276.6 Hz), 120.2, 117.5 (q, J=5.1 Hz), 115.7, 112.0, 101.9, 95.9, 76.7, 59.3, 39.7, 39.4 (spt, DMSO), 23.7, 0.0 (s, TMS) ppm. HRMS and ^{13}C NMR data are provided as Supplementary Material.

CBDIV17 and Bicalutamide Inhibit LNCaP and C4-2 Cell Growth

We first assessed anticancer activity of CBDIV17 and bicalutamide in LNCaP and C4-2 cells. Both cells are AR positive and possess the T877A androgen receptor mutant. As shown in Fig. 2a and b, bicalutamide and CBDIV17 exhibited dose-dependent anticancer activities in both cells when treated with 0, 10, 25 and 50 μM for 72 h. From our results, CBDIV17 was more potent than bicalutamide at each dose in both cell lines. IC_{50} for CBDIV17 was 12 and 21 μM in LNCaP and C4-2 cells, respectively. In contrast, bicalutamide had an IC_{50} of 46 μM in LNCaP with only a modest anticancer effect being observed at 50 μM in C4-2 cells. Furthermore, a time course study using a drug concentration of 25 μM for 24 and 72 h revealed the anticancer effect of bicalutamide and CBDIV17 to be time-dependent (Fig. 2c). Our data suggests CBDIV17 displays superior anticancer activity in LNCaP cells even after a short exposure time. Additionally, there is a dramatic increase in inhibition of prostate cancer cell growth for CBDIV17 compared to bicalutamide when cell exposure to drug is increased from 24 to 72 h.

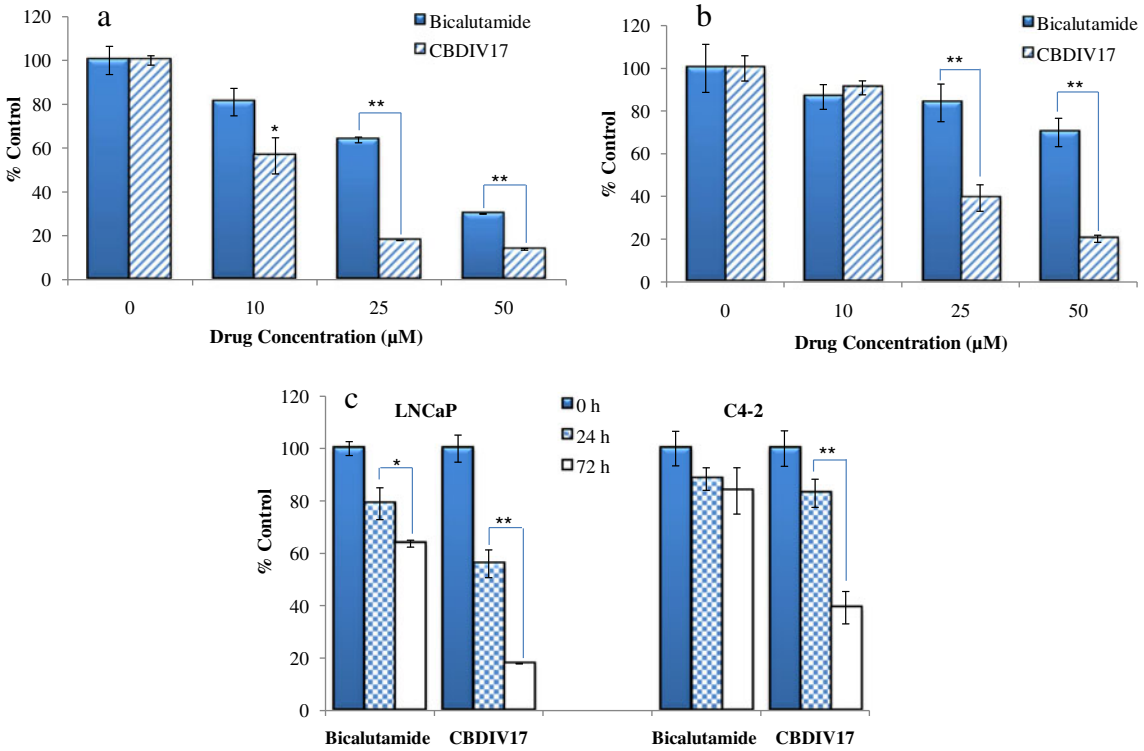

Fig. 2 Anticancer effect of antiandrogen on prostate cancer cells. (**a** and **b**) IC_{50} of bicalutamide and CBDIV17 in LNCaP and C4-2 cells were calculated following treatment with 0, 10, 25 and 50 μM of drug for 72 h and cell viability determined by MTT assay. (**c**) Effect of antiandrogen with time was determined by exposing LNCaP and C4-2 cells to 25 μM of drug for 24 and 72 h. Cell viability was then determined by MTT assay. Results are represented as the mean ± SD of triplicates. *$p < 0.05$; **$p < 0.01$ using Student's unpaired t test.

We next examined the influence of androgens on the anticancer activity of CBDIV17 since it is expected to function as a putative anti-androgen. LNCaP cells were cultured in androgen-depleted media with 5 % charcoal-stripped serum (CSS). Cells were treated for 24 or 72 h with or without 1nM of the synthetic androgen 5α-Dihydrotestosterone (DHT) combined with DMSO (vehicle), CBDIV17 and bicalutamide (positive control). Our data suggests that treatment of cells with DHT stimulated cell growth (Fig. 3). However, even in the presence of DHT, cell growth was inhibited when cells were treated with bicalutamide or CBDIV17, with CBDIV17 being more potent than bicalutamide.

CBDIV17 and Bicalutamide Induce Apoptosis and Alter Cell Cycle of LNCaP and C4-2 Cells

The effect of bicalutamide and CBDIV17 on the cell cycle of LNCaP and C4-2 cells was determined following treatment with 25 μM of these drugs for 72 h. We observed a significant reduction in the percent of cells in S phase in both cell lines (Fig. 4). In LNCaP cells, 27 % of control cells were in the S phase, whereas 16 % of bicalutamide treated cells and 6.5 % of CBDIV17 treated cells were in the S phase. For C4-2 cells, 32.6 % of control cells were in the S phase whilst 27.7 % of bicalutamide treated cells and

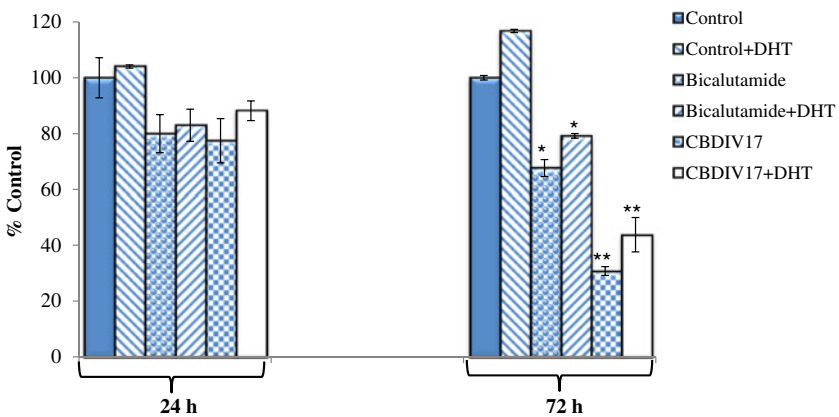

Fig. 3 Effect of bicalutamide and CBDIV17 on cell proliferation in the presence of androgen. LNCaP cells were cultured in androgen-depleted media with 5 % charcoal-stripped serum (CSS). Cells were treated for 24 or 72 h with or without 1 nM of the synthetic androgen 5α-Dihydrotestosterone (DHT) combined with DMSO, bicalutamide and CBDIV17. Results are represented as the mean ± SD of triplicates. *$p < 0.05$; **$p < 0.01$ using Student's unpaired t test.

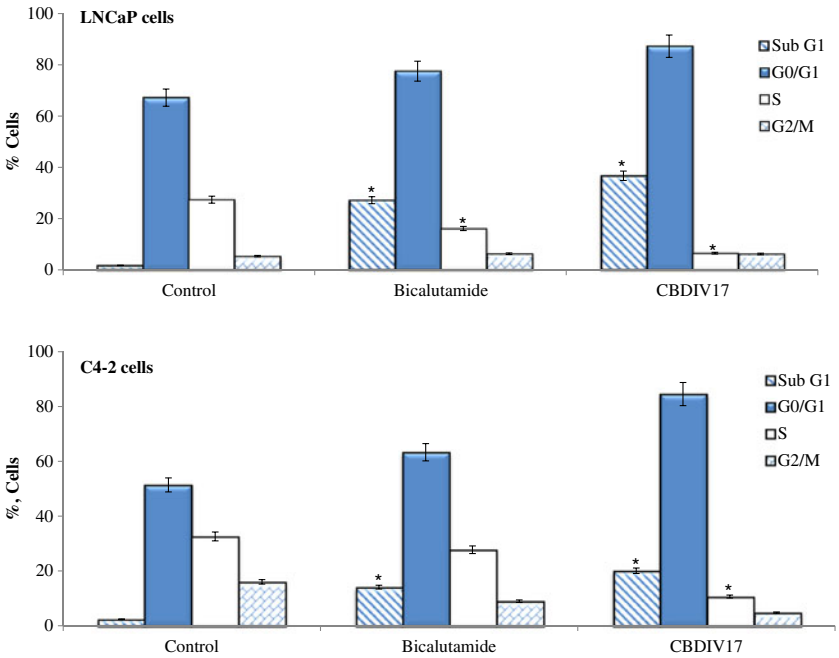

Fig. 4 Effect of bicalutamide and CBDIV17 on apoptosis and cell cycle of LNCaP and C4-2 cells. Cells were treated with antiandrogen (25 μM) for 72 h, stained with propidium iodide and analyzed on a flow cytometer. *$p < 0.05$ using Student's unpaired t-test.

10.7 % of CBDIV17 treated cells were in the S phase. Furthermore, drug treatment in LNCaP cells did not result in significant decrease in percent of cells in the G2/M phase. In contrast, percent of C4-2 cells in the G2/M phase decreased from 16 % in control cells to 8.9 % in bicalutamide treated cells and to 4.8 % in CBDIV17 treated cells.

Treatment with bicalutamide and CBDIV17 resulted in a significant increase in the percentage of cells in the G0/G1 phase in both cell lines. LNCaP cell population in the G0/G1 phase increased from 67 % in control cells to 76 % and 87 % for bicalutamide and CBDIV17 treated cells, respectively. For C4-2 cells, percentage of cells in G0/G1 phase increased from 51.4 % in control cells to 63.3 % and 84.5 % for bicalutamide and CBDIV17 treated cells, respectively. Finally, a significant increase in the sub-G1 phase (indicative of apoptosis) was observed upon administration of bicalutamide (13-fold) and CBDIV17 (18-fold) to LNCaP cells (Fig. 4). In C4-2 cells, treatment with bicalutamide resulted in a 7-fold increase in sub-G1 whereas CBDIV17 led to a 10-fold increase in percentage of cells in subG1 phase. These data demonstrate that CBDIV17 was more potent than bicalutamide in altering cell cycle leading to G1 arrest, reducing DNA synthesis and inducing cell death.

Embelin-6g is More Potent than Embelin in Repressing XIAP Expression

After demonstrating that CBDIV17 is more potent than bicalutamide, we next evaluated the mechanism and therapeutic potential of embelin and embelin-6g (Fig. 5a) to determine which XIAP inhibitor should be used in conjunction with CBDIV17 for combination therapy. Since embelin-6g is reported to be a more potent XIAP inhibitor than embelin (15), we examined its effect on XIAP expression. Our observations indicated that embelin-6g repressed XIAP mRNA expression by 2-fold compared to embelin (Fig. 5b). We also assessed the effect of these drugs on XIAP protein using ELISA. Embelin-6g more potently inhibited XIAP expression compared to embelin with the effect being almost twice that of embelin (Fig. 5c).

Embelin and its Derivative Downregulate AR Expression and Repress AR Mediated Activity

In addition to elucidating the effect of embelin and embelin-6g on XIAP expression, we investigated the effect of these drugs on the androgen receptor signaling axis which is a key regulatory gene involved in prostate cancer. First, we examined the effect of embelin and embelin-6g on AR expression. 1×10^5 C4-2 cells were treated with drug (5 μM) for 48 h and the amount of AR message was quantitatively determined by real-time RT-PCR. There was a significant decrease in AR mRNA levels (Fig. 6a) with both embelin and embelin-6g reducing AR levels by more than 50 % compared to control. Additionally, Western blot analysis revealed a decrease in AR protein amounts when C4-2 cells were treated with 5 μM embelin or embelin-6g for 96 h (Fig. 6b).

Furthermore, we evaluated AR transcriptional activity by examining mRNA expression of prostate specific antigen (PSA). We observed 50 % decrease in PSA mRNA levels for both drugs (Fig. 6a). Additionally, we determined the

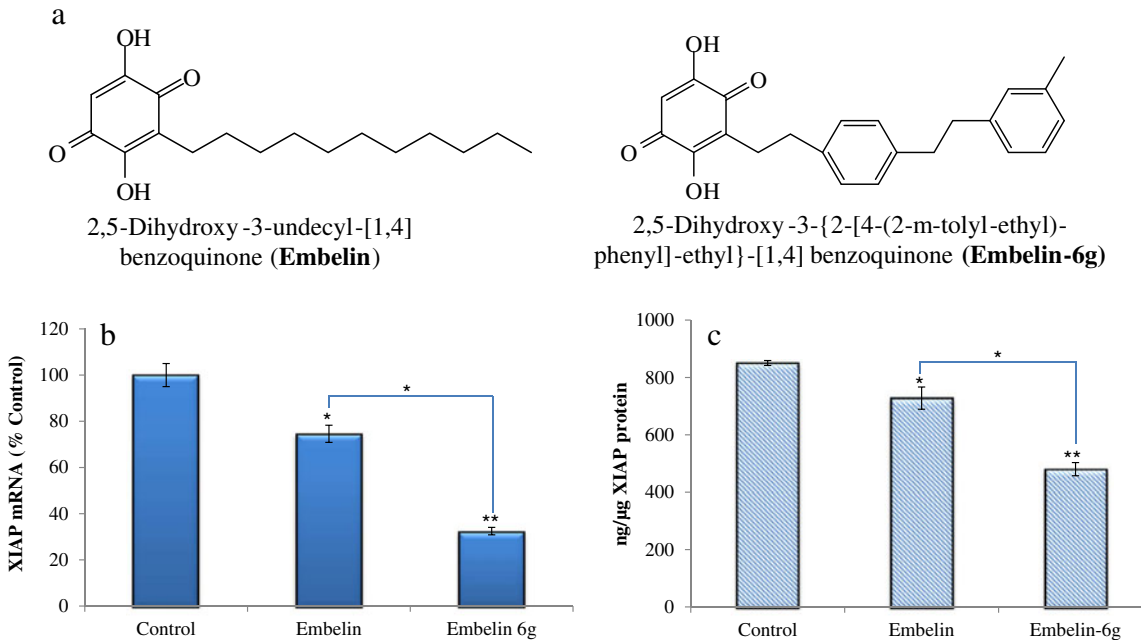

Fig. 5 Embelin and embelin-6g suppress XIAP expression. (**a**) Chemical structures of embelin and embelin-6g. (**b**) 1×10^5 C4-2 cells were treated with embelin or embelin-6g for 48 h, RNA extracted and XIAP expression at mRNA level determined using real-time RT-PCR. (**c**) 1×10^6 C4-2 cells were treated with embelin or embelin-6g for 96 h, protein isolated and XIAP expression at protein level determined using ELISA. $^*p < 0.05$, $^{**}p < 0.01$ using Student's unpaired t-test.

effect of embelin and embelin-6g on intracellular PSA levels. Drug treatment resulted in a decrease in PSA protein expression compared to the control (Fig. 6b). These results demonstrate the ability of embelin to modulate AR levels and show direct correlation between AR protein amount and its subsequent ability to transactivate PSA.

Embelin Blocks DHT-Stimulated AR Nuclear Translocation and Phosphorylation

To determine whether embelin inhibits AR translocation in C4-2 cells we used confocal microscopy to determine the localization of AR in the nucleus. AR was diffusively distributed in the nucleus (Fig. 6c) but cytoplasmic AR translocation to the nucleus was significantly decreased upon incubation with embelin. In contrast, treatment with 1 nM DHT resulted in a majority of cytoplasmic AR translocating into the nucleus. Furthermore, since androgens stimulate phosphorylation of AR Ser81 especially in cells possessing T877A mutation, we examined the effect of embelin on AR phosphorylation (16). C4-2 cells were treated with various concentrations of embelin in the presence or absence of DHT. A concentration-dependent effect of AR Ser81 phosphorylation post embelin treatment was observed strongly suggesting embelin suppressed DHT-induced AR phosphorylation (Fig. 6d).

Embelin and its Derivative Inhibit Prostate Cancer Cell Growth

We next investigated the anticancer activity of embelin and embelin-6g by determining their IC_{50} values in LNCaP and C4-2 cells. Both drugs were found to be equally potent in inhibiting the proliferation of prostate cancer cells regardless of androgen status (Fig. 7a). IC_{50} was approximately 6.5 µM.

To provide mechanistic insight into the effect of embelin and embelin-6g on cell proliferation, we examined whether these drugs modulate the expression of cyclin D1 which is a known marker of cell proliferation. Treatment of C4-2 cells with 5 µM of embelin and embelin-6 g for 48 h resulted in suppression of cyclin D1 expression by ~22 % (Fig. 7b). Western blot analysis also revealed inhibition of cyclin D1 when cells were treated with drug for 96 h (Fig. 7c).

Since we were interested in using a XIAP inhibitor which has fast acting activity for our combination study, we examined the anticancer activity of embelin and embelin-6g in LNCaP and C4-2 cells at 18 h post treatment. Our results (Fig. 7d) suggest embelin to be faster acting and more potent than embelin-6g in inhibiting cell growth especially in C4-2 cells. Therefore, we selected embelin as the XIAP inhibitor for further studies in our combination therapy.

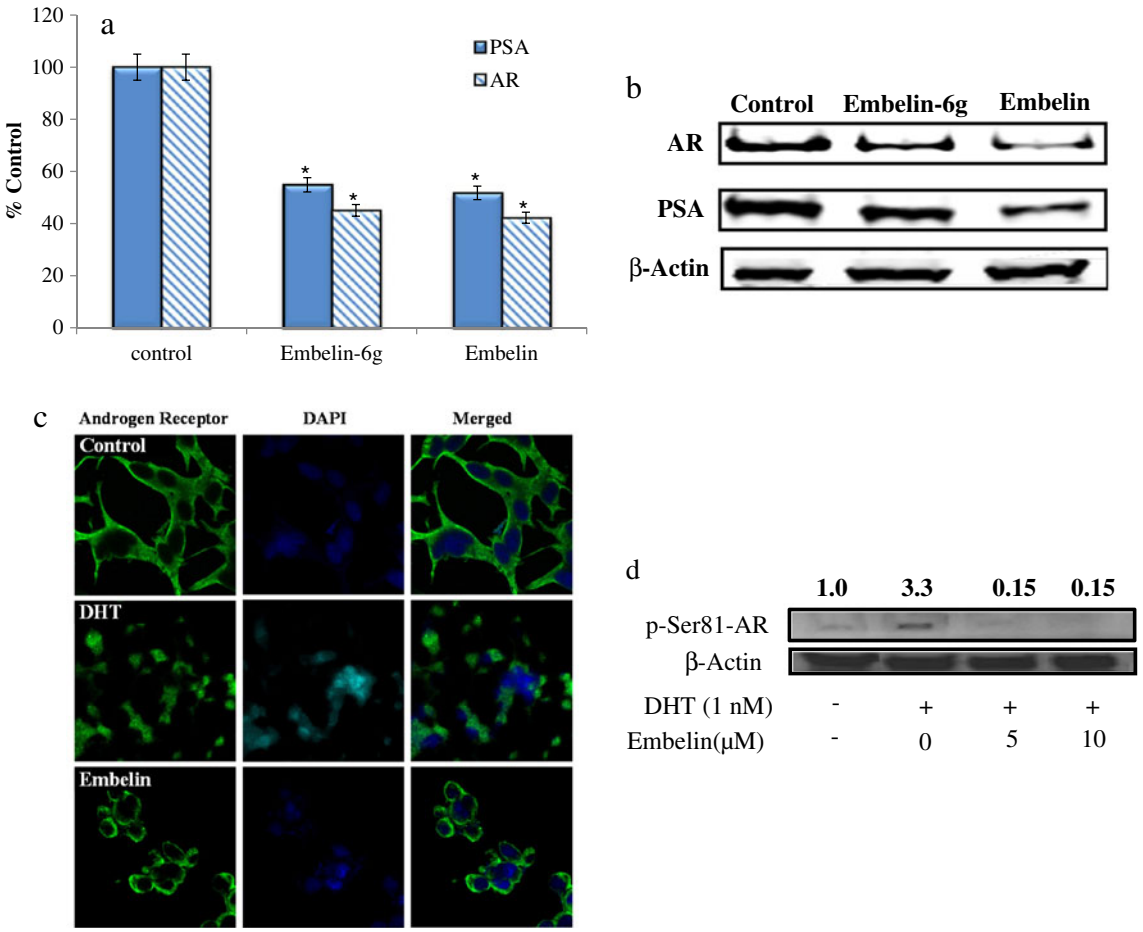

Fig. 6 Effect of embelin and embelin-6g on AR and PSA expression. (**a**) C4-2 cells were treated with embelin and embelin-6g (5 μM) for 48 h, RNA extracted and AR and PSA expression at mRNA level determined using real-time RT-PCR. (**b**) Cells were treated with embelin and embelin-6g (5 μM) for 96 h, protein isolated and AR and PSA expression at protein level determined using Western blot. (**c**) C4-2 cells were grown on chamber slides treated in the presence or absence of 5 μM embelin for 12 h prior to addition of 1 nM DHT. Cells were fixed, permeabilized and AR immunostained with rabbit anti-AR followed by FITC-conjugated secondary antibody and nucleus stained with DAPI. (**d**) Phosphorylated Ser81 AR protein levels in C4-2 cells were determined by Western blot analysis. Cells were grown in CSS and treated with Embelin (5 or 10 μM), in the presence or absence of 1 nM DHT for 48 h.

Formulation of CBDIV17 and Embelin-Loaded PEG-b-p(CB-co-LA) Micelles and Their Effect on Prostate Cancer Cell Growth and Migration

Since CBDIV17 and embelin are extremely hydrophobic and we plan to test our combination therapy *in vivo*, we first formulated these drugs into Poly (ethylene glycol)-b-poly (carbonate-co-lactide) (PEG-b-p(CB-co-LA)) micelles. Micelle size ranged from ~83 to 90 nm (Table I) and the presence of drug did not significantly affect micelles size. Furthermore, (PEG-b-p(CB-co-LA)) micelles were monodisperse and had a PDI of approximately 0.11. Encapsulation efficiency for CBDIV17 was 91.2±2.3 % at 5 % theoretical loading but dropped to 55.7±1.4 % when theoretical loading increased to 10 %. In contrast, encapsulation efficiency for embelin was 38.4±1.0 % at 5 % theoretical loading and 35.0±0.9 % at 10 % theoretical loading. Therefore, a 5 % theoretical loading was used for formulating micelles for further studies.

Following micelle formulation and characterization, we investigated whether the combination of CBDIV17 and embelin was more potent than their monotherapy in treating prostate cancer. C4-2 cells were treated with embelin (5 μM) or CBDIV17 (25 μM) alone or in combination for 24 h. Combination therapy was found to be more effective than control or monotherapy (Fig. 8a). Both embelin and CBDIV17 resulted in approximately 20 % decrease in cell growth while combination therapy inhibited cell growth by about 70 %.

We also determined the effect of combining CBDIV17 and embelin on the migration potential of C4-2 cells using the scratch wound assay. We observed embelin to have no obvious effect on cell migration under our conditions whereas CBDIV17 had some modest effect. The group treated with the combination of CBDIV17 and embelin resulted in superior inhibition of cell migration compared to untreated control and each drug alone (Fig. 8b).

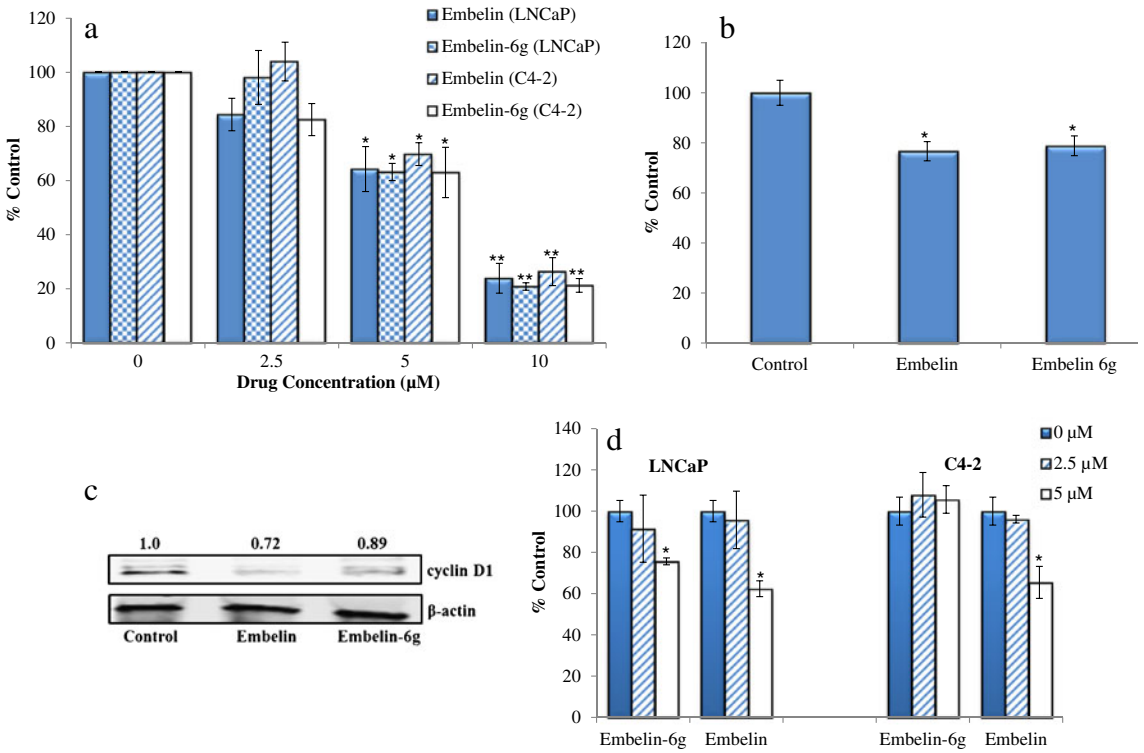

Fig. 7 Effect of embelin and embelin-6g on prostate cancer cell proliferation and cyclin D1, expression. (**a**) LNCaP and C4-2 cells were treated with XIAP inhibitor (0–10 μM) for 96 h and cell viability measured using MTT assay. (**b**) Cells were treated with XIAP inhibitors (5 μM) for 48 h, total RNA extracted and cyclin D1 expression at mRNA level determined using real-time RT-PCR. (**c**) 1×10^6 cells were treated with XIAP inhibitors for 96 h, protein isolated and cyclin D1 expression at protein level determined using Western blot. (**d**) LNCaP and C4-2 cells were treated with XIAP inhibitors (0, 2.5 and 5 μM) for 24 and cell viability measured using MTT assay. *$p < 0.05$, **$p < 0.01$ using Student's unpaired t-test.

Effect of CBDIV17 and Embelin Combination on Apoptosis

Since CBDIV17 and embelin combination effectively inhibited cell proliferation *in vitro*, we further tested their effect on cell cycle and apoptosis in C4-2 cells. From Fig. 9a, there was a decrease in percentage of cells in the G2/M and S phases following treatment with CBDIV17. Treatment with 25 and 50 μM decreased percent of cells in the G2/M phase by 50 % while percentage of cells in the S phase decreased by 30 %. Also, we found CBDIV17 showed dose-dependent increase in apoptosis (sub-G1). The percentage of cells in the sub-G1 phase was around 21 % at 25 μM and 38 % for 50 μM. In contrast, percentage of cells in the sub-G1 phase did not differ significantly from that of control for the concentrations of embelin tested. Notably, we observed combination of CBDIV17 (25 μM) and embelin (5 μM) induced apoptosis more potently compared to control or either treatment alone. Specifically, percentage of cells in the sub-G1 phase for combination therapy was 40-fold, 28-fold and 2-fold more, compared to control, embelin and CBDIV17, respectively. Additionally, combination of CBDIV17 (25 μM) and embelin (5 μM) resulted in percentage of cells in the sub-G1 phase comparable to that of 50 μM CBDIV17.

Table I Effect of Drug Loading on Poly (ethylene glycol)-b-poly (carbonate-co-lactide) (PEG-b-p(CB-co-LA)) Micelle Size and Encapsulation Efficiency

Theoretical loading (%)	Size (nm)	PDI	Encapsulation efficiency (%)
0	89.9 ± 0.7	0.10 ± 0.02	
CBD-IV 17			
5	86.4 ± 0.8	0.11 ± 0.02	91.2 ± 2.3
10	84.8 ± 0.2	0.12 ± 0.01	55.7 ± 1.4
Embelin			
5	85.6 ± 1.2	0.11 ± 0.01	38.4 ± 1.0
10	83.2 ± 0.5	0.10 ± 0.00	35.0 ± 0.9

In Vivo Efficacy of CBD IV17 and Embelin-Loaded Micelles in Mouse Xenografts

Since CBDIV17 and embelin combination therapy effectively inhibited prostate cancer growth *in vitro*, we determined the effect of this combination approach in C4-2 xenograft tumor model. CBDIV17 and embelin were formulated using PEG-b-p(CB-co-LA) micelles and intratumoral injection of 10 mg/kg CBDIV17 and 10 mg/kg embelin-loaded

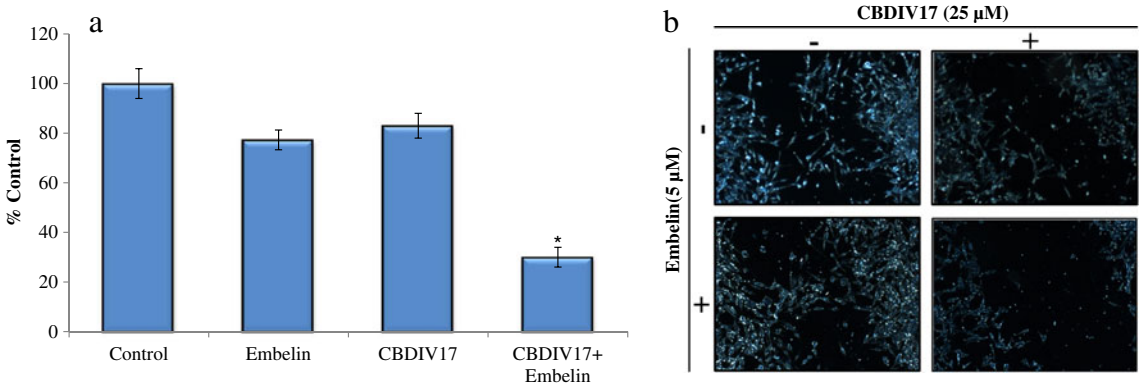

Fig. 8 Effect of CBDIV17 and embelin combination on prostate cancer cell growth and migration. (**a**) Anticancer effect of CBDIV17 and embelin, alone or in combination on C4-2 cells was determined following treatment of cells with 25 μM of CBDIV17 and 5 μM embelin for 24 h. and cell viability determined by MTT assay. *$p < 0.05$ using Student's unpaired t test. (**b**) C4-2 cells were grown to 70 % confluence in six well plates and three parallel wounds made using pipette tip. Cells were treated with CBDIV17 (25 μM) or embelin (5 μM) alone or in combination for 48 h after which cells were washed with ice cold 1× PBS and imaged under microscope.

micelles was administered on days 0, 3 and 7. CBDIV17 and embelin combination inhibited tumor growth more potently compared to the mice treated with empty micelles or monotherapy (Fig. 10a). On day 7 (last day of treatment), the tumor size of the combination group was 50 % of that in CBDIV17 group, 25 % of that in embelin group and 18 % of that in the control group (Fig. 10b). Furthermore, the body weight loss of mice was less than 5 % suggesting minimal toxicity of the treatment (Fig. 10c). Additionally, combination therapy increased tumor-doubling time compared to monotherapy and control. For instance, the time it took for tumor to double from 50 mm^3 to 100 mm^3 are as follows: the combination group took 14 days; CBDIV17 group took 7 days and less than 3 days for embelin and control group. Taken together, these results demonstrate that CBDIV17 and embelin combination therapy effectively inhibited tumor growth and can prolong survival.

DISCUSSION

Since prostate cancer is an androgen-dependent malignancy, current therapies including non-steroidal antiandrogens target the AR. However, first generation non-steroidal antiandrogens do not completely hinder AR activity and eventually become agonists in tumor cells partly due to elevated levels of AR. Furthermore, progression to hormone refractory prostate cancer is also characterized by resistance to apoptosis. Particularly, XIAP is overexpressed and inhibits caspases 9 and 3 thus contributing to a defect in the apoptotic machinery (17–20). Together, AR and XIAP overexpression may be a molecular reason leading to drug resistance and indicate that more potent antiandrogens, AR downregulating agents and XIAP inhibitors or their combination can effectively treat advanced prostate cancer. We have previously demonstrated that combination of bicalutamide and embelin is more effective in treating prostate cancer compared to monotherapy (6). However, bicalutamide has limited efficacy in advanced prostate cancer (e.g., C4-2 cells) and assumes agonistic properties following prolonged treatment. Therefore, the primary objective of this study was to investigate whether a novel antiandrogen (CBDIV17) was more potent than bicalutamide and can effectively inhibit advanced prostate tumor growth when combined with XIAP inhibitor. We also further explored the molecular mechanism for our selected XIAP inhibitors.

To determine the comparative therapeutic benefits of CBDIV17 over bicalutamide, we evaluated the biological effects of both drugs in LNCaP and C4-2 cells by observing their effect on cell proliferation in the presence or absence of synthetic androgen and in inducing apoptosis. Our results show, CBDIV17 to be more potent than bicalutamide in inhibiting cell proliferation in a dose and time dependent manner (Fig. 2). Furthermore, inhibition of cell growth was only modestly reversed in the presence of DHT. This may possibly be due to better cytotoxic effects or its superior ability at the molecular level to retain antagonism and hence bypass antiandrogen resistance. Our observation suggests CBDIV17 analog to be more potent than bicalutamide regardless of AR sensitivity or presence of synthetic androgen and therefore has the potential for treating advanced prostate cancer.

Chen *et al.* synthesized new XIAP inhibitors with better binding affinities than embelin by modifying its hydrophobic tail. It was shown that embelin-6g has a two-fold better binding affinity to XIAP BIR3 compared to embelin and was potent in inhibiting proliferation of human breast and prostate cancer cell lines (15). Therefore, we were interested in how better XIAP binding affinity would translate in terms of potency in inhibiting cell growth and inducing apoptosis in prostate cancer cells. Although Chen *et al.* showed better binding affinity for embelin-6g they did not show its effect on XIAP gene expression. In our studies, we found embelin-6g

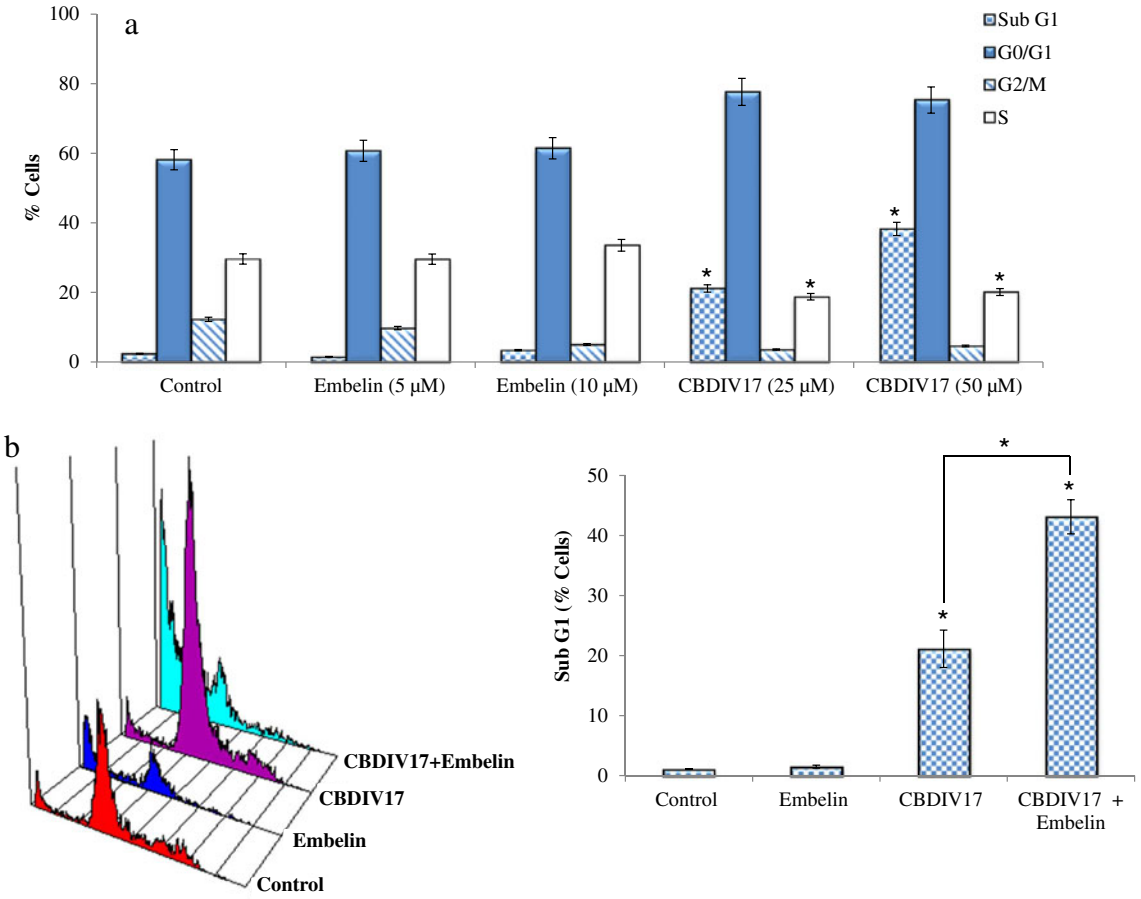

Fig. 9 Effect of embelin and CBDIV17 combination on cell cycle and apoptosis. (**a**) C4-2 cells were treated with vehicle, embelin (5 and 10 μM) and CBDIV17 (25 and 50 μM) for 72 h, stained with propidium iodide and analyzed on a flow cytometer. (**b**) Cells were treated with vehicle, embelin (5 μM) and CBDIV17 (25 μM) alone or in combination for 72 h, stained with propidium iodide and analyzed on a flow cytometer. *Left panel*, cell cycle distribution; *Right panel*, quantitative analysis of sub G1phase. *$p < 0.05$ using Student's unpaired t test.

to be more potent than embelin in repressing XIAP gene expression. At both the mRNA and protein levels, embelin-6g appeared to be twice as effective as embelin (Fig. 5b and c). This result may logically extend from embelin-6g's two-fold better binding affinity compared to embelin. However, we observed embelin and embelin-6g to exhibit similar ability in inhibiting prostate cancer cell growth despite the difference in their effect on XIAP expression. In fact, our findings suggest embelin elicits a quicker therapeutic response compared to embelin-6g and was consequently more potent at short time intervals. Therefore, embelin was selected for combination studies with CBDIV17.

We also made an interesting finding regarding the ability of embelin and embelin-6g to disrupt AR signaling in prostate cancer cells. These XIAP inhibitors also appear to decrease AR levels in LNCaP and C4-2 cells. Similar results have also been reported in the literature where other drugs exhibit the ability to decrease AR expression (21–23). Examples of these AR down-regulating agents (ARDA) include quercetin, epicatechin, and curcumin. Purushottamachar *et al.* provided clear evidence concerning structural requirements common to ARDAs (24). Typical features include one hydrophobic group, one aromatic group, and two hydrogen bond acceptors (24). Both embelin and embelin-6g satisfy these structural criteria and hence it may not be surprising that they are capable of depleting AR expression.

Although the precise mode of action of embelin and embelin-6g in down-regulating AR inhibition is not fully understood, it is likely that both drugs inhibit AR expression through a number of different mechanisms. Since both drugs decrease AR expression by more than 50 % on the mRNA level, it is possible that mRNA stability or inhibition of AR mRNA synthesis may contribute to the effect of these drugs on AR expression levels. It is also possible that embelin and embelin-6g hinder androgen-AR binding or may disrupt the Hsp90-AR complex. The likelihood of these mechanisms which have also been reported by Liu *et al.* (21) would be consistent with our results where we showed the ability of embelin to prevent AR nuclear translocation from the cytoplasm to the nucleus in C4-2 cells (Fig. 6c).

Combination therapy involving XIAP modulation is a promising approach for treating solid tumors including

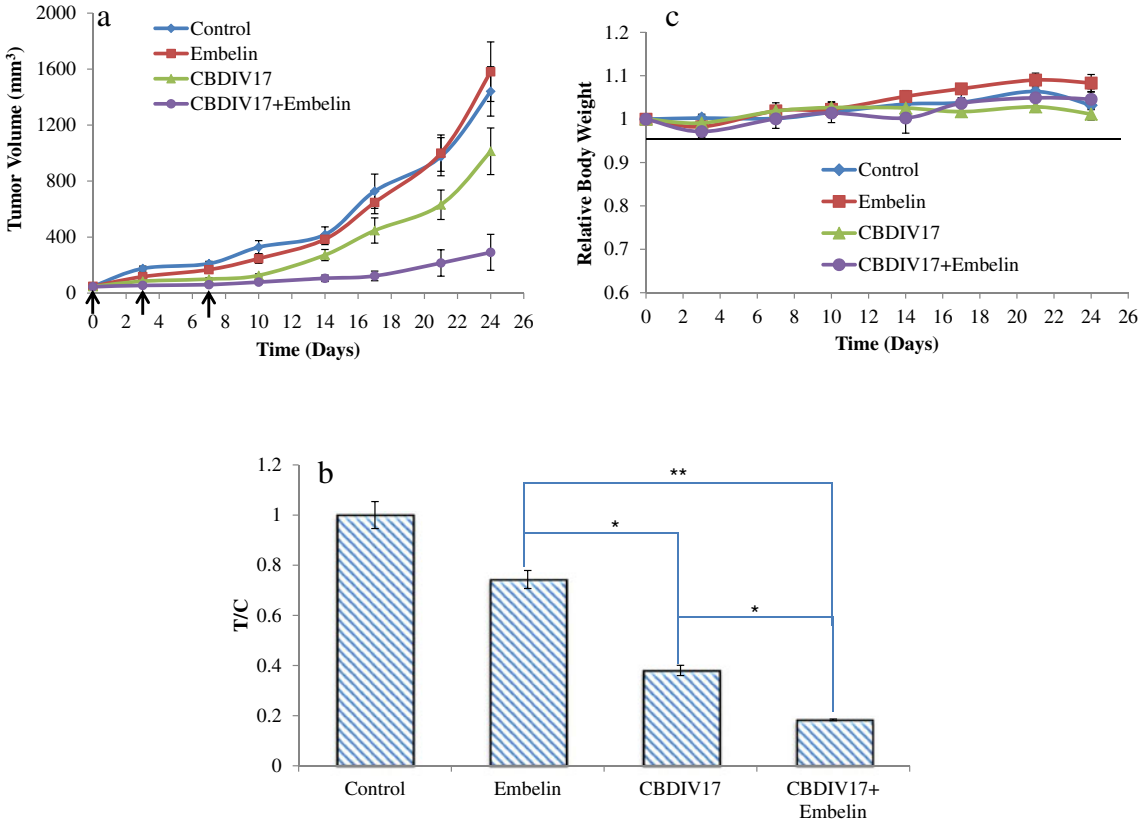

Fig. 10 Effect of CBDIV17 and embelin-loaded micelles on growth of tumors derived from C4-2 prostate cancer cells in nude mice. (**a**) Nude mice bearing 50 mm^3 C4-2 tumors were given an intratumoral injection of 10 mg/kg CBDIV17 and 10 mg/kg embelin, alone or in combination (arrows indicate injection) and tumor size measured. Tumor growth regression was significantly higher for combination therapy group compared to control or monotherapy. Points are mean tumor size ($n=7$); bars, SE. (**b**) Tumor suppression (T/C) was computed as the ratio of mean tumor volume in treated groups compared with control when last injection was administered. (**c**) Relative body weight was expressed as the body weights at various times during treatment normalized with body weights at day 0. *$p < 0.05$, **$p < 0.01$ using Student's unpaired t-test.

prostate cancer (6,25,26). We observed CBDIV17 and embelin combination to be more potent in inhibiting prostate cancer cell growth and in inducing apoptosis in advanced prostate cancer compared to control or monotherapy. This superior effect was found to be supra-additive and is consistent with our previous findings which showed synergism even for simultaneous administration of bicalutamide and embelin in C4-2 cells (6). The greater potency of CBDIV17 and embelin combination therapy may be attributed to the ability of embelin to lower the threshold required by XIAP to inhibit apoptosis thereby enhancing CBDIV17 activity several fold. From our findings, it is also possible that the ability of embelin to downregulate AR may play some role in the observed therapeutic effect of our combination therapy.

Since *in vivo* substantiation of our cellular observations is imperative for clinical translation, CBDIV17 and embelin were formulated into PEG-b-p(CB-co-LA) micelles to test our combination approach *in vivo* due to their extreme hydrophobicity and to avoid the detrimental side effects of solubilizing agents such as DMSO and Cremophor® EL (27). CBDIV17 had higher drug loading compared to embelin. This may be due to the close structural similarity between CBDIV17 and bicalutamide for which PEG-b-p (CB-co-LA) was specifally designed to enhance drug loading (10). Consistent with our *in vitro* data, we found co-administration of embelin and CBDIV17 to be more potent in regressing prostate tumor growth compared to control or monotherapy (Fig. 10a and b). Tumor volume at the last injection and at the end of experiment for the combination group was approximately 20 % of control. A result demonstrating the ability of our combination therapy to suppress growth of advanced prostate cancer tumors. Also, CBDIV17 was effective in regressing tumor growth at the doses studied compared to embelin or control. However, tumor volume increased to 70 % of control at the end of the experiment compared to 40 % of control at the last injection. We found the embelin treated group to have tumor volume 75 % of the control group when the last injection was administered. Nonetheless, there was no difference between embelin treated group and control at the end of the study. Our results are in agreement with the findings of Dai *et al.* (28). However, they orally administered a 6-fold higher dose of embelin (60 mg/

kg) twice a week for three weeks and used PC-3 xenograft tumors which are AR negative.

In conclusion, we have demonstrated that CBDIV17 is more potent than bicalutamide in regressing prostate tumor growth and inducing apoptosis regardless of AR status. Additionally, we have shown that the combination of CBDIV17 and embelin is more potent in inhibiting cell growth and inducing apoptosis compared to control or monotherapy *in vitro* and *in vivo*. Our findings also reveal a novel mechanism regarding the ability of embelin and embelin-6g to alter AR signaling pathway. We are currently investigating the mode of action by which embelin down-regulates AR gene expression. We believe such mechanistic insight will lead to the design of highly potent analogs. The current study provides evidence that CBDIV17 and embelin combination is a promising therapeutic approach for treating hormone refractory prostate cancer.

ACKNOWLEDGMENTS & DISCLOSURES

This work is supported by an Idea Award (W81XWH-10-1-0969) from the Department of Defense Prostate Cancer Research Program. We would also like to thank Dr. Liguo Song for his help in obtaining HRMS data. Molecular weight measurement was performed at the Mass Spectrometry Center of the Department of Chemistry at the University of Tennessee at Knoxville using a JEOL (Peabody, MA) AccuTOF-D time-of-flight (TOF) mass spectrometer with a DART (direct analysis in real time) ionization source.

REFERENCES

1. Jemal A, Siegel R, Xu J, Ward E. Cancer statistics, 2010. CA Cancer J Clin. 2010;60:277–300.
2. Gittes RF. Carcinoma of the prostate. N Engl J Med. 1991;324:236–45.
3. Kozlowski JM, Ellis WJ, Grayhack JT. Advanced prostatic carcinoma. Early *versus* late endocrine therapy. Urol Clin North Am. 1991;18:15–24.
4. Bracarda S, de Cobelli O, Greco C, Prayer-Galetti T, Valdagni R, Gatta G, *et al.* Cancer of the prostate. Crit Rev Oncol Hematol. 2005;56:379–96.
5. Goktasand S, Crawford ED. Optimal hormonal therapy for advanced prostatic carcinoma. Semin Oncol. 1999;26:162–73.
6. Danquah M, Li F, Duke 3rd CB, Miller DD, Mahato RI. Micellar delivery of bicalutamide and embelin for treating prostate cancer. Pharm Res. 2009;26:2081–92.
7. Scherand HI, Sawyers CL. Biology of progressive, castration-resistant prostate cancer: directed therapies targeting the androgen-receptor signaling axis. J Clin Oncol. 2005;23:8253–61.
8. Taplinand ME, Balk SP. Androgen receptor: a key molecule in the progression of prostate cancer to hormone independence. J Cell Biochem. 2004;91:483–90.
9. Danquah MK, Zhang XA, Mahato RI. Extravasation of polymeric nanomedicines across tumor vasculature. Adv Drug Deliv Rev. 2011;63:623–39.
10. Danquah M, Fujiwara T, Mahato RI. Self-assembling methoxypoly (ethylene glycol)-b-poly(carbonate-co-L-lactide) block copolymers for drug delivery. Biomaterials. 2010;31:2358–70.
11. Li F, Danquah M, Mahato RI. Synthesis and characterization of amphiphilic lipopolymers for micellar drug delivery. Biomacromolecules. 2010;11:2610–20.
12. Li F, Danquah M, Singh S, Wu H, Mahato RI. Paclitaxel- and lapatinib-loaded lipopolymer micelles overcome multidrug resistance in prostate cancer. Drug Deliv Transl Res. 2011;1:240–8.
13. Sun C, Shi Y, Xu LL, Nageswararao C, Davis LD, Segawa T, *et al.* Androgen receptor mutation (T877A) promotes prostate cancer cell growth and cell survival. Oncogene. 2006;25:3905–13.
14. Wu Y, Chhipa RR, Zhang H, Ip C. The antiandrogenic effect of finasteride against a mutant androgen receptor. Cancer Biol Ther. 2011;11:902–9.
15. Chen J, Nikolovska-Coleska Z, Wang G, Qiu S, Wang S. Design, synthesis, and characterization of new embelin derivatives as potent inhibitors of X-linked inhibitor of apoptosis protein. Bioorg Med Chem Lett. 2006;16:5805–8.
16. Chang C, Saltzman A, Yeh S, Young W, Keller E, Lee HJ, *et al.* Androgen receptor: an overview. Crit Rev Eukaryot Gene Expr. 1995;5:97–125.
17. Takahashi R, Deveraux Q, Tamm I, Welsh K, Assa-Munt N, Salvesen GS, *et al.* A single BIR domain of XIAP sufficient for inhibiting caspases. J Biol Chem. 1998;273:7787–90.
18. Fesik SW. Insights into programmed cell death through structural biology. Cell. 2000;103:273–82.
19. Riedl SJ, Renatus M, Schwarzenbacher R, Zhou Q, Sun C, Fesik SW, *et al.* Structural basis for the inhibition of caspase-3 by XIAP. Cell. 2001;104:791–800.
20. Chai J, Shiozaki E, Srinivasula SM, Wu Q, Datta P, Alnemri ES, *et al.* Structural basis of caspase-7 inhibition by XIAP. Cell. 2001;104:769–80.
21. Liu S, Yuan Y, Okumura Y, Shinkai N, Yamauchi H. Camptothecin disrupts androgen receptor signaling and suppresses prostate cancer cell growth. Biochem Biophys Res Commun. 2010;394:297–302.
22. Ren F, Zhang S, Mitchell SH, Butler R, Young CY. Tea polyphenols down-regulate the expression of the androgen receptor in LNCaP prostate cancer cells. Oncogene. 2000;19:1924–32.
23. Chen L, Meng S, Wang H, Bali P, Bai W, Li B, *et al.* Chemical ablation of androgen receptor in prostate cancer cells by the histone deacetylase inhibitor LAQ824. Mol Cancer Ther. 2005;4:1311–9.
24. Purushottamachar P, Khandelwal A, Chopra P, Maheshwari N, Gediya LK, Vasaitis TS, *et al.* First pharmacophore-based identification of androgen receptor down-regulating agents: discovery of potent anti-prostate cancer agents. Bioorg Med Chem. 2007;15:3413–21.
25. Lecis D, Drago C, Manzoni L, Seneci P, Scolastico C, Mastrangelo E, *et al.* Novel SMAC-mimetics synergistically stimulate melanoma cell death in combination with TRAIL and Bortezomib. Br J Cancer. 2010;102:1707–16.
26. Huerta S, Gao X, Livingston EH, Kapur P, Sun H, Anthony T. *In vitro* and *in vivo* radiosensitization of colorectal cancer HT-29 cells by the smac mimetic JP-1201. Surgery. 2010;148:346–53.
27. Onetto N, Canetta R, Winograd B, Catane R, Dougan M, Grechko J, *et al.* Overview of Taxol safety. J Natl Cancer Inst Monogr. 1993;131–9.
28. Dai Y, Desano J, Qu Y, Tang W, Meng Y, Lawrence TS, *et al.* Natural IAP inhibitor Embelin enhances therapeutic efficacy of ionizing radiation in prostate cancer. Am J Cancer Res. 2011;1:128–43.

Advanced Drug Delivery Reviews 63 (2011) 623–639

Contents lists available at ScienceDirect

Advanced Drug Delivery Reviews

journal homepage: www.elsevier.com/locate/addr

Extravasation of polymeric nanomedicines across tumor vasculature ☆

Michael K. Danquah [a], Xin A. Zhang [b], Ram I. Mahato [a,*]

[a] Department of Pharmaceutical Sciences, 19. South Manassas St., Memphis, TN, 38103-3308, USA
[b] Department of Medicine, University of Tennessee Health Science Center, 19. South Manassas St., Memphis, TN, 38103-3308, USA

ARTICLE INFO

Article history:
Received 13 October 2010
Accepted 30 November 2010
Available online 6 December 2010

Keywords:
Extravasation
Drug delivery
Nanomedicines
Tumor vasculature
Tumor targeting

ABSTRACT

Tumor microvasculature is fraught with numerous physiological barriers which hinder the efficacy of anticancer agents. These barriers include chaotic blood supply, poor tumor vasculature permeability, limited transport across the interstitium due to high interstitial pressure and absence of lymphatic network. Abnormal microvasculature also leads to hypoxia and acidosis which limits effectiveness of chemotherapy. These barriers restrict drug or drug carrier extravasation which hampers tumor regression. Targeting key features of the tumor microenvironment such as tumor microvessels, interstitial hypertension and tumor pH is a promising approach to improving the efficacy of anticancer drugs. This review highlights the current knowledge on the distinct tumor microenvironment generated barriers which limit extravasation of drugs and focuses on modalities for overcoming these barriers using multi-functional polymeric carriers. Special attention is given to utilizing polymeric nanomedicines to facilitate extravasation of anticancer drugs for future cancer therapy.

Contents

☆ This review is part of the *Advanced Drug Delivery Reviews* theme issue on "Target Cell Movement in Tumor and Cardiovascular Diseases".

* Corresponding author. Department of Pharmaceutical Sciences, University of Tennessee Health Science Center, 19 South Manassas, CRB RM 224, Memphis, TN 38103-3308, USA. Tel.: +1 901 448 6929; fax: +1 901 448 2099.
E-mail address: rmahato@uthsc.edu (R.I. Mahato).
URL: http://www.uthsc.edu/pharmacy/rmahato (R.I. Mahato).

0169-409X/$ – see front matter © 2010 Elsevier B.V. All rights reserved.
doi:10.1016/j.addr.2010.11.005

1. Introduction

Tumors are characterized by poorly differentiated, highly chaotic arrangement of vessels which have unsealed endothelial cell–cell junctions and discontinuous basement membrane. Due to their irregular organization, tumor microvessel walls are leaky and exhibit heterogeneous hyperpermeability compared to normal tissue [1]. Unlike normal tissues, tumors have functionally defective lymphatic vessels because cancer cells compress lymphatic vessels causing their collapse [2]. Also, the decreased lymphatic drainage associated with tumors results in retention of permeated macromolecules in tumors. The fluid that leaves the bloodstream inside the tumor can only escape from the tumor either by feeding back into postcapillary venules or by passage through the tumor interstitium.

Delivery of anticancer agents to solid tumors remains a significant challenge. First, anticancer drugs have low tumor to normal cell selectivity making them potentially toxic to both normal and tumor cells. Moreover, normal tissues possess low intrinsic tolerance compared to tumors severely limiting the dose required for tumor regression [3,4]. Second, most anticancer agents are highly lipophilic, requiring the use of solubilizing agents or surfactants so that they can be used via systemic administration. Paclitaxel, for example, is a potent anticancer drug with aqueous solubility of only ~1 μg/mL [5]. Docetaxel, its more water soluble derivative also has a low aqueous solubility of ~6–7 μg/mL [6]. Hence, solubilizing agents such as dimethyl sulfoxide (DMSO), Cremophor® EL or Tween 80 are typically used to bring these drugs into true solution for systemic administration. However, such agents are harmful to the liver and kidneys [7], cause dose-dependent hemolysis and lead to neurotoxicity [8] thus hindering their medical utility for intravenous applications.

The medical application of nanotechnology (nanomedicines) can overcome potential problems in cancer therapy. For instance, biodegradable polymeric or lipid nanosized carriers are attractive candidates for anticancer drug delivery since they lead to high therapeutic concentrations of anticancer agents to tumors, with minimal systemic exposure. Examples include liposomes [9], micelles [10–12], and polymer–drug conjugates [13] and several of these nano-therapeutics have received FDA approval for clinical use [14]. These nanosized delivery platforms are capable of improving drug solubility and take advantage of the unique pathophysiology of tumor vasculature to ferry hydrophobic drugs with minimal adverse effects upon systemic administration. Typically this occurs by the enhanced permeability and retention (EPR) effect where macromolecular systems preferentially accumulate in tumors when administered systemically [15–17].

Successful treatment of cancer utilizing polymeric nanomedicines requires that once blood borne, they reach the site of action in optimal quantities. To achieve this, they must arrive at the tumor through blood vessels, be transported across vascular walls (extravasation) and then move through the interstitium. Jain and others have shown tremendous heterogeneity in vessel permeability within tumors and between tumor types [18–21]. Aberrant extravasation has been implicated in the heterogeneous distribution of drugs inside tumors accounting for their moderate therapeutic effect in complete tumor eradication. Hence, overcoming this obstacle of nonuniform extravasation is crucial to improving the drug delivery potential of polymeric nanomedicines. This challenge demands an understanding of the mechanisms governing vascular permeability and the spatial and temporal regulation of transport pathways in tumors [22]. Insight from such understanding can be utilized in developing the next generation of polymeric nanomedicines possessing tunable properties that facilitate their extravasation across tumor vasculature and discovering superior approaches for modulating tumor vasculature.

In this review, we summarize current knowledge on the distinct tumor microenvironment and blood vessel structure, discuss barriers to drug delivery to tumors and finally appraise modalities for overcoming these barriers.

2. Microenvironment of solid tumors

To develop potent therapeutic approaches for site-specific delivery of drugs to tumors using polymeric nanomedicines, it is imperative to understand the microenvironment of the tumor. Solid tumors are organ-like entities arising from stem cell populations and consist of cancer cells, non-transformed stromal cells, blood vessels and the interstitium [23]. Cancer and stromal cells comprise the major portion of solid tumors accounting for greater than 50% of tumor volume. Blood vessels nourish both stromal and cancer cells in tumors and constitutes up to 10% of tumor volume, while the interstitium forms the remainder of the tumor and provides the nutritional and structural framework for it to grow.

While the normal cellular microenvironment can inhibit malignant cell growth, the tumor microenvironment supports cell proliferation. Tumors shape their microenvironment and support the tumor and non-malignant cells. Tumor microenvironment greatly influences its development and generate barriers (Fig. 1) that prevent therapeutic agents from accessing and killing cancerous cells in the tumor thereby limiting the efficacy of current chemotherapy [24]. Below, we discuss interstitial hypertension, low extracellular pH, hypoxia, angiogenesis, tumor–stromal cell interaction, cancer stem cells, and abnormal lymphatics. These key microenvironmental features of solid tumors greatly impact the extravasation of polymeric nanomedicines.

2.1. Interstitial hypertension

The interstitium is a collagen rich matrix and serves as a biological scaffold for tissues. It occupies the space between cells and tissues and is bordered by cell membranes and blood vessel walls. Within this matrix is a hydrophilic gel composed of interstitial fluid and

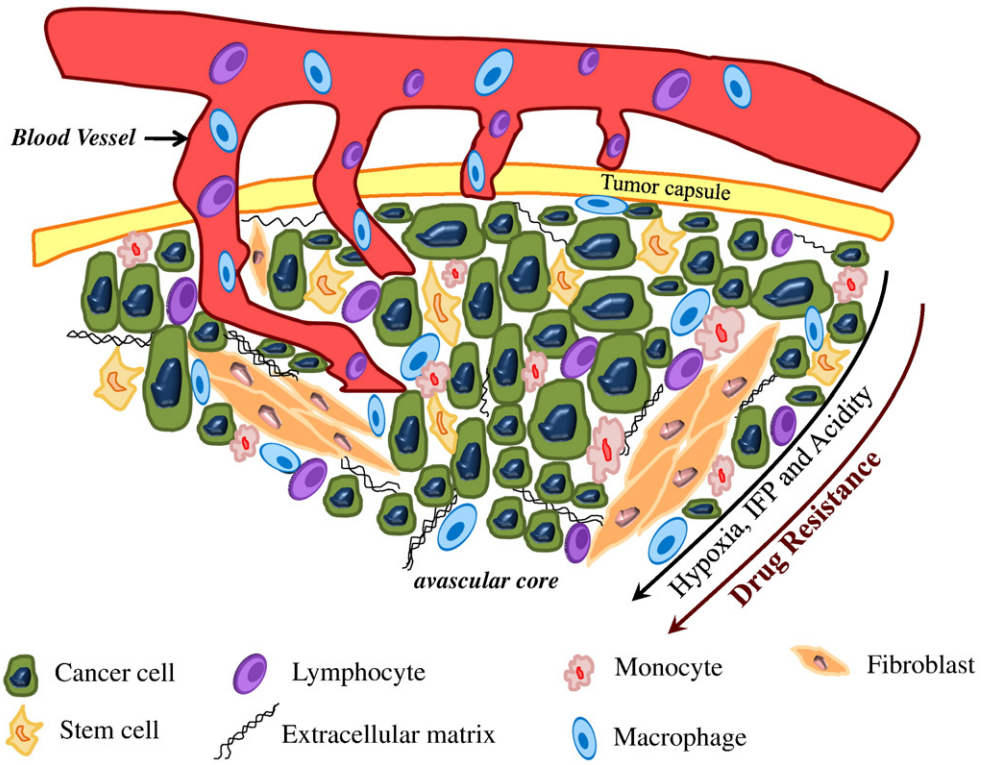

Fig. 1. Schematic portraying complex microenvironment of tumors. Cancer cells are surrounded by cancer stem cells and embedded within the stroma composed of lymphocytes, monocytes, fibroblasts, macrophages and extracellular matrix. Tumor–stroma interaction is bidirectional and may lead to tumor rejection or facilitate tumor growth. Key tumor microenvironmental features: hypoxia, interstitial fluid pressure (IFP) and acidity increase with distance from blood vessels resulting in increasing drug resistance from the tumor periphery to the avascular core.

macromolecular constituents such as proteoglycans and hyaluronate. Tumor interstitium differs greatly from that of normal tissues. Important distinctions include an interstitial space three to five times larger than that of normal tissues, high interstitial hydraulic conductivity and diffusivity, comparatively larger amounts of mobile fluid and faster spread of hydrophilic agents resulting from significant extravascular convection [25].

Leaky tumor vasculature and dysfunctional lymphatics in tumor interstitium result in undesirable accumulation of vascular contents in the tumor leading to interstitial hypertension [26,27]. Physico-chemical properties of the interstitium influence the movement of molecules between blood vessels and the cells. The interstitial pressure in normal tissues is approximately 0 mm Hg while normal capillary pressure is around 1–3 mm Hg. This pressure gradient facilitates convective transport of macromolecules from the vascular compartment to the interstitium. To the contrary, tumors display pressure gradients opposite to that of normal tissues. The presence of osmotic forces drawing solutes into tissue combined with functionally deficient tumor blood vessels and lymphatics as well as the ability of tumor stroma to contract all contribute to the higher interstitial fluid pressure within the tumor compared to blood vessels [27,28]. Several studies have shown IFP of up to 100 mm Hg in the tumor core while the periphery exhibits atmospheric like or slightly negative pressures [29–32]. Consequently, interstitial hypertension results in reduced convection across the walls of tumor blood vessels. Additionally, higher IFP in tumors favor the movement of interstitial fluid into surrounding tissues, flushing out therapeutic agents from the tumor. The combination of these two factors potentially hampers the potency of systemic therapies to tumors, especially delivery of macromolecules, since they depend on convective transvascular transport to cross the endothelial barrier and migrate through the interstitium [33].

2.2. Low extracellular pH

For several decades tumors were generally believed to be acidic since cells actively convert glucose to lactic acid [34–37]. Using techniques that specifically measure intra- or extracellular pH in malignant tumors, it has now been shown that intracellular pH in tumor cells is neutral to alkaline while the extracellular pH is acidic [38–40]. This resulting pH gradient established across tumor cell membranes is preserved by a number of ion pumps which export protons into the extracellular compartment [41]. Aside aerobic and anaerobic glycolysis, other mechanisms have also been implicated in tumor acidosis. Some of these pathogenetic mechanisms include ATP hydrolysis, glutaminolysis, ketogenesis and CO_2/carbonic acid production [42–44]. The pH gradient peculiar to tumors facilitates the accumulation of weakly acidic drugs (e.g., mitomycin C) within tumors and may be utilized as a strategy for treating cancer [45,46].

One such approach involves polymeric micelle or polymer–drug conjugate delivery systems designed to release drugs when they encounter the acidic environment in tumors. These systems are stable at neutral pH but destabilize under mild acidic conditions (pH 4.5–6.0) and facilitate release of anticancer drugs. pH sensitive drug carriers are typically designed by introducing acid labile chemical bonds between drug and carriers (Fig. 2) [47,48]. For instance, Bae and coworkers have utilized pH-sensitive polymers such as poly (l-histidine) as components in amphiphilic copolymers for micellar delivery [49–51]. Poly(l-histidine) (pK_b~7.0) has an imidazole ring with lone electron pairs associated with the unsaturated nitrogen that confer it with pH-dependent amphoteric properties. In one study, Bae et al., developed a pH-sensitive mixed micelles system using poly(l-histidine) (polyHis) (Mw 5000)-*b*-poly (ethylene glycol) (PEG) (Mw 2000) and poly(l-lactic acid) (PLLA) (Mw 3000)-*b*-PEG (Mw 2000)-folate (0–25 wt.%). At pH lower than 7.0, the poly(l-histidine) block ionized leading to a gradual disintegration of the

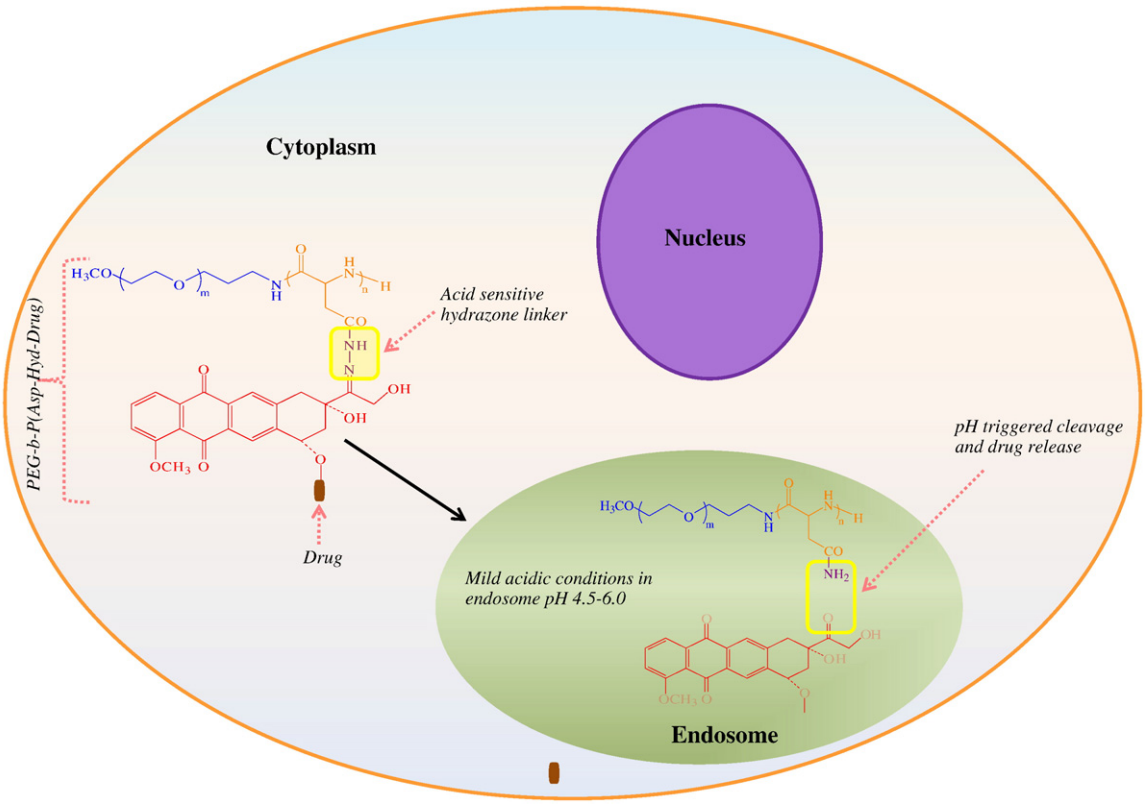

Fig. 2. Schematic depicting pH triggered cleavage and drug release of poly (ethylene glycol)-poly(aspartate-hydrazone-Drug) delivery system in acidic endosomal compartment. Modified from Bae et al., Mol. Biosys, 1: 242–250, 2005 (40).

system. When doxorubicin was incorporated, their studies showed 32 wt.% of doxorubicin (DOX) was released at pH 7.0, 70 wt.% of DOX at pH 6.8, and 82 wt.% at pH 5.0 in 24 h [49]. Furthermore, it has been demonstrated that pH-triggered micelle dissociation may enhance extravasation of subsequent micelles by creating space for the newly arriving micelles [52].

2.3. Hypoxia

From a pathophysiological standpoint, hypoxia refers to the condition in which tissues are deprived of oxygen or the partial pressures of oxygen falls below critical levels leading to hindered clinical and biological functioning of cells or organs [53]. For normal tissues, consumption of O_2 for metabolic requirements is equaled by supply. In contrast, O_2 demand far exceeds supply in tumors as they grow. High cell density caused by excessive rates of cell proliferation in tumors places a huge demand on local supply of oxygen. Furthermore, abnormal tumor vasculature (characteristic of tumors) reduces blood flow and limits delivery of oxygen throughout the tumor resulting in regions of hypoxia.

Several factors contribute to hypoxia in tumors (Fig. 3) and the different types of hypoxia are characterized accordingly. These include: inadequate perfusion (ischemic or acute hypoxia), increased diffusion distances (chronic hypoxia), anemia (anemic hypoxia) and hypoxemia (hypoxemic hypoxia). Generally, 50–60% of solid tumors display heterogeneous distribution of hypoxic regions within the tumor. However, despite the type of hypoxia, controlling oxygen consumption within tumor cells is equally important as reduced oxygen delivery in determining tumor hypoxia [54].

Hypoxic tumors facilitates activation of hypoxia inducible factor-1 (HIF-1) which has been implicated in regulating gene transcription of ATP-Binding Cassette (ABC) transporters in cancer cells and plays a key role in tumor progression [55–58]. Hence, a major consequence of tumor hypoxia is resistance to chemotherapy due to the over-expression of ATP-Binding Cassette (ABC) transporters which pump anticancer drugs out of cancer cells [59].

2.4. Angiogenesis

Tumor growth and metastasis requires the formation of new blood vessels from pre-existing vessels. This process is known as angiogenesis. Tumor microenvironment is replete with pro-angiogenic factors originating from neoplastic, stromal and infiltrating cells which affect angiogenesis. Tumor angiogenesis is characterized by an abundance of functionally defective and structurally abnormal blood vessels and occurs due to a disparity between the pro-angiogenic and anti-angiogenic factors [33,60]. A consequence of these defective vessels is an inflamed tumor environment which encourages thrombosis and impaired blood supply resulting in hindered drug delivery to the tumor. Vascular endothelial growth factor (VEGF)/vascular permeability factor (VPF) is one of the most important angiogenic factors responsible for inducing proliferation and migration of endothelial cells and increasing vascular permeability

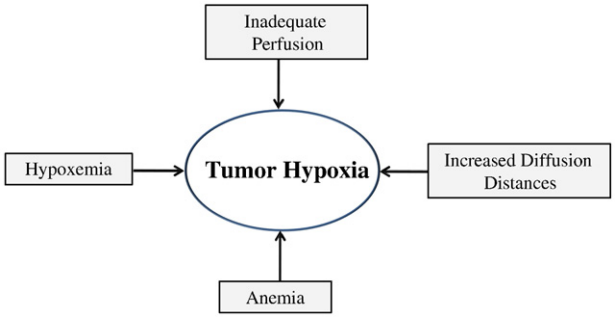

Fig. 3. Crucial factors contributing to hypoxia in tumors.

[61]. Recently, VEGF was found to negatively regulate the maturation of blood vessels and the function of pericytes [62]. Other pro-angiogenic factors such as transforming growth factor-β (TGF-β), interleukin (IL)-8 and basic fibroblast growth factor (bFGF) are produced as tumors begin to grow [63]. The key role blood vessels play in tumor growth and metastasis makes tumor angiogenesis a rational and well studied target for cancer therapy. Anti-angiogenic therapy such as blockade of VEGF can lead to normalization of tumor vasculature by restoring the balance of pro- and anti-angiogenic factors [64].

2.5. Tumor–stromal cell interaction

Tumor microenvironment consists of neoplastic cells embedded within the stroma. Major cell types of which tumor stroma is composed include fibroblasts, myofibroblasts, immune cells, pericytes, adipocytes and endothelial cells [65,66]. Several studies have shown the peculiar interaction between tumor and stroma cells and how this distinctive interplay governs growth, invasion and metastasis [67,68]. Generally, stromal cells are actively recruited by the tumor to provide blood supply through the production and secretion of cytokines and stimulatory growth factors. To understand the intricate processes involved in tumor–stroma interaction and how to exploit it, we briefly discuss unique contributions of the most abundant and well studied stromal cells: fibroblasts and immune cells.

Fibroblasts constitute a sizeable portion of tumor stroma. How these cancer associated fibroblasts (CAF) originate is still unclear. However, tumor generating parenchyma [69]; transdifferentiation of neighboring endothelial cells, pericytes and adipocytes [70] and differentiation of fibrocytes are all potential sources [71]. CAFs are functionally and phenotypically different from normal fibroblasts. In tumors, CAFs produce growth factors and matrix metalloproteinase (MMPs) which facilitate proliferation, invasion and metastasis.

A large number of immune cells (macrophages, neutrophils and lymphocytes) are also recruited to tumor locations from blood or lymphatic vessels. Tumor associated macrophages (TAM) are readily attracted to necrotic and hypoxic tumor regions where they release a number of pro-angiogenic factors including VEGF, interleukin-8 (IL-8), hepatocyte growth factor (HGF) and MMP2. Neutrophils also secrete VEGF, IL-8, HGF and MMP2 and together with TAM promote angiogenesis and facilitate tumor growth and metastasis. However, TAM may also promote tumor rejection and regression by secreting anti-angiogenic factors. These proteins are capable of producing cytotoxic molecules which directly kill tumor cells. They also kill tumor cells indirectly through induction of antitumor effects in T-lymphocytes and natural killer (NK) cells.

Considering the role stromal cells play in cancer development, they are potential therapeutic targets for tumor therapy. However, since different tumors have differing requirements for stromal support and stromal cells themselves are non-malignant, targeted therapy should be specific for their unique phenotypic signatures. Hence, a thorough understanding of interactions between different stroma cell components that either support tumor growth or tumor rejection is important since this interaction is crucial to cancer development at the primary site and metastasis.

2.6. Cancer stem cells

Like normal adult tissues, solid tumors contain a population of cells that self-renew and resupply the tumor with the various cell lineages of which it is composed of. These cells known as cancer stem cells (CSCs) are associated with tumor stromal components such as fibroblasts and blood vessels. They compose the cancer stem cell niche from which factors that support CSC renewal are released. CSCs form approximately 1% of the tumor. However, since they are the only cells that can maintain tumor growth indefinitely due to their self-renewal properties, they are the actual driving force behind tumor growth. The rest of the cells in the tumor microenvironment vigorously proliferate, differentiate and eventually die.

It is known that CSCs exhibit similar properties to normal stem cells. Among these, CSCs are hypothesized to be relatively quiescent and have protracted life span, are refractory to apoptosis and resistant to toxins and drugs since they express at least one ATP-binding cassette (ABC) efflux transporter [72–75]. Since these drug efflux pumps occur naturally in CSCs, this hypothesis offers an additional mechanism by which tumors acquire multidrug resistance. A number of studies confirm this hypothesis. Recently, Hu et al. have shown a side population of ovarian cancer cells to possess ABC transporters and be drug resistant [76]. These cancer stem-like cell side populations were found to be responsible for tumorigenesis and grew more rapidly in xenogeneic transplant mice compared to ovarian cancer cells without such side population cells. Furthermore, drug efflux transporters have also been shown to be present in leukemic stem cells making them resistant to chemotherapeutic agents such as daunorubicin [77,78]. The purported role of CSCs in tumorigenesis and metastasis suggests targeting CSCs to be a potential therapeutic strategy for chemoprevention and cancer therapy.

2.7. Abnormal lymphatics

The lymphatic network transports interstitial fluid and immune cells out of normal tissue and is essential for immune function and maintenance of fluid balance in tissue interstitium. In contrast to normal tissues, the lymph vessels in tumors are compressed by solid stresses induced by tumor cells within the microenvironment [2]. Therefore, the functional performance of lymphatic vessels within the tumor microenvironment depends on their location. Lymphatic vessels situated at the periphery of the tumor or the periphery-tumor interface possess functionality while those within the tumor are functionally defective [79,80]. Lymphangiogenesis is facilitated by the same factors responsible for angiogenesis such as VEGF, angiopoietins and platelet-derived growth factor (PDGF). For instance, lymphangiogenesis and angiogenesis can be triggered by VEGF-C and -D and have been implicated in increased lymphatic metastases in numerous tumors [81,82]. Abnormal lymphatics encourage retrograde flow in lymphatic vessels, allow tumor cells to invade the periphery of lymphatic vessels and promote metastases within the lymphatic system [83,84].

3. Anatomical pathways of macromolecular extravasation

The efficacy of blood borne therapeutic agents in cancer therapy depends on their extravasation across tumor blood vessels. Significant differences exist between the mechanism of extravasation of small molecules and macromolecules. However, the extent of extravasation in both cases is influenced by the macroscopic arrangement and wall structure of tumor microvessels. Also, the endothelial cell lining of microvessels function as a rate-limiting barrier for extravasation of plasma components. In normal tissues, transvascular transport of plasma water and small solutes (less than 2 nm) occurs through gaps between adjacent cells [85]. However, since macromolecules have comparatively larger sizes they are unable to pass through these gaps. Although microvessels are more permeable than normal vessels, it has been shown that additional anatomical pathways are responsible for movement of macromolecules across blood vessels in normal tissues and tumors [86]. Presently, the dominant channels involved in macromolecule extravasation include endothelial openings (open gaps) and vesiculovacuolar organelle mediated extravasation [87–89]. Therefore, understanding the macroscopic and microscopic arrangement of tumor vasculature and the pathways responsible for transvascular transport of macromolecules is crucial to how they can be exploited to maximize extravasation of polymeric nanomedicines and enhance drug delivery.

3.1. Macroscopic arrangement

For a tumor to grow beyond a few millimeters, new blood vessels are required to increase blood supply to meet metabolic demands of malignant and non-malignant cells. Tumor angiogenesis leads to a variety of peculiar inter- and intra-tumor vascular morphologies partly driven by growth patterns of cancer cells. Two ideal classifications of vascular macroscopic arrangement are peripheral and central vascularization [90].

In peripheral vascularized tumors, blood vessels are confined to tumor periphery which is well-vascularized compared to the avascular core. The absence of vascular volume in the core implies systemic agents extravasate poorly in the center of the tumor. Contrarily, for central vascularization, blood vessels are localized and form dendrimer like patterns in the tumor core. Typically, macroscopic arrangement of tumor vasculature represents various degrees of these categories. Regardless of the organization of microvessels in tumors, it is clear that heterogeneity in vascular distribution and low vascular volume pose serious barriers to drug delivery. Hence, approaches that facilitate vascularization of tumors may improve polymeric nanomedicine extravasation and cancer therapy.

3.2. Tumor blood vessel wall structure

Tumor blood vessels can be classified into nine categories as described by Warren [91]. These include: arteries and arterioles, non-fenestrated capillaries, fenestrated capillaries, discontinuous capillaries, blood channels without endothelial lining, capillary sprouts, post-capillary sprouts, venules and veins and arterio-venous anastomoses. Among the blood vessels, extravasation occurs primarily at the capillaries and post-capillary venules due to their thin walls and large surface area [92]. The capillary wall structure is composed of a single layer of endothelial cells surrounded by a basement membrane. Capillary walls are leaky and have a distribution of pores with diameters less than 100 nm. Depending on the frequency of pores in the endothelial layer, capillaries can be classified as non-fenestrated, fenestrated and sinusoidal [92,93].

3.2.1. Continuous capillaries

Non-fenestrated capillaries, also known as continuous capillaries, are commonly found in cardiac, skeletal and smooth muscles as well as the skin and brain. Due to the tight junctions and uninterrupted subendothelial basement membranes, transport of molecules across the continuous capillaries is negligible. Since these vessels have an intact endothelial basement membrane with pore size less than 2 nm, only small molecules can extravasate across continuous capillaries. An important difference between normal and tumor vessels is that tumor vessels are dilated and do not contain basement membrane leading to seepage of plasma oncotic contents into the interstitium. Unlike peripheral endothelium, the endothelial layer of the brain microvasculature is the tightest endothelium and has virtually no fenestrations. Therefore, extravasation of macromolecules across the brain is particularly difficult due to the presence of continuous capillaries between the blood and brain interstitium [94]. However, certain regions of the brain, such as choroids plexus and medion eminence are not part of the blood-brain barrier and are more permeable. Moreover, the microvascular permeability of other cancers which metastasize to the brain is lowered to approximately that of orthotopic brain tumors [95].

3.2.2. Fenestrated capillaries

Fenestrated capillaries possess a continuous basement membrane but have pores (fenestrae) of 40–60 nm in diameter in the endothelium which allows large molecules such as proteins to pass through [93]. Fenestrated capillaries are found in the kidney, small intestine and salivary glands. The basement membrane surrounding fenestrated capillaries reduces the extravasation of nanomedicines, whereas macromolecules or drug-polymer conjugates of less than 11 nm in diameter extravasate freely. In contrast, glomerular capillaries have fenestrae of 60–80 nm, which allow effective permeation of macromolecules or nanomedicines of less than 30 nm in diameter. Fenestrated capillaries abound in various tumors, are partly accountable for tumor vessel permeability and permit extravasation of macromolecules [96–98].

3.2.3. Discontinuous capillaries

Discontinuous or sinusoidal capillaries have fenestrations of approximately 150 nm and are common in the liver, spleen, bone marrow, lymph nodes and adrenal cortex. The basal membrane in sinusoidal capillaries is absent in the liver, but present in spleen and bone marrow. While liver sinusoids contain phagocytic kupffer cells, those of bone marrow contain phagocytic reticuloendothelial cells and the spleen contains a large number of pinocytic vesicles.

3.3. Endothelial openings

It is widely believed that the increased permeability of tumor vessels is due to the presence of endothelial openings. Evidence provided by Majno and coworkers suggested these endothelial openings to be intercellular in nature [99]. These openings occur when neighboring endothelial cells sufficiently contract to overcome cell–cell and cell–matrix adhesion forces and pull away from each other. Using scanning electron microscopy (SEM), McDonald et al. have shown that inter-endothelial openings are not simply holes in tumor vasculature. From their studies, they demonstrated inter-endothelial openings to be of two types: vertical gaps and oblique slits [100]. These pores range from 0.1 to 3 μm in diameter and have been shown to occur 100 times more frequently than trans-endothelial openings [89,100]. Hence, this has led to the long-standing assumption that inter-endothelial openings may account for abnormal leakiness of tumor vessels. Although the mechanism for pore formation and closure is still not well understood, vascular endothelial growth factor (VEGF)/vascular permeability factor (VPF) and other cytokines have been shown to induce pores in endothelium that otherwise possessed no gaps [87,101].

3.4. Vesiculo-vacuolar organelle mediated extravasation

The other competing hypothesis proposes extravasation via interconnected vesiculovacuolar organelles (VVOs). Dvorak and coworkers have demonstrated that VVOs are a major route of macromolecule extravasation at VEGF/VPF and tumor-derived cytokine augmented hyperpermeable sites [102]. VVOs are morphologically similar to bunches of grape-like clusters approximately 50 to 415 nm in diameter and are frequently deployed at intervals in the cytoplasm of endothelial cells [103–105]. In one study where macromolecular tracers (e.g., anionic ferritn) were injected intravenously in TA3/St mammary carcinoma bearing mice, these tracers were found in VVOs within seconds and the VVOs provided a transcytotic pathway for the macromolecules to extravasate from tumor blood vessels [103]. Regardless of the controversy surrounding the dominant pathway for macromolecule extravasation, the consensus is that extravasation pathways for macromolecules and nanoparticles are channel-like structures [106].

4. Extravasation across microvascular wall

Solute transport across vessel walls are either diffusion or convection controlled (Fig. 4). Diffusion is a function of vessel surface area and the driving force for this mode of transport is the concentration gradient established by plasma and interstitial concentration differences. Convection on the other hand is governed by the rate of fluid flow which in turn is determined by a pressure gradient. This pressure gradient is the difference between the resultant hydrostatic pressure (i.e., vascular minus interstitial) and the resultant osmotic pressure. The vascular permeability (P) constant relates the diffusive mass flux to the concentration gradient

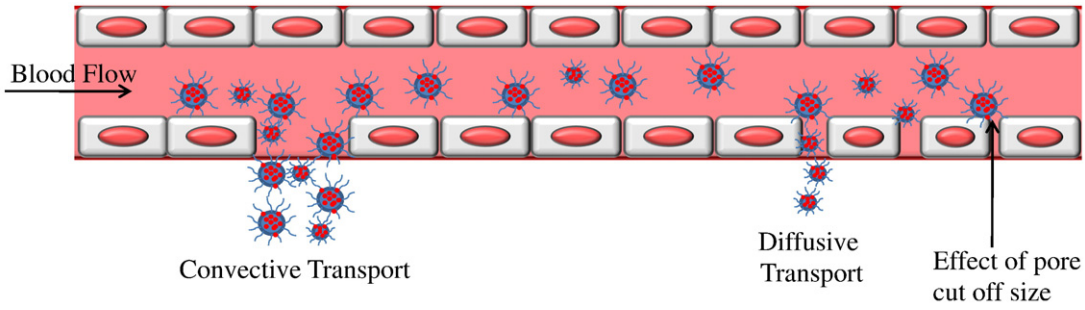

Fig. 4. Schematic representation of convective and diffusive transport of polymeric nanomedicines across microvascular wall and the effect of pore cut off size.

while the hydraulic conductivity (L_p) relates fluid flux to pressure gradients. For transport of macromolecules in normal tissue the primary mode of transport is convection, whilst that for small molecules is diffusion [107]. However, the mechanism of macromolecule extravasation in tumors is different due to high interstitial fluid pressure and leaky vasculature. Paradoxically, macromolecules generally exhibit poor extravasation in tumors although their blood vessels are leakier compared to normal tissue. Here, interstitial hypertension reduces fluid movement into the interstitium and consequently convective transport, thus overcompensating for potential enhanced extravasation which may result from the leaky vasculature. Since the pressure gradient progressively gets steeper from tumor periphery to the core, extravasation of macromolecules is superior in the tumor periphery as against the tumor core [108]. For instance, Jain and colleagues showed higher accumulation of monoclonal antibodies at the tumor-normal tissue interface [24].

5. Barriers to drug delivery across tumor capillaries

As alluded above, a number of important factors related to the pathophysiology of tumors limit optimal drug delivery. These barriers vary depending on tumor type and microenvironment. The key then in successfully utilizing polymeric nanomedicines for treating solid tumors is to overcome or exploit these obstacles. Below we highlight some important barriers which hinder drug delivery and extravasation.

5.1. Chaotic blood supply

The first barrier is the chaotic blood supply to tumors. Significant structural and functional differences exist between tumor and normal vessels. In contrast to well organized microvessels in normal tissue, tumor vessels are frequently saccular, dilated and tortuous [92,109,110]. Their distribution, density, diameter as well as blood flow rate also differ throughout the tumor. Presently, it is still not clear the relationship between the number of blood vessels in the tumor and its volume. For example, Jain and collaborators report a decrease in vascular volume while others report a constant vascular fraction over the tumor life span. Typically, tumors have a well-vascularized periphery, a seminecrotic core and an avascular necrotic central region. Hence, the extravasation of polymer therapeutics is often restricted to the tumor periphery. Polymeric nanomedicines however need to be sufficiently perfused to optimally deliver drugs to tumors. As such, attention has been given to normalizing the tumor vasculature to enhance perfusion and the consequent extravasation of polymeric nanomedicines into tumors [111,112].

5.2. Poor permeability of tumor vasculature

The next barrier is the poor permeability of tumor vasculature. Permeability of tumor blood vessels vary based on the type and location of tumors, leading to heterogeneous distribution of blood-borne therapies [19,87,113]. Hence, it is possible that tumor vessels in different locations (or in a similar microenvironment within the same tumor) display contrasting degrees of vascular leakiness. This structural feature often results in erratic interstitial drug delivery.

Blood brain barrier (BBB) consists of endothelial cells, pericytes, astrogline and macrophages and serves as a physical barrier to drug permeability to the brain. Drug permeability across BBB greatly depends on its octanol/water partition coefficient. Drugs with high octanol/water partition coefficient easily extravasate the BBB. However, some drugs with low octanol/water partition coefficient can also permeate BBB due to active or facilitated transport, while some substances with high octanol/water permeability poorly penetrate the BBB due to active transport back to the blood [114].

5.3. Limited transport across the interstitium

The third barrier relates to the ability of drug delivery systems to traverse the interstitium and selectively target and eliminate cancerous cells. Two key issues here are interstitial transport and interstitial hypertension. Size, charge, shape and physicochemical properties of the interstitium are important parameters governing interstitial transport. For example, large size hinders tissue penetration of macromolecules, while cationic liposomes have been shown to target the intravascular tumor compartment better than anionic and neutral liposomes of similar size [115,116]. Hence, studies elucidating the effects of size, charge and shape of macromolecules on their transport in a variety of tumor types and locations are important in overcoming this obstacle. Interstitial hypertension creates a pressure gradient favoring the movement of drug molecules out of the tumor into the vascular compartment [117]. This results in reduced macromolecular delivery and transport since convection is its major mode of transport [28].

5.4. Multidrug resistance

Multidrug resistance (MDR) is another important barrier limiting the success of chemotherapy and resulting in observed clinical drug resistance. MDR arises when cancer cells become insensitive and cross-resistant to cytotoxic effects of structural and functionally diverse anticancer agents targeting a range of distinct molecular targets [118]. Since MDR implies cancer cells are irresponsive to normal dosing regimen of chemotherapeutic drugs, higher doses and frequency are often required in the clinic. A major consequence of this is the detrimental side effects on otherwise healthy organs and tissues due to high dose intake of anticancer agents to obtain desired therapeutic effect. The mechanisms responsible for MDR and approaches for reversing MDR using polymeric nanomedicines are discussed below.

5.4.1. Mechanism responsible for multidrug resistance

The mechanisms underlying MDR may broadly be classified as pump or non-pump mediated [119]. Table 1 summarizes some of these mechanisms and therapeutic strategies for overcoming them. For pump mediated MDR, it has been shown that overexpression of members of the ABC transporter super-family such as p-glycoprotein (P-gp), multidrug resistance-associated proteins (MRP) and breast

Table 1
Multidrug resistance mechanisms.

Type of multidrug resistance	Mechanism	Therapeutic agents and strategies to overcome drug resistance
Pump mediated mechanism		
Enhanced cellular drug efflux	Overexpression of ATP-binding cassette transporters (e.g., P-gp, MRP,BCRP)	Polymeric nanomedicines (e.g., Pluronics); MDR reversal agents (e.g., PSC833, XR9576, Ixabepilone, SMART compounds); Combination therapy (e.g., bicalumatide and embelin)
Non-pump mediated mechanism		
Dysfunctional apoptotic pathway	Overexpression of antiapoptotic proteins (XIAP and Bcl-2)	XIAP inhibitor (e.g., embelin), Bcl-2 inhibitor (e.g., ABT-737), antisense therapy (e.g., Genasense, G3139)
	Reduced sphingolipid ceramide generation or enhanced ceramide metabolism	Ceremide generation activator (e.g., gefitinib); ceramide metabolism inhibitors (e.g., LCL204, N-oleoylethanolamine)
Drug detoxification	Overexpressed glutathione S-transferase	γ- Glutamylcysteine synthestase

P-gp, P-glycoprotein; MRP, multidrug resistance-associated protein; XIAP, X-linked inhibitor of apoptosis; SMART methoxybenzoyl-ary-thiazole. Part of this table adapted from Wong et al., Multidrug Resistance in Solid Tumor and Its Reversal, in R.I. Mahato, Y. Lu (Eds.), Pharmaceutical Perspectives of Cancer Therapeutics, Springer, New York, 2009, pp. 121–148.

cancer resistance protein (BCRP) are responsible for increased cellular drug efflux [120–122]. These transporters compromise potency of chemotherapy when they reduce drug concentration within the cell after pumping penetrated anticancer drugs out of the cells cytoplasm. To date, P-gp is the most well studied and characterized ABC transporter. It is a 170-kDa ATP-dependent glycoprotein capable of transporting a wide range of structurally and functionally different therapeutic moieties and hence causes cross-resistance to a host of drugs. Some P-gp substrates include taxanes (docetaxel, paclitaxel) and anthracyclines (doxorubicin, epirubicin) [123]. In contrast to P-gp, multiple MRP (MRP-1 to MRP-8) members are responsible for drug resistance in cancer with each member being highly specific for a particular substrate. Although BCRP was originally identified in breast cancer, it has been shown to be present in other normal tissues such as the colon [124]. However, BCRP is overexpressed in tumors and is highly resistant to mitoxantrone [125]. A key question is how ABC transporter MDR phenotype is conferred in solid tumors. In the case of P-gp, MDR phenotype has been shown to be native or acquired. For example, it is intrinsically expressed in epithelial cells of kidney, liver and pancreas and higher basal expression is observed in cancers related to these organs [123]. P-gp MDR phenotype may also be acquired after short exposure to high doses or prolonged exposure to sub-therapeutic levels of anticancer agents.

Although overexpression of ABC transporters may be considered the primary cause of MDR, other non-pump mediated mechanisms prevent cancer cell death and lead to drug resistance. Most of these mechanisms result in reduced drug activity due to dysfunctional molecular pathways. For example, a defect in the apoptotic machinery leading to overexpression of antiapoptotic proteins (e.g., BCl-2, XIAP) does not prevent intracellular drug accumulation but rather simply prevents cells from undergoing programmed cell death. Also, Minko and coworkers have shown that doxorubicin treated cancer cells resulted in overexpression of glutathione-S and UDP transferases [126]. These two proteins detoxify drugs and reduce drug efficacy in tumors. Additionally, the structural complexity of solid tumors poses multiple pharmacokinetic and pharmacodynamic barriers which lead to drug resistance. Some examples include the loss of drug activity in the acidic tumor microenvironment due to the deactivation and acquisition of drug resistance mechanisms in cancer cells located in hypoxic regions of tumors.

5.4.2. Reversing multidrug resistance using polymeric nanomedicines

Polymeric nanomedicines are well suited for overcoming MDR in a number of ways. First, the delivery vehicles themselves can hinder the proper functioning of ABC transporters [127]. Recently, it has been hypothesized that block-copolymers such as pluronics may disturb the configuration of the lipid bilayer anchoring ABC transporters and consequently hinders their ability to pump drugs out of the cell [128,129]. In addition, it has been suggested that pluronics decrease enzymatic activity of glutathione/glutathione *S*-transferase (GSH/GST) and hence decrease drug detoxification by these enzymes [130]. Furthermore, pluronics tilt the balance of the apoptotic machinery in favor of pro-apoptotic signaling by reducing mitochondrial membrane potential of MDR cells and facilitating cytochrome *C* release [131]. Experimental evidence demonstrates the validity of these hypotheses. Recently, Batrakova et al., have shown that pluronics P85 can enhance accumulation of P-gp substrates in tumors and promote apoptosis in preclinical mice models bearing leukemia and Lewis lung MDR tumors [132]. In another study, ε-caprolactone modified poloxomer 188 nanoparticles containing paclitaxel increased uptake in MCF-7 paclitaxel resistant human breast cancer cell lines [133].

Second, MDR reversal agents may be encapsulated in polymeric nanomedicines to facilitate drug delivery and overcome MDR. Since most MDR reversal agents are lipophilic and have other unfavorable physicochemical properties, they can be more selectively and efficiently administered to target sites using lipophilic-based polymeric vehicles thereby improving efficacy. In a recent study, D-α-tocopheryl polyethylene glycol 1000 succinate (TPGS, a known P-gp modulator)-poly lactide (PLA) nanoparticles was used to efficiently encapsulate and deliver doxorubicin to drug resistant breast cancer cells (MCF-7/ADR). This system resulted in increased inhibition of P-gp activity, cell proliferation and enhanced intracellular drug accumulation and nuclear localization [134]. We have also used PEG-PLA copolymer to significantly increase the solubility of a novel microtubule destabilizer substituted methoxybenzoyl-ary-thiazole (SMART-100) (Fig. 5A) highly potent in a broad-spectrum of cancer cell types by up to 100,000 fold and an excellent inhibitor of P-gp activity [135,136]. In addition, our studies revealed that while paclitaxel was effective in inhibiting the proliferation of DU-145 (IC_{50} < 50 nM), its efficacy was severely diminished in DU-145-TXR (drug resistant prostate cancer cells with high P-gp activity), killing approximately 20% of cells at 1 μM (Fig. 5B). In contrast, SMART-100 was observed to be highly potent regardless of P-gp status with IC_{50} of 70 nM in both DU-145 and DU-145-TXR cells (Fig. 5C).

Finally, combination therapy using multiple anticancer drugs is a promising approach to overcome drug resistance. This strategy appears to outsmart cancer cells since it becomes difficult for them to simultaneously develop multiple resistance mechanisms to counteract treatment. We have shown that combining bicalutamide (non-steroidal antiandrogen) and embelin (XIAP inhibitor) (Fig. 6A) leads to synergistic anticancer effects in hormone refractory human prostate cancer cells (C4-2) [12]. Our strategy involved concurrently targeting the androgen receptor and XIAP signaling pathways (Fig. 6B) both of which are pivotal to the progression and metastasis of prostate cancer. We found anticancer effect to be schedule dependent with simultaneous treatment being more efficacious than sequential administration (Fig. 6C). Polymeric nanomedicines can be used to enhance the efficacy of combination therapy in vivo as we demonstrated using PEG-PLA micelles. It has also been shown that

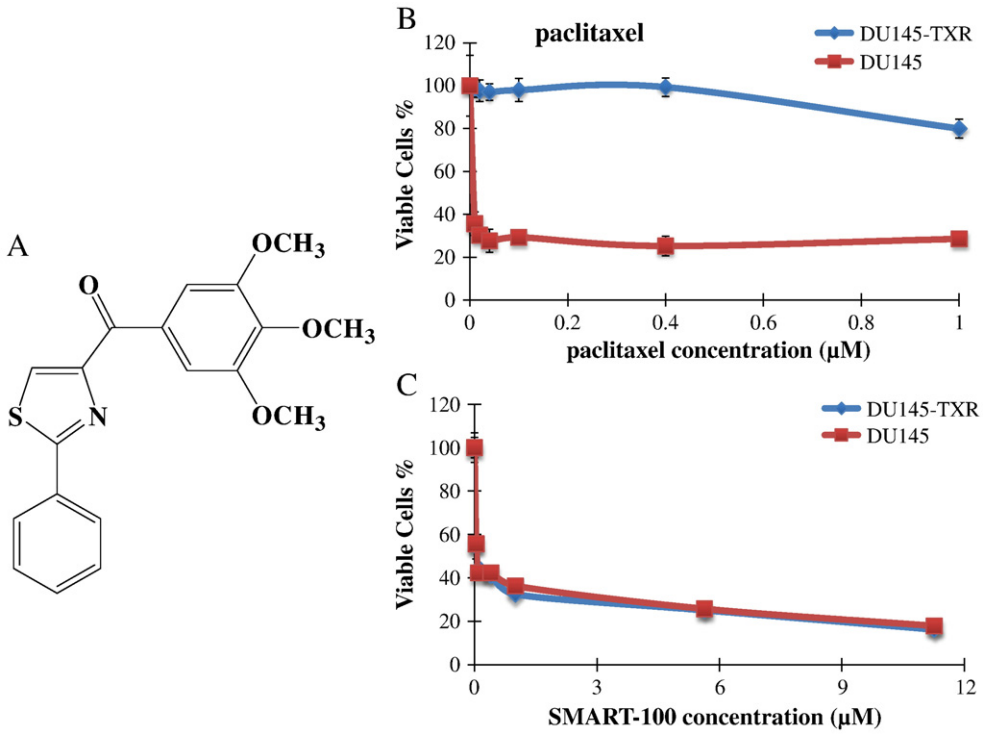

Fig. 5. Chemical structure of SMART-100 (A). Anticancer effect of SMART-100 on DU-145 and DU145-TXR cells growth by paclitaxel (B) and SMART-100 (C). SMART-100 is highly potent regardless of MDR status. Reproduced with permission from Li et al., J. Control. Release, 143: 151–158, 2010.

polymer–lipid hybrid nanoparticles (PLN) used to administer doxorubicin and mitomycin-C inhibited colony-forming potential in drug resistant breast cancer cells [137].

5.5. Inappropriate animal models

While several animal models are presently used in studying drug delivery systems in cancer, these models are typically xenografts generated by injecting a variety of cell lines subcutaneously. Although adequate for proof of concept studies, the tumor microenvironment in xenografts is distinctly different from that in human tumors and does not truly reflect what pertains in humans. Orthotopic models are more appropriate since tumors are established in the organ of interest and can result in metastatic disease. However, these models often require invasive procedures and are difficult to establish (e.g., injecting tumor cells into the prostate of mouse models). Additionally, tumor growth and metastasis in orthotopic models cannot typically be visualized with the naked eye. However, orthotopic tumor growth can now be monitored using current technologies such as bioluminescence and microultrasound.

6. Strategies for enhanced extravasation

To improve the therapeutic potential of polymeric nanomedicines, they should be designed to bypass at least one of the physiological barriers described above. To date, approaches taken to overcome these barriers have relied on either targeting the tumor vasculature, lowering interstitial hypertension or increasing aqueous solubility of potent anticancer drugs. A few of these strategies are highlighted below.

6.1. Targeting the tumor vasculature

Tumor blood vessels are excellent therapeutic targets due to their peculiar features which distinguish them from normal blood vessels. Furthermore, they lack the genetic stability which facilitates the development of drug resistance in cancer cells.

Extravasation of polymeric nanomedicines can be improved by radiation, which is known to further increase the permeability of the tumor vessels. This can be done using an external source or radioisotope targeted macromolecules. To date, tremendous effort has been channeled using this approach to investigate the effects of radiation on tumor blood flow and vascular volume. Typically, scientists have reported on the extent of macromolecule extravasation in one hour or the effects of radiation on the time course of tissue uptake. Potchen and coworkers [138] determined tissue pharmacokinetics of albumin in Gardener lymphosarcoma tumors, skin, muscle and plasma in C3H mice 48 h after radiation (3000 R; single dose). The tissue to plasma ratio increased by ~200%, 80% and 70% in tumor, muscle and skin, respectively 48 h after albumin injection. The authors also observed no significant increase in tumor vascular volume (using labeled RBCs). From these results, they surmised that radiation resulted in an increase in vascular permeability in tumors.

Hyperthermia can also boost tumor blood vessel permeability and lead to enhanced drug delivery which could possibly translate into better efficacy [139–142]. To date, elevated temperatures have been shown to increase the permeability of tumor vessels to ferretin [143], Evans blue dye [144], antibodies [145–147], and liposomes [139,148]. Recently Kong et al. showed mild heating of tumors to confer the most benefit for nanoparticle based drug delivery [148]. Several scientists have tried to elucidate the mechanism by which hyperthermia affects vascular permeability. For example, Wilhelm and Mason [149] explained the observed thermal induced increase in vascular permeability to be due to the liberation of endogeneous vasoactive agents such as bradykinin, histamine, and serotonin.

Another approach to targeting tumor vasculature involves coupling chemotherapeutic drugs to ligands (antibodies, peptides and proteins) that bind specifically to markers such as aminopeptidase-N, $\alpha v\beta 3$ and $\alpha v\beta 5$ overexpressed on tumor vasculature [150]. For example, pro-apoptotic peptides and tumor necrosis factor-α coupled to peptides

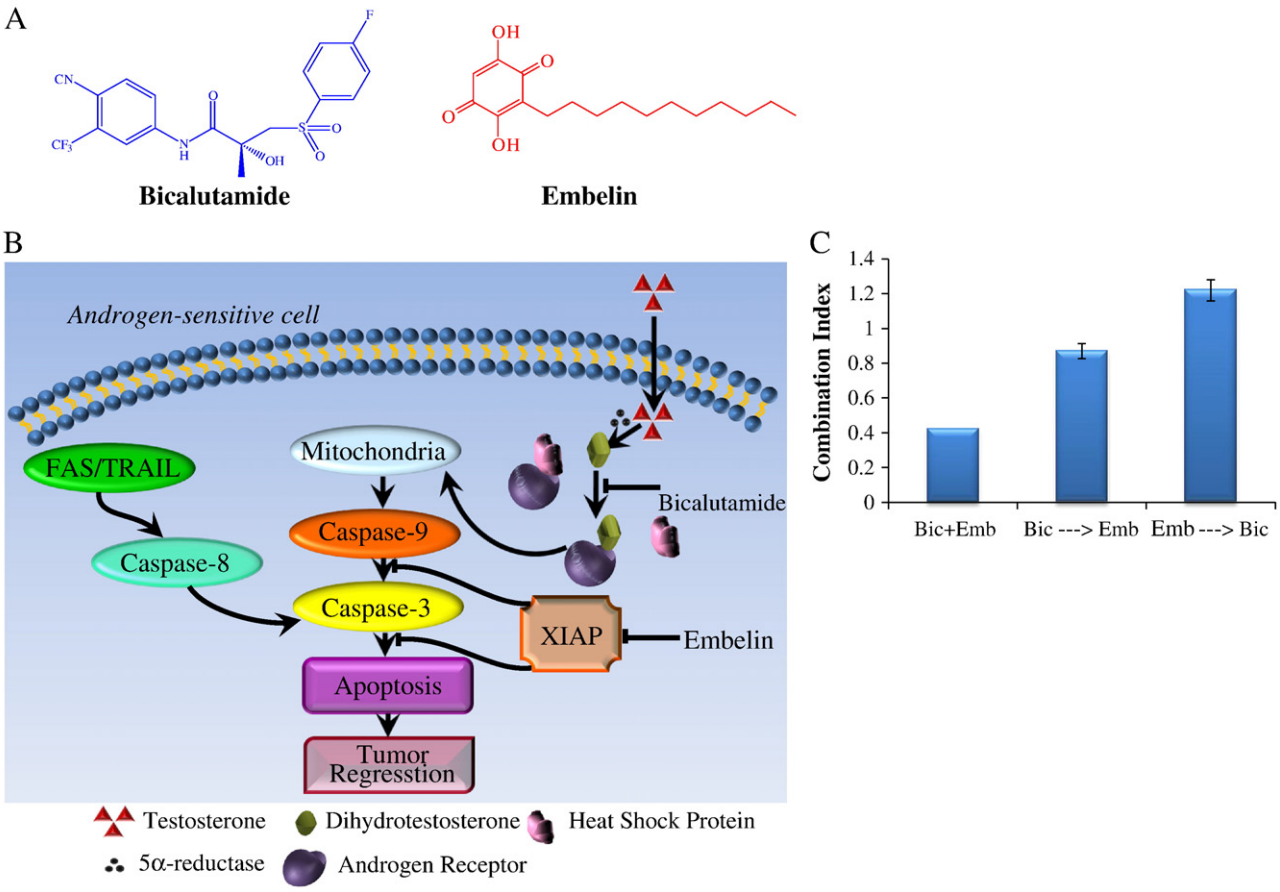

Fig. 6. Chemical structures of bicalutamide (Bic) and embelin (Emb) (A). Schematic diagram showing the combined effect of bicalutamide and embelin on apoptosis in androgen-sensitive cells and on tumor regression (B) and Combination Index (CI) of simultaneous and sequential treatment of bicalutamide and embelin in C4–2 cells (C). 5×10^3 cells were simultaneously treated with a combination of bicalutamide and embelin or sequentially [(bicalutamide followed by embelin) or (embelin followed by bicalutamide)]. Combination index (CI) was calculated by the formula: $CI=(d1/D_{50}1)+(d2/D_{50}2)$, where $D_{50}1$ is the dose of bicalutamide required to produce 50% effect alone, and d1 is the dose of bicalutamide required to produce the same 50% effect in combination with d2. $D_{50}2$ is similarly the dose of embelin required to produce 50% effect alone, and d2 is the dose of embelin required to produce the same 50% effect in combination with d1. 10 μM bicalutamide was combined with 0, 5, 10, 25 and 50 μM embelin. The CI values are interpreted as follows: <1.0, synergism; 1.0, additive; and >1.0, antagonism. Reproduced with permission from Danquah et al., Pharm Res, 26: 2081–2092, 2009.

targeting the above-mentioned such markers have been shown to reduce tumor growth in vivo [150–152].

6.2. Lowering tumor interstitial hypertension

Since interstitial hypertension correlates with inefficient extravasation of macromolecules it is an attractive target for improving transvascular transport. One way this may be achieved is by using drugs designed to increase systemic blood pressure or reduce contractility of extracellular matrix [27,153]. Currently, the use of VEGF inhibitors such as bevacizumab or anti-VEGF antibody is a popular approach that has proved potent in animals and patients [154]. VEGF is overexpressed in tumors and known to account for leakiness in tumor vasculature [155]. In one study, a monoclonal antibody against VEGF was used to treat mice bearing subcutaneous human glioblastoma tumors and it was found to reduce tumor IFP by more than 70% [156]. Tong and coworkers recently showed decreased interstitial hypertension caused by targeting VEGF to result in pressure gradients favoring extravasation and hence improving drug penetration in tumors [111]. Similar results have been demonstrated in clinical studies where decreased IFP was observed in patients with rectal carcinomas upon treatment with bevacizumab and when combined with 5-fluorouracil and leucovorin significantly improved patient survival [157,158]. The enhanced therapeutic effect of VEGF inhibitors is considered to occur via normalization of tumor vessels resulting in reduced vascular permeability and consequently decreased IFP in tumors.

Tumor IFP can also be lowered using platelet-derived growth factor (PDGF) antagonists. Unlike VEGF inhibitors, PDGF antagonists target the interaction between stromal fibroblast and the extracellular matrix. Imatinib is a selective small-molecule PDGF receptor inhibitor which has been shown to lower IFP [159] and increase delivery and potency of taxol, 5-fluorouracil [160] and epthilone B [161] when used in combination. PDGF specific DNA aptamers have also been found to lower IFP in mice bearing KAT-4 thyroid carcinoma [160].

Transforming growth factor-β (TGF-β) receptors antagonists have been found to lower interstitial hypertension by decreasing the amount of extracellular-matrix molecules [162] and also through normalization of tumor vessels [163]. Lammerts and coworkers [162] observed that blockade of TGF-β resulted in a dose-dependent decrease of IFP in mice bearing KAT-4 thyroid carcinoma. Interestingly, this effect was seen 5–10 days after administration of the TGF-β inhibitor, suggesting that a reorganization of the tumor tissue was necessary to observe the effect. Furthermore, one study showed that the combination of a prostaglandin E1 and 5-fluorouracil resulted in enhanced therapeutic effect in rodent tumors by reducing IFP [164].

Finally, administration of anti-inflammatory and chemotherapy agents has been shown to lower IFP in tumors. For instance, dexamethasone was observed to lower IFP in xenograft human colon

carcinoma LSI74T tumors. It was suggested that dexamethasone decreased the matrix molecule content and reduced the permeability of tumor blood vessels. Recently, paclitaxel was shown to reduce compression of tumor vessels leading to lower IFP in preclinical studies [165]. Taghian et al. [166] also showed in their experiments that breast cancer patients treated with paclitaxel displayed a lowering of interstitial hypertension. In contrast, treatment with doxorubicin did not reduce IFP. Consequently, combination therapy utilizing paclitaxel in conjunction with other target specific chemotherapy drugs can improve therapeutic outcome in cancer patients.

6.3. Increasing aqueous solubility of potent anticancer drugs

As mentioned previously, low aqueous solubility of potent anticancer drugs is a major impediment to their delivery and efficacy. Nanomedicines are capable of increasing the aqueous solubility of lipophilic drugs and offer a number of important advantages over traditional solubilizing agents such as DMSO. First, they are less toxic than their traditional counterparts and consequently prevent adverse effects on healthy tissues. These adverse effects often result in termination of therapy or at best limit use to sub therapeutic doses.

Second, nanomedicines can be actively targeted to make them site-specific. The need for tumor targeting depends on the site and type of tumor. For some tumors, passive targeting is sufficient to allow delivery systems to ferry their cargo drug to tumors. By enhanced permeability and retention effect (EPR) such delivery platforms are able to provide adequate quantities of drug to obtain therapeutic effect. However, in some cases where drug potency and loading is low, passive targeting alone may lead to adverse effects on visceral organs before therapeutic levels can be obtained in tumors. Addition of targeting ligands to delivery systems (active targeting) is advantageous in lowering toxicity to healthy organs, reducing the amount of drug required for therapeutic effect and bypassing multidrug resistance. While active targeting is good, the complexity of such systems presents an additional layer of difficulty in product development and in obtaining approval from regulatory agencies since approval is needed for each step. However, it is anticipated that the steps involved in developing targeted delivery systems will be significantly simplified and the processes involved obtaining regulatory approval streamlined in the future.

Nanomedicines may be lipid-based (e.g., liposomes) or polymer-based (e.g. polymeric micelles, polymer–drug conjugates) and can broadly be classified as particulate carriers and bioconjugates. While liposomes are a mature drug delivery system, we will not address this technology since it is beyond the scope of this manuscript. Interested readers are referred to the following excellent review on liposomes [9]. Below, we briefly discuss polymer–drug conjugates and focus on polymeric micelles which are classic examples of bioconjugate carriers and particulates respectively.

6.3.1. Polymer–drug conjugates

Polymer–drug conjugates are drug delivery systems composed of a drug chemically bound to a polymeric carrier by a biodegradable covalent bond. The attachment of drug to polymeric carrier can result in several important advantages compared to free drug which can potentially facilitate extravasation and cancer therapy. These include: (i) enhanced drug solubility, (ii) longer circulation times and consequent passive targeting [167], (iii) reduced toxicity [168], (iv) ability to bypass drug resistance [169] and (v) ability to be actively targeted [170]. However, to achieve such benefits, special attention should be given to a number of features required for effective design. For example, the polymer must be non-toxic and capable of decent drug loading to potency ratio. Also, the polymer–drug system should be stable whilst in transit to the tumor site but be able to release the drug in a desired manner once it reaches the tumor. To date several polymer–drug conjugates are in clinical trials [171,172]. Most of these systems are designed for one drug moiety. However, polymer–drug conjugates for combination therapy are presently being actively designed to treat cancer [13].

6.3.2. Polymeric micelles

Polymeric micelles are nanosized self-assembled supramolecular core-shell spherical structures typically fabricated from amphiphilic di- or tri-block copolymers. The core is composed of the hydrophobic portion of the copolymer and is capable of solubilizing a considerable amount of highly water insoluble drugs. In contrast, the hydrophilic component of the copolymer forms the shell (corona) which provides steric stabilization. The corona also provides stealth properties which prevent recognition by the reticuloendothelial system (RES) and therefore minimize the elimination of the micelles from the bloodstream [173]. These so called 'stealth' properties of the PEO shell result in increased blood circulation times and prevention of plasma protein binding [174].

In addition, the small size ensures preferential accumulation in tumor cells via the enhanced permeability and retention (EPR) effect [167,175]. In solid tumors, particulate carriers which typically would be excluded from normal tissues, extravasate and lodge in tissue intrastitium due to increase in permeability of tissue vasculature [89]. While several preclinical studies on EPR abound, there appears to be very little literature directly examining its existence in humans. The best examples of EPR in a clinical setting include a study of SMANCS ([polystyrene-co-maleic acid-half-butylate] copolymer conjugated with neocarzinostatin) by Maeda and coworkers [176]. When SMANCS was administered via the hepatic artery for treating hepatoma or the renal artery for treating renal tumor, drug concentration in tumor compared to plasma was observed to be more than 2000-fold higher and drug remained in the tumor for several weeks. This work led to the discovery of EPR. Another clinical example of the EPR effect is the study by Harrington et al., in which ^{111}In-diethylenetriaminepentaacetic (DTPA)-labeled PEG liposome showed preferential tumor accumulation [177]. These studies strongly suggest the existence of EPR in humans and provide an impetus to develop polymeric nanomedicines which exploit EPR for enhanced cancer treatment.

6.3.2.1. Physics of drug encapsulation. Polymeric micelles can enhance drug solubility by physical entrapment (encapsulation) or chemical conjugation. Chemical conjugation is not suitable for all drugs since some therapeutic agents do not have functional groups necessary for conjugation and cannot be modified without altering pharmacologic effect. In contrast, physical entrapment is suitable for a wide range of drugs. However, the extent of drug encapsulation depends on the compatibility between drug and core-forming block of micelle [178,179] and core-forming block length [180,181]. The effect of these parameters is measured in terms of drug loading density (ratio of weight of encapsulated drug to weight of micelle) and drug loading efficiency (ratio of weight of encapsulated drug to weight of drug initially fed). High drug loading density and encapsulation efficiency are desirable to facilitate clinical translation of micelles since this translates into smaller amount of polymer and processing cost.

6.3.2.1.1. Compatibility between drug-core forming block. Improvement in the extent of compatibility between a drug and the core forming block of the micelle may translate into superior encapsulation efficiency [182–185]. Polymer/drug compatibility may be characterized by Flory–Huggins interaction parameter (χ_{FH}) which accounts for the forces of interaction between the polymer and the drug. The low χ_{FH} values suggest that the polymer is thermodynamically a good solvent for the drug. Flory–Huggins interaction parameter (χ_{FH}) which characterizes polymer–drug compatibility is calculated using Eqs. (1) and (2):

$$\Delta = \left[\left(\delta_d - \delta_p\right)^2_{polarity} + \left(\delta_d - \delta_p\right)^2_{dispersion} + \left(\delta_d - \delta_p\right)^2_{hydrogen} \right]^{\frac{1}{2}} \quad (1)$$

$$\chi_{FH} = \frac{\Delta^2 V_d}{RT} \quad (2)$$

here Δ^2 is the solubility difference between the drug (d) and the core of the polymeric micelle (p). V_d is the molar volume of the drug, T is the temperature in Kelvin and R is the gas constant. $(\delta_x)_d$, $(\delta_x)_p$ and $(\delta_x)_h$ are Hansen partial solubility parameters for the drug and the hydrophobic block of the block copolymer.

To design a micelle system with improved drug loading, it is prudent to first perform an *in silico* study to assess the Flory–Huggins interaction parameter (χ_{FH}) between drug and the block copolymers. As χ_{FH} approaches zero, compatibility between the polymer and the drug progressively increases since the polymer increasingly becomes a better thermodynamic solvent for the drug, resulting in improved drug solubilization.

Our group and others have explored the possibility of predicting drug solubilization in micelles based on thermodynamics and found our predictions to closely approximate experimental results [183,186–190]. For example, we recently utilized this approach to match two anticancer drugs: bicalutamide and embelin with novel block copolymers. In one study, 5-methyl-5-benzyloxycarbonyl-1,3-dioxane-2-one (carbonate monomer) was introduced into the poly (ethylene glycol)-b-poly (L-Lactide) (PEG-b-PLLA) copolymer backbone to form poly (ethylene glycol)-b-poly (carbonate-co-lactide) (PEG-b-(CB-co-LA)) copolymer. The chemical structure and molecular model of (PEG-b-(CB-co-LA)) copolymer are shown in (Fig. 7A and B). Our predictions based on χ_{FH} values of PEG-b-(CB-co-LA) and PEG-b-PLLA copolymers indicated PEG-b-(CB-co-LA) to be a better thermodynamic solvent for bicalutamide due to its lower χ_{FH} value. Experimental evidence confirmed this prediction since PEG-b-(CB-co-LA) increased drug loading of bicalutamide by up to four-fold and improved thermodynamic solubility by 10 fold. It is noteworthy that both drug loading and thermodynamic stability were carbonate content dependent.

Using a dodecanol lipid grafted onto a poly (ethylene glycol)-b-poly carbonate (PEG-b-PBC) copolymer, we were able to increase loading efficiency of embelin from 40% for PEG-b-PBC to 100% for poly(ethylene glycol)-*block*-poly(2-methyl-2-carboxyl-propylene carbonate-graft-dodecanol) (PEG-PCD) lipopolymer at 5% theoretical loading (Fig. 8A and C). This observed increase in drug loading is partly due to structural similarity between embelin and the lipid modified hydrophobic core of PEG-PCD copolymer. Furthermore, it has been shown that polymer–drug compatibility heavily depends on the three-dimensional arrangement and conformation of the different moieties composing the structure of polymer and drug. Mahmud and coworkers have also reported similar results for increasing loading of cucurbitacin I by attaching cholesterol to the poly (caprolactone) of poly(ethylene glycol)-*b*-poly(caprolactone) copolymer. Although the underlying assumptions governing χ_{FH} are not entirely applicable to micelles, the trend of its value still provides good indication of drug-core compatibility and can be a logical justification to match a drug to a specific polymer or tailor a new one for it.

Another important feature of PEG-PCD lipopolymer is its potential to enhance both thermodynamic and kinetic stability. When compared to conventional PEG–lipid conjugates, PEG–PCD lipopolymer carries multiple dodecanol lipid chains grafted onto the polycarbonate backbone (Fig. 8B). Hence, PEG–PCD lipopolymer is capable of forming physical entanglement based cross-linked structures which can enhance hydrophobic interaction in the hydrophobic core. Our studies show PEG–PCD lipopolymer to have a lower CMC value (~10^{-8} M) compared to traditional PEG–lipid conjugates and is expected to demonstrate better in vivo stability.

6.3.2.1.2. Length of core forming block. The length of the hydrophobic core is an important factor which determines the cargo space available for a drug. For a constant hydrophilic block length, an increase in hydrophobic core length typically results in higher drug loading density [191,192]. This is made possible partly due to a reduction in the pressure-volume work needed to put a drug molecule into the micelle resulting from a larger hydrophobic cargo space. For instance, we have shown that increasing PCD block molecular weights

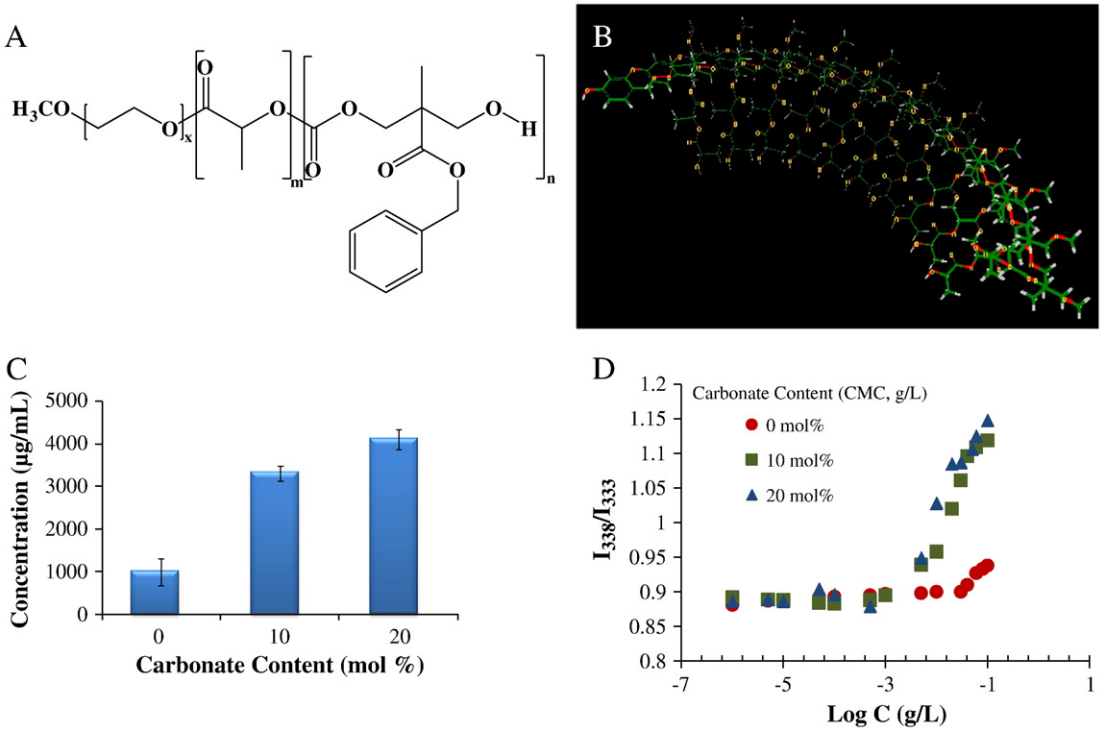

Fig. 7. Chemical structure of poly (ethylene glycol)-b-poly (carbonate-co-lactide) (A). Molecular modeling of PEG-b-P(CB-co-LA) block copolymer; molecular modeling was performed using Molecular Pro Software (B). Effect of carbonate content on bicalutamide loading. Reproduced with permission from Danquah et al., Biomaterials, 31: 2358–2370, 2010.

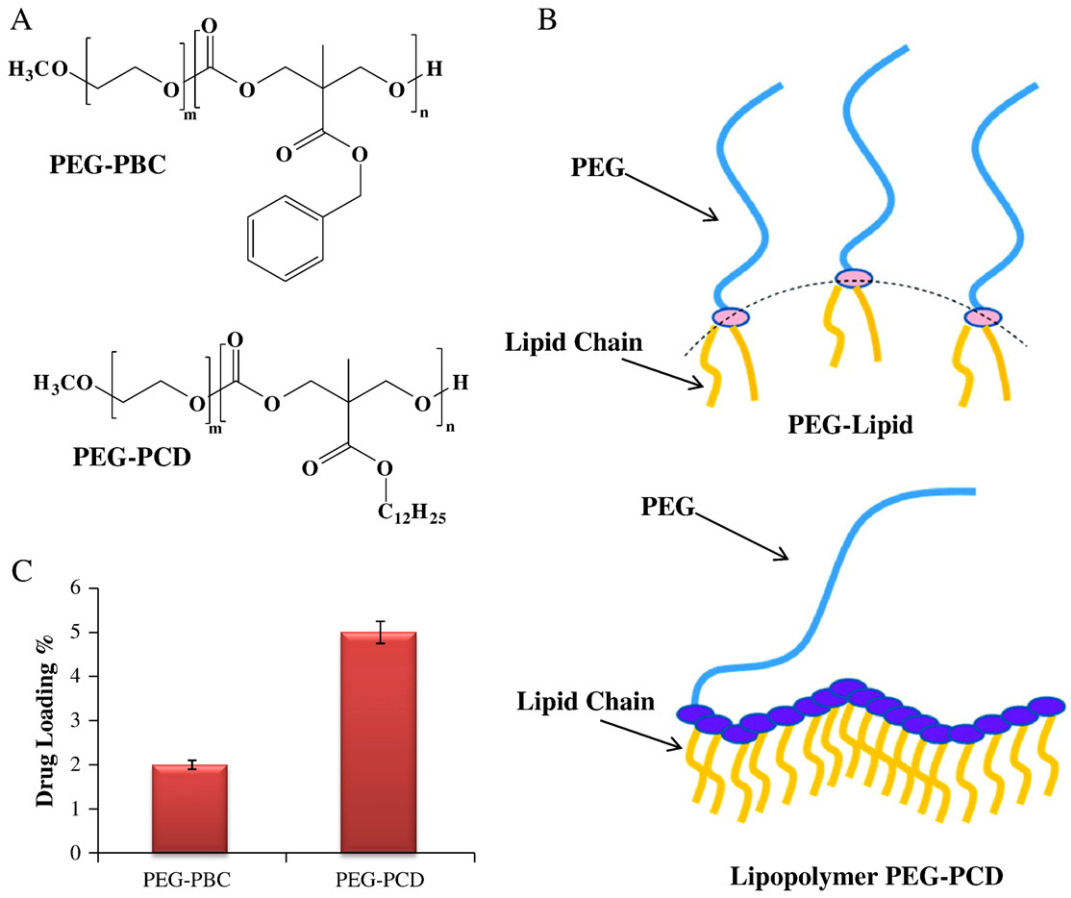

Fig. 8. Chemical structure of poly (ethylene glycol)-b-poly (carbonate) (PEG-PBC) and poly(ethylene glycol)-*block*-poly(2-methyl-2-carboxyl-propylene carbonate-graft-dodecanol) (PEG-PCD) (A). Schematic of architectural structure of PEG-lipid and PEG-PCD lipolymer (B) and effect of dodecanol grafted carbonate hydrophobic core on embelin loading (C). Reproduced with permission from Li et al., Biomacromolecules, 11: 2610–2620, 2010.

of 1.5 k, 4 k and 7.25 k of PEG-b-PCD copolymer correspondingly increased micelle size from 25 nm to 42.6 to 129 nm, respectively.

7. Conclusions and future perspectives

The potency of an anticancer drug in eradicating tumors depends on its effective dose and mechanism of action. Drug release rates of a given drug delivery system can severely impact its therapeutic effects. The drug is usually inactive while associated with the carrier and failure to release the drug from the carrier in a timely manner may result in a reduced therapeutic effect relative to free drug. In contrast, rapid release of the drug from the carrier may result in therapeutic effects that are similar to those seen for administration of the free drug [4]. Once polymeric nanomedicines enter the tumor, ideally, there should be an initial burst release to attain therapeutic levels for therapeutic effect. Once this has been achieved, there should be a subsequent sustained release to maintain therapeutic levels and efficacy.

Experimental evidence suggests that the barrier posed by tumor vasculature can potentially be overcome thereby enhancing the extravasation of polymeric nanomedicines to tumors. With advances made in targeting tumor blood vessels and lowering IFP, research focus should be placed on elucidating mechanisms responsible for barrier formation. Future studies should also be centered on "tailor-made" polymeric carriers highly efficient and effective in circumventing these barriers to chemotherapy. In particular, thought should be given to site-specific multicompartment polymeric nanomedicines. Such systems will be composed of high binding affinity ligands specific for overexpressed proteins in tumor blood vessels and possess at the minimum a bicompartmental core containing agents capable of lowering IFP or altering tumor vasculature as well as potent anticancer agents. Time invested in refining the components of these systems will result in design rules which will facilitate customization of polymeric nanomedicines with phenomenal extravasation for various cancers. Finally, another key challenge which needs to be addressed is improving drug delivery to the avascular core. Logical steps will be to find ways that can re-establish the vascular network in the core of the tumor and improve extravasation at these sites.

Acknowledgements

This work is supported by an Idea Award (W81XWH-10-1-0969) from the Department of Defense Prostate Cancer Research Program.

References

[1] R.K. Jain, T. Stylianopoulos, Delivering nanomedicine to solid tumors, Nat. Rev. Clin. Oncol. 7 (2010) 653–664.
[2] T.P. Padera, B.R. Stoll, J.B. Tooredman, D. Capen, E. di Tomaso, R.K. Jain, Pathology: cancer cells compress intratumour vessels, Nature 427 (2004) 695.
[3] R.K. Jain, Delivery of molecular and cellular medicine to solid tumors, Adv. Drug Deliv. Rev. 46 (2001) 149–168.
[4] T.M. Allen, P.R. Cullis, Drug delivery systems: entering the mainstream, Science 303 (2004) 1818–1822.
[5] R.T. Liggins, H.M. Burt, Polyether-polyester diblock copolymers for the preparation of paclitaxel loaded polymeric micelle formulations, Adv. Drug Deliv. Rev. 54 (2002) 191–202.
[6] W. Du, L. Hong, T. Yao, X. Yang, Q. He, B. Yang, Y. Hu, Synthesis and evaluation of water-soluble docetaxel prodrugs-docetaxel esters of malic acid, Bioorg. Med. Chem. 15 (2007) 6323–6330.
[7] D.R. Luke, B.L. Kasiske, G.R. Matzke, W.M. Awni, W.F. Keane, Effects of cyclosporine on the isolated perfused rat kidney, Transplantation 43 (1987) 795–799.

[8] N. Onetto, R. Canetta, B. Winograd, R. Catane, M. Dougan, J. Grechko, J. Burroughs, M. Rozencweig, Overview of Taxol safety, J. Natl Cancer Inst. Monogr. (1993) 131–139.
[9] V.P. Torchilin, Recent advances with liposomes as pharmaceutical carriers, Nat. Rev. Drug Discov. 4 (2005) 145–160.
[10] K. Kataoka, A. Harada, Y. Nagasaki, Block copolymer micelles for drug delivery: design, characterization and biological significance, Adv. Drug Deliv. Rev. 47 (2001) 113–131.
[11] Y. Matsumura, Poly (amino acid) micelle nanocarriers in preclinical and clinical studies, Adv. Drug Deliv. Rev. 60 (2008) 899–914.
[12] M. Danquah, F. Li, C.B. Duke III, D.D. Miller, R.I. Mahato, Micellar delivery of bicalutamide and embelin for treating prostate cancer, Pharm. Res. 26 (2009) 2081–2092.
[13] F. Greco, M.J. Vicent, Combination therapy: opportunities and challenges for polymer–drug conjugates as anticancer nanomedicines, Adv. Drug Deliv. Rev. 61 (2009) 1203–1213.
[14] M.E. Davis, Z.G. Chen, D.M. Shin, Nanoparticle therapeutics: an emerging treatment modality for cancer, Nat. Rev. Drug Discov. 7 (2008) 771–782.
[15] Y. Matsumura, H. Maeda, A new concept for macromolecular therapeutics in cancer chemotherapy: mechanism of tumoritropic accumulation of proteins and the antitumor agent smancs, Cancer Res. 46 (1986) 6387–6392.
[16] H. Maeda, Y. Matsumura, Tumoritropic and lymphotropic principles of macromolecular drugs, Crit. Rev. Ther. Drug Carrier Syst. 6 (1989) 193–210.
[17] H. Maeda, L.W. Seymour, Y. Miyamoto, Conjugates of anticancer agents and polymers: advantages of macromolecular therapeutics in vivo, Bioconjug. Chem. 3 (1992) 351–362.
[18] F. Yuan, M. Leunig, S.K. Huang, D.A. Berk, D. Papahadjopoulos, R.K. Jain, Microvascular permeability and interstitial penetration of sterically stabilized (stealth) liposomes in a human tumor xenograft, Cancer Res. 54 (1994) 3352–3356.
[19] F. Yuan, M. Dellian, D. Fukumura, M. Leunig, D.A. Berk, V.P. Torchilin, R.K. Jain, Vascular permeability in a human tumor xenograft: molecular size dependence and cutoff size, Cancer Res. 55 (1995) 3752–3756.
[20] F. Yuan, Y. Chen, M. Dellian, N. Safabakhsh, N. Ferrara, R.K. Jain, Time-dependent vascular regression and permeability changes in established human tumor xenografts induced by an anti-vascular endothelial growth factor/vascular permeability factor antibody, Proc. Natl Acad. Sci. USA 93 (1996) 14765–14770.
[21] W.L. Monsky, C. Mouta Carreira, Y. Tsuzuki, T. Gohongi, D. Fukumura, R.K. Jain, Role of host microenvironment in angiogenesis and microvascular functions in human breast cancer xenografts: mammary fat pad versus cranial tumors, Clin. Cancer Res. 8 (2002) 1008–1013.
[22] R.K. Jain, The next frontier of molecular medicine: delivery of therapeutics, Nat. Med. 4 (1998) 655–657.
[23] R.K. Jain, Barriers to drug delivery in solid tumors, Sci. Am. 271 (1994) 58–65.
[24] R.K. Jain, 1995 Whitaker Lecture: delivery of molecules, particles, and cells to solid tumors, Ann. Biomed. Eng. 24 (1996) 457–473.
[25] H.S. Reinhold, Improved microcirculation in irradiated tumours, Eur. J. Cancer 7 (1971) 273–280.
[26] R.K. Jain, Transport of molecules in the tumor interstitium: a review, Cancer Res. 47 (1987) 3039–3051.
[27] C.H. Heldin, K. Rubin, K. Pietras, A. Ostman, High interstitial fluid pressure – an obstacle in cancer therapy, Nat. Rev. Cancer 4 (2004) 806–813.
[28] K. Aukland, R.K. Reed, Interstitial-lymphatic mechanisms in the control of extracellular fluid volume, Physiol. Rev. 73 (1993) 1–78.
[29] R. Gutmann, M. Leunig, J. Feyh, A.E. Goetz, K. Messmer, E. Kastenbauer, R.K. Jain, Interstitial hypertension in head and neck tumors in patients: correlation with tumor size, Cancer Res. 52 (1992) 1993–1995.
[30] M. Milosevic, A. Fyles, D. Hedley, M. Pintilie, W. Levin, L. Manchul, R. Hill, Interstitial fluid pressure predicts survival in patients with cervix cancer independent of clinical prognostic factors and tumor oxygen measurements, Cancer Res. 61 (2001) 6400–6405.
[31] J.R. Less, M.C. Posner, Y. Boucher, D. Borochovitz, N. Wolmark, R.K. Jain, Interstitial hypertension in human breast and colorectal tumors, Cancer Res. 52 (1992) 6371–6374.
[32] M. Milosevic, A. Fyles, D. Hedley, R. Hill, The human tumor microenvironment: invasive (needle) measurement of oxygen and interstitial fluid pressure, Semin. Radiat. Oncol. 14 (2004) 249–258.
[33] R.K. Jain, Normalization of tumor vasculature: an emerging concept in antiangiogenic therapy, Science 307 (2005) 58–62.
[34] P.M. Gullino, F.H. Grantham, S.H. Smith, A.C. Haggerty, Modifications of the acid-base status of the internal milieu of tumors, J. Natl Cancer Inst. 34 (1965) 857–869.
[35] A.J. Thistlethwaite, D.B. Leeper, D.J. Moylan 3rd, R.E. Nerlinger, pH distribution in human tumors, Int. J. Radiat. Oncol. Biol. Phys. 11 (1985) 1647–1652.
[36] P. Vaupel, F. Kallinowski, P. Okunieff, Blood flow, oxygen and nutrient supply, and metabolic microenvironment of human tumors: a review, Cancer Res. 49 (1989) 6449–6465.
[37] G. Helmlinger, F. Yuan, M. Dellian, R.K. Jain, Interstitial pH and pO_2 gradients in solid tumors in vivo: high-resolution measurements reveal a lack of correlation, Nat. Med. 3 (1997) 177–182.
[38] P. Vaupel, Physiological properties of malignant tumours, NMR Biomed. 5 (1992) 220–225.
[39] P. Vaupel, C. Schaefer, P. Okunieff, Intracellular acidosis in murine fibrosarcomas coincides with ATP depletion, hypoxia, and high levels of lactate and total Pi, NMR Biomed. 7 (1994) 128–136.
[40] P. Vaupel, D.K. Kelleher, T. Engel, Stable bioenergetic status despite substantial changes in blood flow and tissue oxygenation in a rat tumour, Br. J. Cancer 69 (1994) 46–49.
[41] H. Izumi, T. Torigoe, H. Ishiguchi, H. Uramoto, Y. Yoshida, M. Tanabe, T. Ise, T. Murakami, T. Yoshida, M. Nomoto, K. Kohno, Cellular pH regulators: potentially promising molecular targets for cancer chemotherapy, Cancer Treat. Rev. 29 (2003) 541–549.
[42] P. Vaupel, Pathophysiology of Solid Tumors, in: M. Molls, P. Vaupel, C. Nieder, M. S. Anscher (Eds.), The Impact of Tumor Biology on Cancer Treatment and Multidisciplinary Strategies, Springer, Berlin Heidelberg, 2009, pp. 52–83.
[43] M. Yamagata, K. Hasuda, T. Stamato, I.F. Tannock, The contribution of lactic acid to acidification of tumours: studies of variant cells lacking lactate dehydrogenase, Br. J. Cancer 77 (1998) 1726–1731.
[44] G. Helmlinger, A. Sckell, M. Dellian, N.S. Forbes, R.K. Jain, Acid production in glycolysis-impaired tumors provides new insights into tumor metabolism, Clin. Cancer Res. 8 (2002) 1284–1291.
[45] M. Stubbs, P.M. McSheehy, J.R. Griffiths, C.L. Bashford, Causes and consequences of tumour acidity and implications for treatment, Mol. Med. Today 6 (2000) 15–19.
[46] L.E. Gerweck, Tumor pH: implications for treatment and novel drug design, Semin. Radiat. Oncol. 8 (1998) 176–182.
[47] Y. Bae, W.D. Jang, N. Nishiyama, S. Fukushima, K. Kataoka, Multifunctional polymeric micelles with folate-mediated cancer cell targeting and pH-triggered drug releasing properties for active intracellular drug delivery, Mol. Biosyst. 1 (2005) 242–250.
[48] Y. Bae, N. Nishiyama, S. Fukushima, H. Koyama, M. Yasuhiro, K. Kataoka, Preparation and biological characterization of polymeric micelle drug carriers with intracellular pH-triggered drug release property: tumor permeability, controlled subcellular drug distribution, and enhanced in vivo antitumor efficacy, Bioconjug. Chem. 16 (2005) 122–130.
[49] E.S. Lee, K. Na, Y.H. Bae, Doxorubicin loaded pH-sensitive polymeric micelles for reversal of resistant MCF-7 tumor, J. Control. Release 103 (2005) 405–418.
[50] G. Mohajer, E.S. Lee, Y.H. Bae, Enhanced intercellular retention activity of novel pH-sensitive polymeric micelles in wild and multidrug resistant MCF-7 cells, Pharm. Res. 24 (2007) 1618–1627.
[51] E.S. Lee, D. Kim, Y.S. Youn, K.T. Oh, Y.H. Bae, A virus-mimetic nanogel vehicle, Angew. Chem. Int. Ed Engl. 47 (2008) 2418–2421.
[52] A.K. Iyer, G. Khaled, J. Fang, H. Maeda, Exploiting the enhanced permeability and retention effect for tumor targeting, Drug Discov. Today 11 (2006) 812–818.
[53] M. Hockel, P. Vaupel, Tumor hypoxia: definitions and current clinical, biologic, and molecular aspects, J. Natl Cancer Inst. 93 (2001) 266–276.
[54] L.I. Cardenas-Navia, D. Yu, R.D. Braun, D.M. Brizel, T.W. Secomb, M.W. Dewhirst, Tumor-dependent kinetics of partial pressure of oxygen fluctuations during air and oxygen breathing, Cancer Res. 64 (2004) 6010–6017.
[55] T. Kaneta, Y. Takai, R. Iwata, T. Hakamatsuka, H. Yasuda, K. Nakayama, Y. Ishikawa, S. Watanuki, S. Furumoto, Y. Funaki, E. Nakata, K. Jingu, M. Tsujitani, M. Ito, H. Fukuda, S. Takahashi, S. Yamada, Initial evaluation of dynamic human imaging using 18F-FRP170 as a new PET tracer for imaging hypoxia, Ann. Nucl. Med. 21 (2007) 101–107.
[56] K.M. Comerford, T.J. Wallace, J. Karhausen, N.A. Louis, M.C. Montalto, S.P. Colgan, Hypoxia-inducible factor-1-dependent regulation of the multidrug resistance (MDR1) gene, Cancer Res. 62 (2002) 3387–3394.
[57] K.M. Comerford, E.P. Cummins, C.T. Taylor, c-Jun NH2-terminal kinase activation contributes to hypoxia-inducible factor 1alpha-dependent P-glycoprotein expression in hypoxia, Cancer Res. 64 (2004) 9057–9061.
[58] G.L. Semenza, P.H. Roth, H.M. Fang, G.L. Wang, Transcriptional regulation of genes encoding glycolytic enzymes by hypoxia-inducible factor 1, J. Biol. Chem. 269 (1994) 23757–23763.
[59] W.A. Denny, Prodrug strategies in cancer therapy, Eur. J. Med. Chem. 36 (2001) 577–595.
[60] G.D. Yancopoulos, S. Davis, N.W. Gale, J.S. Rudge, S.J. Wiegand, J. Holash, Vascular-specific growth factors and blood vessel formation, Nature 407 (2000) 242–248.
[61] R.K. Jain, D.G. Duda, J.W. Clark, J.S. Loeffler, Lessons from phase III clinical trials on anti-VEGF therapy for cancer, Nat. Clin. Pract. Oncol. 3 (2006) 24–40.
[62] J.I. Greenberg, D.J. Shields, S.G. Barillas, L.M. Acevedo, E. Murphy, J. Huang, L. Scheppke, C. Stockmann, R.S. Johnson, N. Angle, D.A. Cheresh, A role for VEGF as a negative regulator of pericyte function and vessel maturation, Nature 456 (2008) 809–813.
[63] P. Carmeliet, R.K. Jain, Angiogenesis in cancer and other diseases, Nature 407 (2000) 249–257.
[64] R.K. Jain, Normalizing tumor vasculature with anti-angiogenic therapy: a new paradigm for combination therapy, Nat. Med. 7 (2001) 987–989.
[65] M.J. Bissell, D. Radisky, Putting tumours in context, Nat. Rev. Cancer 1 (2001) 46–54.
[66] N.A. Bhowmick, E.G. Neilson, H.L. Moses, Stromal fibroblasts in cancer initiation and progression, Nature 432 (2004) 332–337.
[67] K. Polyak, I. Haviv, I.G. Campbell, Co-evolution of tumor cells and their microenvironment, Trends Genet. 25 (2009) 30–38.
[68] J.A. Joyce, J.W. Pollard, Microenvironmental regulation of metastasis, Nat. Rev. Cancer 9 (2009) 239–252.
[69] P. Micke, A. Ostman, Tumour-stroma interaction: cancer-associated fibroblasts as novel targets in anti-cancer therapy? Lung Cancer 45 (Suppl 2) (2004) S163–S175.
[70] R. Kalluri, M. Zeisberg, Fibroblasts in cancer, Nat. Rev. Cancer 6 (2006) 392–401.

[71] A. Bellini, S. Mattoli, The role of the fibrocyte, a bone marrow-derived mesenchymal progenitor, in reactive and reparative fibroses, Lab. Invest. 87 (2007) 858–870.
[72] M. Dean, T. Fojo, S. Bates, Tumour stem cells and drug resistance, Nat. Rev. Cancer 5 (2005) 275–284.
[73] S. Zhou, J.D. Schuetz, K.D. Bunting, A.M. Colapietro, J. Sampath, J.J. Morris, I. Lagutina, G.C. Grosveld, M. Osawa, H. Nakauchi, B.P. Sorrentino, The ABC transporter Bcrp1/ABCG2 is expressed in a wide variety of stem cells and is a molecular determinant of the side-population phenotype, Nat. Med. 7 (2001) 1028–1034.
[74] M. Kim, H. Turnquist, J. Jackson, M. Sgagias, Y. Yan, M. Gong, M. Dean, J.G. Sharp, K. Cowan, The multidrug resistance transporter ABCG2 (breast cancer resistance protein 1) effluxes Hoechst 33342 and is overexpressed in hematopoietic stem cells, Clin. Cancer Res. 8 (2002) 22–28.
[75] C.W. Scharenberg, M.A. Harkey, B. Torok-Storb, The ABCG2 transporter is an efficient Hoechst 33342 efflux pump and is preferentially expressed by immature human hematopoietic progenitors, Blood 99 (2002) 507–512.
[76] L. Hu, C. McArthur, R.B. Jaffe, Ovarian cancer stem-like side-population cells are tumourigenic and chemoresistant, Br. J. Cancer 102 (2010) 1276–1283.
[77] D. Steinbach, O. Legrand, ABC transporters and drug resistance in leukemia: was P-gp nothing but the first head of the Hydra? Leukemia 21 (2007) 1172–1176.
[78] R.T. Costello, F. Mallet, B. Gaugler, D. Sainty, C. Arnoulet, J.A. Gastaut, D. Olive, Human acute myeloid leukemia CD34+/CD38− progenitor cells have decreased sensitivity to chemotherapy and Fas-induced apoptosis, reduced immunogenicity, and impaired dendritic cell transformation capacities, Cancer Res. 60 (2000) 4403–4411.
[79] T.P. Padera, A. Kadambi, E. di Tomaso, C.M. Carreira, E.B. Brown, Y. Boucher, N.C. Choi, D. Mathisen, J. Wain, E.J. Mark, L.L. Munn, R.K. Jain, Lymphatic metastasis in the absence of functional intratumor lymphatics, Science 296 (2002) 1883–1886.
[80] A.J. Leu, D.A. Berk, A. Lymboussaki, K. Alitalo, R.K. Jain, Absence of functional lymphatics within a murine sarcoma: a molecular and functional evaluation, Cancer Res. 60 (2000) 4324–4327.
[81] M. Skobe, T. Hawighorst, D.G. Jackson, R. Prevo, L. Janes, P. Velasco, L. Riccardi, K. Alitalo, K. Claffey, M. Detmar, Induction of tumor lymphangiogenesis by VEGF-C promotes breast cancer metastasis, Nat. Med. 7 (2001) 192–198.
[82] S.A. Stacker, C. Caesar, M.E. Baldwin, G.E. Thornton, R.A. Williams, R. Prevo, D.G. Jackson, S. Nishikawa, H. Kubo, M.G. Achen, VEGF-D promotes the metastatic spread of tumor cells via the lymphatics, Nat. Med. 7 (2001) 186–191.
[83] D. Fukumura, R.K. Jain, Tumor microenvironment abnormalities: causes, consequences, and strategies to normalize, J. Cell. Biochem. 101 (2007) 937–949.
[84] N. Isaka, T.P. Padera, J. Hagendoorn, D. Fukumura, R.K. Jain, Peritumor lymphatics induced by vascular endothelial growth factor-C exhibit abnormal function, Cancer Res. 64 (2004) 4400–4404.
[85] N. Simionescu, Cellular aspects of transcapillary exchange, Physiol. Rev. 63 (1983) 1536–1579.
[86] E.M. Renkin, Cellular and intercellular transport pathways in exchange vessels, Am. Rev. Respir. Dis. 146 (1992) S28–S31.
[87] W.G. Roberts, G.E. Palade, Neovasculature induced by vascular endothelial growth factor is fenestrated, Cancer Res. 57 (1997) 765–772.
[88] C.R. Neal, C.C. Michel, Transcellular gaps in microvascular walls of frog and rat when permeability is increased by perfusion with the ionophore A23187, J. Physiol. 488 (Pt 2) (1995) 427–437.
[89] H. Hashizume, P. Baluk, S. Morikawa, J.W. McLean, G. Thurston, S. Roberge, R.K. Jain, D.M. McDonald, Openings between defective endothelial cells explain tumor vessel leakiness, Am. J. Pathol. 156 (2000) 1363–1380.
[90] P. Rubin, G. Casarett, Microcirculation of tumors. I. Anatomy, function, and necrosis, Clin. Radiol. 17 (1966) 220–229.
[91] B.A. Warren, The vascular morphology of tumors, in: H.I. Peterson (Ed.), Tumor Blood Circulation, CRC Press, Boca Raton, 1979, pp. 1–47.
[92] R.K. Jain, Transport of molecules across tumor vasculature, Cancer Metastasis Rev. 6 (1987) 559–593.
[93] Y. Takakura, R.I. Mahato, M. Hashida, Extravasation of macromolecules, Adv. Drug Deliv. Rev. 34 (1998) 93–108.
[94] I.A. Romero, K. Radewicz, E. Jubin, C.C. Michel, J. Greenwood, P.O. Couraud, P. Adamson, Changes in cytoskeletal and tight junctional proteins correlate with decreased permeability induced by dexamethasone in cultured rat brain endothelial cells, Neurosci. Lett. 344 (2003) 112–116.
[95] H. Hasegawa, Y. Ushio, T. Hayakawa, K. Yamada, H. Mogami, Changes of the blood-brain barrier in experimental metastatic brain tumors, J. Neurosurg. 59 (1983) 304–310.
[96] P. Groscurth, G. Kistler, Human renal cell carcinoma in the "nude" mouse: long-term observations (author's transl), Beitr. Pathol. 160 (1977) 337–360.
[97] A. Hirano, T. Matsui, Vascular structures in brain tumors, Hum. Pathol. 6 (1975) 611–621.
[98] B.A. Warren, The ultrastructure of the microcirculation at the advancing edge of Walker 256 carcinoma, Microvasc. Res. 2 (1970) 443–453.
[99] G. Majno, S.M. Shea, M. Leventhal, Endothelial contraction induced by histamine-type mediators: an electron microscopic study, J. Cell Biol. 42 (1969) 647–672.
[100] D.M. McDonald, G. Thurston, P. Baluk, Endothelial gaps as sites for plasma leakage in inflammation, Microcirculation 6 (1999) 7–22.
[101] W.G. Roberts, G.E. Palade, Increased microvascular permeability and endothelial fenestration induced by vascular endothelial growth factor, J. Cell Sci. 108 (Pt 6) (1995) 2369–2379.
[102] H.F. Dvorak, J.A. Nagy, D. Feng, L.F. Brown, A.M. Dvorak, Vascular permeability factor/vascular endothelial growth factor and the significance of microvascular hyperpermeability in angiogenesis, Curr. Top. Microbiol. Immunol. 237 (1999) 97–132.
[103] A.M. Dvorak, S. Kohn, E.S. Morgan, P. Fox, J.A. Nagy, H.F. Dvorak, The vesiculo-vacuolar organelle (VVO): a distinct endothelial cell structure that provides a transcellular pathway for macromolecular extravasation, J. Leukoc. Biol. 59 (1996) 100–115.
[104] D. Feng, J.A. Nagy, J. Hipp, H.F. Dvorak, A.M. Dvorak, Vesiculo-vacuolar organelles and the regulation of venule permeability to macromolecules by vascular permeability factor, histamine, and serotonin, J. Exp. Med. 183 (1996) 1981–1986.
[105] A.M. Dvorak, D. Feng, The vesiculo-vacuolar organelle (VVO). A new endothelial cell permeability organelle, J. Histochem. Cytochem. 49 (2001) 419–432.
[106] F. Yuan, Transvascular drug delivery in solid tumors, Semin. Radiat. Oncol. 8 (1998) 164–175.
[107] B. Rippe, B. Haraldsson, Fluid and protein fluxes across small and large pores in the microvasculature. Application of two-pore equations, Acta Physiol. Scand. 131 (1987) 411–428.
[108] Y. Boucher, L.T. Baxter, R.K. Jain, Interstitial pressure gradients in tissue-isolated and subcutaneous tumors: implications for therapy, Cancer Res. 50 (1990) 4478–4484.
[109] R.K. Jain, Vascular and interstitial barriers to delivery of therapeutic agents in tumors, Cancer Metastasis Rev. 9 (1990) 253–266.
[110] S. Morikawa, P. Baluk, T. Kaidoh, A. Haskell, R.K. Jain, D.M. McDonald, Abnormalities in pericytes on blood vessels and endothelial sprouts in tumors, Am. J. Pathol. 160 (2002) 985–1000.
[111] R.T. Tong, Y. Boucher, S.V. Kozin, F. Winkler, D.J. Hicklin, R.K. Jain, Vascular normalization by vascular endothelial growth factor receptor 2 blockade induces a pressure gradient across the vasculature and improves drug penetration in tumors, Cancer Res. 64 (2004) 3731–3736.
[112] W. Arap, R. Pasqualini, E. Ruoslahti, Cancer treatment by targeted drug delivery to tumor vasculature in a mouse model, Science 279 (1998) 377–380.
[113] S.K. Hobbs, W.L. Monsky, F. Yuan, W.G. Roberts, L. Griffith, V.P. Torchilin, R.K. Jain, Regulation of transport pathways in tumor vessels: role of tumor type and microenvironment, Proc. Natl Acad. Sci. USA 95 (1998) 4607–4612.
[114] J.M. Provenzale, S. Mukundan, M. Dewhirst, The role of blood-brain barrier permeability in brain tumor imaging and therapeutics, AJR Am. J. Roentgenol. 185 (2005) 763–767.
[115] R.B. Campbell, D. Fukumura, E.B. Brown, L.M. Mazzola, Y. Izumi, R.K. Jain, V.P. Torchilin, L.L. Munn, Cationic charge determines the distribution of liposomes between the vascular and extravascular compartments of tumors, Cancer Res. 62 (2002) 6831–6836.
[116] G. Thurston, J.W. McLean, M. Rizen, P. Baluk, A. Haskell, T.J. Murphy, D. Hanahan, D.M. McDonald, Cationic liposomes target angiogenic endothelial cells in tumors and chronic inflammation in mice, J. Clin. Invest. 101 (1998) 1401–1413.
[117] R.K. Jain, M. The Eugene, Landis Award Lecture, Delivery of molecular and cellular medicine to solid tumors, Microcirculation 4 (1997) (1996) 1–23.
[118] J.L. Biedler, H. Riehm, Cellular resistance to actinomycin D in Chinese hamster cells in vitro: cross-resistance, radioautographic, and cytogenetic studies, Cancer Res. 30 (1970) 1174–1184.
[119] T. Minko, HPMA copolymers for modulating cellular signaling and overcoming multidrug resistance, Adv. Drug Deliv. Rev. 62 (2010) 192–202.
[120] R.Z. Yusuf, Z. Duan, D.E. Lamendola, R.T. Penson, M.V. Seiden, Paclitaxel resistance: molecular mechanisms and pharmacologic manipulation, Curr. Cancer Drug Targets 3 (2003) 1–19.
[121] L.A. Doyle, D.D. Ross, Multidrug resistance mediated by the breast cancer resistance protein BCRP (ABCG2), Oncogene 22 (2003) 7340–7358.
[122] H.W. van Veen, W.N. Konings, The ABC family of multidrug transporters in microorganisms, Biochim. Biophys. Acta 1365 (1998) 31–36.
[123] R. Krishna, L.D. Mayer, Multidrug resistance (MDR) in cancer. Mechanisms, reversal using modulators of MDR and the role of MDR modulators in influencing the pharmacokinetics of anticancer drugs, Eur. J. Pharm. Sci. 11 (2000) 265–283.
[124] M. Maliepaard, G.L. Scheffer, I.F. Faneyte, M.A. van Gastelen, A.C. Pijnenborg, A.H. Schinkel, M.J. van De Vijver, R.J. Scheper, J.H. Schellens, Subcellular localization and distribution of the breast cancer resistance protein transporter in normal human tissues, Cancer Res. 61 (2001) 3458–3464.
[125] L.A. Doyle, W. Yang, L.V. Abruzzo, T. Krogmann, Y. Gao, A.K. Rishi, D.D. Ross, A multidrug resistance transporter from human MCF-7 breast cancer cells, Proc. Natl Acad. Sci. USA 95 (1998) 15665–15670.
[126] T. Minko, P. Kopeckova, J. Kopecek, Comparison of the anticancer effect of free and HPMA copolymer-bound adriamycin in human ovarian carcinoma cells, Pharm. Res. 16 (1999) 986–996.
[127] Y.P. Hu, S. Jarillon, C. Dubernet, P. Couvreur, J. Robert, On the mechanism of action of doxorubicin encapsulation in nanospheres for the reversal of multidrug resistance, Cancer Chemother. Pharmacol. 37 (1996) 556–560.
[128] C.A. Doige, X. Yu, F.J. Sharom, The effects of lipids and detergents on ATPase-active P-glycoprotein, Biochim. Biophys. Acta 1146 (1993) 65–72.
[129] A.V. Kabanov, E.V. Batrakova, V.Y. Alakhov, Pluronic block copolymers for overcoming drug resistance in cancer, Adv. Drug Deliv. Rev. 54 (2002) 759–779.
[130] E.V. Batrakova, S. Li, V.Y. Alakhov, W.F. Elmquist, D.W. Miller, A.V. Kabanov, Sensitization of cells overexpressing multidrug-resistant proteins by pluronic P85, Pharm. Res. 20 (2003) 1581–1590.
[131] T. Minko, E.V. Batrakova, S. Li, Y. Li, R.I. Pakunlu, V.Y. Alakhov, A.V. Kabanov, Pluronic block copolymers alter apoptotic signal transduction of doxorubicin in drug-resistant cancer cells, J. Control. Release 105 (2005) 269–278.

[132] E.V. Batrakova, S. Li, A.M. Brynskikh, A.K. Sharma, Y. Li, M. Boska, N. Gong, R.L. Mosley, V.Y. Alakhov, H.E. Gendelman, A.V. Kabanov, Effects of pluronic and doxorubicin on drug uptake, cellular metabolism, apoptosis and tumor inhibition in animal models of MDR cancers, J. Control. Release 143 (2010) 290–301.
[133] Y. Zhang, L. Tang, L. Sun, J. Bao, C. Song, L. Huang, K. Liu, Y. Tian, G. Tian, Z. Li, H. Sun, L. Mei, A novel paclitaxel-loaded poly(epsilon-caprolactone)/Poloxamer 188 blend nanoparticle overcoming multidrug resistance for cancer treatment, Acta Biomater. 6 (2010) 2045–2052.
[134] P.Y. Li, P.S. Lai, W.C. Hung, W.J. Syu, Poly(l-lactide)-vitamin E TPGS nanoparticles enhanced the cytotoxicity of doxorubicin in drug-resistant MCF-7 breast cancer cells, Biomacromolecules 11 (2010) 2576–2582.
[135] F. Li, Y. Lu, W. Li, D.D. Miller, R.I. Mahato, Synthesis, formulation and in vitro evaluation of a novel microtubule destabilizer, SMART-100, J. Control. Release 143 (2010) 151–158.
[136] Y. Lu, C.M. Li, Z. Wang, C.R. Ross 2nd, J. Chen, J.T. Dalton, W. Li, D.D. Miller, Discovery of 4-substituted methoxybenzoyl-aryl-thiazole as novel anticancer agents: synthesis, biological evaluation, and structure-activity relationships, J. Med. Chem. 52 (2009) 1701–1711.
[137] A.J. Shuhendler, P. O'Brien, A.M. Rauth, X.Y. Wu, On the synergistic effects of of doxorubicin and mitomycin C against breast cancer cells, Drug Metab. Drug Int. 22 (2008) 201–233.
[138] E.J. Potchen, J. Kinzie, C. Curtis, B.A. Siegel, R.K. Studer, Effect of irradiation on tumor microvascular permeability to macromolecules, Cancer 30 (1972) 639–643.
[139] M.H. Gaber, N.Z. Wu, K. Hong, S.K. Huang, M.W. Dewhirst, D. Papahadjopoulos, Thermosensitive liposomes: extravasation and release of contents in tumor microvascular networks, Int. J. Radiat. Oncol. Biol. Phys. 36 (1996) 1177–1187.
[140] M.L. Hauck, M.W. Dewhirst, D.D. Bigner, M.R. Zalutsky, Local hyperthermia improves uptake of a chimeric monoclonal antibody in a subcutaneous xenograft model, Clin. Cancer Res. 3 (1997) 63–70.
[141] K. Engin, Biological rationale for hyperthermia in cancer treatment (II), Neoplasma 41 (1994) 277–283.
[142] M.W. Dewhirst, Future directions in hyperthermia biology, Int. J. Hyperthermia 10 (1994) 339–345.
[143] K. Fujiwara, T. Watanabe, Effects of hyperthermia, radiotherapy and thermoradiotherapy on tumor microvascular permeability, Acta Pathol. Jpn 40 (1990) 79–84.
[144] A.T. Lefor, S. Makohon, N.B. Ackerman, The effects of hyperthermia on vascular permeability in experimental liver metastasis, J. Surg. Oncol. 28 (1985) 297–300.
[145] M.N. Hosono, M. Hosono, K. Endo, R. Ueda, Y. Onoyama, Effect of hyperthermia on tumor uptake of radiolabeled anti-neural cell adhesion molecule antibody in small-cell lung cancer xenografts, J. Nucl. Med. 35 (1994) 504–509.
[146] J.M. Schuster, M.R. Zalutsky, M.A. Noska, R. Dodge, H.S. Friedman, D.D. Bigner, M.W. Dewhirst, Hyperthermic modulation of radiolabelled antibody uptake in a human glioma xenograft and normal tissues, Int. J. Hyperthermia 11 (1995) 59–72.
[147] M.L. Hauck, D.O. Coffin, R.K. Dodge, M.W. Dewhirst, J.B. Mitchell, M.R. Zalutsky, A local hyperthermia treatment which enhances antibody uptake in a glioma xenograft model does not affect tumour interstitial fluid pressure, Int. J. Hyperthermia 13 (1997) 307–316.
[148] G. Kong, R.D. Braun, M.W. Dewhirst, Characterization of the effect of hyperthermia on nanoparticle extravasation from tumor vasculature, Cancer Res. 61 (2001) 3027–3032.
[149] D.L. Wilhelm, B. Mason, Vascular permeability changes in inflammation: the role of endogenous permeability factors in mild thermal injury, Br. J. Exp. Pathol. 41 (1960) 487–506.
[150] H.M. Ellerby, W. Arap, L.M. Ellerby, R. Kain, R. Andrusiak, G.D. Rio, S. Krajewski, C.R. Lombardo, R. Rao, E. Ruoslahti, D.E. Bredesen, R. Pasqualini, Anti-cancer activity of targeted pro-apoptotic peptides, Nat. Med. 5 (1999) 1032–1038.
[151] Y. Chen, X. Xu, S. Hong, J. Chen, N. Liu, C.B. Underhill, K. Creswell, L. Zhang, RGD-Tachyplesin inhibits tumor growth, Cancer Res. 61 (2001) 2434–2438.
[152] F. Curnis, A. Sacchi, L. Borgna, F. Magni, A. Gasparri, A. Corti, Enhancement of tumor necrosis factor alpha antitumor immunotherapeutic properties by targeted delivery to aminopeptidase N (CD13), Nat. Biotechnol. 18 (2000) 1185–1190.
[153] P.A. Netti, L.M. Hamberg, J.W. Babich, D. Kierstead, W. Graham, G.J. Hunter, G.L. Wolf, A. Fischman, Y. Boucher, R.K. Jain, Enhancement of fluid filtration across tumor vessels: implication for delivery of macromolecules, Proc. Natl Acad. Sci. USA 96 (1999) 3137–3142.
[154] L.G. Presta, H. Chen, S.J. O'Connor, V. Chisholm, Y.G. Meng, L. Krummen, M. Winkler, N. Ferrara, Humanization of an anti-vascular endothelial growth factor monoclonal antibody for the therapy of solid tumors and other disorders, Cancer Res. 57 (1997) 4593–4599.
[155] D.R. Senger, S.J. Galli, A.M. Dvorak, C.A. Perruzzi, V.S. Harvey, H.F. Dvorak, Tumor cells secrete a vascular permeability factor that promotes accumulation of ascites fluid, Science 219 (1983) 983–985.
[156] C.G. Lee, M. Heijn, E. di Tomaso, G. Griffon-Etienne, M. Ancukiewicz, C. Koike, K.R. Park, N. Ferrara, R.K. Jain, H.D. Suit, Y. Boucher, Anti-vascular endothelial growth factor treatment augments tumor radiation response under normoxic or hypoxic conditions, Cancer Res. 60 (2000) 5565–5570.
[157] C.G. Willett, Y. Boucher, E. di Tomaso, D.G. Duda, L.L. Munn, R.T. Tong, D.C. Chung, D.V. Sahani, S.P. Kalva, S.V. Kozin, M. Mino, K.S. Cohen, D.T. Scadden, A.C. Hartford, A.J. Fischman, J.W. Clark, D.P. Ryan, A.X. Zhu, L.S. Blaszkowsky, H.X. Chen, P.C. Shellito, G.Y. Lauwers, R.K. Jain, Direct evidence that the VEGF-specific antibody bevacizumab has antivascular effects in human rectal cancer, Nat. Med. 10 (2004) 145–147.
[158] H.I. Hurwitz, L. Fehrenbacher, J.D. Hainsworth, W. Heim, J. Berlin, E. Holmgren, J. Hambleton, W.F. Novotny, F. Kabbinavar, Bevacizumab in combination with fluorouracil and leucovorin: an active regimen for first-line metastatic colorectal cancer, J. Clin. Oncol. 23 (2005) 3502–3508.
[159] K. Pietras, Increasing tumor uptake of anticancer drugs with imatinib, Semin. Oncol. 31 (2004) 18–23.
[160] K. Pietras, A. Ostman, M. Sjoquist, E. Buchdunger, R.K. Reed, C.H. Heldin, K. Rubin, Inhibition of platelet-derived growth factor receptors reduces interstitial hypertension and increases transcapillary transport in tumors, Cancer Res. 61 (2001) 2929–2934.
[161] K. Pietras, M. Stumm, M. Hubert, E. Buchdunger, K. Rubin, C.H. Heldin, P. McSheehy, M. Wartmann, A. Ostman, STI571 enhances the therapeutic index of epothilone B by a tumor-selective increase of drug uptake, Clin. Cancer Res. 9 (2003) 3779–3787.
[162] E. Lammerts, P. Roswall, C. Sundberg, P.J. Gotwals, V.E. Koteliansky, R.K. Reed, N.E. Heldin, K. Rubin, Interference with TGF-beta1 and -beta3 in tumor stroma lowers tumor interstitial fluid pressure independently of growth in experimental carcinoma, Int. J. Cancer 102 (2002) 453–462.
[163] A.V. Salnikov, P. Roswall, C. Sundberg, H. Gardner, N.E. Heldin, K. Rubin, Inhibition of TGF-beta modulates macrophages and vessel maturation in parallel to a lowering of interstitial fluid pressure in experimental carcinoma, Lab. Invest. 85 (2005) 512–521.
[164] A.V. Salnikov, V.V. Iversen, M. Koisti, C. Sundberg, L. Johansson, L.B. Stuhr, M. Sjoquist, H. Ahlstrom, R.K. Reed, K. Rubin, Lowering of tumor interstitial fluid pressure specifically augments efficacy of chemotherapy, FASEB J. 17 (2003) 1756–1758.
[165] G. Griffon-Etienne, Y. Boucher, C. Brekken, H.D. Suit, R.K. Jain, Taxane-induced apoptosis decompresses blood vessels and lowers interstitial fluid pressure in solid tumors: clinical implications, Cancer Res. 59 (1999) 3776–3782.
[166] A.G. Taghian, R. Abi-Raad, S.I. Assaad, A. Casty, M. Ancukiewicz, E. Yeh, P. Molokhia, K. Attia, T. Sullivan, I. Kuter, Y. Boucher, S.N. Powell, Paclitaxel decreases the interstitial fluid pressure and improves oxygenation in breast cancers in patients treated with neoadjuvant chemotherapy: clinical implications, J. Clin. Oncol. 23 (2005) 1951–1961.
[167] H. Maeda, T. Sawa, T. Konno, Mechanism of tumor-targeted delivery of macromolecular drugs, including the EPR effect in solid tumor and clinical overview of the prototype polymeric drug SMANCS, J. Control. Release 74 (2001) 47–61.
[168] P.A. Vasey, S.B. Kaye, R. Morrison, C. Twelves, P. Wilson, R. Duncan, A.H. Thomson, L.S. Murray, T.E. Hilditch, T. Murray, S. Burtles, D. Fraier, E. Frigerio, J. Cassidy, Phase I clinical and pharmacokinetic study of PK1 [N-(2-hydroxypropyl)methacrylamide copolymer doxorubicin]: first member of a new class of chemotherapeutic agents-drug-polymer conjugates. Cancer Research Campaign Phase I/II Committee, Clin. Cancer Res. 5 (1999) 83–94.
[169] T. Minko, P. Kopeckova, V. Pozharov, J. Kopecek, HPMA copolymer bound adriamycin overcomes MDR1 gene encoded resistance in a human ovarian carcinoma cell line, J. Control. Release 54 (1998) 223–233.
[170] J. Kopecek, P. Kopeckova, T. Minko, Z. Lu, HPMA copolymer-anticancer drug conjugates: design, activity, and mechanism of action, Eur. J. Pharm. Biopharm. 50 (2000) 61–81.
[171] S.D. Chipman, F.B. Oldham, G. Pezzoni, J.W. Singer, Biological and clinical characterization of paclitaxel poliglumex (PPX, CT-2103), a macromolecular polymer–drug conjugate, Int. J. Nanomedicine 1 (2006) 375–383.
[172] J.W. Singer, Paclitaxel poliglumex (XYOTAX, CT-2103): a macromolecular taxane, J. Control. Release 109 (2005) 120–126.
[173] A. Lavasanifar, J. Samuel, G.S. Kwon, Poly(ethylene oxide)-block-poly(l-amino acid) micelles for drug delivery, Adv. Drug Deliv. Rev. 54 (2002) 169–190.
[174] Y. Yamamoto, Y. Nagasaki, Y. Kato, Y. Sugiyama, K. Kataoka, Long-circulating poly (ethylene glycol)-poly(D, L-lactide) block copolymer micelles with modulated surface charge, J. Control. Release 77 (2001) 27–38.
[175] H. Maeda, J. Wu, T. Sawa, Y. Matsumura, K. Hori, Tumor vasculature permeability and the EPR effect in macromolecular therapeutics: a review, J. Control. Release 65 (2000) 271–284.
[176] H. Maeda, T. Sawa, T. Konno, Mechanism of tumor-targeted delivery of macromolecular drugs, including the EPR effect in solid tumor and clinical overview of the prototype polymeric drug SMANCS, J. Control. Release 74 (2001) 47–61.
[177] K.J. Harrington, S. Mohammadtaghi, P.S. Uster, D. Glass, A.M. Peters, R.G. Vile, J.S. Stewart, Effective targeting of solid tumors in patients with locally advanced cancers by radiolabeled pegylated liposomes, Clin. Cancer Res. 7 (2001) 243–254.
[178] F. Gadelle, W. Koros, R. Schechter, Solubilization of aromatic solutes in block copolymers, Macromolecules 28 (1995) 4883–4892.
[179] R. Nagarajan, M. Barry, E. Ruckenstein, Unusual selectivity in solubilization by block copolymer micelles, Langmuir 2 (1986) 210–215.
[180] L. Xing, W. Mattice, Strong solubilization of small molecules by triblock-copolymer micelles in selective solvents, Macromolecules 30 (1997) 1711–1717.
[181] M. Tian, E. Arca, Z. Tuzar, S. Webber, P. Munk, Light scattering study of solubilization of organic molecules by block copolymer micelles in aqueous media, J. Polym. Sci. B Pol. Phys. 33 (1995) 1713–1722.
[182] Y. Zhang, L. Taiming, J. Liu, Low temperature and glucose enhanced T7 RNA polymerase-based plasmid stability for increasing expression of glucagon-like peptide-2 in *Escherichia coli*, Protein Expr. Purif. 29 (2003) 132–139.
[183] J.P. Latere Dwan'Isa, L. Rouxhet, V. Preat, M.E. Brewster, A. Arien, Prediction of drug solubility in amphiphilic di-block copolymer micelles: the role of polymer–drug compatibility, Pharmazie 62 (2007) 499–504.

[184] L. Huynh, J. Grant, J.C. Leroux, P. Delmas, C. Allen, Predicting the solubility of the anti-cancer agent docetaxel in small molecule excipients using computational methods, Pharm. Res. 25 (2008) 147–157.
[185] A. Mahmud, S. Patel, O. Molavi, P. Choi, J. Samuel, A. Lavasanifar, Self-associating poly(ethylene oxide)-b-poly(alpha-cholesteryl carboxylate-epsilon-caprolactone) block copolymer for the solubilization of STAT-3 inhibitor cucurbitacin I, Biomacromolecules 10 (2009) 417–478.
[186] A. Forster, J. Hempenstall, I. Tucker, T. Rades, Selection of excipients for melt extrusion with two poorly water-soluble drugs by solubility parameter calculation and thermal analysis, Int. J. Pharm. 226 (2001) 147–161.
[187] P.J. Marsac, S.L. Shamblin, L.S. Taylor, Theoretical and practical approaches for prediction of drug-polymer miscibility and solubility, Pharm. Res. 23 (2006) 2417–2426.
[188] J. Liu, Y. Xiao, C. Allen, Polymer–drug compatibility: a guide to the development of delivery systems for the anticancer agent, ellipticine, Eur. J. Pharm. Sci. 93 (2003) 132–143.
[189] M. Danquah, T. Fujiwara, R.I. Mahato, Self-assembling methoxypoly(ethylene glycol)-b-poly(carbonate-co-L-lactide) block copolymers for drug delivery, Biomaterials 31 (2010) 2358–2370.
[190] F. Li, M. Danquah, R.I. Mahato, Synthesis and characterization of amphiphilic lipopolymers for micellar drug delivery, Biomacromolecules 11 (2010) 2610–2620.
[191] X. Shuai, H. Ai, N. Nasongkla, S. Kim, J. Gao, Micellar carriers based on block copolymers of poly(-caprolactone) and poly(ethylene glycol) for doxorubicin delivery, J. Control. Release 98 (2004) 415–426.
[192] X. Shuai, T. Merdan, A. Schaper, F. Xi, T. Kissel, Core-cross-linked polymeric micelles as paclitaxel carriers, Bioconjug. Chem. 15 (2004) 441–448.

Synthesis and Characterization of Amphiphilic Lipopolymers for Micellar Drug Delivery

Feng Li, Michael Danquah, and Ram I. Mahato*

Department of Pharmaceutical Sciences, University of Tennessee Health Science Center, Memphis, Tennessee 38103

Received May 24, 2010; Revised Manuscript Received July 23, 2010

The objective of this study was to design lipopolymers for hydrophobic drug delivery. Poly(ethylene glycol)-*block*-poly(2-methyl-2-carboxyl-propylene carbonate-graft-dodecanol) (PEG-PCD) lipopolymers were synthesized and characterized by ^{1}H NMR, FT-IR, GPC, and DSC. The critical micelle concentration (CMC) of PEG-PCD micelles was around 10^{-8} M and decreased with increasing length of hydrophobic block. PEG-PCD micelles could efficiently load a model drug embelin into its hydrophobic core and significantly improve its solubility. The loading capacity was dependent on the polymer core structure, but the length of hydrophobic core had little effect. PEG-PCD formed both spherical and cylindrical micelles, which were dependent on the copolymer structure and composition. PEG-PCD lipopolymers with various hydrophobic core lengths showed similar drug release profiles, which were slower than that of poly(ethylene glycol)-*block*-poly(2-methyl-2-benzoxycarbonyl-propylene carbonate) (PEG-PBC) micelles. Embelin loaded PEG-PCD micelles showed significant inhibition of C4-2 prostate cancer cell proliferation, while no obvious cellular toxicity was observed for blank micelles.

1. Introduction

Many anticancer agents are poorly soluble in water, which can cause serious problems for their clinical application. Dimethyl sulfoxide (DMSO), Ctenophore EL, Tween 80, or other surfactants are commonly used to solubilize these drugs. However, these solubilizing agents are harmful to the liver and kidney and cause dose-dependent hemolysis and acute hypersensitivity reactions.[1,2] In addition, because of high critical micelle concentration (CMC) values associated with low molecular weight surfactant micelles, they are not stable after systemic administration and thus result in the precipitation of solubilized drugs.

Poly(ethylene glycol)(PEG)-lipid conjugates, such as PEG-phosphatidylethanolamie (PEG-PE) have been used for micellar drug delivery.[3,4] The use of PEG-lipid conjugates for drug delivery are superior to conventional small molecular weight surfactants, because PEG-lipid conjugates have lower critical micelle concentration (CMC: $\sim 10^{-5}$ M) than conventional surfactants (CMC: $\sim 10^{-3}$ M), suggesting PEG-lipid conjugate micelles are more stable than those formed by conventional surfactants. A typical PEG-lipid conjugate structure includes a hydrophilic PEG corona and a hydrophobic lipid core, which, in turn, is composed of two lipid chains varying from C12 to C18 in chain length. Although we could conjugate PEG with different lipids to make different PEG-lipid conjugates, the flexibility in the design of hydrophobic core is still limited.

Alternatively, amphiphilic copolymers have become promising materials for micellar drug delivery. Pluronic is a triblock copolymer composed of a central hydrophobic chain of poly(propylene oxide) (PPO) flanked by two hydrophilic chains of poly(ethylene glycol) (PEG) and has been widely used for drug delivery.[5] It not only increases drug solubility, but also overcomes drug resistance in cancer.[6,7] The CMC of Pluronic copolymers ranges from 5.3×10^{-3} to 2.8×10^{-6} M, depending on the molecular weight and composition of copolymers.[5] However, the use of Pluronic for drug delivery is somewhat problematic because they are nonbiodegradable. Therefore, biodegradable copolymers such as PEG-PLLA-PEG were designed to facilitate the elimination of polymers from the body.[8] In addition, the structure and size of hydrophobic core block could be properly designed to improve the micelle stability and drug loading. A significantly reduced CMC (10^{-6} to 10^{-7} M) is observed in a diblock copolymer, which is 10 to 100 folds lower than PEG-lipid conjugates.[9] For examples, the CMC of PEG_{5100}-PLA_{4500} was around 3×10^{-6} M, as determined by Danquah et al.[10] Similar results were also reported by Yasugi et al.,[11] who showed that the CMC of PEG_{5700}-PLA_{5400} was around 3×10^{-7} M. The low CMC of micelles formed by amphiphilic copolymers indicates that they are more stable than PEG-lipid conjugate micelles and can maintain the integrity of micelles upon dilution. In addition, we and others have showed that the drug solubility has been significantly improved by properly designing the hydrophobic core structure to improve the compatibility between the hydrophobic core and drugs.[12] For an example, PEG-*b*-poly(*N*-alkyl stearate L-aspartamide), a lipid conjugated polymer, has been used to improve the solubility of a hydrophobic drug, amphotericin B, and demonstrated the possibility of using lipopolymers for solubilization of lipidlike drugs.[13–14]

In this study, we synthesized a novel amphiphilic lipopolymer, poly(ethylene glycol)-*block*-poly(2-methyl-2-carboxyl-propylene carbonate-graft-dodecanol) (PEG-PCD). The polymer synthesis procedures were optimized and the properties of polymers were characterized. PEG-PCD lipopolymers could form micelles and effectively incorporate embelin and improve its water solubility. PEG-PCD lipopolymers were compared with similar polymers with different core structures to investigate the effect of core structure on micelle properties, such as stability, drug loading, particle size and morphology, and in vitro drug release. In addition, we also investigated the effect of hydrophobic core size on the properties of PEG-PCD lipopolymer micelles.

* To whom correspondence should be addressed. Tel.: 901-448-6929. Fax: 901-448-2099. E-mail: rmahato@uthsc.edu.

10.1021/bm100561v
Published on Web 08/30/2010

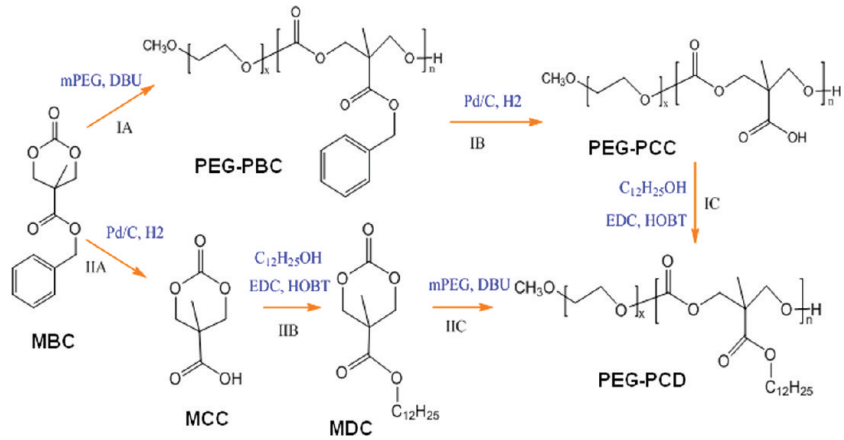

Figure 1. Synthesis of PEG-PCD lipopolymer. Conditions: (**IA**) DBU, CH_2Cl_2, RT, 3 h. (**IB**) Pd/C (10%), H_2, THF/methanol (1:1), RT, 18 h. (**IC**) EDC, HOBT, TEA, DMF, RT, 18 h. (**IIA**) Pd/C (10%), H_2, EtOAc, RT, 3 h. (**IIB**) EDC, HOBT, TEA, DMF, RT, 18 h. (**IIC**) DBU, CH_2Cl_2, RT, 3 h.

Finally, the anticancer activities of embelin loaded micelles were determined in vitro with prostate cancer cells.

2. Experimental Section

2.1. Materials. Hydroxybenzotriazole (HOBT), 1-ethyl-3-(3-dimethylaminopropyl)carbodiimide (EDC), dodecanol, triethylamine (TEA), stannous 2-ethylhexanoate ($Sn(Oct)_2$), diethyl zinc (Et_2Zn), 1,8-diazabicyclo[5.4.0]undec-7-ene (DBU), 2,2-bis(hydroxymethyl) propionic acid, methoxy poly(ethylene glycol) (mPEG, M_n = 5000, PDI = 1.03), and all other reagents were purchased from Sigma Aldrich (St. Louis, MO) and used as received.

2.2. Synthesis of Poly(ethylene glycol)-*block*-poly(2-methyl-2-carboxyl-propylene carbonate-graft-dodecanol) (PEG-PCD). PEG-PCD lipopolymer was synthesized using the following two methods (Figure 1):

Method I. (A) Synthesis of Poly(ethylene glycol)-block-poly(2-methyl-2-benzoxycarbonyl-propylene carbonate) (PEG-PBC). Monomer 2-methyl-2-benzyloxycarbonyl-propylene carbonate (MBC) was synthesized as described by Danquah et al.[12] Briefly, a mixture of 0.168 mol 2,2-bis(hydroxymethyl)propionic acid and 0.169 mol potassium hydroxide was dissolved in 125 mL of dimethylformamide (DMF) by heating to 100 °C for 1 h with stirring. Then, 0.202 mol benzyl bromide was added dropwise to the warm solution and stirred at 100 °C for 16 h. At the end of reaction, the solvent was removed under reduced pressure. The residue was dissolved in 150 mL of ethyl acetate, washed with water, and dried over $MgSO_4$. The solvent was removed to yield a crude product, which was recrystallized from toluene to give pure benzyl 2,2-bis(methylol)propionate. Then, 0.05 mol benzyl 2,2-bis(methylol)-propionate was dissolved in 150 mL of CH_2Cl_2 containing 25 mL of pyridine, and the solution was chilled to 78 °C. A solution of CH_2Cl_2 containing 25 mmol triphosgene was dripped into the solution over 1 h. The reaction mixture was stirred for an additional 2 h at the room temperature before quenched with 75 mL of saturated aqueous NH_4Cl. Subsequently, the organic layer was sequentially washed with aqueous HCl (1 M, 300 mL) and saturated aqueous $NaHCO_3$ (300 mL), dried with Na_2SO_4, and evaporated to give 2-methyl-2-benzyloxycarbonyl-propylene carbonate (MBC) as a crude product, which was further recrystallized from ethyl acetate to give white crystals.

Three methods with different catalysts were investigated in this study to synthesize PEG-PBC from copolymerization of mPEG with monomer MBC. (1) $Sn(Oct)_2$ (10 mol % relative to mPEG) was added to the mixture of given amounts of mPEG and MBC dissolved in anhydrous toluene in a dried polymerization flask under the protection of a nitrogen atmosphere. To optimize the reaction condition, the reaction mixture was heated to 80 °C for 3 and 16 h under stirring, respectively. (2) DBU (40 μL) was added to the mixture of a given amount of mPEG and MBC dissolved in 10 mL of anhydrous CH_2Cl_2 and reacted at RT for 3 h under stirring. (3) Et_2Zn (10 mol % relative to mPEG) was added to the mixture of given amount of mPEG and MBC dissolved in anhydrous toluene in a dried polymerization flask under the protection of nitrogen atmosphere and reacted at 80 °C for 16 h under stirring. At the end of reaction, the reaction mixture was dissolved in $CHCl_3$ and the product was precipitated with a large amount of ice-cold diethyl ether and dried under vacuum at room temperature.

(B) Hydrogenation of PEG-PBC. To remove protective benzyl groups, PEG-PBC was subjected to hydrogenation. Briefly, 1 g of PEG-PBC was dissolved in 12 mL of tetrahydrofuran (THF) and methanol mixture (1:1) containing 200 mg palladium on charcoal (Pd/C). The reaction flask was purged with N_2 thrice and charged with H_2 using a balloon. The reaction was carried out for 18 h with stirring. At the end of reaction, Pd/C was removed by centrifugation. The solvent was removed under reduced pressure to get poly(ethylene glycol)-*block*-poly(2-methyl-2-carboxyl-propylene carbonate) (PEG-PCC).

(C) Lipid Conjugation to PEG-PCC. For lipid conjugation to PEG-PCC, 300 mg PEG-PCC, 260 mg dodecanol, 223 mg hydroxybenzotriazole (HOBT), and 317 mg 1-ethyl-3-(3-dimethylaminopropyl) carbodiimide (EDC) were dissolved in 10 mL of DMF and 340 μL of triethylamine (TEA) was then added to the mixture with stirring. After reaction for 18 h, products were precipitated with a large amount of cold isopropyl alcohol twice and diethyl ether once and then dried under vacuum at room temperature to afford poly(ethylene glycol)-*block*-poly(2-methyl-2-carboxyl-propylene carbonate-*graft*-dodecanol) (PEG-PCD).

Method II. (A) Synthesis of 2-Methyl-2-carboxyl-propylene Carbonate (MCC). MCC was synthesized by hydrogenation of MBC, as described previously.[12] Briefly, 1 g of monomer MBC was dissolved in 10 mL of ethyl acetate containing 100 mg Pd/C. The reaction flask was purged with N_2 three times and charged with H_2 to 45 psi. The reaction was carried out for 3 h. Then, Pd/C was removed by centrifugation. The solvent was removed under reduced pressure to give MTC-OH as a white crystal.

(B) Synthesis of 2-Methyl-2-dodecanoxycarbonyl-propylene Carbonate (MDC). To synthesize MDC, 480 mg MTC-OH, 465 mg dodecanol, 506 mg HOBT, and 720 mg EDC were dissolved in 20 mL of DMF and 490 μL of TEA was then added to the mixture with stirring for 18 h. The reaction mixture was diluted with ethyl acetate (20 mL), washed with water, and dried over $MgSO_4$. The solvent was removed under reduced pressure to yield a crude product, which was further purified by column chromatography to get MDC as a white powder.

(C) Synthesis of PEG-PCD from Copolymerization of mPEG with MDC. DBU (40 μL) was added to the mixture of a given amount of mPEG, and MDC was dissolved in anhydrous CH_2Cl_2 and reacted under stirring for 3 h. The reaction mixture was dissolved in $CHCl_3$, and the

product was precipitated with a large amount of cold isopropyl alcohol and diethyl ether and dried under vacuum at room temperature to get PEG-PCD lipopolymer.

2.3. Polymer Characterization. *2.3.1. Nuclear Magnetic Resonance (NMR).* ^{1}H NMR spectra were recorded on a Varian (500 MHz) using deuterated chloroform ($CDCl_3$) as a solvent, unless otherwise noted. The chemical shifts were calibrated using tetramethylsilane as an internal reference and given in parts per million.

2.3.2. Infrared (IR) Spectra. The composition of synthesized polymers was also confirmed with infrared (IR) spectra using a Perkin-Elmer IR spectrometer.

2.3.3. Gel Permeation Chromatography (GPC). The weight (M_w) and number (M_n) average molecular weight and polydispersity index (PDI) of synthesized polymers were determined by a Waters GPC system equipped with a GPC column (AM Gel 10^3/5) and a differential refractive index detector. THF was used as an eluent at a flow rate of 1 mL/min. A series of narrow polystyrene standards (700−40000 g/mol) were used for calibration.

2.3.4. Differential Scanning Calorimetry (DSC). The thermal properties, including glass transition temperature (T_g), melting temperature (T_m), crystalline temperature (T_c) of the synthesized polymers were determined by differential scanning calorimetry (DSC; TA Instrument DSC Q2000 module). Samples were placed in aluminum pans under nitrogen heated from 25 to 100 °C, cooled to −70 °C to remove thermal history, and heated from −70 to 100 °C at a rate of 5 °C/min.

2.4. Critical Micelle Concentration. Critical micelle concentration (CMC) was determined with fluorescent spectroscopy using pyrene as a hydrophobic fluorescent probe, as previously described.[11] Briefly, 40 μL of pyrene stock solution (2.4×10^{-3} M) in acetone was added to 40 mL of water to prepare a saturated pyrene aqueous solution. Polymer samples were dispersed in water with concentration ranges from 0.5 to 4.8×10^{-7} mg/mL and mixed thoroughly with above pyrene solution at a volume ratio of 1:1. The fluorescent intensity was recorded with a Molecular Devices SpectraMax M2/M2e spectrofluorometer (Sunnyvale, CA) with a $E_X = 338$ nm (I_3) and 333 (I_1) and $E_m = 390$ nm. The intensity ratio (I_{338}/I_{333}) was plotted against the logarithm of polymer concentration. The CMC value was obtained as the point of intersection of two tangents drawn to the curve at high and low concentrations, respectively.

2.5. Preparation of Polymeric Micelles. Polymeric micelles were prepared with a film dispersion method as previously reported with some modifications.[15] Briefly, 15 mg polymer and a given amount of embelin were dissolved in 0.5 mL of CH_2Cl_2, and then the solvent was removed under reduced pressure. The resulting film was hydrated in 3 mL of PBS (pH 7.4) and sonicated for 1 min. Then, the residue-free drug was removed by centrifugation at 12000 rpm for 5 min. The supernatant was filtered using a 0.22 μM filter.

2.6. Drug Loading and Encapsulation Efficiency. To determine drug loading, 10 μL of embelin-loaded micelle solution was diluted with methanol. Then drug concentration was determined using a UV spectrometer at 310 nm (Thermo Spectronic). Embelin concentration was calculated based on the UV absorbance using a standard curve. Drug loading and encapsulation efficiency were then determined using the following equations, respectively.

$$\text{drug loading}(\%) = (\text{amount of loaded drug/amount of polymer}) \times 100\%$$

$$\text{drug encapsulation efficiency}(\%) = (\text{amount of loaded drug/amount of drug added}) \times 100\%$$

$$\text{theoretical loading}(\%) = (\text{amount of drug added/amount of polymer}) \times 100\%$$

Theoretical loading is equal to drug loading when the loading efficiency is 100%.

2.7. Morphology and Particle Size. The particle size of polymeric micelles was determined by dynamic light scattering (Malvern Nano ZS). The intensity of scattered light was detected at 90°. The particle size measurement was repeated three times and the data were reported as the mean ± SD. The morphology of polymeric micelles were observed using a transmission electron microscope (TEM, JEM-100S) using an acceleration voltage of 60 kV. Micelles was loaded on a copper grid and stained with 1% uranyl acetate. The grid was visualized under the electron microscope with magnifications of 75,000.

2.8. In Vitro Drug Release. The dialysis technique was employed to determine the release of embelin from polymeric micelles in PBS (pH 7.4) with 0.1% Tween-80. The micelles used for in vitro release study have a polymer concentration of 5 mg/mL. A total of 800 μL of micelles with 5% drug loading were used to compare the release profiles of PEG-PCD with different PCD length. In addition, 2 mL micelles with 2% drug loading were also used to compare the release profiles of PEG_{114}-PCD_{29} and PEG_{114}-PBC_{30}. Embelin-loaded micelles were placed into a dialysis tube with a molecular weight cutoff of 3500 Da and dialyzed against 50 mL of release medium in a thermocontrolled shaker with a stirring speed of 180 rpm at 37 °C. At specified time, 1 mL release medium was withdrawn and embelin concentration was determined with a UV spectrophotometer based on UV absorbance at 310 nm. All experiments were performed in triplicate and the data reported as the mean of the three individual experiments. The release profiles were assessed as described previously[16] using a similarity factor (f2). The percentage of cumulative drug release was calculated with the following equation:

$$\text{cumulative drug release}(\%) = \frac{\text{cumulative amount of released drug}}{\text{total amount of drug added}} \times 100\%$$

2.9. In Vitro Cytotoxicity of Embelin-Loaded Micelles. C4-2 prostate cancer cell line was used to determine the cell growth inhibition ability of embelin-loaded micelles. Cells were cultured in RPMI 1640 media supplemented with 10% fetal bovine serum (FBS) and 1% antibiotic-antimycotic at 37 °C in humidified environment of 5% CO_2. Cells were seeded in 96-well plates at a density of 5000 cells per well 18 h before treatment. Then, cells were treated with drug-loaded micelles or equivalent amount of blank micelles for additional 72 h. At the end of treatment, cell culture medium was replaced by 100 μL of medium with 0.5 mg/mL 3-(4,5-dimethyl-thiazol-2-yl)-2,5-diphenyl tetrazolium bromide (MTT) and incubated for 1 h at 37 °C. Then the medium was carefully removed and 200 μL of DMSO was added into each well to dissolve the formazan crystals. The absorbance was measured in a microplate reader at a wavelength of 560 nm. Cell viability was expressed as the percentage of control group.

$$\text{cell viability}(\%) = A_{\text{test}}/A_{\text{control}} \times 100\%$$

3. Results

3.1. Synthesis and Characterization of Polymers. As summarized in Figure 1, the target lipopolymer PEG-PCD was synthesized by two approaches. In the first approach, PEG was copolymerized with MBC to afford poly(ethylene glycol)-*block*-poly(2-methyl-2-benzoxycarbonyl-propylene carbonate) (PEG-PBC). Then, the pendant benzyl group was removed by hydrogenation to expose carboxyl groups to get poly(ethylene glycol)-*block*-poly(2-methyl-2-carboxyl-propylene carbonate) (PEG-PCC). Finally, poly(ethylene glycol)-*block*-poly(2-methyl-2-carboxyl-propylene carbonate-*graft*-dodecanol) (PEG-PCD) lipopolymer was synthesized by conjugating dodecanol to the carboxyl groups. In the second approach, PEG was copolymerized with a lipid modified monomer 2-methyl-2-dodecanoxy-carbonyl-propylene carbonate (MDC). MCC and MDC were

Table 1. Effect of Different Catalyst on the Polymerization of PEG-PBC Copolymer

catalyst[a]	[MBC]/[PEG-OH][e]	$M_{n,target}$[f]	DP_{MBC}[g]	M_n[h]	conversion (%)[i]
DBU[b]	10	7500	8	7000	80
DBU[b]	20	10000	17	9250	85
DBU[b]	34	13500	30	12500	88
$Sn(oct)_2$[c]	34	13500	17	9250	50
$Sn(oct)_2$[d]	34	13500	22	10500	65
Et_2Zn[d]	20	10000	6	6500	30

[a] DBU, 1,8-diazabicyclo[5.4.0]undec-7-ene; $Sn(oct)_2$, stannous 2-ethylhexanoate; Et_2Zn, diethy zinc. [b] Reaction condition: RT, 3 h. [c] Reaction condition: 80 °C, 3 h. [d] Reaction condition: 80°, 16 h. [e] Molar ratio of monomer (MBC) to PEG in the feed. [f] $M_{n,target}$ = [MBC]/[PEG−OH] × $M_{monomer\ unit}$ (250) + M_{PEG-OH} (5000). [g] DP: degree of polymerization, determined by ^1H NMR. [h] M_n = DP × $M_{monomer\ unit}$ (250) + M_{PEG-OH} (5000). [i] Determined by ^1H NMR, conversion (%) = DP/([MBC]/[PEG-OH]) × 100%.

characterized with ^1H NMR (Figure S1) and ESI-MS. MCC: ^1H NMR (500 MHz, DMSO) δ 13.35 (s, 1H), 4.57 (d, 2H), 4.32 (d, 2H), 1.18 (s, 3H). MS (ESI) *m/z* 159 $[M-H]^-$. MCC: ^1H NMR (500 MHz, $CDCl_3$) δ 4.50 (d, 2H), 4.2 (d, 4H), 1.65 (m, 2H), 1.4−1.2 (m, 21H), 0.85 (t, 3H). MS (ESI) *m/z* 351 $[M + Na]^+$. Although we could synthesize the lipopolymers with both approaches, the second approach involves column purification of MDC, which is a time-consuming process. Therefore, the first approach was selected to generate lipopolymer PEG-PCD.

To achieve the optimal polymerization efficiency, three different catalysts were tested for copolymerization of PEG and MBC, as summarized in Table 1. Among three catalysts tested, DBU was the best, as the conversion rate was 80−88% at the molar ratio of monomer and PEG ranging from 10 to 34. Both $Sn(oct)_2$ and Et_2Zn were used at 80 °C and the degree of polymerization (DP) was increased with prolonged reaction time from 3 to 16 h for $Sn(oct)_2$. However, both of these two catalysts gave less DP under the reaction conditions described in Table 1. Therefore, DBU was selected in the current study.

The structures of PEG-PBC, PEG-PCC, and PEG-PCD were confirmed by ^1H NMR (Figure 2). From Figure 2A, the following peaks were observed for PEG-PBC polymer at δ 1.2 (CH_3 in BC unit), δ 3.6 (CH_2 in PEG), δ 4.3(CH_2 in BC main chain), δ 5.2 (CH_2 in BC side group), and δ 7.3 (phenyl ring). All signals are assigned as methoxy poly(ethylene glycol) (mPEG) and polymerized BC units. In addition, the success of polymerization was confirmed by the disappearance of signal at δ 4.2 and 4.6 in the MBC monomer and appearance of a new peak at δ 4.3. The degree of polymerization and molecular weight of the polymers was estimated based on the peak areas of PEG CH_2 groups at δ 3.6 and those of CH_2 in BC main chain at δ 4.3.

The benzyl groups were removed via Pd/C catalyzed hydrogenation. The peaks at δ 5.2 (CH_2 in BC side group) and δ 7.3 (phenyl ring) disappeared after hydrogenation (Figure 2B), which indicates the complete removal of pendant benzyl group. In addition, a peak at δ 13 was observed, which belongs to the exposed carboxyl group after removing protective benzyl group. Dodecanol was conjugated onto the polymer backbone using EDC/HOBT chemistry. The success of dodecanol conjugation to PEG-PCC carboxyl group was confirmed by the appearance of new peaks at δ 4.1, 1.6, 1.2−1.4, and 0.9, which could be assigned to different groups in the lipid as shown in Figure 2C.

The FT-IR of PEG-PBC, PEG-PCC, and PEG-PCD also confirmed the success of the reaction (Figure 3). In FT-IR spectra of PEG-PBC, there were peaks at 736 and 696 cm^{-1},

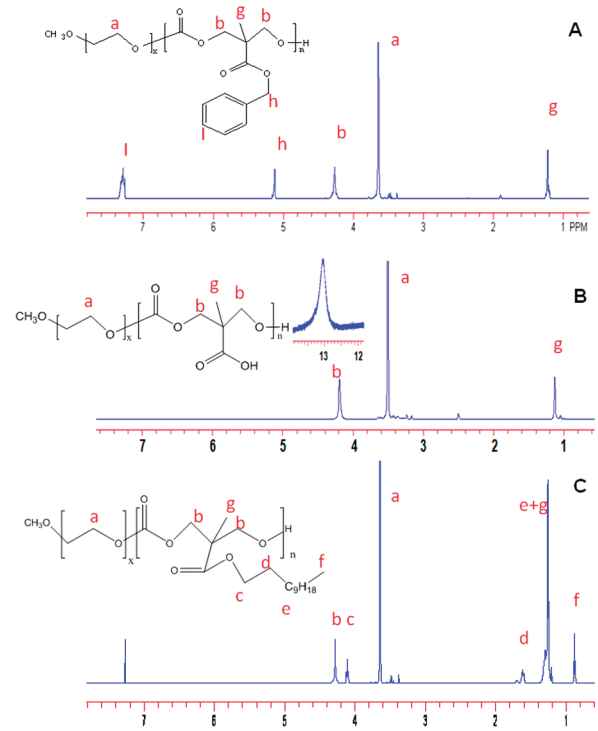

Figure 2. ^1H NMR of polymers: (A) PEG_{114}-PBC_{30} in $CDCl_3$, (B) PEG_{114}-PCC_{30} in DMSO, and (C) PEG_{114}-PCD_{29} in $CDCl_3$.

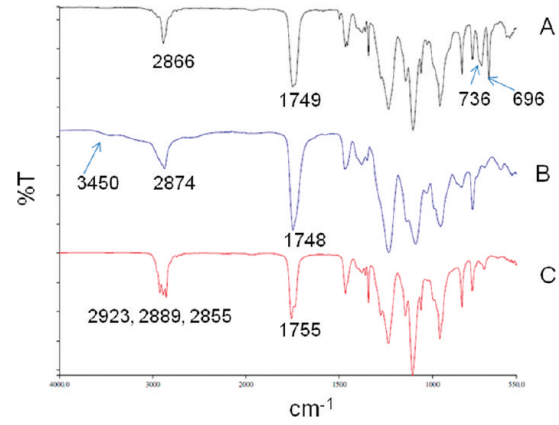

Figure 3. FT-IR spectra of polymers: (A) PEG_{114}-PBC_{30}, (B) PEG_{114}-PCC_{30}, and (C) PEG_{114}-PCD_{29}.

which were due to the CH vibrations of benzyl groups. These two peaks were absent in the FT-IR spectra of PEG-PCC and PEG-PCD, indicating the removal of the pendant benzyl groups during hydrogenation. In addition, we also observed a broad OH stretch band, which was centered at 3450 cm^{-1} and partially overlapped with C−H stretch. This further confirmed the presence of pendant COOH groups. Besides, we also observed absorbance bands due to the C═O stretching vibration at 1749 cm^{-1} (PEG-PBC), 1748 cm^{-1} (PEG-PCC), and 1755 cm^{-1} (PEG-PCD), respectively. The C−H stretch band was observed at 2886 cm^{-1} for PEG-PBC, 2874 cm^{-1} for PEG-PCC. In addition, three bands at 2923, 2889, and 2855 cm^{-1} were observed for PEG-PCD, indicating the presence of pendant long alkanes.

The characteristics of PEG-PBC, PEG-PCC, and PEG-PCD polymers are summarized in Table 2. The molecular weight of PEG-PBC and PEG-PCC were calculated based on the peak areas of PEG CH_2 groups at δ 3.6 and those of CH_2 in BC main chain at δ 4.3 in the ^1H NMR spectrum. In addition, the

Table 2. Characteristics of PEG Copolymers with Different Core Structure

polymer[a]	M_n (NMR)	M_w (GPC)[b]	M_n (GPC)[b]	PDI[b]	CMC (g/L)	CMC (M)[c]	crystallinity
PEG_{114}-PBC_{30}	12500	11140	9703	1.15	4.0×10^{-4}	3.2×10^{-8}	semicrystalline
PEG_{114}-PCC_{30}	9800	7447	6563	1.13	2.2×10^{-2}	2.3×10^{-6}	amorphous
PEG_{114}-PCD_{29}	13561	13342	11636	1.15	3.6×10^{-4}	2.6×10^{-8}	crystalline
PEG_{114}-PCD_{16}	10248	11794	9590	1.23	9.0×10^{-4}	$8.7 \times {}^{-8}$	crystalline
PEG_{114}-PCD_6	6968	6580	6203	1.06	1.4×10^{-3}	2.0×10^{-7}	crystalline

[a] PEG-PBC, poly(ethylene glycol)-*block*-poly(2-methyl-2-benzoxycarbonyl-propylene carbonate); PEG-PCD, poly(ethylene glycol)-*block*-poly(2-methyl-2-carboxyl-propylene carbonate-graft-dodecanol); PEG-PCC, poly(ethylene glycol)-*block*-poly(2-methyl-2-carboxyl-propylene carbonate). [b] M_w and M_n were apparent molecular weight determined by GPC; PDI = $(M_w/M_n) \times 100\%$. [c] CMC (g/L) normalized with M_n from ^{1}H NMR.

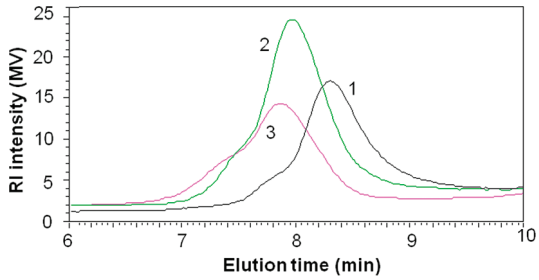

Figure 4. Gel permeation chromatography (GPC) of (1) PEG_{114}-PCC_{30} [M_n = 6563 g/mol, M_w/M_n = 1.13]; (2) PEG_{114}-PBC_{30} [M_n = 9703 g/mol, M_w/M_n = 1.15]; (3) PEG_{114}-PCD_{29} [M_n = 11636 g/mol, M_w/M_n = 1.15].

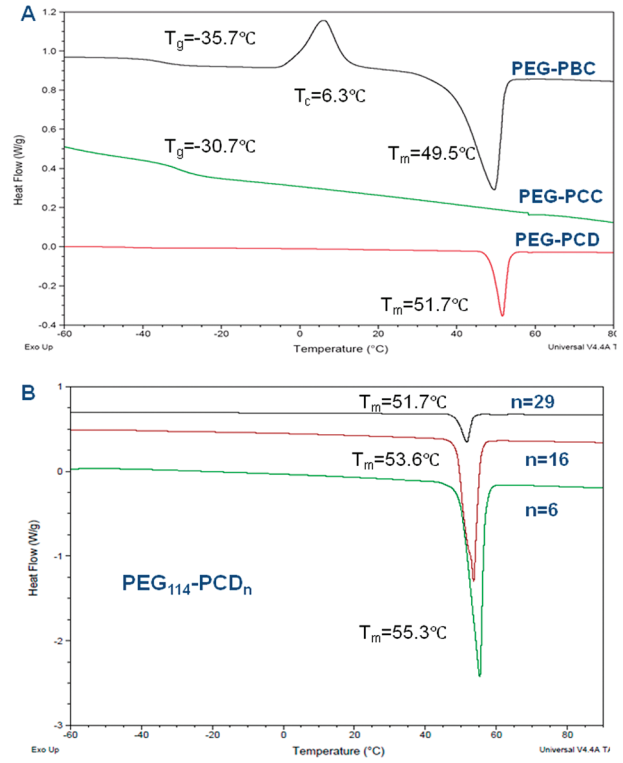

Figure 5. Thermal analysis of polymers by differential scanning calorimetry (DSC). (A) Polymers of different core structures: PEG_{114}-PBC_{30}, PEG_{114}-PCC_{30}, and PEG_{114}-PCD_{29}. (B) PEG-PCD polymers with different PCD core length: n = 6, 16, and 29.

percentage of conjugation and molecular weight of the lipopolymer was calculated by the peak areas at δ 4.3 (belongs to polymer backbone) and at δ 4.1 (belongs to the conjugated pendant lipid) in the ^{1}H NMR spectrum. The M_n determine by ^{1}H NMR were 12500 g/mol for PEG_{114}-PBC_{30}, 9800 g/mol for PEG_{114}-PCC_{30}, 13561 g/mol for PEG_{114}-PCD_{29}, 10248 g/mol for PEG_{114}-PCD_{16}, and 6968 g/mol for PEG_{114}-PCD_6, respectively. GPC was also used to determine the apparent weight (M_w) and number (M_n) average molecular weight of polymers and their polydispersity index. A good correlation was observed between the molecular weight estimated from NMR and M_w or M_n determined by GPC. All of the polymers showed narrow distribution as revealed by the small polydispersity index (1.06−1.23). A representative plot comparing the GPC chromatograms for PEG_{114}-PCC_{30}, PEG_{114}-PBC_{30}, and PEG_{114}-PCD_{29} was shown in Figure 4.

DSC was used to determine the thermal properties of the synthesized block copolymers. The thermograms of diblock copolymers with different core structures are shown in Figure 5. PEG_{114}-PBC_{30} has a T_g = −35.7 °C, T_c = 6.3 °C, and T_m = 49.5 °C, respectively. PEG_{114}-PCC_{30}, which is a transparent viscous liquid, showed a T_g of −30.7 °C, but no obvious T_c or T_m. PEG_{114}-PCD_{29} showed a T_m of −35.7 °C, but no obvious T_g or T_c. The different thermal properties observed with DSC suggesting different properties of the copolymers. Only T_g was observed in PEG_{114}-PCC_{30}, indicating it is an amorphous polymer. PEG_{114}-PCD_{29} has a high degree of crystallinity, because there was no T_g observed. The observed T_g, T_c, and T_m in PEG-PBC indicate the existence of both amorphous domain and crystalline domains in PEG_{114}-PBC_{30}, which is a semicrystalline polymer. We also calculated the degree of crystallinity based on the DSC peak areas, which was 57.1%. Different degrees of crystallinity of PEG_{114}-PCC_{30}, PEG_{114}-PBC_{30}, and PEG_{114}-PCD_{29} might be due to the different intermolecular forces among these three polymers with different hydrophobic core structures. We also determined the effect of hydrophobic core size on the T_m of PEG-PCD. As shown in Figure 5B, the T_m for PEG_{114}-PCD_{29}, PEG_{114}-PCD_{16}, and PEG_{114}-PCD_6 were 51.7, 53.6, 55.3 °C, respectively.

The polymers were further characterized by fluorescence spectroscopy to determine the CMC (Figure 6). PEG_{114}-PBC_{30} and PEG_{114}-PCD_{29} had low CMC values of 4.0×10^{-4} g/L and 3.6×10^{-4} g/L, respectively. In contrast, the CMC of PEG_{114}-PCC_{30} was 2.2×10^{-2} g/L, which was around 50 folds higher than those of PEG_{114}-PBC_{30} or PEG_{114}-PCD_{29}. The low CMC indicates the good stability of micelles prepared from PEG_{114}-PBC_{30} and PEG_{114}-PCD_{29}. The effect of hydrophobic core size on PEG-PCD micelle stability was also determined. The CMC of PEG-PCD micelles decreased significantly from 1.4×10^{-3} g/L to 3.6×10^{-4} g/L when the DP(n) increased from 6 to 29 (Figure 6B).

3.2. Preparation and Characterization of Micelles. *3.2.1. Drug Loading Efficiency.* The amount of embelin loaded into polymeric micelles and loading efficiency were calculated using the equations described in the experimental methods. As demonstrated in Figure 7, PEG-PBC showed 2% drug loading at 5% theoretical loading, which corresponds to 40% loading efficiency, in contrast, 5% drug loading was achieved by PEG-PCD with different hydrophobic core lengths, which corresponds to 100% loading efficiency. Increase in theoretical loading from 5 to 10% showed little effect on the drug loading of PEG-PBC micelles and the loading efficiency decreased correspondingly.

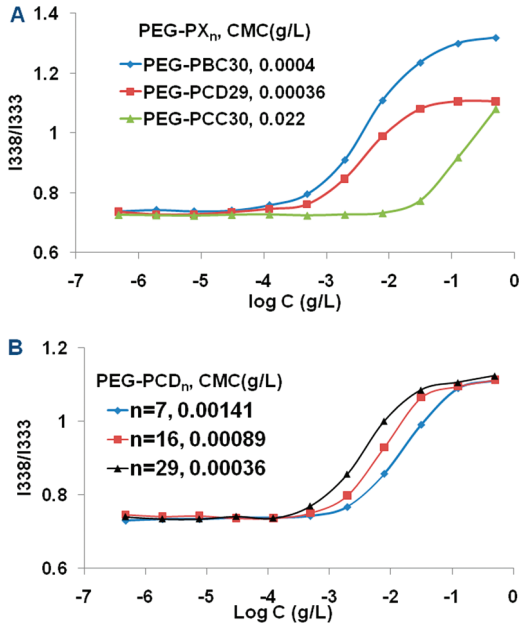

Figure 6. Plots of the intensity ratio I_{338}/I_{333} from pyrene excitation spectra at $\lambda_{em} = 390$ nm vs log C for (A) polymer with different core structures: PEG_{114}-PBC_{30}, PEG_{114}-PCD_{29}, and PEG_{114}-PCC_{30}. (B) PEG-PCD polymers with different PCD core length: $n = 6$, 16, and 29.

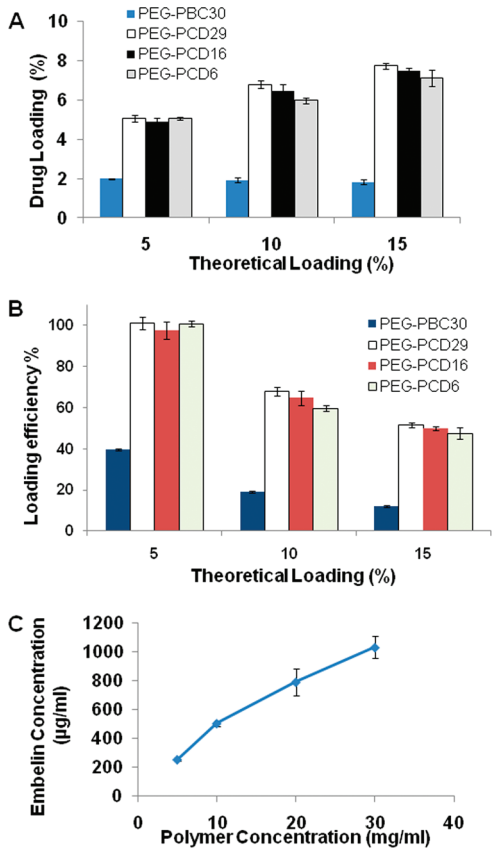

Figure 7. Optimization of embelin-loaded micelle formulations. (A) Effect of hydrophobic core structure and length on drug loading and (B) loading efficiency. Embelin-loaded PEG-PBC and PEG-PCD micelles were prepared at 5, 10, and 15% of theoretical drug loading. (C) Encapsulation of embelin by PEG-PCD micelles as a function of polymer concentration.

However, the drug loading increased from 5 to 6 and 7% for PEG-PCD micelles, when theoretical loading increased from 5

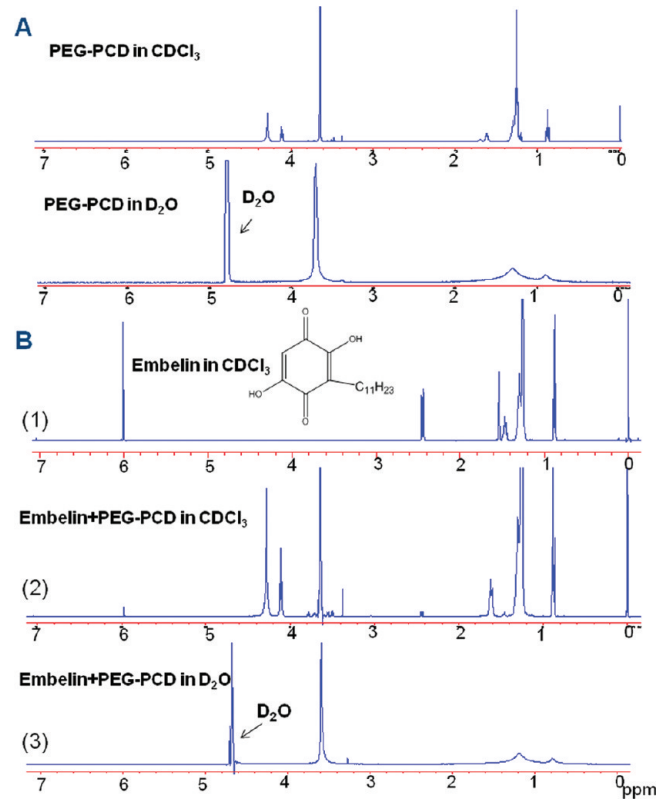

Figure 8. Core−shell structure formed by PEG_{114}-PCD_{29} lipopolymer. (A) ^{1}H NMR of blank PEG_{114}-PCD_{29} in $CDCl_3$ and D_2O. (B) ^{1}H NMR of PEG_{114}-PCD_{29} and emblin: (1) free embelin dissolved in $CDCl_3$; (2) embelin and PEG_{114}-PCD_{29} dissolved in $CDCl_3$ at embelin to polymer ratio of 3%; (3) embelin-loaded PEG_{114}-PCD_{29} micelles in D_2O at embelin to polymer ratio of 3%.

to 10 and 15%, with decrease in loading efficiency from 100 to 60 and 50%, respectively. There was no significant difference among three PEG-PCD lipopolymers with different hydrophobic core lengths.

3.2.2. Core−Shell Structure Formation. ^{1}H NMR spectroscopy was used to demonstrate the formation of core−shell of PEG-PCD lipopolymer micelles (Figure 8). In $CDCl_3$, peaks from both the hydrophilic PEG block (3.6 ppm) and the hydrophobic core block (4.3, 4.1, 1.6, 1.2−1.4, and 0.9 ppm) was observed. In D_2O, all the peaks corresponding to the hydrophobic core block were significantly diminished in contrast to the strong peaks for hydrophilic PEG block (Figure 8A). This is consistent with a core−shell structure with a collapsed hydrophobic core. In addition, we also compared ^{1}H NMR spectra of embelin-loaded PEG-PCD lipopolymer in $CDCl_3$ and D_2O. Although the specific peaks for embelin at 6 and 2.4 ppm was observed when dissolved in $CDCl_3$, they disappeared when they formed micelles in D_2O. These results indicate that PEG-PCD lipopolymer will form micelles in water with a PEG hydrophilic shell and a hydrophobic core, and embelin is incorporated into the hydrophobic core.

3.2.3. Physical Appearance and Particle Size Distribution. The physical appearance of blank and drug-loaded micelles is shown in Figure 9A. Both PEG-PCD and PEG_{114}-PBC_{30} formed a translucent micelle solution, which was stable at room temperature and showed no precipitation on storage at the room temperature for one week. In contrast, there was a milk-like suspension formation of PEG_{114}-PCC_{30} copolymer micelles and precipitation was observed after overnight storage of these micelles. Also, the drug-loaded micelles showed a pink color

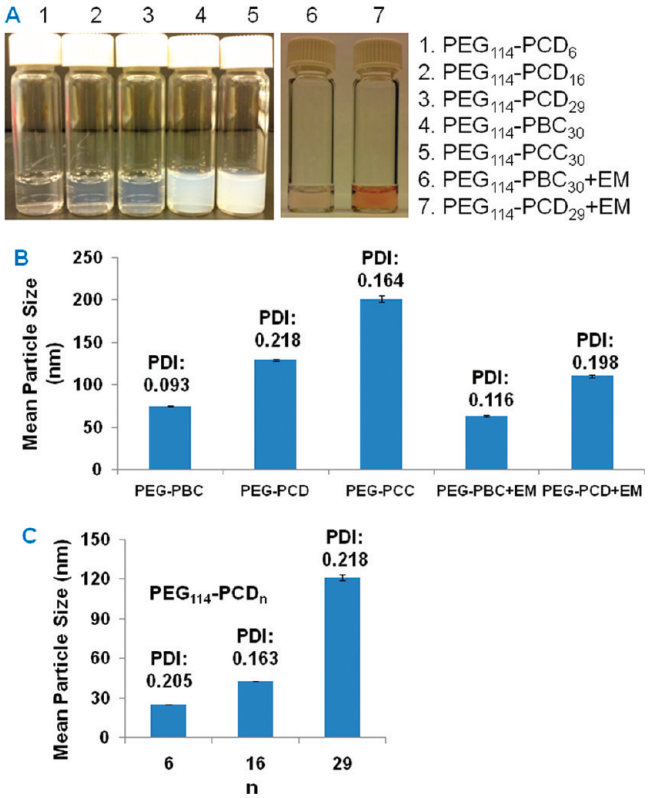

Figure 9. Physical appearance and particle size of micelles. (A) Appearance of blank or embelin-loaded micelles prepared from polymers with different core structure and length (polymer concentration 5 mg/mL). (B) Mean particle size of blank or embelin-loaded micelles prepared from PEG_{114}-PCD_{29}, PEG_{114}-PBC_{30}, and PEG_{114}-PCC_{30}. (C) Mean particle size of micelles prepared from PEG-PCD polymers with different PCD core length: $n = 6$, 16, and 29.

due to the solubilized embelin (EM). The color observed in PEG_{114}-PCD_{29} micelles was darker than those of PEG_{114}-PBC_{30} micelles prepared at the same theoretical loading (5%), and this was consistent with the high drug loading in PEG_{114}-PCD_{29} micelles. We also determined the particle size and size distribution of blank and embelin-loaded micelles by dynamic light scattering (Figure 9B). The blank and embelin-loaded PEG_{114}-PCB_{30} micelles had the mean particle size of 74 and 64 nm, respectively. The particle size of blank and embelin-loaded PEG_{114}-PCD_{29} micelles was 129 and 110 nm, respectively. There was no increase in the mean particle size after embelin loading. In contrast, micelles formed by PEG_{114}-PCC_{30} showed a particle size of 204 nm. We also determined the particle size of PEG-PCD with different PCD core lengths; the mean particle sizes were 129 nm for PEG_{114}-PCD_{29}, 42.6 nm for PEG_{114}-PCD_{16}, and 25 nm for PEG_{114}-PCD_{6}, respectively.

3.2.4. Morphology of Micelles. The morphology of micelles formed by PEG-PBC and PEG-PCD was determined by transmission electron micrography (TEM; Figure 10). PEG-PCD formed micelles with different morphologies and sizes, depending on the ratio of hydrophobic core (Figure 10A−C). PEG_{114}-PBC_{30} formed spherical micelles (Figure 10D). PEG_{114}-PCD_{29} formed both spherical and cylindrical micelles with a diameter less than 50 nm, and the cylindrical micelle was the dominant form. The contour length of the cylindrical micelles ranged from several hundred nanometers to several micrometers. However, PEG_{114}-PCD_{16} and PEG_{114}-PCD_{6} formed only spherical micelles. We also determined the morphology of embelin loaded micelles prepared from PEG_{114}-PCD_{6}, PEG_{114}-PCD_{16}, PEG_{114}-PCD_{29}, and PEG_{114}-PBC_{30}. As shown in Figure S2, the loading of embelin

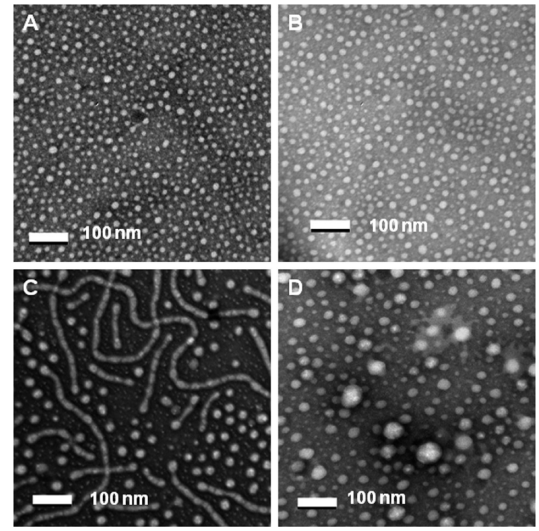

Figure 10. Transmission electron microscopy (TEM) of micelle prepared from (A) PEG_{114}-PCD_{6}, (B) PEG_{114}-PCD_{16}, (C) PEG_{114}-PCD_{29}, and (D) PEG_{114}-PBC_{30}.

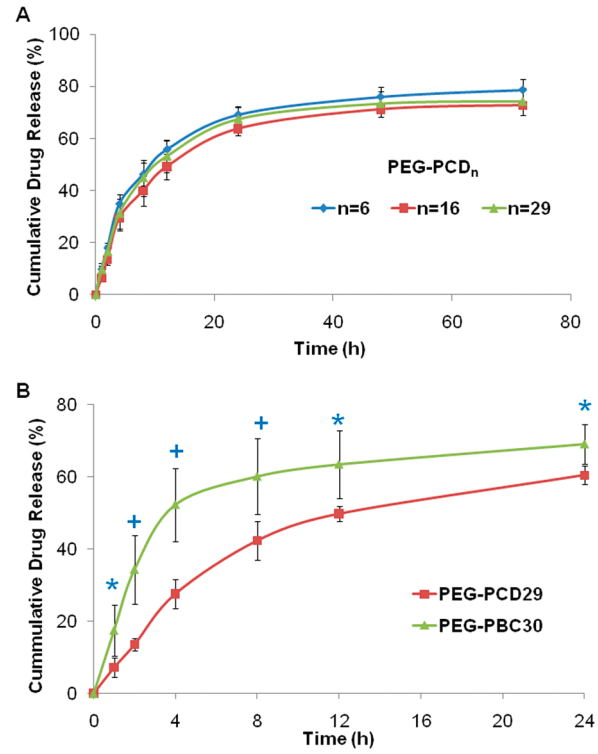

Figure 11. In vitro release of embelin from polymeric micelles. (A) Release profiles of PEG-PCD micelles with different PCD core lengths at drug loading of 5%. (B) Release profiles of PEG_{114}-PCD_{29} and PEG_{114}-PBC_{30} micelles at drug loading of 2%. * $P < 0.05$, + $P < 0.01$, compared with PEG_{114}-PBC_{30} micelles using Student's unpaired *t* test. Results were expressed as mean ± SD ($n = 3$).

at 5% in PEG-PCD and 2% at PEG_{114}-PBC_{30} had no effect on the morphology of micelles.

3.2.6. In Vitro Drug Release. The cumulative percentage of embelin released from PEG-PCD micelles with different PCD block length was shown in Figure 11A. Similarity factors (f_2) were calculated to compare the drug release profiles of micelles with various hydrophobic core lengths. The similarity factors were 63 ($n = 6$ vs 16), 78 ($n = 6$ vs 29), and 74 ($n = 16$ vs 29), respectively. Therefore, these micelles showed similar release profiles because the release profiles are considered as the same when the similarity factors are greater than 50. The

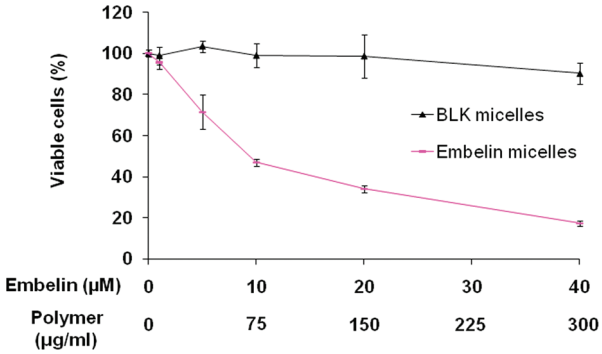

Figure 12. Inhibition of C4-2 cell proliferation by blank and PEG_{114}-PCD_{29} micelle formulated embelin. The weight ratio of embelin and polymer was 4% (embelin/polymer). Blank micelles with same polymer concentration were served as control. Cell viability was determined by MTT assay at 72 h post treatment. Results were expressed as mean ± SD ($n = 4$).

release of embelin from PEG-PCD micelles was fit to a first-order process for the first 24 h. The release half-life was around 12 h. The effect of hydrophobic core on embelin release was also investigated (Figure 11B). The release of embelin from PEG_{114}-PCD_{30} was significantly slower compared to PEG_{114}-PBC_{30} with a similarity factor of 38. In addition, the embelin release half-life from PEG_{114}-PBC_{30} micelles was 4 h, which was much shorter than that of PEG_{114}-PCD_{30}.

3.2.7. Bioevaluation of Drug Loaded Micelles. The anticancer activity of embelin loaded PEG-PCD micelles was determined in C4−2 prostate cancer cells. As shown in Figure 12, while blank PEG_{114}-PCD_{29} polymer showed negligible effect on cell proliferation at polymer concentration up to 0.3 mg/mL, embelin-loaded PEG_{114}-PCD_{29} micelles showed significant inhibition of C4-2 cell proliferation in a dose-dependent manner, with the IC_{50} of 10 μM. The free drug dissolved in DMSO showed similar anticancer effects to micelle formulated embelin (data not shown). No direct comparison can be made with the results of embelin formulated in micelles and dissolved in DMSO, as DMSO is known to kill tumor cells and may not be suitable for in vivo applications. However, this finding is significant because the application of polymeric micelles could avoid the use of toxic solubilzing agents such as DMSO, Cremophore EL, and Tween 80.

4. Discussion

Polymeric micelles can serve as a vehicle, which self-assemble into a core−shell structure with a hydrophobic core capable of loading hydrophobic drugs.[17,18] The stealth properties associated with hydrophilic PEG corona of micelles prevent their aggregation, restrict plasma protein adsorption, prevent recognition by the reticuloendothelial system (RES), and minimize their rapid elimination from the bloodstream. The small size of micelles ensures their accumulation preferentially in the tumor via EPR effects.[19,20] However, successful micellar drug delivery into tumor requires the micelles remain stable during blood circulation upon systemic administration. The stability of micelles could be enhanced by cross-linking of the shell, core−shell interface, or the core of the micelles.[21−23] However, the application of chemical cross-linked micelles is limited due to the complexity of cross-linking process, possible effects on the structure and properties of loaded drugs, and problems associated with drug release. Alternatively, the stability of micelles could also be improved by engineering the structure of hydrophobic block by introducing aromatic moieties.[24,25]

We have successfully synthesized PEG-PCD lipopolymer with two different approaches (Figure 1). However, the first approach was selected due to the relative simplicity in the synthesis process, which is critical for its application. In this synthesis approach, PEG-PBC was synthesized by ring-opening polymerization of MBC in the presence of PEG carrying a hydroxyl end group with one of the following catalysts: DBU, $Sn(oct)_2$, and Et_2Zn (Table 1). Relatively lower reaction efficiency was observed with $Sn(oct)_2$ and Et_2Zn; this is due to the high reaction temperature and long reaction time required for these two catalysts, which is usually associated with the potential polymer degradation due to transesterification or backbiting side reaction.[24,26] In addition, the use of these metallic catalysts is also associated with safety issues due to the presence of trace metal residue in the polymer. Therefore, DBU was used in the current study, which is purely organic and suitable for the synthesis of biomaterials. Besides, the reaction was carried out in solution and at room temperature, which is superior to bulk reaction that usually results in broad polydispersity due to the inefficient mixing of reactants. To optimize the reaction time, molecular weight of the polymer was monitored during the reaction. We found that the reaction was almost completed after 3 h and the DP of polymerization decreased after reaction for 24 h. This may be due to the occurring of transesterification of polymer, which becomes dominant when the monomer is consumed.[26] Therefore, the reaction time was set to 3 h to achieve optimal polymerization efficiency and polydispersity. Subsequently, the benzyl groups in the PEG-PBC were removed via hydrogenation to expose COOH function group. This reaction was also carried out under at the room temperature to avoid the potential degradation of polymer backbone, while still maintaining the high reaction efficiency to completely remove benzyl groups. The dodecanol was conjugated to the COOH groups in the polymer backbone through EDC/HOBT coupling chemistry with conjugation efficiency of around 95%. This is much higher than the previous report, where less than 70% of conjugation efficiency was achieved in conjugating fatty acids to poly(ethylene glycol)-*block*-poly(β-benzyl-L-aspartate) through a link molecule.[27] Because of the commercial availability of starting materials, simple synthesis procedure, and high reaction efficiency, this synthesis procedure will have a broad application in the drug delivery and bioengineering.

PEG-PCD lipopolymer synthesized in the current study has the polycarbonate backbone and dodecanol was conjugated to this backbone with an ester bond. Therefore, this is a biodegradable polymer, which is expected to degrade in vivo through hydrolysis of the ester linkages. The hydrolysis of polycarbonate backbone was facilitated at the presence of esterase such as lipase or cholesterol esterase.[28,29] In addition, the final degradation product was CO_2, dual alcohol, dodecanol, and PEG_{5000}, which have less effect on pH change in vivo compared to poly(D,L-lactide) and thus are less likely to cause inflammation.[30] These degradation products are nontoxic and could be eliminated from the body.

PEG-PCD lipopolymer has multiple dodecanol lipid chains attached to the polycarbonate backbone, which mimics the structure of interface cross-linked PEG-lipids (Figure 13) and could enhance the hydrophobic interaction among the hydrophobic cores. Because the cross-linking of micelles are known to improve stability, it is not surprising to observe significantly reduced CMC values for PEG-PCD lipopolymer compared to conventional PEG-lipid conjugates. Due to its low CMC value ($\sim 10^{-8}$ M), the concentration of PEG-PCD in the bloodstream is expected to be much higher than the CMC value of PEG-

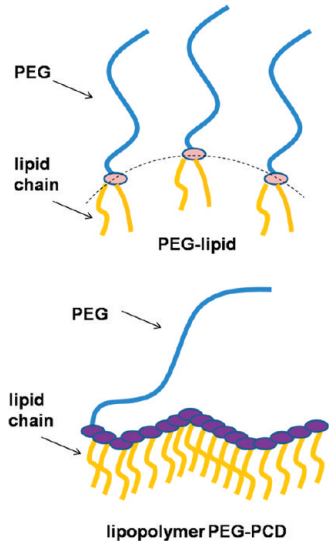

Figure 13. Structure of PEG-lipid and lipopolymer PEG-PCD.

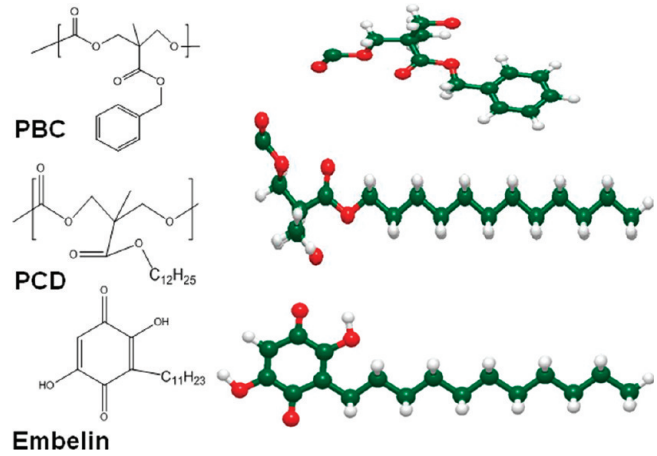

Figure 14. Structure of embelin and the repeating unit of the hydrophobic core.

PCD after systemic administration, which indicates its good in vivo stability. Therefore, PEG-PCD lipopolymer micelles can serve as an alternative to cross-linked PEG-lipid micelles for in vivo drug delivery.

Among PEG-PCD series, we found that the CMC decreased with increasing the number of lipid in the hydrophobic core (Figure 6B). This is due to the increased length of hydrophobic block, which is known to enhance the hydrophobic interaction among the core block.[31] The effects of core structure were also investigated and the results showed that the CMC of PEG-PCD or PEG-PBC was around 50-fold lower than corresponding PEG-PCC (Figure 6A). This is because of the presence of hydrophobic aromatic rings in PEG-PBC and lipid chains in PEG-PCD, which will all facilitate the hydrophobic interaction within the core of micelles and promote the self-assembly of polymeric micelles. However, PEG-PCC has a higher CMC due to the presence of COOH group which significantly reduced the hydrophobicity of the core block. Comparable CMC values were observed for PEG-PBC and PEG-PCD, though the structure of PBC and PCD are significantly different (Figure 6A). Because the backbone is the same for PEG-PBC and PEG-PCD, the close similarity in CMC values are due to comparable contributions by the pedant phenyl rings in the PBC and the pedant dodecanol carbon chain in PCD to the core block hydrophobicity.

Spherical, cylindrical, and vesicular assemblies are three commonly observed morphologies of micelles prepared from amphiphilic block copolymers. Recently, interest has shifted from spherical to cylindrical micelles due to their longer systemic circulation time compared to spherical micelles.[32–34] The cylindrical micelles prepared from poly(ethylene glycol)-*b*-poly(caprolactone) (PEG-PCL) showed significantly longer circulation time than that of spherical micelles prepared from the same polymer and was persistent up to several days after intravenous injection.[32] In addition, paclitaxel-loaded cylindrical micelles were more effective to induce apoptosis and reduce the tumor size in tumor bearing mice.[33,34] Several approaches have been investigated to control the morphology of micelles, including kinetic control,[35] the use of interfacial instability,[36] aromatic oxidation,[37] and the use of nanopore extruder.[38] The most important parameter that determines the morphology and architecture of micelles is the copolymer composition and volume ratio between insoluble and soluble blocks. Sumeet et al. have studied the effect of molecular size and composition using poly(ethylene glycol)-*b*-poly(1,2-butadiene) (PEG-PB) as a model diblock copolymer. These authors found that PEG-PB form spheres, cylinders, and bilayers in water, sequentially, with decreased ratio of PEG block.[39] This could explain the transition from spherical to cylindrical micelles with the increased hydrophobic length of PEG-PCD. In the current study, the use of PEG-PCD_{29} with a PEG ratio of 0.37 produced cylindrical micelles, while PEG-PCD_6 (PEG ratio: 0.49) and PEG-PCD_{16} (PEG ratio: 0.72) produced only spherical micelles. Although PEG-PCD_{29} formed cylindrical micelles, PEG-PBC_{30}, a polymer with similar hydrophobic core length did not form cylindrical micelles, but instead formed spherical micelles (Figure 10). This indicates that not only the PEG ratio but also the structure of hydrophobic core determines the morphology of micelles. Thus, the morphology of micelles can be controlled by changing the length and structure of the hydrophobic core of the polymer. The preparation of micelles of different morphologies will help us to understand the effect of micelles morphology and their in vivo biodistribution and bioactivities.

The compatibility of core-forming block and the drug to be loaded is critical for drug loading capacity.[12] One objective of this study was to design an engineered polymeric micelle for improved solubilization and delivery of embelin based on the polymer−drug compatibility. PEG-PCD showed significantly high embelin loading capacity compared with PEG-PBC (Figure 7), although these two polymers have similar CMC value and comparable thermodynamic stability. The compatibility is highly dependent on the three-dimensional arrangement and conformation of different groups in the structure of drug and polymer core.[25] Figure 14 illustrates the structure of embelin and the repeating units of the PEG-PBC and PEG-PCD hydrophobic core block. In contrast to PEG-PBC, the structure of the repeating unit of PEG-PCD is similar to that of embelin. A similar finding was reported previously, where the attachment of cholesterol to the poly(caprolactone) block of a poly(ethylene glycol)-*b*-poly(caprolactone) copolymer significantly improved the loading of cucurbitacin I, which is similar to cholesterol in the structure.[25] Our previous data also showed that the introduction of carbonate moiety into a PEG-PLA copolymer significantly increased the micellar solubility and loading of bicalutamide into micelles.[12] In this study, we also found that PEG-PCD lipopolymers with different core block lengths (repeating unit number ranges from 6 to 29) did not show significant differences in the drug loading (Figure 7). Although an increased drug loading efficiency was observed with an increased length

of PCL blocks in PEG-PCL polymer,[40] this may not be applicable for PEG-PCD, which has a highly branched structure in contrast to the linear structure of PEG-PCL. In fact, a good drug loading was observed in PEG-lipid conjugates with a much shorter hydrophobic core length,[3] indicating that the further increase in hydrophobic length might not be able to improve the drug loading of lipopolymers with similar structure as PEG-PCD. Similarly, we also observed there was no significant difference in the in vitro drug release profiles among these PEG-PCD polymers with different block lengths (Figure 11A). The drug release profiles of polymeric micelles are influenced by several factors including strength of the interaction between drug and hydrophobic core, physical state of the core, the amount of drug loaded, the length of the hydrophobic core, and the location of the drug inside the micelle core.[31] In addition, the highly branched structure in the hydrophobic core of PEG-PCD may have contributed to the observation in this study. We also found that the release of embelin from PEG-PCD was much slower than that from PEG-PBC (Figure 11B). This might due to the fact that the interaction between PEG-PCD and embelin was stronger than those of PEG-PBC and embelin.

5. Conclusion

We have successfully synthesized a novel lipopolymer poly(ethylene glycol)-*block*-poly(2-methyl-2-carboxyl-propylene carbonate-graft-dodecanol) (PEG-PCD) for delivery of a hydrophobic anticancer drug, embelin. PEG-PCD lipopolymer could form micelles in water through self-assembly and significantly improved embelin solubility by loading drugs inside its hydrophobic core. The drug loading and encapsulation efficiency were dependent on the length and structure of the polymer hydrophobic core block. The CMC of PEG-PCD micelles was around 10^{-8} M and decreased with increasing the length of hydrophobic block, indicating good thermodynamic stability of PEG-PCD micelles. The particle size and morphology of micelles were also dependent on the structure and length of the hydrophobic core. Embelin-loaded PEG-PCD micelles showed significant inhibition of C4-2 prostate cancer cell proliferation in a dose-dependent manner, while no obvious cellular toxicity was observed with blank micelles themselves. Thus, these lipopolymer have the potential to be used as vehicles for anticancer hydrophobic drug delivery.

Acknowledgment. This work is partially supported by the teaching assistantship from the University of Tennessee College of Pharmacy to F.L.

Supporting Information Available. (1) ^{1}H NMR of 2-methyl-2-carboxyl-propylene carbonate (MCC) in DMSO and 2-methyl-2-dodecanoxycarbonyl-propylene carbonate (MDC) in $CDCl_3$. (2) Transmission electron microscopy (TEM) of embelin-loaded micelles (A) PEG_{114}-PCD_6, (B) PEG_{114}-PCD_{16}, (C) PEG_{114}-PCD_{29}, and (D) PEG_{114}-PBC_{30}. This material is available free of charge via the Internet at http://pubs.acs.org.

References and Notes

(1) Hennenfent, K. L.; Govindan, R. Novel formulations of taxanes: a review. Old wine in a new bottle. *Ann. Oncol.* **2006**, *17* (5), 735–49.
(2) Gaucher, G.; Marchessault, R. H.; Leroux, J. C. Polyester-based micelles and nanoparticles for the parenteral delivery of taxanes. *J. Controlled Release* **2010**, *143* (1), 2–12.
(3) Lukyanov, A. N.; Torchilin, V. P. Micelles from lipid derivatives of water-soluble polymers as delivery systems for poorly soluble drugs. *Adv. Drug Delivery Rev.* **2004**, *56* (9), 1273–89.
(4) Torchilin, V. P. Lipid-core micelles for targeted drug delivery. *Curr. Drug Delivery* **2005**, *2* (4), 319–27.
(5) Kabanov, A. V.; Batrakova, E. V.; Alakhov, V. Y. Pluronic block copolymers as novel polymer therapeutics for drug and gene delivery. *J. Controlled Release* **2002**, *82* (2−3), 189–212.
(6) Kabanov, A. V.; Batrakova, E. V.; Alakhov, V. Y. Pluronic block copolymers for overcoming drug resistance in cancer. *Adv. Drug Delivery Rev.* **2002**, *54* (5), 759–79.
(7) Kabanov, A. V.; Batrakova, E. V.; Alakhov, V. Y. An essential relationship between ATP depletion and chemosensitizing activity of Pluronic block copolymers. *J. Controlled Release* **2003**, *91* (1−2), 75–83.
(8) Jeong, B.; Bae, Y. H.; Lee, D. S.; Kim, S. W. Biodegradable block copolymers as injectable drug-delivery systems. *Nature* **1997**, *388* (6645), 860–2.
(9) Nishiyama, N.; Kataoka, K. Current state, achievements, and future prospects of polymeric micelles as nanocarriers for drug and gene delivery. *Pharmacol. Ther.* **2006**, *112* (3), 630–48.
(10) Danquah, M.; Li, F.; Duke, C. B., 3rd; Miller, D. D.; Mahato, R. I. Micellar delivery of bicalutamide and embelin for treating prostate cancer. *Pharm. Res.* **2009**, *26* (9), 2081–92.
(11) Yasugi, K.; Nagasaki, Y.; Kato, M.; Kataoka, K. Preparation and characterization of polymer micelles from poly(ethylene glycol)-poly(D,L-lactide) block copolymers as potential drug carrier. *J. Controlled Release* **1999**, *62* (1−2), 89–100.
(12) Danquah, M.; Fujiwara, T.; Mahato, R. I. Self-assembling methoxy-poly(ethylene glycol)-*b*-poly(carbonate-*co*-L-lactide) block copolymers for drug delivery. *Biomaterials* **2010**, *31* (8), 2358–70.
(13) Lavasanifar, A.; Samuel, J.; Kwon, G. S. Micelles of poly(ethylene oxide)-*block*-poly(*N*-alkyl stearate L-aspartamide): synthetic analogues of lipoproteins for drug delivery. *J. Biomed. Mater. Res.* **2000**, *52* (4), 831–5.
(14) Lavasanifar, A.; Samuel, J.; Kwon, G. S. Micelles self-assembled from poly(ethylene oxide)-*block*-poly(*N*-hexyl stearate L-aspartamide) by a solvent evaporation method: effect on the solubilization and haemolytic activity of amphotericin B. *J. Controlled Release* **2001**, *77* (1−2), 155–60.
(15) Li, F.; Lu, Y.; Li, W.; Miller, D. D.; Mahato, R. I. Synthesis, formulation and in vitro evaluation of a novel microtubule destabilizer, SMART-100. *J. Controlled Release* **2010**, *143* (1), 151–8.
(16) Koester, L. S.; Ortega, G. G.; Mayorga, P.; Bassani, V. L. Mathematical evaluation of in vitro release profiles of hydroxypropylmethylcellulose matrix tablets containing carbamazepine associated to beta-cyclodextrin. *Eur. J. Pharm. Biopharm.* **2004**, *58* (1), 177–9.
(17) Yamamoto, T.; Yokoyama, M.; Opanasopit, P.; Hayama, A.; Kawano, K.; Maitani, Y. What are determining factors for stable drug incorporation into polymeric micelle carriers? Consideration on physical and chemical characters of the micelle inner core. *J. Controlled Release* **2007**, *123* (1), 11–8.
(18) Leung, S. Y.; Jackson, J.; Miyake, H.; Burt, H.; Gleave, M. E. Polymeric micellar paclitaxel phosphorylates Bcl-2 and induces apoptotic regression of androgen-independent LNCaP prostate tumors. *Prostate* **2000**, *44* (2), 156–63.
(19) Maeda, H.; Wu, J.; Sawa, T.; Matsumura, Y.; Hori, K. Tumor vascular permeability and the EPR effect in macromolecular therapeutics: a review. *J. Controlled Release* **2000**, *65* (1−2), 271–84.
(20) Greish, K.; Nagamitsu, A.; Fang, J.; Maeda, H. Copoly(styrene-maleic acid)-pirarubicin micelles: high tumor-targeting efficiency with little toxicity. *Bioconjugate Chem.* **2005**, *16* (1), 230–6.
(21) Shuai, X.; Merdan, T.; Schaper, A. K.; Xi, F.; Kissel, T. Core-cross-linked polymeric micelles as paclitaxel carriers. *Bioconjugate Chem.* **2004**, *15* (3), 441–8.
(22) Xu, Y.; Meng, F.; Cheng, R.; Zhong, Z. Reduction-sensitive reversibly crosslinked biodegradable micelles for triggered release of doxorubicin. *Macromol. Biosci.* **2009**, *9* (12), 1254–61.
(23) Tian, L.; Yan, L.; Wang, J.; Tat, H.; Uhrich, K. Core crosslinkable polymeric micelles from PEG-lipid amphiphiles as drug carriers. *J. Mater. Chem.* **2004**, *14*, 2317–2324.
(24) Mahmud, A.; Xiong, X.; Lavasanifar, A. Novel self-associating poly(ethylene oxide)-*block*-poly(epsilon-caprolactone) block copolymers with functional side groups on the polyester block for drug delivery. *Macromolecules* **2006**, *39*, 9419–28.
(25) Mahmud, A.; Patel, S.; Molavi, O.; Choi, P.; Samuel, J.; Lavasanifar, A. Self-associating poly(ethylene oxide)-*b*-poly(α-cholesteryl carboxylate-ε-caprolactone) block copolymer for the solubilization of STAT-3 inhibitor Cucurbitacin I. *Biomacromolecules* **2009**, *10* (3), 471–478.
(26) Seow, W. Y.; Yang, Y. Y. Functional polycarbonates and their self-assemblies as promising nonviral vectors. *J. Controlled Release* **2009**, *139* (1), 40–7.

(27) Lavasanifar, A.; Samuel, J.; Kwon, G. S. The effect of fatty acid substitution on the in vitro release of amphotericin B from micelles composed of poly(ethylene oxide)-*block*-poly(*N*-hexyl stearate-L-aspartamide). *J. Controlled Release* **2002**, *79* (1−3), 165–72.
(28) Zhu, K.; Hendren, R.; Jensen, K.; Pitt, C. Synthesis, properties, and biodegradation of poly(1,3-trimethylene carbonate. *Macromolecules* **1991**, *24* (8), XXX.
(29) Tang, Y. W.; Labow, R. S.; Santerre, J. P. Enzyme-induced biodegradation of polycarbonate-polyurethanes: Dose dependence effect of cholesterol esterase. *Biomaterials* **2003**, *24* (12), 2003–11.
(30) Gao, J.; Guo, Y.; Gu, Z.; Zhang, X. Micellization and controlled release properties of methoxy poly(ethylene glycol)-*b*-poly(D,L-lactide-*co*-trimethylene carbonate. *Front. Chem. China* **2009**, *4* (1), .
(31) Allen, C.; Maysinger, D.; Eisenberg, A. Nano-engineering block copolymer aggregates for drug delivery. *Colloids Surf., B* **1999**, *16*, 3–27.
(32) Geng, Y.; Dalhaimer, P.; Cai, S.; Tsai, R.; Tewari, M.; Minko, T.; Discher, D. E. Shape effects of filaments versus spherical particles in flow and drug delivery. *Nat. Nanotechnol.* **2007**, *2* (4), 249–55.
(33) Cai, S.; Vijayan, K.; Cheng, D.; Lima, E. M.; Discher, D. E. Micelles of different morphologies—advantages of worm-like filomicelles of PEO-PCL in paclitaxel delivery. *Pharm. Res.* **2007**, *24* (11), 2099–109.
(34) Christian, D. A.; Cai, S.; Garbuzenko, O. B.; Harada, T.; Zajac, A. L.; Minko, T.; Discher, D. E. Flexible filaments for in vivo imaging and delivery: persistent circulation of filomicelles opens the dosage window for sustained tumor shrinkage. *Mol. Pharm.* **2009**, *6* (5), 1343–52.
(35) Cui, H.; Chen, Z.; Zhong, S.; Wooley, K. L.; Pochan, D. J. Block copolymer assembly via kinetic control. *Science* **2007**, *317* (5838), 647–50.
(36) Zhu, J.; Hayward, R. C. Spontaneous generation of amphiphilic block copolymer micelles with multiple morphologies through interfacial Instabilities. *J. Am. Chem. Soc.* **2008**, *130* (23), 7496–502.
(37) Baram, J.; Shirman, E.; Ben-Shitrit, N.; Ustinov, A.; Weissman, H.; Pinkas, I.; Wolf, S. G.; Rybtchinski, B. Control over self-assembly through reversible charging of the aromatic building blocks in photofunctional supramolecular fibers. *J. Am. Chem. Soc.* **2008**, *130* (45), 14966–7.
(38) Chen, Q.; Zhao, H.; Ming, T.; Wang, J.; Wu, C. Nanopore extrusion-induced transition from spherical to cylindrical block copolymer micelles. *J. Am. Chem. Soc.* **2009**, *131* (46), 16650–1.
(39) Jain, S.; Bates, F. S. On the origins of morphological complexity in block copolymer surfactants. *Science* **2003**, *300* (5618), 460–4.
(40) Park, E. K.; Lee, S. B.; Lee, Y. M. Preparation and characterization of methoxy poly(ethylene glycol)/poly(ε-caprolactone) amphiphilic block copolymeric nanospheres for tumor-specific folate-mediated targeting of anticancer drugs. *Biomaterials* **2005**, *26* (9), 1053–61.

BM100561V

Biomaterials 31 (2010) 2358–2370

Contents lists available at ScienceDirect

Biomaterials

journal homepage: www.elsevier.com/locate/biomaterials

Self-assembling methoxypoly(ethylene glycol)-b-poly(carbonate-co-L-lactide) block copolymers for drug delivery

Michael Danquah [a], Tomoko Fujiwara [b], Ram I. Mahato [a,*]

[a] Department of Pharmaceutical Sciences, University of Tennessee Health Science Center, 19 South Manassas (Room 224), Memphis, TN 38103-3308, USA
[b] Department of Chemistry, The University of Memphis, Memphis, TN 38152, USA

ARTICLE INFO

Article history:
Received 11 September 2009
Accepted 24 November 2009
Available online 17 December 2009

Keywords:
Micelles
Copolymer
Polyethylene glycol
Polycarbonate
Poly lactic acid
Bicalutamide

ABSTRACT

Bicalutamide is the most widely used non-steroidal antiandrogen for treating early stage prostate cancer, but suffers variable oral absorption due to its limited aqueous solubility. Thus, our objective was to synthesize novel biodegradable copolymers for the systemic micellar delivery of bicalutamide. Flory–Huggins interaction parameter (χ_{FH}) was used to assess compatibility between bicalutamide and poly(L-lactide) or poly(carbonate-co-lactide) polymer pairs. Polyethylene glycol-b-poly(carbonate-co-lactide) [PEG-b-P(CB-co-LA)] copolymers were synthesized and characterized by NMR and gel permeation chromatography. These micelles had average diameter of 100 nm and had a smooth surface and distinct spherical shape. Drug loading studies revealed that adding the carbonate monomer could increase bicalutamide loading. Among the series, drug loading of micelles formulated with PEG-b-P(CB-co-LA) copolymer containing 20 mol% carbonate was about four-fold higher than PEG-b-PLLA and aqueous solubility of bicalutamide increased from 5 to 4000 μg/mL. CMC values for PEG-b-P(CB-co-LA) copolymers was up to 10-fold lower than those of PEG-b-PLLA. *In vitro* release experiments showed PEG-b-P(CB-co-LA) copolymers to be more efficient in sustaining the release of bicalutamide compared to PEG-b-PLLA. Bicalutamide-loaded PEG-b-P(CB-co-LA) micelles showed significant inhibition of LNCaP cell growth in a dose-dependent manner which was similar to the methanol solution of free drug.

1. Introduction

Androgens are known to play a pivotal role in the development and maintenance of the prostate by interacting with the androgen receptor (AR) [1]. Consequently, androgen ablation, especially the use of antiandrogens, has been used as a standard treatment for men with prostate cancer. Among various antiandrogens, bicalutamide (Casodex™) is the most widely used non-steroidal antiandrogen for treating early stage prostate cancer due to its relatively long half life and tolerable side effects [2]. However, bicalutamide exhibits poor aqueous solubility (5 μg/mL), which results in poor and variable drug absorption across the gastro intestinal tract. Furthermore, bicalutamide cannot be administered systemically, as traditional approaches to increase its aqueous solubility using solubilizing agents such as dimethyl sulfoxide (DMSO) and Cremophor EL is not practical in humans due to hemolysis, acute hypertensive reactions and neuropathies [3].

One way of improving the solubility of hydrophobic drugs and in particular bicalutamide is by using polymeric micelles. Micelles are attractive drug delivery vehicles primarily because they can solubilize hydrophobic drugs in their core leading to improved bioavailability and drug stability. Furthermore, micelles are capable of preventing drug degradation, minimizing the adverse effects of the drug on visceral organs and have the possibility of being made site-specific [4]. A number of amphiphilic diblock copolymers composed of polyethylene glycol (PEG) and various biodegradable hydrophobic cores capable of forming micelles have been reported in the literature. Examples include: poly(ethylene glycol)-b-poly(aspartic acid) [PEG-b-PAA] [5], poly(ethylene glycol)-b-poly(lactide-co-glycolic acid) [PEG-b-PLGA][6], poly(ethylene glycol)-b-poly(caprolactone) [PEG-b-PCL] [7] and poly(ethylene glycol)-b-poly(D,L-lactide) [PEG-b-PDLLA] [8]. Key properties of these micelle systems such as size, stability, drug release kinetics and drug loading have also been well studied.

We have recently demonstrated the feasibility of using PEG-b-PDLLA micelles to increase the aqueous solubility of bicalutamide [9]. Although we were able to increase the aqueous solubility of bicalutamide, we observed only moderate drug loading levels

* Corresponding author. Tel.: +1 901 448 6929; fax: +1 901 448 2099.
E-mail address: rmahato@uthsc.edu (R.I. Mahato).
URL: http://www.uthsc.edu/pharmacy/rmahato

0142-9612/$ – see front matter © 2009 Elsevier Ltd. All rights reserved.
doi:10.1016/j.biomaterials.2009.11.081

which may not be high enough for systemic administration. To solve this problem, the focus of the present study was to specifically design and develop a new family of biodegradable amphiphilic copolymers to improve the aqueous solubility of bicalutamide by enhancing its loading levels. Our strategy involves modifying the polyester component of the well established PEG-b-polyester copolymer into polyester/polycarbonate copolymer system. The semicrystalline poly(L-lactide) was chosen as the polyester block because it is FDA approved, possesses good mechanical properties which may provide adequate stability to the micelle system and is known for its application as a drug delivery material [10–12]. For the carbonate block we selected the cyclic 5-methyl-5-benzyloxycarbonyl-1,3-dioxane-2-one carbonate monomer. 5-methyl-5-benzyloxycarbonyl-1,3-dioxane-2-one is a modification of 5-benzyloxycarbonyl-1,3-dioxane-2-one which is an intermediate in the synthesis of numerous antiviral compounds [13]. This carbonate monomer was chosen since polycarbonates are biodegradable, exhibit low toxicity and possess tunable mechanical properties [14–16]. Furthermore, polycarbonate degrades into carbon dioxide and benzyl alcohol, which unlike the degradation products of poly(L-lactide) [*e.g.* lactic acid] are less acidic, has less effect on microenvironment pH and as such will not result in local inflammation. We hypothesize that the introduction of the carbonate monomer would provide additional degrees of freedom to tailor a micelle delivery system that is relatively stable, exhibits improved sustained release and has a hydrophobic core that is more compatible with bicalutamide leading to enhanced drug loading.

Improvement in the extent of compatibility between a drug and the core-forming block of the micelle may translate into superior encapsulation efficiency [17–20]. A number of groups have explored the possibility of predicting drug solubilization in micelles based on thermodynamics and found their predictions to closely approximate experimental results [18,21–23]. Polymer/drug compatibility may be characterized by the Flory–Huggins interaction parameter (χ_{FH}) which accounts for the forces of interaction between the polymer and the drug; and low χ_{FH} values suggest that the polymer is thermodynamically a good solvent for the drug. To design a micelle system with improved drug loading, we first performed an *in silico* study using the Molecular Pro Software to assess the Flory–Huggins interaction parameter (χ_{FH}) between bicalutamide and poly(L-lactide) (PLLA) and a series of poly(carbonate-co-lactide) copolymer with varying carbonate to lactide ratios based on group contribution method.

In this study, a series of poly(ethylene glycol)-b-poly(carbonate-co-lactide) copolymers were synthesized and characterized. Also, the influence of carbonate content on key micelle properties such as size, drug loading, stability and release kinetics was investigated. Furthermore, the microstructure of the micelle core block was analyzed to examine the influence of co-monomer sequence distribution on the physicochemical properties of the copolymer and thermal analysis was used to elucidate the impact of carbonate introduction on the crystalline or amorphous nature of the hydrophobic core. Finally, the efficacy of bicalutamide-loaded micelles was assessed in lymph node adenocarcinoma (LNCaP) human prostate cancer cell lines.

2. Materials and methods

2.1. Materials

2,2-Bis(hydroxymethyl) propionic acid, methoxy poly(ethylene glycol) (mPEG, M_n = 5000, PDI = 1.03), stannous 2-ethylhexanoate ($Sn(Oct)_2$), dicyclohexylcarbodiimide (DCC), dimethylaminopyridine (DMAP) and benzyl bromide were purchased from Sigma Aldrich (St. Louis, MO) and used as received. L-lactide (LA) was purchased from PURAC Biochem bv (Gorinchem, The Netherlands) and recrystallized from ethyl acetate several times. All other reagents were obtained from Sigma Aldrich and used without further purification.

2.2. Computation of solubility and Flory–Huggins interaction parameters (χ_{FH}) of bicalutamide with core of PEG-b-PLLA/PEG-poly(carbonate-co-lactide) micelles

The Flory–Huggins interaction parameter (χ_{FH}) which characterizes polymer–drug compatibility was calculated using equations (1) and (2):

$$\Delta = \left[(\delta_d - \delta_p)^2_{polarity} + (\delta_d + \delta_p)^2_{dispersion} + (\delta_d - \delta_p)^2_{hydrogen}\right]^{\frac{1}{2}} \quad (1)$$

$$\chi_{FH} = \frac{\Delta^2 V_d}{RT} \quad (2)$$

where Δ^2 is the solubility difference between the drug (d) and the core of the polymeric micelle (p). V_d is the molar volume of the drug, T is the temperature in Kelvin and R is the gas constant.

The Hansen partial solubility parameters [$(\delta_x)_d$, $(\delta_x)_p$, $(\delta_x)_h$] for the drug (bicalutamide) and the hydrophobic block of PEG-b-PLLA and PEG-b-poly(carbonate-co-lactide) [PEG-b-P(CB-co-LA)] copolymers used in equation (1) were estimated using the Molecular Modeling Pro software from ChemSW (Fairfield, CA). This software approximates solubility parameters using the Hansen theory of solubility group contribution method. $(\delta_x)_d$, $(\delta_x)_p$ and $(\delta_x)_h$ refers to the partial solubility parameters accounting for Van der Waals forces of dispersion between atoms, permanent dipole–dipole forces between molecules and the proclivity of molecules hydrogen bonding, respectively. Here, subscript x refers to the drug or polymer core.

2.3. Synthesis of 5-methyl-5-benzyloxycarbonyl-1,3-dioxane-2-one

A mixture of 2,2-bis(hydroxymethyl)propionic acid (22.5 g, 0.168 mol), potassium hydroxide (88% assay; 10.75 g, 0.169 mol), and dimethylformamide (DMF) (125 mL) was heated to 100 °C for 1 h with stirring at which point homogenous potassium salt solution was formed. Benzyl bromide (34.5 g, 0.202 mol) was added dropwise to the warm solution, and stirring was continued at 100 °C for 15 h. Upon completion of the reaction, the mixture was cooled and the solvent was removed under vacuum. The residue was dissolved in ethyl acetate (150 mL), hexanes (150 mL), and water (100 mL). The organic layer was retained, washed with water (100 mL), dried (Na_2SO_4), and evaporated. The resulting solid was recrystallized from toluene to give pure benzyl 2,2-bis(methylol)propionate, as white crystals (20 g, 58%).

Benzyl 2,2-bis(methylol)propionate (11.2 g, 0.05 mol) was dissolved in pyridine (25 mL, 0.3 mol) and CH_2Cl_2 (150 mL), and the solution was chilled to −78 °C under N_2. A solution of triphosgene (7.5 g, 25.0 mmol) in CH_2Cl_2 was added dropwise over 1 h, after which the reaction mixture was stirred at room temperature for 2 h. The reaction was quenched by the addition of saturated aqueous NH_4Cl (75 mL). Subsequently, the organic layer was washed with 1 M aqueous HCl (3 × 100 mL), saturated aqueous $NaHCO_3$ (1 × 100 mL), dried (Na_2SO_4), filtered and evaporated to give 5-methyl-5-benzyloxycarbonyl-1,3-dioxane-2-one as a white solid (10.6 g, 95%). The ensuing solid was recrystallized from ethyl acetate prior to polymerization.

2.4. Synthesis of PEG-Poly(carbonate-co-lactide)

Stannous 2-ethylhexanoate (10 mol% relative to mPEG) was added to the mixture of prescribed quantities of PEG, lactide and base monomer in a dried polymerization flask under the protection of nitrogen atmosphere. The reaction mixture was heated to 130 °C for 24 h with stirring. Afterward, the product was cooled to room temperature to terminate the reaction. The copolymer was dissolved in chloroform and precipitated in a large amount of diethyl ether and hexane (1:2), filtered and dried under vacuum at room temperature.

2.5. Polymer characterization

2.5.1. Nuclear magnetic resonance (NMR)

^{1}H NMR spectra were recorded on a JOEL (270 MHz, T = 25 °C) and ^{13}C spectra were recorded with a Varian (500 MHz, T = 25 °C) using deuterated chloroform ($CDCl_3$) and deuterated dimethyl sulfoxide (DMSO-d_6), respectively as solvents. The chemical shifts were calibrated using tetramethylsilane as an internal reference and given in parts per million.

2.5.2. Gel permeation chromatography (GPC)

A Shimadzu 20A GPC system equipped with two Jordi Gel DVB500 columns and a differential refractive index detector was used to determine the molecular weight and polydispersity index (PDI) of the copolymers. Tetrahydrofuran (THF) was used as eluent at a flow rate of 1 mL/min at 35 °C. A series of narrow polystyrene standards (900–100,000 g/mol) were used for calibration and the data was processed using a LCSolution ver.1.21 GPC option software.

2.5.3. Differential scanning calorimetry (DSC)

A TA Instruments DSC Q 2000 module was used to determine the thermal properties of the synthesized copolymers. Samples were placed in aluminum pans under nitrogen heated from 25 °C to 100 °C, cooled to −90 °C to remove thermal history and heated to 100 °C at a rate of 10 °C/min.

2.6. Critical micelle concentration (CMC)

Fluorescence spectroscopy was used to estimate the critical micelle concentration (CMC) of PEG-b-PLLA and PEG-b-P(CB-co-LA) copolymer using pyrene as a hydrophobic fluorescent probe. Twelve samples of PEG-b-PLLA or PEG-b-P(CB-co-LA) dissolved in methanol with concentrations ranging from 1×10^{-8} to 1 g/L were prepared and allowed to equilibrate with a constant pyrene concentration of 6×10^{-7} M for 48 h at room temperature. The fluorescence spectra of pyrene were recorded with a Molecular Devices SpectraMax M2/M2e spectrofluorometer (Sunnyvale, CA). An excitation wavelength of 390 nm was used and the emission spectra recorded from 320 to 450 nm with both bandwidths set at 2 nm. Peak height intensity ratio (I_3/I_1) of the third peak (I_3 at 338 nm) to the first peak (I_1 at 333 nm) was plotted against the logarithm of polymer concentration. The value of the CMC was obtained as the point of intersection of two tangents drawn to the curve at high and low concentrations, respectively.

2.7. Preparation of bicalutamide-loaded micelles

Bicalutamide-loaded micelles were prepared using the film sonication method as previously described with slight modifications [9]. In brief, 5 mg of bicalutamide and 95 mg of PEG-b-PLLA or PEG-b-P(CB-co-LA) were dissolved in 5 mL chloroform. The mixture was vortexed for 5 min to ensure homogeneity and the solvent evaporated under N_2 flow. The resulting film was hydrated in 10 mL phosphate buffered saline (PBS) to yield a final concentration of 10 mg/mL and sonicated for 10 min using a Misonix ultrasonic liquid processor (Farmingdale, NY) with an amplitude of 50. The ensuing formulation was then centrifuged at 5000 rpm for 10 min to separate micelles from residual free drug. Subsequently, the supernatant was filtered using a 0.22 μm nylon filter. The micelle preparation was lyophilized for 48 h and stored at 4 °C to prolong shelf-life and avoid untimely release of the drug.

2.8. Drug loading and encapsulation efficiency

Drug loading was determined as follows: 100 mg lyophilized bicalutamide-loaded micelles were dissolved in chloroform and the drug present in solution measured by ultraviolet spectroscopy. The weight of drug loaded in the micelles was calculated using a calibration curve and background absorbance interference from PEG-b-PLLA or PEG-b-P(CB-co-LA) copolymer was accounted for by measuring the absorbance of blank PEG-b-PLLA or PEG-b-P(CB-co-LA) under the same conditions. Drug loading content and encapsulation efficiency were then determined using equations 3 and 4 as follows:

$$\text{drug loading density} = \frac{\text{weight of drug in micelles}}{\text{weight of micelles}} \times 100\% \quad (3)$$

$$\text{drug encapsulation effciency} = \frac{\text{weight of drug in micelles}}{\text{weight of drug originally fed}} \times 100 \quad (4)$$

2.9. Particle size distribution

Mean particle size and size distribution of drug-loaded micelles were determined by dynamic light scattering (DLS) using a Zetasizer (Malvern Instruments, Worcestershire, UK) at a 1 mg/mL polymer concentration. Samples were analyzed at room temperature with a 90° detection angle and the mean micelle size was obtained as a *Z*-average. All measurements were repeated seven times and reported as the mean diameter ±SD for triplicate samples.

2.10. Transmission electron microscopy

Micelles prepared using PEG-b-P(CB-co-LA) copolymer were visualized using a JEM-100S (Japan) transmission electron microscope (TEM). 5 μl of micelle suspension was loaded on a copper grid, followed by blotting of excess liquid and air-dried before negative staining with 1% uranyl acetate. The grid was visualized under the electron microscope at 60 kV and magnifications ranging from 50,000× to 100,000×.

2.11. Bicalutamide release from micelles

The dialysis technique was employed to study the release of bicalutamide from the various copolymer micelles in PBS (pH 7.2). Bicalutamide-loaded micelles with a final bicalutamide concentration of 0.2 mg/mL were placed into a dialysis membrane with a molecular weight cut-off of 8000 Da and dialyzed against 50 mL PBS (pH 7.2) in a thermo-controlled shaker with a stirring speed of 100 rpm. 1 mL samples were withdrawn at specified times for a period of seven days and assayed with a validated UV spectrophotometer by measuring the absorbance of the solution at 270 nm. The samples taken for measurement were replaced with fresh media and the cumulative amount of drug released into the media at each time point was evaluated as the percentage of total drug release to the initial amount of the drug. All experiments were performed in triplicate and the data reported as the mean of the three individual experiments.

2.12. In vitro cytotoxicity of bicalutamide-loaded micelles

The ability of bicalutamide and bicalutamide-loaded micelles to inhibit cell proliferation was evaluated using LNCaP human prostate cell line. Cells were cultured in RPMI 1640 media supplemented with 2 mM L-glutamine, 10% fetal bovine serum (FBS) and 1% antibiotic-antimycotic at 37 °C in humidified environment of 5% CO_2 and subcultured every 3 days to ensure exponential growth. The cells were then seeded in 96-well plates at a density of 5×10^3 viable cells/well and incubated for 48 h to permit cell attachment. The cells were exposed to bicalutamide dissolved in methanol or bicalutamide-loaded micelles at concentrations ranging from 1 to 100 μM for 48 h. At the end of treatment, 20 μl of MTT solution (5 mg/mL) was added to each well and incubated for 4 h. The plates were then centrifuged at 1500*g* for 2 min and the medium aspirated. The residual formazan crystals were solubilized with 100 μl DMSO and the plate analyzed using a microplate reader. The absorbance values were recorded at a test wavelength of 560 nm. Cell viability for a given concentration was expressed as a percentage of the intensity of controls. The data was reported as the mean of triplicate experiments.

3. Results

3.1. Design of diblock copolymer based on enhanced compatibility between bicalutamide and hydrophobic core

Using PEG-b-PLLA copolymer as a template, a series of diblock copolymers were designed by modifying the PLLA hydrophobic core with a carbonate monomer (*i.e.* 5-methyl-5-benzyloxycarbonyl-1,3-dioxane-2-one). The goal here was to enhance the compatibility between bicalutamide and the hydrophobic core of the micelle. Since the Flory–Huggins interaction parameter (χ_{FH}) has been shown to be a good indicator of polymer–drug compatibility [18,20,23], we determined χ_{FH} for PLLA and P(CB-co-LA) using equation (2). The Hansen partial solubility parameters for bicalutamide, PLLA and P(CB-co-LA) were obtained based on the group contribution method using the Molecular Modeling Pro software (Table 1). The partial solubility parameters which account for dispersive forces between atoms, permanent dipole interactions between molecules and the tendency of molecules to hydrogen bond were used to calculate the solubility parameter which was subsequently used to compute the interaction parameter. Generally, as χ_{FH} approaches zero, compatibility between the polymer and the drug progressively increases since the polymer increasingly becomes a better thermodynamic solvent for the drug, resulting in improved drug solubilization. The interaction parameter between bicalutamide and PLLA was calculated to be *11.06* while the interaction parameter between bicalutamide and P(CB-co-LA) was computed to be *7.34*. Hence, by introducing a carbonate monomer (5-methyl-5-benzyloxycarbonyl-1,3-dioxane-2-one) into the PLLA hydrophobic core, our design suggested a potential increase in compatibility between bicalutamide and the micelle core and provided a logical justification for the synthesis of the poly(ethylene glycol)-b-poly(carbonate-co-lactide) [PEG-b-P(CB-*co*-LA)] copolymers.

3.2. Synthesis and characterization of 5-methyl-5-benzyloxycarbonyl-1,3-dioxane-2-one

The cyclic carbonate monomer (5-methyl-5-benzyloxycarbonyl-1,3-dioxane-2-one) was synthesized as described by Pratt et al.

Table 1
Calculated Hansen solubility parameters of bicalutamide, PLLA and P(CB-co-LA).

Drug/polymer	δ polarity $(J/cm^3)^{1/2}$	δ dispersion $(J/cm^3)^{1/2}$	δ hydrogen $(J/cm^3)^{1/2}$	Total solubility parameters[a]	χ_{sps}[b]
Bicalutamide	8.89	19.66	12.43	24.90	–
PLLA	2.48	19.73	20.92	28.68	11.06
P(CB-co-LA)	1.43	21.62	8.48	23.27	7.34

[a] Total solubility parameters computed using partial solubility parameters and equation (1).
[b] Flory–Huggins interaction parameters between bicalutamide and PLLA/P(CB-co-LA) were calculated using equation (2).

with slight modifications (Scheme 1, Stage 1) [24]. Briefly, 2,2-bis(hydroxymethyl)propionic acid was used to obtain benzyl 2,2-bis(methylol)propionate as an intermediate compound which was subsequently reacted with triphosgene to obtain the cyclic carbonate monomer. The chemical structure of the monomer was confirmed by mass and ^{1}H NMR spectroscopy. From the mass spectrum, the molecular ion peak agreed with the calculated molecular weight of the synthesized monomer (250 g/mol). Also, as depicted in Fig. 1A, the signal *d* at 7.5 ppm is characteristic of the phenyl ring protons in the monomer; while the signal *b* at 4.2 and 4.7 ppm was assigned to the methylene protons present in the carbonate ring. Other peak assignments include signals *a* and *c* at 1.3 and 5.2 ppm, representing methyl and benzyl CH_2 protons, respectively in the monomer.

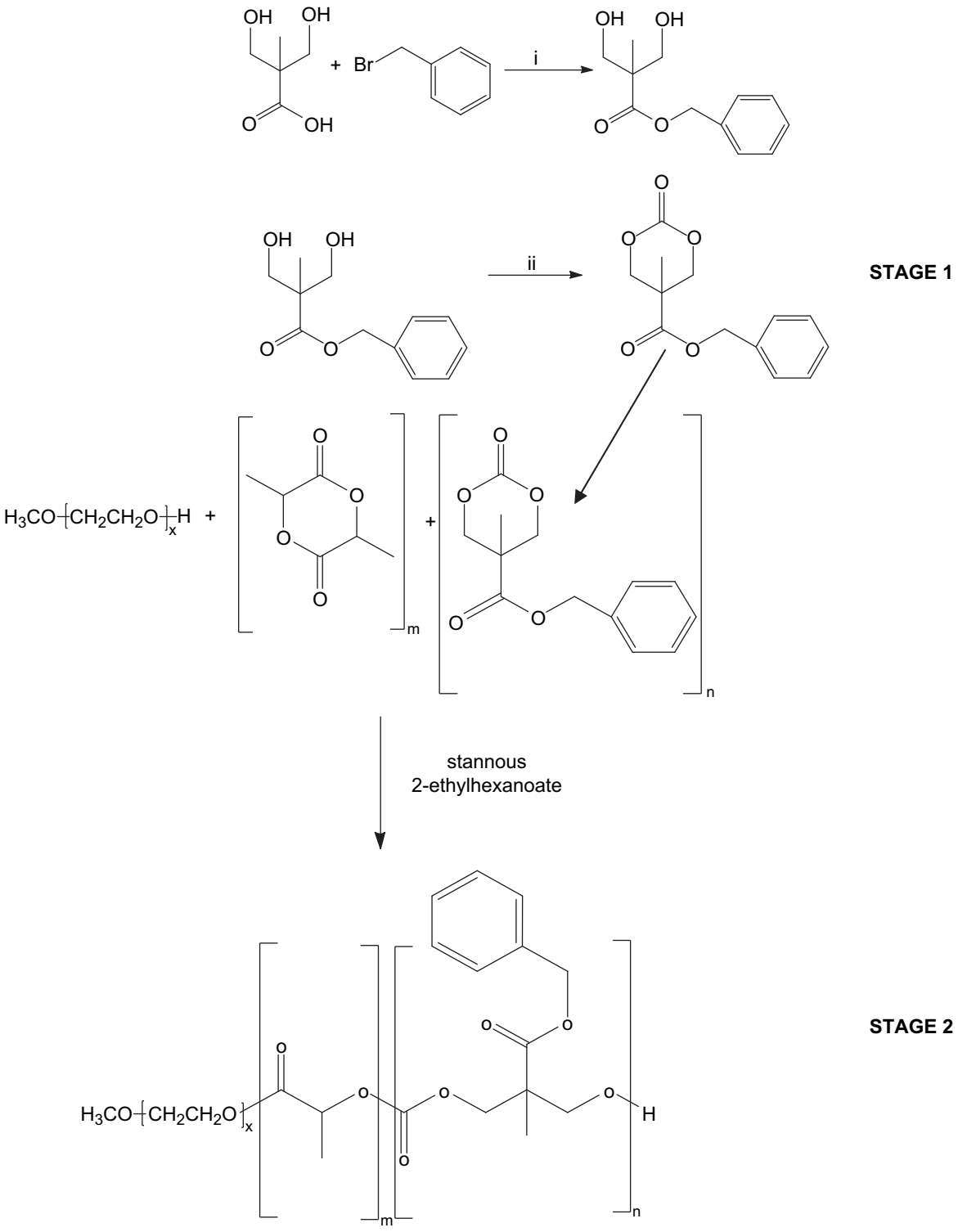

Scheme 1. Synthesis of PEG-b-P(CB-*co*-LA) copolymers. Stage 1: 5-Methyl-5-benzyloxycarbonyl-1,3-dioxane-2-one. Conditions: (i) KOH, DMF, 100 °C, 15 h (ii) Triphosgene, pyridine, CH_2Cl_2, -78–0 °C. Stage 2: Ring opening polymerization of L-Lactide and 5-Methyl-5-benzyloxycarbonyl-1,3-dioxane-2-one initiated by poly(ethylene glycol).

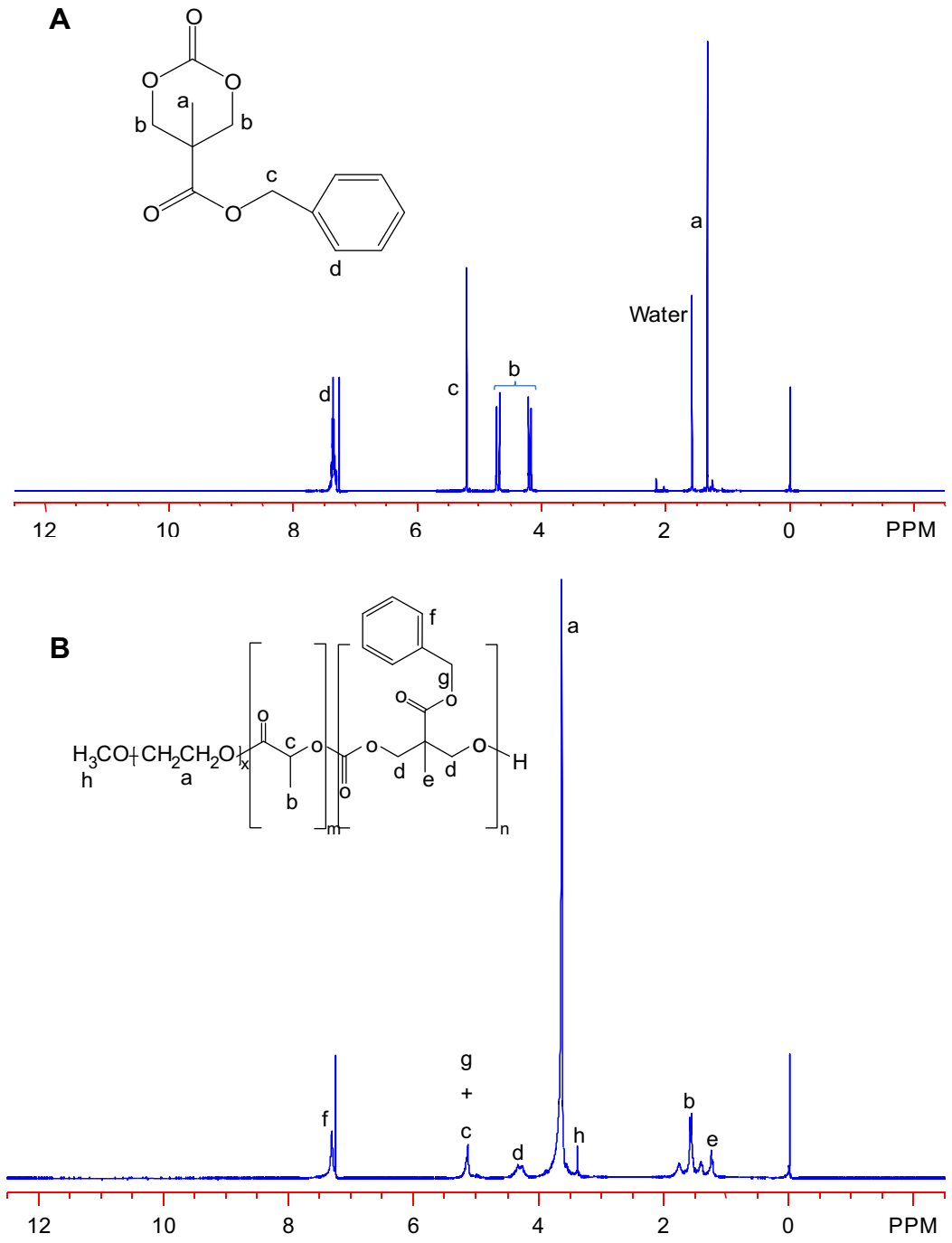

Fig. 1. ^{1}H NMR spectra in $CDCl_3$ of (A) 5-methyl-5-benzyloxycarbonyl-1,3-dioxane-2-one (carbonate monomer) and (B) PEG_{114}-b-P(CB_8-co-LA_{24}) copolymer.

3.3. Synthesis and characterization of PEG-b-P(carbonate-co-lactide) copolymer

The synthesis route of PEG-b-P(CB-co-LA) is delineated in Scheme 1, Stage 2. A series of PEG-b-P(CB-co-LA) copolymers with varying carbonate (10, 20 and 40 mol%) content were synthesized by a one pot ring opening polymerization of L-lactide and 5-methyl-5-benzyloxycarbonyl-1,3-dioxane-2-one using methoxy-PEG as the macroinitiator and stannous 2-ethylhexanoate as a catalyst. Among the series, the percent conversion of PEG-b-P(CB-co-LA) copolymer from carbonate was the highest for the 10 mol% series and was estimated to be 87% based on ^{1}H NMR spectroscopy. Further ^{1}H NMR analyses were used to verify the composition of PEG-b-P(CB-co-LA) copolymers. From Fig. 1B, the following resonance peaks were observed for the copolymers at δ: 1.24 (CH_3 in CB unit, s, 3H); δ: 1.55–1.57 (CH_3 in LA unit, s, 3H); δ: 3.65 (CH_2 in PEG, m, 4H); δ: 4.25–4.35 (CH_2 in CB main chain m, 4H); δ: 5.12 (CH in LA unit q, 1H, and CH_2 in CB side group, s, 2H) δ: 7.3 (phenyl, m, 5H). All signals are assigned as methoxy poly(ethylene glycol) [mPEG], polymerized LA and CB units. The presence of the 7.3 ppm multiplet peak indicates the existence of the carbonate group in the copolymer structure. In addition, the disappearance of the signal *b* at 4.2 and 4.7 ppm in the carbonate monomer (Fig. 1A) and the emergence of the multiplet peak at δ: 4.25–4.35 ppm in the copolymer (Fig. 1B) confirms the

Table 2
Effect of carbonate content on the molecular weight and CMC of PEG-b-P(CB-co-LA) copolymers.

Block copolymer[a]	Carbonate (mol%)[b]	Theoretical mol. wt. (g/mol)	M_n (NMR)	M_n (GPC)	M_w (GPC)	M_w/M_n (GPC)	CMC (g/L)	CMC × 10^7 (mol^{-1})[c]
PEG_{114}-b-$PLLA_{62}$	0	10,000	9460	9104	9741	1.07	0.03	32.95
PEG_{114}-b-P(CB_5-co-LA_{32})	10	10,000	8604	6228	8533	1.37	0.005	8.03
PEG_{114}-b-P(CB_8-co-LA_{24})	20	10,000	8679	6384	8925	1.40	0.002	3.13
PEG_{114}-b-P(CB_9-co-LA_5)	40	10,000	7510	5694	8573	1.51	0.004	7.02

[a] Subscripts reflect degree of polymerization of each monomer obtained from ^{1}H NMR spectroscopy.
[b] Mol% indicates carbonate content in P(CB-co-LA) block copolymer. Molecular weight calculated from ^{1}H NMR spectroscopy, $M_{n,NMR} = M_{n,PEG} + M_{n,Carbonate} + M_{n,L\text{-}Lactide}$.
[c] CMC (g/L) normalized with M_n from GPC. Critical micelle concentration (CMC) was determined at 25 °C using pyrene as hydrophobic probe.

successful ring opening polymerization of the carbonate monomer and the formation of PEG-b-P(CB-co-LA) copolymers.

Table 2 summarizes some characteristics of the synthesized PEG-b-PLLA and PEG-b-P(CB-co-LA) copolymers. The block copolymer molecular weight was calculated based on a comparative analysis of the four methylene protons of PEG ($\delta = 3.65$ ppm), one methylene proton of lactide ($\delta = 5.12$ ppm) and the five protons associated with the phenyl ring in the carbonate monomer observed in the ^{1}H NMR spectrum. It is worth mentioning that since the lactide proton peak at 5.12 ppm is confounded with the signal from the two protons of the carbonate monomer, two- fifth of the carbonate signal at 7.3 ppm was subtracted from the 5.12 ppm signal to obtain the actual lactide peak intensity used for molecular weight calculations. For the three copolymers studied: PEG_{114}-b-P(CB_5-co-LA_{32}), PEG_{114}-b-P(CB_8-co-LA_{24}) and PEG_{114}-b-P(CB_9-co-LA_5); the molecular weight were 8604 g mol^{-1}, 8679 g mol^{-1} and 7510 g mol^{-1}, respectively. Hence, the calculated molecular weight from ^{1}H NMR spectroscopy was less than the predicted value of 10,000 g/mol. The computed molecular weights suggests the degree of polymerization (DP) of the P(CB-co-LA) core to be lower than the theoretical value. The calculated DP for 10, 20 and 40 mol% carbonate is 37, 32 and 14, respectively; while the theoretical DP for 10, 20 and 40 mol% carbonate is 54, 44 and 34, respectively. Gel permeation chromatography (GPC) analysis revealed PEG-b-P(CB-co-LA) copolymers to be broader than PEG-b-PLLA as evinced by the polydispersity index (M_w/M_n = 1.37, 1.40 and 1.51) for PEG-b-P(CB-co-LA) copolymers compared to M_w/M_n = 1.07 for PEG-b-PLLA with the breadth of polydispersity increasing with carbonate. Furthermore, PEG-b-P(CB-co-LA) copolymers exhibited an unimodal peak and a representative plot comparing the GPC chromatograms for PEG-b-PLLA and PEG_{114}-b-P(CB_8-co-LA_{24}) is shown in Fig. 2. The unimodal peaks observed for the copolymer series suggests that successful copolymerization took place and that the insertion of carbonate and lactide monomers in the P(CB-co-LA) core was random.

3.4. Preparation and characterization of PEG-b-P(CB-co-LA) copolymer micelles

The film sonication method described in a previous publication [9] was used to prepare both unloaded and bicalutamide-loaded polymeric micelles from the synthesized PEG-b-PLLA and PEG-b-P(CB-co-LA) copolymers [9]. The size distribution for both unloaded and bicalutamide-loaded polymeric micellar formulations as determined by dynamic light scattering (DLS) was relatively broad with a PDI of approximately 0.2, reflecting the possible presence of a population of

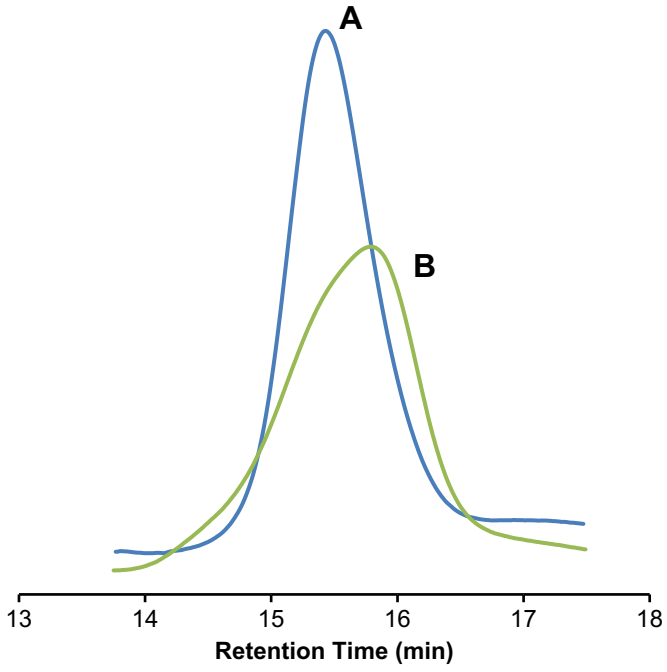

Fig. 2. Gel permeation chromatograms of (A) PEG-b-PLLA [M_n = 9460 g/mol, M_w/M_n = 1.07] and (B) PEG_{114}-b-P(CB_8-co-LA_{24}) [M_n = 9720 g/mol, M_w/M_n = 1.40] copolymers, both acquired in THF.

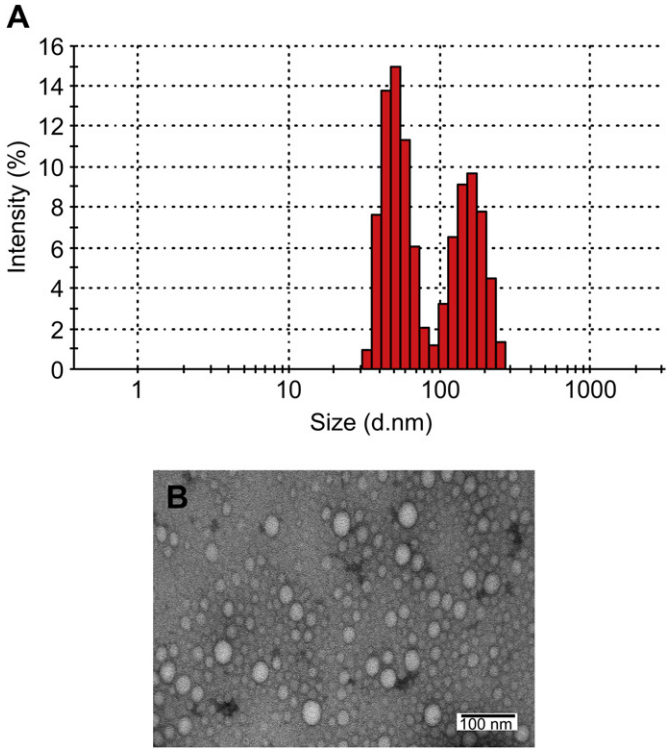

Fig. 3. Micelle size distribution and surface morphology. (A) Dynamic light scattering histogram; and (B) transmission electron micrograph of micelle formulated with PEG-b-P(CB-co-LA) copolymer obtained using uranyl acetate staining.

aggregates. Fig. 3A shows a typical size distribution plot obtained from DLS of PEG-b-P(CB-co-LA) micelles using a polymer concentration of 10 mg/mL. The size distribution is bimodal with a smaller size population ~53 nm (58%) and a larger population ~162 nm (42%). Effective hydrodynamic diameter for both unloaded and bicalutamide-loaded PEG-b-PLLA and PEG-b-P(CB-co-LA) micelles reported as the *z*-average based on mean intensity was determined by DLS. In the case of the unloaded micelles, the average diameter was found to range from 107 to 135 nm, while the average diameter of bicalutamide-loaded micelles ranged from 99 to 123 nm (Table 3). In both cases the 20 mol% carbonate copolymer had the largest average diameter whilst the 40 mol% carbonate copolymer had the smallest average diameter.

Particle size and surface morphology of these micelles were also determined by transmission electron microscopy (TEM). The polymer micelles have a broad size distribution with mean number average diameter below 50 nm (Fig. 3B) which is lower than the *z*-average diameters obtained from DLS. TEM images also reveal a tendency for micellar aggregation and confirm that PEG-b-P(CB-co-LA) formed true spherical micelles in water with distinct boundaries as anticipated.

The polymer micelles were further characterized by fluorescence spectroscopy to determine the critical micelle concentration (CMC). The CMC of the synthesized block copolymers decreased upon introduction of the carbonate monomer from ~3.3 to ~0.3 μM for 0 and 20 mol% carbonate, respectively (Fig. 4 and Table 2). The lower CMC values suggest that the inclusion of the carbonate moiety results in block copolymers thermodynamically more favored to self-assemble.

The amount of bicalutamide loaded into micelles was calculated using equation (3) based on a 5% theoretical loading (*i.e.*, 5 mg drug/100 mg polymer). PEG-b-P(CB-co-LA) copolymers exhibited higher drug loading compared to PEG-b-PLLA copolymer (Table 3). Among PEG-b-P(CB-co-LA) copolymer series, the highest loading (4.10%) was observed for PEG_{114}-b-P(CB_8-co-LA_{24}) copolymers which was at least four-fold better than PEG-b-PLLA copolymer with regards to drug loading and had an encapsulation efficiency of approximately 82%. For PEG_{114}-b-P(CB_5-co-LA_{32}) the drug loading was 3.36% which is about three times higher than that of PEG-b-PLLA and its encapsulation efficiency was roughly 73%. PEG_{114}-b-P(CB_9-co-LA_5) copolymer had a drug loading of 1.38% and an encapsulation efficiency of 28% which is only slightly better than PEG-b-PLLA which had a drug loading of 1% and an encapsulation efficiency of 22%. Since the degree of polymerization of P(CB-co-LA) hydrophobic core varied across the series, the drug loading was also assessed on a molar basis with respect to just the hydrophobic core (*i.e.*, mol bicalutamide/mol hydrophobic core) to normalize the data. Here again, PEG_{114}-b-P(CB_8-co-LA_{24}) had the highest loading (1097%), followed by PEG_{114}-b-P(CB_5-co-LA_{32}) and then PEG_{114}-b-P(CB_9-co-LA_5) which had 876% and 779% loading, respectively. In all cases, the drug loading on a molar basis in PEG-b-P(CB-co-LA) copolymer series was several fold higher than that of PEG-b-PLLA copolymer.

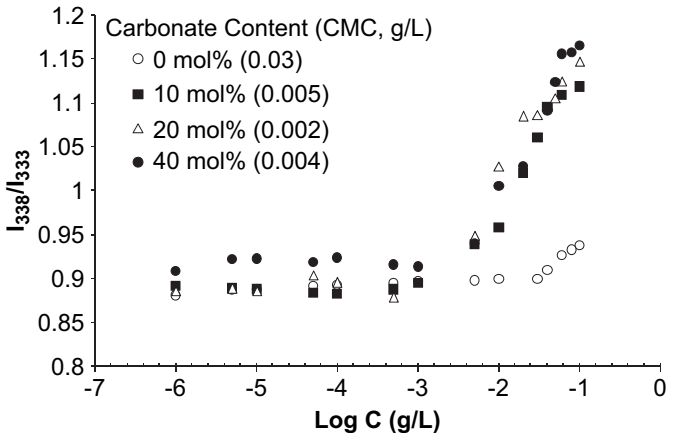

Fig. 4. Plots of intensity ratio I_{338}/I_{333} from pyrene fluorescence emission spectra versus log concentration (g/L) of PEG-b-PLLA and PEG-b-P(CB-co-LA) copolymers.

To establish that PEG-b-P(CB-co-LA) micelles are capable of forming core–shell structures, the ^{1}H NMR spectra of micelle samples in deuterated water (D_2O) and DMSO-d_6 were compared. Typical spectra for PEG_{114}-b-P(CB_8-co-LA_{24}) micelles are shown in Fig. 5. In D_2O, only the PEG proton peaks can be detected while the signals for PLLA and polycarbonate are not evident. On the contrary, distinct peaks for PLLA and polycarbonate were observed in DMSO-d_6 in addition to the PEG signal, suggesting that PEG-b-P(CB-co-LA) micelle form core–shell structures capable of encapsulating bicalutamide. This result is consistent with what is reported in the literature since the PEG forms the corona of the micelle and enhances its solvation in D_2O while PLLA, polycarbonate and the encapsulated bicalutamide are in the core of the micelle and have restricted mobility in D_2O.

3.5. Sequence analysis

Sequence distribution in a copolymer is frequently analyzed in terms of monomer triads. Considering that the hydrophobic core of the synthesized PEG-b-P(CB-co-LA) copolymers is made up of two monomers: carbonate (C) and lactide (L), this system has eight possible theoretical triads. Prior to the analysis of triads in the copolymer, the complete assignment for the carbonyl peaks in PEG-b-P(CB-co-LA) copolymer based on ^{13}C NMR spectra of homopolymers (PLLA and polycarbonate) was first determined and the results are shown in Fig. 6A. To elucidate the arrangement of triads in PEG-b-P(CB-co-LA) copolymer, ^{13}C NMR spectrum was expanded for clarity (Fig. 6B): expansion of peak "a" (upper) and peak "d" (lower). The resonance peak at 169.6 ppm is assigned to the central carbonyl of LLL and LLC triads. Further upfield the resonance peak occurring at 169.45 ppm which is due to the central carbonyl in the CLC and CLL triads. The resonance peak at 154.35 ppm is assigned to

Table 3
Effect of polymer composition on drug loading and particle size of bicalutamide-loaded micelles.

Block copolymer[a]	Drug loading (%) ± SD[b]	Encap. efficiency (%) ± SD	Bicalutamide/polymer core (mol%)	Mean diameter ± SD (nm)[c]
PEG_{114}-b-$PLLA_{62}$	1.0 ± 0.31	22.04 ± 3.82	22	110 ± 0.9
PEG_{114}-b-P(CB_5-co-LA_{32})	3.36 ± 0.18	72.68 ± 4.27	876	101 ± 1.0
PEG_{114}-b-P(CB_8-co-LA_{24})	4.10 ± 0.23	81.96 ± 2.54	1097	123 ± 1.5
PEG_{114}-b-P(CB_9-co-LA_5)	1.38 ± 0.46	27.56 ± 2.91	779	99 ± 1.4

[a] Subscripts reflect degree of polymerization of each monomer obtained from ^{1}H NMR spectroscopy.
[b] Percentage of drug loaded into micelles based on 5% theoretical loading.
[c] Mean particle size was determined by dynamic light scattering.

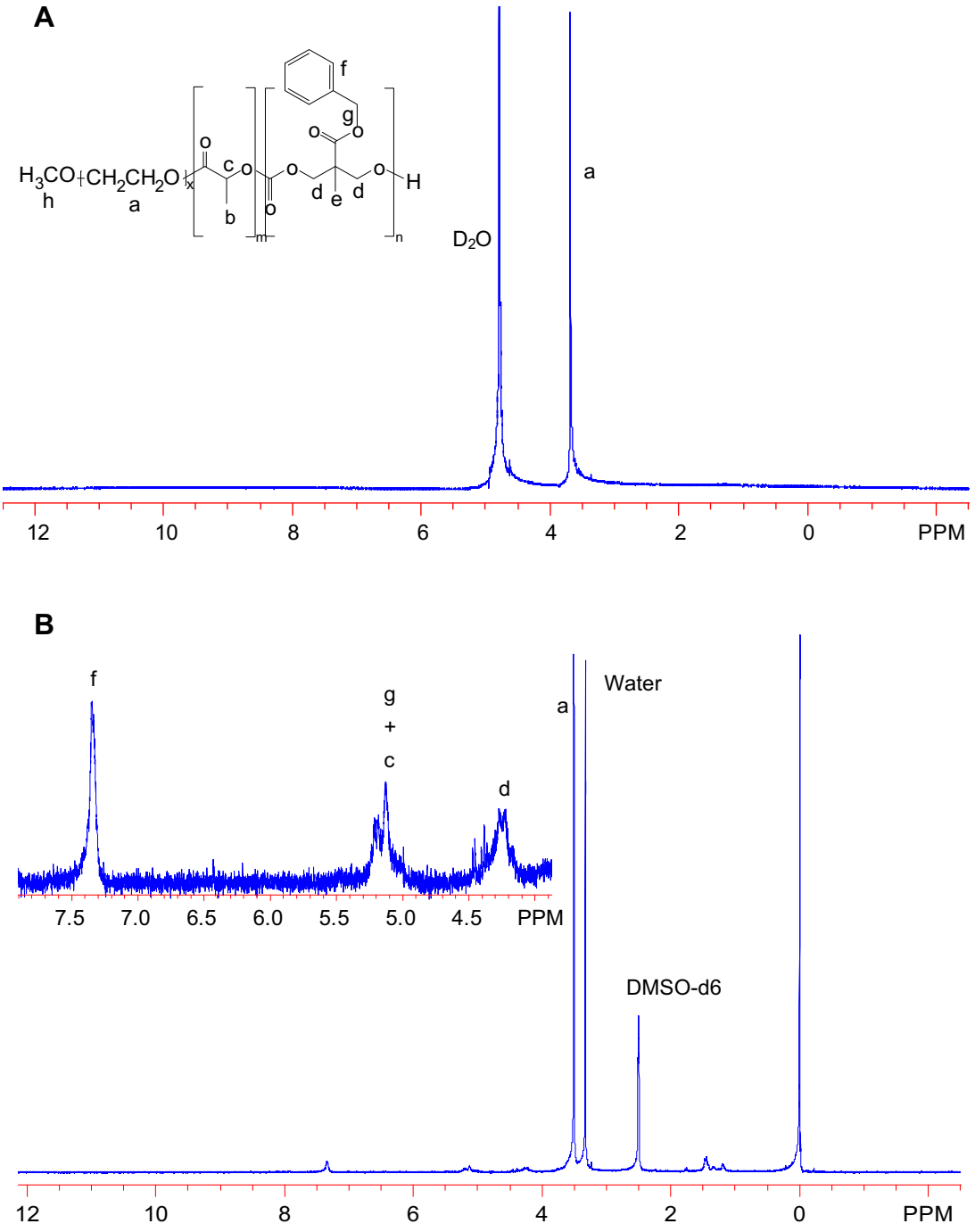

Fig. 5. ^{1}H NMR spectra of bicalutamide-loaded PEG_{114}-b-P(CB_8-co-LA_{24}) micelles in (A) deuterated water (D_2O) and (B) DMSO-d_6.

the central carbonyl of CCC and CCL triads, while the resonance peak at 154.15 ppm is due to the central carbonyl of the LCL and LCC triads. The above data together with the observed splitting of the carbonyl peaks strongly suggests that the hydrophobic core PEG-b-P(CB-co-LA) is a random copolymer. Having confirmed the formation of random copolymers, the influence of carbonate monomer on the distribution of L–L and C–C sequence was assessed by comparing the ^{13}C NMR spectra of 10, 20 and 40 mol% carbonate copolymers. From Fig. 7, increasing CB contents from 10 to 40 mol% decreases L–L sequence and increases C–C sequence (particularly for 40%).

3.6. Thermal analysis

The thermal properties of the synthesized block copolymers were examined using differential scanning calorimetry (DSC) and the thermograms of PEG-b-PLLA and PEG-b-P(CB-*co*-LA) copolymers are shown in Fig. 8. Within the temperature range examined (−90 to 175 °C), two endotherm peaks at 51.5 and 155 °C were observed for PEG-b-PLLA copolymer. An exotherm peak was also observed occurring at 88.5 °C. To the contrary, only one endotherm peak, the fusion of PEG block, was observed for all the PEG-b-P(CB-co-LA) copolymers which appeared to shift slightly to higher

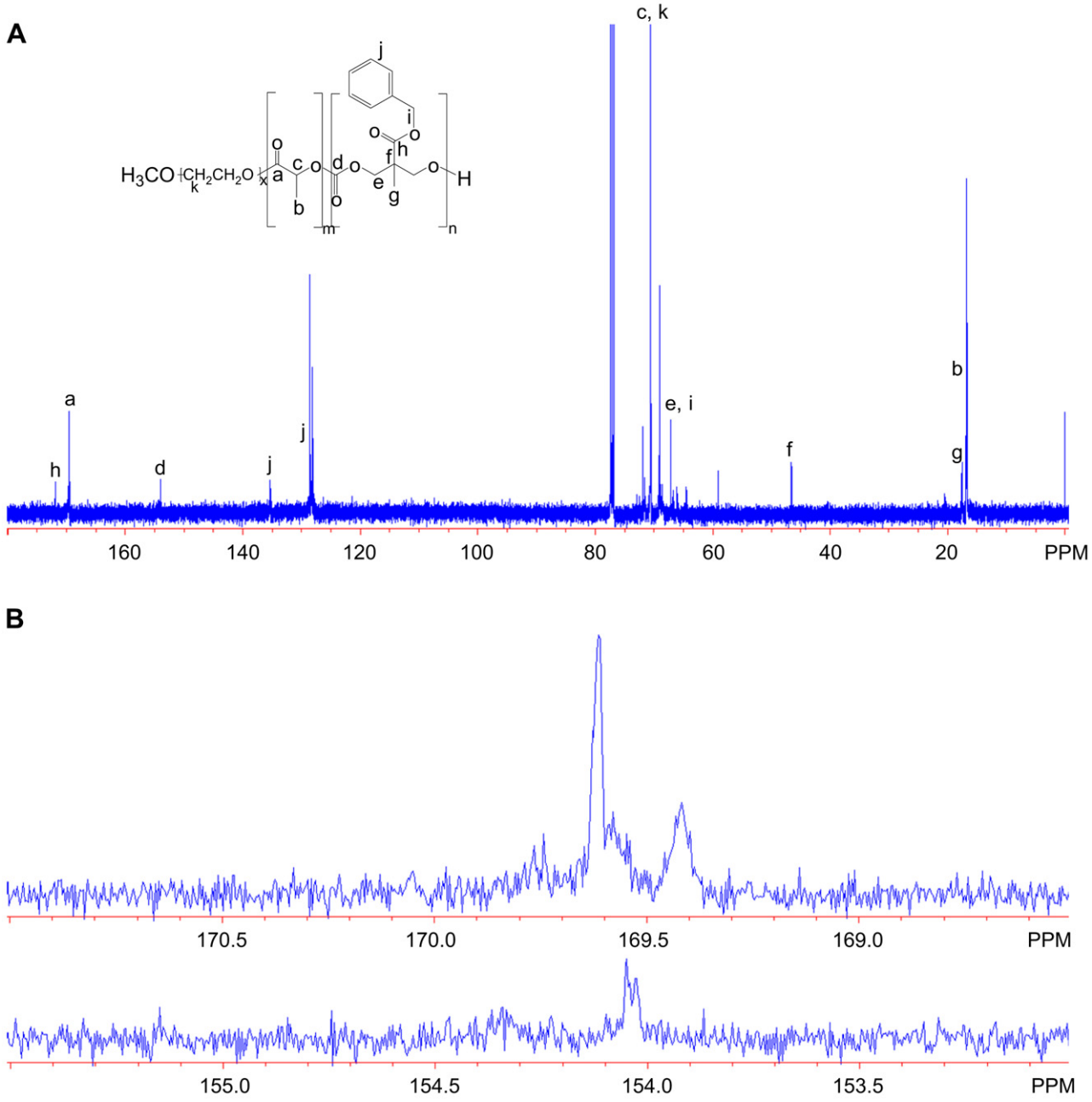

Fig. 6. ^{13}C NMR spectra of PEG_{114}-b-P(CB_8-co-LA_{24}) copolymer. (A) Complete spectrum with peak assignments. (B) Expanded spectrum of specified regions (152–170 ppm) illustrating carbonyl regions of interest for sequence distribution analysis.

temperatures with increasing carbonate content: 52.1, 52.9 and 53.8 °C for 10, 20 and 40 mol%, respectively.

3.7. *In vitro release studies of bicalutamide from micelles*

The *in vitro* bicalutamide release study was performed in phosphate buffered saline (PBS, pH 7.4) at 37 °C and 100 rpm. Fig. 9 shows the cumulative percentage of bicalutamide released from PEG-b-PLLA (0 mol% carbonate) and PEG-b-P(CB-co-LA) [10, 20 and 40 mol% carbonate] micelles. From the data, the release of bicalutamide is rapid from the micelles with 0 mol% carbonate content compared to micelles formulated using copolymers containing carbonate monomer. About 60% of the total drug was released within 6 h for 0 mol% carbonate content while the 10, 20 and 40 mol% carbonate content had a burst release of 40%. The 0 mol% carbonate copolymer used in this study had a GPC molecular weight of 5200 g mol^{-1} to ensure that all copolymers used in the release study had similar molecular weights Fig. 10.

3.8. *Evaluation of in vitro cytotoxicity*

To determine inhibitory effect of bicalutamide-loaded micelles formulated with PEG-b-P(CB-co-LA) copolymer on cell proliferation, the cytotoxicity of free bicalutamide dissolved in methanol and that of bicalutamide formulated in micelles was evaluated in LNCaP human prostate cancer cell line for 48 h. From Fig. 10, micelle-formulated drug showed significant inhibition of LNCaP cell growth in a dose-dependent manner, which was similar to that obtained

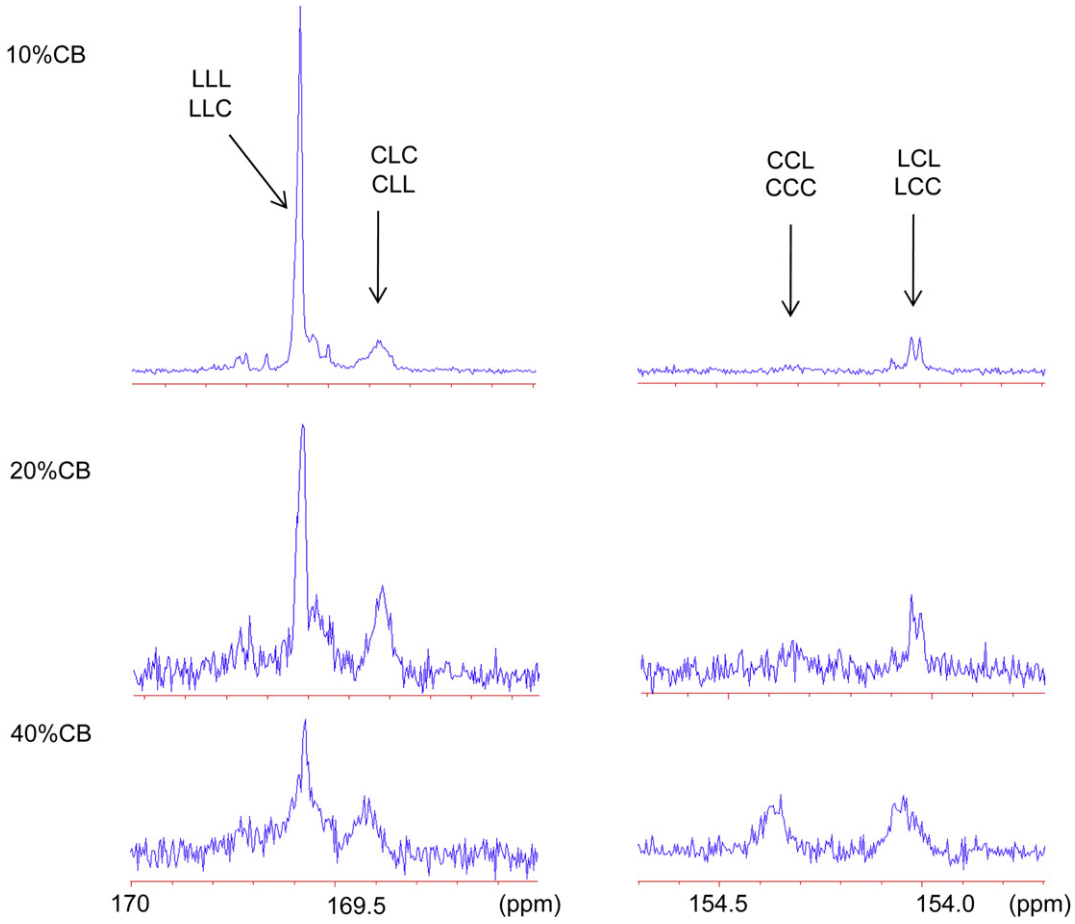

Fig. 7. ^{13}C NMR spectra comparative plot for 10, 20 and 40 mol% carbonate content demonstrating decrease in LLL sequence and increase in CCC sequence with increasing carbonate content.

using free drug. The IC_{50} of bicalutamide-loaded micelles was 74 μM while that of free drug was 80 μM. However, no direct comparison can be made since we had to dissolve free drug in methanol, whereas we prepared micelles in PBS.

4. Discussion

In spite of the numerous advantages associated with polymeric micelles as drug delivery systems, their application as therapeutics has been limited by low loadings and stability. The equilibrium partitioning of a hydrophobic drug into the hydrophobic core of polymeric micelles at a specific temperature is governed by the molar free energy of the drug, which depends on the mixing entropy and the enthalpy interaction between the drug and the polymer, as well as the amount of pressure–volume work required

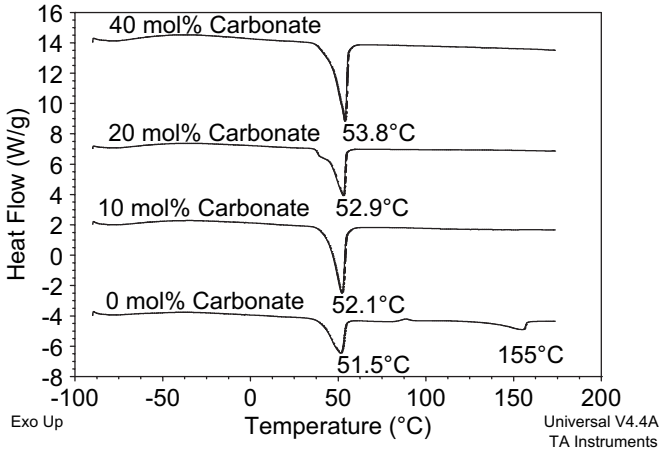

Fig. 8. DSC thermograms of PEG-b-PLLA and PEG-b-P(CB-co-LA) copolymers.

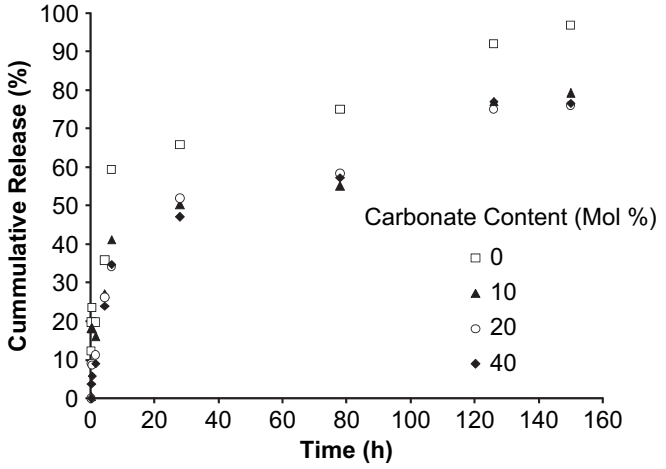

Fig. 9. Effect of carbonate content on bicalutamide release from PEG-b-PLLA and PEG-b-P(CB-co-LA) micelles. Release experiments were performed in triplicate in PBS at 37 °C and 100 rpm.

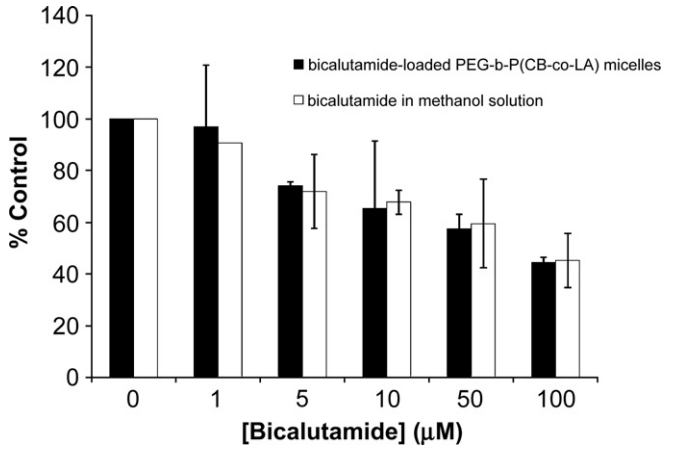

Fig. 10. Effect of free and PEG-b-P(CB-co-LA) micellar formulation of bicalutamide on inhibition of LNCaP cell proliferation 48 h post treatment. Cell viability was estimated by MTT assay and expressed as percent of 1% methanol or blank micelle controls. All data represent the mean ± S.D. of triplicates.

in putting a drug molecule into the lipophilic core [25]. It has been shown for polymeric micelles that lowering the enthalpy interaction contribution of the free energy improves drug loading. This may be achieved by carefully selecting the core-forming block such that its solubility parameters and that of the drug are essentially of the same order, indicating superior drug–polymer compatibility. The Flory–Huggins interaction parameter (χ_{FH}) is a good measure of the compatibility between the core-forming block of the copolymer and the drug, with lower values pointing to enhanced compatibility and superior loading.

The purpose of this study was to increase bicalutamide loading into micelles by designing polymers based on improved drug–polymer solubility determined using the Flory–Huggins interaction parameter. Inclusion of carbonate monomer which contains a bulky phenyl ring resulted in decreased χ_{FH} values. In the strictest sense, χ_{FH} values above the 0.5 critical value allude to immiscibility between drug and polymer since phase separation of the polymer–drug mixture commences, while χ_{FH} values below 0.5 suggest that the drug and polymer are soluble in each other. The Flory–Huggins theory is based on the assumption that the orientation of molecules within the polymer–drug system is completely random and that upon mixing the polymer and drug no specific interactions are created or destroyed. However, since these assumptions are not entirely true for our system, the χ_{FH} values obtained were merely used as a guide in predicting enhanced compatibility in relative terms based on the observed trend of lower χ_{FH} values. It also provided a reasonable estimate of the closeness of the solubility parameters of P(CB-co-LA) hydrophobic core and that of bicalutamide in the Hansen partial solubility three dimensional space compared to PLLA and bicalutamide.

A two-step reaction from 2,2-bis(hydroxymethyl)propionic acid was used to obtain the cyclic carbonate monomer (5-methyl-5-benzyloxycarbonyl-1,3-dioxane-2-one) which was subsequently employed in the synthesis of PEG-b-P(CB-co-LA) copolymer (Scheme 1). All copolymers were obtained through ring opening polymerization of PEG, lactide and carbonate. Since our objective was to vary hydrophobic group to increase drug loading into micelles, we did not vary the molecular of PEG in our copolymers to determine the effect of PEG molecular weight on micelle number and diameter.

Various synthetic schemes have been reported for synthesizing 5-methyl-5-benzyloxycarbonyl-1,3-dioxane-2-one [24,26–28]. However, we employed the method described by Pratt et al. since the yield of the cyclic carbonate monomer is higher for this method. The yield of the carbonate monomer (95%) we obtained was similar to that obtained by Pratt et al. [24] and our characterization data matched the literature [27,29]. The ring opening polymerization of Lactide (LA) and the carbonate monomer was performed in bulk at 130 °C with $Sn(Oct)_2$ as catalyst (10 mol% relative to mPEG) (Scheme 1). We chose $Sn(Oct)_2$ as a catalyst since it is FDA approved and $Sn(Oct)_2$-catalyzed polymerization does not result in racemization of lactide at temperatures below 200 °C [30]. Also, $Sn(Oct)_2$ is a strong transesterification agent yielding copolymers with a randomized microstructure. Guan and coworkers reported synthesizing and characterizing a similar copolymer, however, they used Et_2Zn as the catalyst and a reaction temperature of 100 °C [28]. While a 7 h reaction time was sufficient for complete polymerization of PEG-b-PLLA, it resulted in incomplete polymerization of PEG-b-P(CB-co-LA) copolymers. A reaction time of 24 h was used for PEG-b-P(CB-co-LA) copolymers since complete polymerization was observed after 24 h. The observed lower DP of P(CB-co-LA) core compared to the predicted DP suggests a lowering of the carbonate and lactide monomer reactivity with increasing carbonate content. From ^{1}H NMR spectroscopy, the carbonate monomer was observed to have higher reactivity compared to lactide. Also, increasing carbonate content from 10 to 40 mol% resulted in lower reactivity for both carbonate and lactide monomers: carbonate reactivity decreased from 87% to 61% while lactide reactivity decreased from 66% to 24%. Overall, the molecular weight decreases while the molecular weight distribution increases with increasing carbonate content. This may be due to progressively higher levels of intra-(backbiting) and intermolecular (redistribution) transesterification side reactions resulting in the formation of cyclic oligomers as the carbonate content increases.

PEG-b-P(CB-co-LA) copolymers self assembled into micelles with a core–shell structure (Fig. 5). The average diameter of micelles formulated from PEG-b-P(CB-co-LA) copolymers was in the range of 99–123 nm and appeared to be independent of carbonate content but correlated well with molecular weight. The introduction of carbonate monomer enhanced bicalutamide loading (Table 3) which confirmed our prediction based on the Flory–Huggins interaction parameter of PEG-b-P(CB-co-LA) having superior bicalutamide loading to PEG-b-PLLA copolymer. However, this increase was not linear with carbonate content and seemed to peak at the 20 mol% content where a four-fold increase in bicalutamide loading was observed compared to PEG-b-PLLA copolymer. We also observed that while the drug loading (as defined by equation (3)) in PEG_{114}-b-P(CB_5-co-LA_{32}) copolymer was approximately 3-fold higher than that of PEG_{114}-b-P(CB_9-co-LA_5), the drug loading on a molar basis in the hydrophobic core was about the same. Hence, the rather low drug loading observed for the 40 mol% carbonate series may be due to a couple of factors: (1) its relatively smaller molecular weight compared to the 10 and 20 mol% carbonate series and (2) the decreased PEG-b-P(CB-co-LA) copolymer solubility with increasing carbonate content. As the feed carbonate content increases, the reactivity of both the lactide and carbonate decreases. Lactide reactivity decreases from 86% to 24% while carbonate reactivity decreases from 82% to 64% for 0 mol% to 40 mol% carbonate content. This coupled with the polymer degradation effect associated with intramolecular transesterification leads to the decreased molecular weight observed with increasing carbonate content. It is well known, that drug loading is related to the molecular weight of the hydrophobic core. Large hydrophobic blocks form large micelle cores and require less amount of work to put a molecule of drug into the hydrophobic core due to relatively lower internal pressure. Drug loading is also influenced by the interaction between the drug and the copolymer as well as the solubility of the copolymer. As the carbonate content increases

the interaction between bicalutamide and the copolymer increases, however, the solubility of the copolymer decreases. Hence, the trade-off between drug–polymer interaction and polymer solubility influences the extent of drug loading. At carbonate content up to 20 mol% the effect of drug–polymer interaction predominates resulting in the observed improved drug loading, while at 40 mol% carbonate content the effect of decreased copolymer solubility dominates contributing to the observed reduction in drug loading. As such, the PEG-b-P(CB-co-LA) 20 mol% carbonate series exhibit optimum drug loading. It is worth mentioning that we also synthesized PEG-b-Polycarbonate (PEG-b-PCB) using the same polymerization conditions for PEG-b-P (CB-co-LA) copolymer. However, the solubility of this polymer in tetrahydrofuran (THF) and commonly used organic solvents was poor; making characterization using GPC and NMR difficult. From Table 2, drug solubility appears to correlate with the CMC. Among the series of copolymers, 0 mol% carbonate has the highest CMC value of 32.95×10^{-7} mol^{-1} and the lowest drug loading of 1.0% ± 0.31, while the 20 mol% carbonate series has the lowest CMC value 3.13×10^{-7} mol^{-1} and the highest drug loading 4.1% ± 0.23. The decrease in the CMC upon inclusion of the carbonate monomer clearly demonstrates that they have higher thermodynamic stability compared to PEG-b-PLLA. A high thermodynamic stability is desirable for *in vivo* stability of polymeric micellar systems.

Sequence distribution of random copolymers can influence fundamental polymer properties such as solubility, mechanical and thermal properties. The observed decrease in L–L sequence and increase in C–C sequence as carbonate content increases can be used to elucidate the behavior of the PEG-b-P(CB-co-LA) copolymers. When the ratio of lactide to carbonate monomer is small, the lactide segments in the random copolymer are sparsely distributed and have a lower probability of interacting with the ethylene oxide segments since the lactide is buried in the carbonate segments hence preventing intermolecular interactions. This may explain the observed sharp decrease in lactide reactivity (from 66 to 24%). Conversely, at high lactide to carbonate ratios, lactide segments tend to undergo intramolecular transesterification and lead to smaller molecular weight polymers due to degradation. Hence, these two competing phenomena affect polymer molecular weight depending on which factor is more dominant and the optimum molecular weight is obtained when they are balanced. In the present study, the 20 mol% carbonate series exhibited optimum molecular weight which translated into superior drug loading and thermodynamic stability.

Thermal analysis of the copolymers by differential scanning calorimetry confirmed the semicrystalline nature of PLLA. The two endotherm peaks observed for PLLA reflect the melting temperature of PEG (T_m = 51.5 °C) and melting temperature of PLLA (T_m = 155 °C), respectively. Also the exotherm peak occurring at 88.5 °C was also observed which may signify the onset of cold crystallization. More importantly, the data revealed that the introduction of the carbonate monomer into the poly(L-lactide) chain resulted in a reduction in crystallinity as demonstrated by the absence of the cold crystallization and melting peaks in the copolymers. These results suggest that the carbonate monomer randomly incorporated into the PLLA chain and resulted in a shortening of lactide sequences thereby hindering the crystallization process. Our data is consistent with the literature and other groups have reported similar trends [28,31].

In vitro release studies clearly showed the introduction of the carbonate monomer to result in better sustained release of bicalutamide from the micelle core compared to PEG-b-PLLA. The improved sustained release of the carbonate modified copolymers can be attributed to better compatibility between bicalutamide and the hydrophobic block of the copolymer as well as the they being more amorphous compared to PEG-b-PLLA. Both PEG-b-PLLA and PEG-b-P(CB-co-LA) copolymers exhibited fast release during the first 6 h. This burst release is assumed to be due to drug trapped with the PEG corona and at the corona–core interface. Increasing carbonate content from 10 to 40 mol% does not appear to alter the release profile of bicalutamide over the 150 h period studied. The release behavior of hydrophobic drugs from spherical micelles is known to depend on the properties of the hydrophobic core. The inhibitory effect of bicalutamide-loaded micelles formulated with PEG-b-P(CB-co-LA) copolymer on cell proliferation was comparable to free drug solubilized in methanol in LNCaP cells. This result suggests that bicalutamide-loaded micelles formulated with PEG-b-P(CB-co-LA) copolymer did not diminish the inhibitory effect of bicalutamide on cell proliferation since the PEG-b-P(CB-co-LA) copolymers themselves were not toxic in LNCaP cells. Although methanol is a toxic reagent, we do not anticipate its intrinsic toxicity to significantly alter our results since we used the equivalent of 1% v/v methanol and had appropriate controls. Moreover, we have previously used dimethyl sulfoxide (DMSO) which was found to kill tumor cells.

5. Conclusion

We have established that chemical tailoring of the PEG-b-PLLA micelle core through the introduction of carbonate moieties enhanced the solubilization of the highly lipophilic drug bicalutamide. This result was consistent with predictions made based on the Flory–Huggins interaction parameters computed for polymer/bicalutamide pairs using the group contribution method. Bicalutamide loading in PEG-b-P(CB-co-LA) micelles was four times better than in PEG-b-PLLA. PEG-b-P(CB-co-LA) copolymers were also shown to significantly solubilize bicalutamide as aqueous micellar solutions had drug concentrations approximately 800-fold higher than the saturated solubility of bicalutamide in water. In water, PEG-b-P(CB-co-LA) copolymers formed spherical micelles with CMC values up to 10 times lower than PEG-b-PLLA copolymers (*i.e.*, 0.31 μM for 20 mol% carbonate and 3.3 μM for 0 mol% carbonate), indicating that introduction of carbonate monomer results in copolymers which are more thermodynamically favored for self-assembly and exhibit better thermodynamic stability. Finally, PEG-b-P(CB-co-LA) copolymers were found to result in slower bicalutamide release compared to PEG-b-PLLA copolymers. Even though the inhibitory effect of bicalutamide-loaded PEG-b-P(CB-co-LA) micelles on LNCaP cell proliferation was similar to free drug these results are quite significant since drug dissolved in methanol would not be suitable for clinical application. In conclusion, these studies highlight the effect of chemically modifying the PEG-b-PLLA micelle core with a carbonate monomer on drug loading, release and stability and demonstrate their potential use as drug delivery vehicles. *In vivo* testing of bicalutamide-loaded PEG-b-P(CB-co-LA) micelles for tumor treatment is ongoing and would be reported in a separate paper.

Acknowledgement

The authors thank Davita Watkins for her help in obtaining ^{13}C NMR and GPC spectra.

Appendix

Figure with essential color discrimination. Figs. 1–3, 5–7 in this article have parts that are difficult to interpret in black and white. The full colour images can be found in the on-line version, at doi:10.1016/j.biomaterials.2009.11.081.

References

[1] Zhang S, Hsieh ML, Zhu W, Klee GG, Tindall DJ, Young CY. Interactive effects of triiodothyronine and androgens on prostrate cell growth and gene expression. Endocrinology 1999;140:1665–71.

[2] Blackledge G. Casodex-mechanisms of action and opportunities for usage. Cancer 1993;72:3830–3.

[3] Hennenfent KL, Govindan R. Novel formulations of taxanes: a review. Old wine in a new bottle? Ann Oncol 2006;17:735–49.

[4] Otsuka H, Nagasaki Y, Kataoka K. PEGylated nanoparticles for biological and pharmaceutical applications. Adv Drug Deliv Rev 2003;55:403–19.

[5] Yokoyama M, Miyauchi M, Yamada N, Okano T, Sakurai Y, Kataoka K, et al. Characterization and anticancer activity of the micelle-forming polymeric anticancer drug adriamycin-conjugated poly(ethylene glycol)-poly(aspartic acid) block copolymer. Cancer Res 1990;50:1693–700.

[6] Yoo HS, Park TG. Biodegradable polymeric micelles composed of doxorubicin conjugated PLGA-PEG block copolymer. J Control Release 2001;70:63–70.

[7] Liu J, Zeng F, Allen C. In vivo fate of unimers and micelles of a poly(ethylene glycol)-block-poly(caprolactone) copolymer in mice following intravenous administration. Eur J Pharm Biopharm 2007;65:309–19.

[8] Ramaswamy M, Zhang X, Burt HM, Wasan KM. Human plasma distribution of free paclitaxel and paclitaxel associated with diblock copolymers. J Pharm Sci 1997;86:460–4.

[9] Danquah M, Li F, Duke 3rd CB, Miller DD, Mahato RI. Micellar delivery of bicalutamide and embelin for treating prostate cancer. Pharm Res 2009;26:2081–92.

[10] Frazza EJ, Schmitt EE. A new absorbable suture. J Biomed Mater Res 1971; 5:43–58.

[11] Hench LL, Polak JM. Third-generation biomedical materials. Science 2002; 295:1014–7.

[12] Uhrich KE, Cannizzaro SM, Langer RS, Shakesheff KM. Polymeric systems for controlled drug release. Chem Rev 1999;99:3181–98.

[13] Schaffer JH. Journal of Eur Patent 1988;82:107247.

[14] Wang XL, Zhuo RX, Liu LJ, He F, Liu G. Synthesis and characterization of novel aliphatic polycarbonates. J Polym Sci Part A Polym Chem 2002;40:70–5.

[15] Zhu KJ, Hendren RW, Jensen KJ, Pitt CG. Synthesis, properties and biodegradation of poly(1,3-trimethylene carbonate). Macromolecules 1991;24:1736–40.

[16] Watanabe J, Kotera H, Akashi M. Reflective interfaces of poly(trimethylene carbonate)-based polymers: enzymatic degradation and selective adsorption. Macromolecules 2007;40:8731–6.

[17] Zhang Y, Taiming L, Liu J. Low temperature and glucose enhanced T7 RNA polymerase-based plasmid stability for increasing expression of glucagon-like peptide-2 in *Escherichia coli*. Protein Expr Purif 2003;29:132–9.

[18] Latere Dwan'Isa JP, Rouxhet L, Preat V, Brewster ME, Arien A. Prediction of drug solubility in amphiphilic di-block copolymer micelles: the role of polymer–drug compatibility. Pharmazie 2007;62:499–504.

[19] Huynh L, Grant J, Leroux JC, Delmas P, Allen C. Predicting the solubility of the anti-cancer agent docetaxel in small molecule excipients using computational methods. Pharm Res 2008;25:147–57.

[20] Mahmud A, Patel S, Molavi O, Choi P, Samuel J, Lavasanifar A. Self-associating poly(ethylene oxide)-b-poly(alpha-cholesteryl carboxylate-epsilon-caprolactone) block copolymer for the solubilization of STAT-3 inhibitor cucurbitacin I. Biomacromolecules 2009.

[21] Forster A, Hempenstall J, Tucker I, Rades T. Selection of excipients for melt extrusion with two poorly water-soluble drugs by solubility parameter calculation and thermal analysis. Int J Pharm 2001;226:147–61.

[22] Marsac PJ, Shamblin SL, Taylor LS. Theoretical and practical approaches for prediction of drug–polymer miscibility and solubility. Pharm Res 2006;23:2417–26.

[23] Liu J, Xiao Y, Allen C. Polymer–drug compatibility: a guide to the development of delivery systems for the anticancer agent, ellipticine. J Pharm Sci 2003;93:132–43.

[24] Pratt RC, Nederberg F, Waymouth RM, Hedrick JL. Tagging alcohols with cyclic carbonate: a versatile equivalent of (meth)acrylate for ring-opening polymerization. Chem Commun (Camb) 2008:114–6.

[25] Morton M, Kaizerman S, Altier MW. Swelling of latex particles. J Colloid Sci 1954;9:300.

[26] Guan H, Xie Z, Tang Z, Xu X, Chen X, Jing X. Preparation of block copolymer of ε-caprolactone and 2-methyl-2-carboxyl-propylene carbonate. Polymer 2004;46:2817.

[27] Xie Z, Hu X, Chen X, Sun J, Shi Q, Jing X. Synthesis and characterization of novel biodegradable poly(carbonate ester)s with photolabile protecting groups. Biomacromolecules 2008;9:376–80.

[28] Guan H, Xie Z, Zhang P, Wang X, Chen X, Wang X, et al. Synthesis and characterization of novel biodegradable block copolymer poly(ethylene glycol)-block-poly(ι-lactide-co-2-methyl-2-carboxyl-propylene carbonate). J Polym Sci Part A Polym Chem 2005;43:4771–80.

[29] Al-Azemi TF, Bisht KS. Novel functional polycarbonate by lipase-catalyzed ring-opening polymerization of 5-methyl-5-benzyloxcarbonyl-1,3-dioxan-2-one. Macromolecules 1999;32:6536–40.

[30] Tsuji H, Ikada Y. Stereocomplex formation between enantiomeric poly(lactic acid)s. 6. Binary blends from copolymers. Macromolecules 1992;25: 5719–23.

[31] Ray WC, Grinstaff MW. Polycarbonate and poly(carbonate-ester)s synthesized from biocompatible building blocks of glycerol and lactic acid. Macromolecules 2002;36:3557–62.

Pharmaceutical Research, Vol. 26, No. 9, September 2009 (© 2009)
DOI: 10.1007/s11095-009-9903-5

Research Paper

Micellar Delivery of Bicalutamide and Embelin for Treating Prostate Cancer

Michael Danquah,[1] Feng Li,[1] Charles B. Duke III,[1] Duane D. Miller,[1] and Ram I. Mahato[1,2]

Received January 30, 2009; accepted April 23, 2009; published online May 5, 2009

Purpose. To examine the effect of bicalutamide and embelin on the growth of prostate cancer cells *in vitro* and *in vivo*
Methods. Cell viability was determined by MTT assay. Micelles were fabricated with polyethylene glycol-*b*-polylactic acid (PEG-PLA) copolymer and characterized in terms of particle size, micellar solubilization and drug loading, followed by evaluation in nude mice bearing LNCaP xenografts.
Results. Embelin induced caspase 3 and 9 activation in LNCaP and C4–2 cells by decreasing XIAP expression and was more potent than bicalutamide in killing prostate tumor cells irrespective of their androgen status. As analyzed by isobologram analysis the combination of bicalutamide and embelin was synergistic for C4–2 but additive and slightly antagonistic for LNCaP cells. Micellar formulation resulted in at least 60-fold increase in the aqueous solubility of bicalutamide and embelin. Tumor growth was effectively regressed upon treatment with bicalutamide, but the extent of tumor regression was significantly higher when bicalutamide was formulated in micelles. However, tumor response to bicalutamide stopped after prolonged treatment and began to grow. Sequential treatment with XIAP inhibitor embelin resulted in regression of these hormone refractory tumors.
Conclusion. Combined treatment with bicalutamide and embelin may be an effective strategy for treating hormone refractory prostate cancer.

KEY WORDS: androgen; bicalutamide; embelin; micelles; prostate cancer.

INTRODUCTION

Prostate cancer is the most pervasive malignancy diagnosed in men and remains the second leading cause of cancer-related mortality affecting men in the USA (1). The progression of prostate cancer has been found to be androgen-dependent with androgen playing a key role in the proliferation, differentiation, and survival of prostate cancer cells (2–5). Consequently, androgen ablation, especially the use of antiandrogens, has been used as a standard treatment for men with prostate cancer. Antiandrogens may be divided into two classes: steroidal and nonsteroidal. Steroidal antiandrogens, including cyproterone acetate, interfere with androgen receptor (AR) binding, blocks 5α-reductase, and have progesterone-like antigonadotropic activity. The clinical potency of cyproterone has been limited due to loss of erectile potency, influence on carbohydrate metabolism, and associated cardiovascular and hepatocellular toxicity (6,7).

Nonsteroidal antiandrogens have been developed to avoid the side effects associated with steroidal antiandrogen therapy. Three compounds, namely: flutamide (Eulexin™), nilutamide and bicalutamide (Casodex™), are available for clinical use. Among them, bicalutamide is the most widely used in androgen ablation therapy due to its relatively long half-life and tolerable side effects (8). The initial treatment of prostate cancer with bicalutamide yields response in up to 85% of patients. However, it is not curative, since prolonged treatment results in mutations in the AR, which converts bicalutamide from an antagonist into an agonist leading to drug resistance and the occurrence of hormone-refractory prostate cancer (HRPC).

Resistance to apoptosis is a common feature associated with the progression of prostate cancer from androgen-dependence to HRPC. This defect in the apoptotic machinery prevents neoplastic cells from being naturally eliminated due to the downregulation of proapoptotic and overexpression of antiapoptotic proteins, resulting in an imbalance between the rates of proliferation and apoptosis. Hence, regulators of apoptosis have emerged as attractive targets in the development of therapeutic strategies for treating prostate cancer. Among the key regulators of apoptosis is the inhibitor of apoptosis (IAP) family which suppress caspase activity endogenously preventing cell death (9–11). The most thoroughly characterized and most potent IAP protein is the X-chromosome-linked IAP (XIAP) (11). XIAP protein binds and inhibits the initiator caspase-9 and effector caspase-3 and caspase-7 through the binding of its BIR3 domain and the linker region between BIR1 and BIR2, respectively; consequently inhibiting both intrinsic and extrinsic apoptotic pathways (12–15). Recently, expression levels of XIAP in human

[1] Department of Pharmaceutical Sciences, University of Tennessee Health Science Center, 19 South Manassas (Room 224), Memphis, Tennessee 38103-3308, USA.
[2] To whom correspondence should be addressed. (e-mail: rmahato@utmem.edu; URL: http://cop.utmem.edu/rmahato)

prostate cancer cells was found to correlate with apoptotic resistance (16,17).

Embelin is a novel cell permeable small molecule inhibitor of XIAP, which was discovered by structure-based computational screening of a three-dimensional structure library of natural products derived from traditional Chinese medicine (18). Embelin binds to the XIAP BIR3 domain preventing its binding to and inhibition of caspase-9 and effector caspase-3 and caspase-7 (18). Also, embelin has been shown to possess antitumor and anti-inflammatory properties, as well as decrease testosterone levels (19,20). Recently, embelin was shown to block nuclear factor-κB (NF-κB) signaling pathway resulting in the suppression of NF-κB-regulated antiapoptotic and metastatic gene products, making it a potential effective suppressor of tumor cell survival, proliferation, angiogenesis, invasion, and inflammation (21).

Presently, there are limited treatment options for HRPC and a number of therapeutic strategies including combination therapy are the subject of intense research. Several studies have examined the effect of combining radiation, chemotherapeutic, and hormonal agents in treating prostate cancer. Traditionally, the exploration of combination therapy for treating hormone-refractory prostate cancer involves clinically combining well known cytotoxic chemotherapeutic agents (e.g., docetaxel and paclitaxel) and testing their potency in man. While these studies have shown some drug combinations to have synergistic effect in treating prostate cancer, the advantage may be marginal since their toxicity might exceed their benefit. A current approach in combination therapy requires a paradigm shift, in which the drug regimen incorporates chemotherapeutic agents which are selectively toxic to cancer cells. Therefore, one of our goals was to identify and explore a new combination of therapeutic agents for treating HRPC which is simultaneously potent and less toxic to humans; and can potentially be used for clinical treatment. Since embelin is a powerful inhibitor of XIAP and has minimal effects on normal human prostate epithelial cells (18), we investigated its cytotoxic effect as a single-agent and possible synergism in combination with bicalutamide in two androgen receptor containing human prostate cancer cell lines: LNCaP, which is androgen dependent and C4–2, which is androgen independent. The structures of bicalutamide and embelin are shown in Fig. 1A. We hypothesize that therapeutic combinations of bicalutamide and embelin will have a synergistic effect on growth inhibition and apoptosis of LNCaP and C4–2 cells as well as tumor regression in xenograft mouse models considering their mechanism of action (Fig. 1B).

Polymeric micelles are known to improve the solubility, stability, site specificity and hence therapeutic efficacy of hydrophobic drugs. These micelles self-assemble into nano-sized (20–60 nm), spherical structures with a hydrophobic core capable of solubilizing a considerable amount of highly water insoluble drugs. The stealth properties associated with poly(ethylene oxide) (PEO) hydrophilic corona of polymeric micelles prevents recognition by the reticuloendothelial system (RES) and therefore minimizes elimination of the micelles from the bloodstream (22). Thus, these so called 'stealth' properties of the PEO shell result in increased blood circulation times and prevention of plasma protein binding (23). In addition, the small size ensures preferential accumulation in tumor cells via the enhanced permeability and retention (EPR) effect (24,25).

In this study, polymeric micelles were fabricated using poly(ethylene glycol)-*b*-poly(lactic acid) [PEG-PLA] copolymer and used for enhancing the water solubility and bioavailability of bicalutamide and embelin to improve their efficacy. The enhanced drug water solubility and bioavailability translate into a reduction in the administered dose and possible toxicity in normal cells. In the current study, PLA was selected as the hydrophobic core-forming block since it is Food and Drug Administration (FDA) approved for clinical use and hence may facilitate the translation of our therapeutic agents for clinical applications. In addition, the *in vitro* synergistic or additive antiproliferative effects of combined bicalutamide and embelin, each possessing distinct cytotoxic mechanisms, was studied in both androgen dependent (LNCaP) and androgen independent (C4–2) human prostate cancer cells, while mechanistic studies on the induction of apoptotic cell death was also conducted. Finally, the ability of sequential exposure to bicalutamide-loaded micelles followed by embelin-loaded micelles to regress prostate cancer tumors in xenograft mice models was examined.

MATERIALS AND METHODS

Materials

PEG (5100)-b-PLA (4500) copolymer (Mn=9,600) was purchased from Polymer Source (Montreal, Canada). Embelin was purchased from Sigma–Aldrich (St. Louis, MO) while bicalutamide was synthesized as described by Mukherjee *et al.* (26) RPMI 1640 medium was obtained from Invitrogen (Carlsbad, CA) and human prostate cancer cells C4–2 and lymph node prostate adenocarcinoma (LNCaP) were purchased from American Type Culture Collection (ATCC, Manassas, VA). Caspase-Glo™ 3/7, 8 and 9 assay and RNA extraction kits were purchased from Promega (Madison, WI). SYBR Green real time PCR master mix and reverse transcription reagents were purchased from Applied Biosystems (Foster city, CA). Human Total XIAP ELISA kit was purchased from R&D Systems (Minneapolis, MN). All other reagents were obtained from Sigma–Aldrich (St. Louis, MO) unless otherwise stated and were used as received.

In vitro Cell Viability Assays

Human prostate cancer cells, LNCaP and C4–2 cells (American Type Culture Collection) were incubated in RPMI 1640 media supplemented with 2 mM L-glutamine, 10% fetal bovine serum and 1% penicillin-streptomycin at 37°C in humidified environment of 5% CO_2 and subcultured every 3–4 days to maintain exponential growth.

Cells were seeded in 96-well plates at a density of 5×10^3 viable cells/well and incubated for 48 h to permit cell attachment. The cells were exposed to bicalutamide or embelin at concentrations ranging from 1 to 100 μM for 24 h. At the end of treatment, 20 μl of MTT (5 mg/ml) was added to each well and incubated for 3–4 h. The plates were then centrifuged at 1,500×*g* for 2 min and the medium aspirated. The residual formazan crystals were solubilized

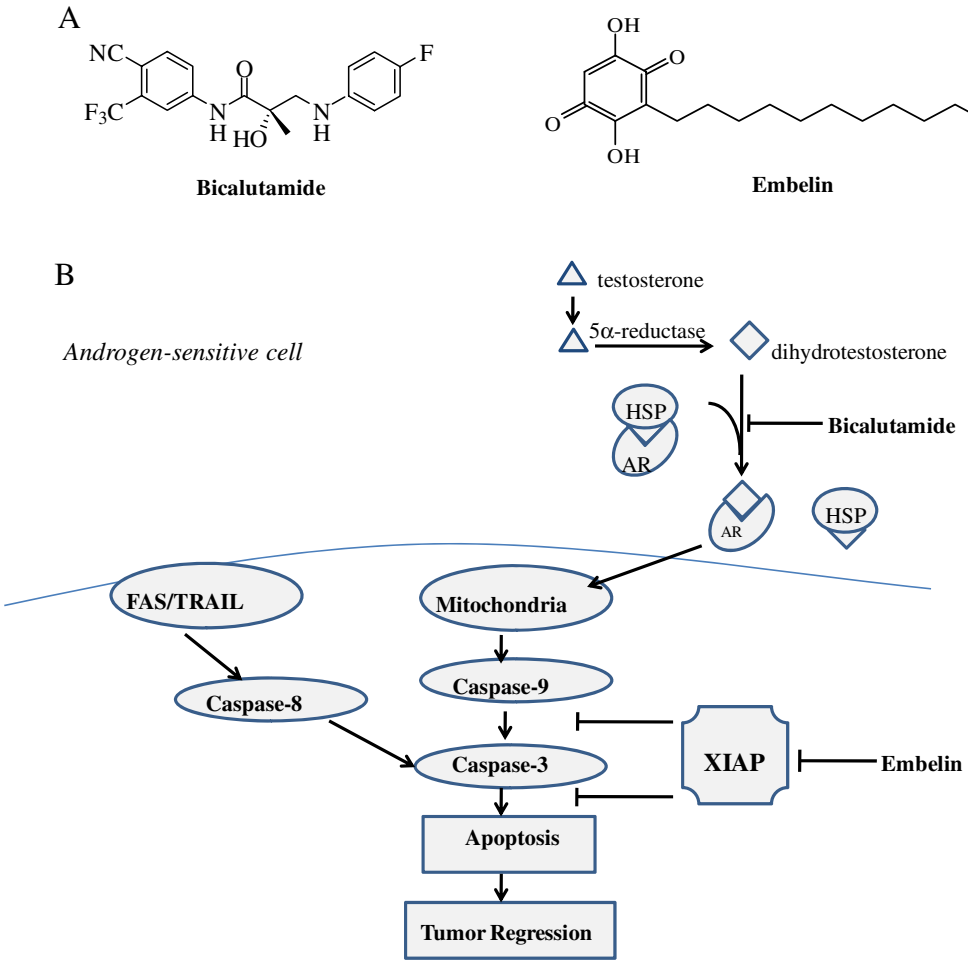

Fig. 1. Chemical structures of bicalutamide and embelin (**A**) and schematic diagram showing the combined effect of bicalutamide and embelin on apoptosis in androgen-sensitive cells and on tumor regression (**B**).

with 100 μl DMSO and the plate analyzed using a microplate reader recording absorbance values at a test wavelength of 560 nm. Cell viability for a given concentration was expressed as a percentage of the intensity of controls.

Caspase Detection

Caspase-Glo 3/7, 8 and 9 assay kits purchased from Promega (Madison, WI) were used to analyze caspase 3, 8 and 9 activities, respectively, as per the manufacturer's protocol. Briefly, 100 μl Caspase-Glo reagent was added to 100 μl of culture supernatants in 96-well plates and incubated at room temperature for 1 hour. The contents were then transferred into disposable culture tubes and luminescence was determined using a Berthold Detection Systems Sirius luminometer (Pforzheim, Germany).

XIAP Expression Analysis

The mRNA and protein level expression of XIAP in LNCaP and C4–2 cells after treatment with embelin for 48 h was assayed using quantitative real-time PCR and ELISA, respectively. Briefly, total RNA was isolated using RN easy mini isolation kit from Qiagen. RNA concentration was measured by UV spectrophotometry with a Biomate 3 spectrophotometer. One hundred and fifty nanograms of extracted RNA was converted into cDNA using Multi-Scribe reverse transcriptase and random hexamers (Applied Biosystems, Inc., Foster City, CA) by incubation at 25°C for 10 min, followed by reverse transcription at 48°C for 30 min and enzyme inactivation at 95°C for 5 min. To determine the level of XIAP expression, the following XIAP-specific primers were used: Forward: 5′-TGT TTC AGC ATC AAC ACT GGC ACG-3′; Reverse: 5′-TGC ATG ACA ACT AAA GCA CCG GAC-3′ (NM_001167). The PCR conditions included denaturation at 95°C for 10 min, followed by 40 cycles of amplification by sequential denaturation at 95°C for 15 s and primer annealing as well as strand extension for 1 min. XIAP gene expression was normalized to β-actin as internal control. To confirm the amplification specificity, the PCR products were subjected to melting curve analysis. The expressed XIAP levels were quantified and normalized to the total amount of cDNA used.

For XIAP protein expression, total protein was isolated by lysing cells. XIAP levels were measured as per the protocol of Human Total XIAP ELISA kit obtained from R&D Systems (Minneapolis, MN). Results were normalized by measuring the total protein using a BCA assay kit.

Isobologram Analysis

The dose-response interaction between bicalutamide and embelin at the point of IC_{50} was assessed to be synergistic, additive or antagonistic using the isobologram method of analysis of Steel and Peckham (27). Dose–response curves were plotted for the effects of bicalutamide and embelin on human prostate cancer LNCaP and C4–2 cell viability. From these curves, the combined drug IC_{50} values were determined for each curve. Specifically, LNCaP and C4–2 cells were treated with embelin (0, 5, 10, 25 and 50 μM) and bicalutamide (0, 10, 25 and 50 μM) either simultaneously or sequentially and cell viability assessed using MTT assay resulting in the above-mentioned dose-response curves. The combination index (CI) was calculated by the formula:

$$CI = \frac{d1}{D_{50}1} + \frac{d2}{D_{50}2} \quad (1)$$

where $D_{50}1$ is the dose of agent 1 (bicalutamide) required to produce 50 percentage effect alone, and $d1$ is the dose of agent 1 required to produce the same 50 percentage effect in combination with $d2$. Similarly, $D_{50}2$ is the dose of agent 2 (embelin) required to produce 50 percentage effect alone, and $d2$ is the dose of agent 2 required to produce the same 50 percentage effect in combination with d1. The CI values were interpreted as follows: <1.0, synergism; 1.0, additive effect; >1.0, antagonism. Each experiment was performed three times. The parameters $d1$ and $d2$ in Eq. 1 were obtained as follows: when a dose of bicalutamide ($d1$) was selected the incremental effect produced by adding embelin starting from 0 to 50 μM was assessed. The concentration of embelin that when combined with d1 resulted in the inhibition of 50% cell growth was designated $d2$.

Fabrication of Drug-Loaded Micelles

The film sonication method was used to load bicalutamide and embelin into the core of polyethylene glycol-polylactic acid (PEG-PLA) micelles. All experiments were performed using a theoretical loading of 5% unless otherwise stated. Briefly, 1 mg of bicalutamide or embelin and 19 mg of PEG-PLA was dissolved in 5 ml methanol. The mixture was allowed to stir for 5 min and the solvent evaporated. The resulting film was hydrated and sonicated for 7 min using a Misonix ultrasonic liquid processor (Farmingdale, NY) with an output power of 25 W. The resultant formulation was then centrifuged at 5,000 rpm for 10 min to separate micelles from residual free drug. Subsequently, the supernatant was filtered using a 0.22 μm nylon filter. The micelle preparation was immediately lyophilized for 2 days and stored at 4°C to prolong shelf-life and avoid untimely release of the drug. The micelle yield was calculated using the equation below.

$$\text{Yield} = \frac{\text{weight of micelle}}{\text{weight of micelle} + \text{initial drug fed}} \times 100\% \quad (2)$$

Critical Micelle Concentration

Fluorescence spectroscopy was used to estimate the critical micelle concentration (CMC) of PEG-PLA copolymer using pyrene as a hydrophobic fluorescent probe. Nine samples of PEG-PLA dissolved in methanol with concentrations ranging from 1×10^{-8} to 1 g/L were prepared and allowed to equilibrate with a constant pyrene concentration of 6×10^{-7} M for 48 h at room temperature. The fluorescence spectra of pyrene were recorded with a Molecular Devices SpectraMax M2/M2^e spectrofluorometer (Sunnyvale, CA). An excitation wavelength of 390 nm was used and the emission spectra recorded from 320 to 450 nm with both bandwidths set at 2 nm. Peak height intensity ratio (I_3/I_1) of the third peak (I_3 at 338 nm) to the first peak (I_1 at 333 nm) was plotted against the logarithm of polymer concentration. The value of the CMC was obtained as the point of intersection of two tangents drawn to the curve at high and low concentrations, respectively.

Drug Loading Density and Encapsulation Efficiency

Drug loading was determined as follows: Lyophilized drug-loaded micelles were dissolved in methanol and the drug present in solution measured by ultraviolet spectroscopy. The weight of drug loaded in the micelles was calculated using a calibration curve. Background absorbance interference from PEG-PLA copolymer was accounted for by measuring the absorbance of blank PEG-PLA micelles under the same conditions. The micelle drug loading content and encapsulation efficiency were obtained by Eqs. 2 and 3.

$$\text{drug loading density} = \frac{\text{weight of drug in micelle}}{\text{weight of micelle}} \times 100\% \quad (3)$$

$$\text{drug encapsulation efficiency} = \frac{\text{weight of drug in micelle}}{\text{weight of drug originally fed}} \times 100\% \quad (4)$$

Size and Size Distribution

Mean particle size and size distribution of drug-loaded micelles were measured via dynamic light scattering using a Malvern instruments Zetasizer Nano Series (Worcestershire, UK). Samples were diluted to appropriate concentrations and analyzed at room temperature with a 90° detection angle. Mean micelle size was obtained as a Z-average which is an intensity mean. All measurements were repeated seven times and reported as the mean diameter ±SD for triplicate samples.

Solubility Studies of Drug-Loaded Micelles

The water solubility of free drug (bicalutamide or embelin) and drug-loaded micelles was determined by shaking an excess amount of free drug and 3 mg of drug-loaded micelles in 1 mL water, respectively. The suspension was then centrifuged at 8,000×g for 10 min and filtered on 0.2 μm cellulose membrane. The amount of bicalutamide in the saturated solution was evaluated by UV spectroscopy as described above.

In vivo Efficacy Assessment of Bicalutamide-Loaded Micelles in Xenografts

All animal experiments were performed in accordance with NIH animal use guidelines and the protocol approved by the Animal Care and Use Committee at the University of Tennessee Health Science Center. Xenograft flank tumors were induced in 8 week old male BALB/C nude mice purchased from The Jackson Laboratory (Bar Harbor, ME) by subcutaneous injection of three million LNCaP cells suspended in 1:1 media and matrigel. When tumors reached approximately 150 mm^3, mice were randomized into three groups of five mice, minimizing weight and tumor size differences. Each group was treated with intratumoral injection of saline, sonicated bicalutamide suspension or bicalutamide-loaded micelles (20 mg/kg) three times a week. Tumors were measured with a caliper prior to each injection, and their volumes calculated using the formula: $(\text{width}^2 \times \text{length})/2$.

RESULTS

Effect of Bicalutamide on Apoptosis

To determine whether prostate cancer cell death by bicalutamide is also associated with apoptosis, we determined the activation of initiator caspases 8 and 9, and effector caspase 3 at 48 h post-incubation of LNCaP cells with bicalutamide using caspase luminescence assay. Results were normalized by measuring the total protein using BCA protein assay kit. As shown in Fig. 2, relatively high levels of caspases 3 and 9 compared to caspase 8 were observed at the drug concentration of 50 and 100 μg/ml.

Effect of Embelin on Caspase Activation and XIAP Inhibiton

Resistance to apoptosis is a characteristic feature of prostate cancer and XIAP is known to inhibit the activation of the initiator caspase 9 and the effector caspase 3 which is the committed step in the apoptotic pathway. Hence, we determined the levels of caspase activation and XIAP expression levels in LNCaP and C4–2 cells after treatment with 5 μM embelin (XIAP inhibitor) for 48 h. As demonstrated in Fig. 3A, caspase activation was higher in the embelin treated cells. Specifically, caspase 8 had lower activation levels compared to caspases 3 and 9, with caspase 9 activity being the highest. However, the caspase 3 and 9 activation was found to be lower in C4–2 cells compared to LNCaP cells. To determine whether the differential levels of caspase activity in LNCaP and C4–2 cells correlate with XIAP expression, we measured baseline XIAP expression in both cells and the effect of embelin in inhibiting XIAP expression using ELISA and real time RT-PCR, respectively (Fig. 3B). The data show that C4–2 cells have higher baseline XIAP expression levels than LNCaP, and treatment with 5 μM embelin resulted in a decrease in XIAP expression in both cell lines. However, the decrease in XIAP expression upon treatment with embelin was more pronounced in LNCaP cells compared to C4–2 cells.

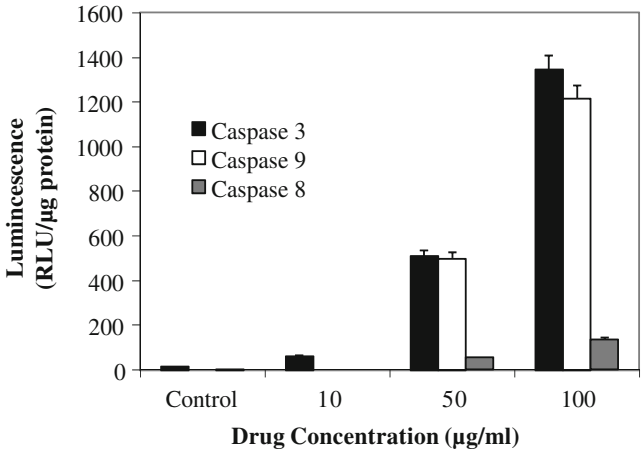

Fig. 2. Effect of bicalutamide on the activation of caspases in LNCaP cells. At 48 h postincubation with the drug at a dose of 0 (control), 10, 50 and 100 μg/ml, cells were lyzed to determine caspase 3, 8 and 9 activities in terms of relative light units (RLU) and total protein using a BCA protein assay kit. Results are presented as the mean ± SD of triplicates.

Effect of Bicalutamide and Embelin on Prostate Cancer Cell Growth

To determine whether embelin can be used for treating androgen dependent and hormone refractory prostate cancer, we determined the IC_{50} values of both bicalutamide and embelin in two androgen receptor containing human prostate cancer cells, androgen sensitive LNCaP and hormone refractory C4–2 prostate cancer cells. As shown in Fig. 4, embelin was more potent than bicalutamide in killing prostate tumor cells irrespective of their androgen status. LNCaP cells were more sensitive to bicalutamide compared to C4–2 cells, with a 50% inhibitory concentration (IC_{50}) of approximately 43 and 93 μM, respectively (Fig. 4A). Hence, C4–2 cells which are androgen independent and AR positive displayed a two-fold resistance to bicalutamide compared to LNCaP cells which are androgen dependent. In contrast, embelin exhibited superior antiproliferative activity in LNCaP and C4–2 cells, with IC_{50} of ~5 μM (Fig. 4B). However, both cell lines displayed similar sensitivity to embelin at the concentrations examined.

We used the isobologram method of Steel and Peckham (27) to assess whether the simultaneous or sequential combination of these two drugs could confer synergistic, additive, or antagonistic effects. Combination index (CI) was determined after treating 1×10^4 C4–2 cells with a combination of bicalutamide and embelin. Cell viability was determined by MTT assay and the resulting dose-response curves are shown in Fig. 5**.** CI was calculated by the formula: $CI=(d1/D_{50}1)+(d2/D_{50}2)$, where $D_{50}1$ is the dose of bicalutamide required to produce 50% effect alone, and $d1$ is the dose of bicalutamide required to produce the same 50% effect in combination with $d2$. $D_{50}2$ is similarly the dose of embelin required to produce 50% effect alone, and $d2$ is the dose of embelin required to produce the same 50% effect in combination with $d1$. The CI values are interpreted as follows: <1.0, synergism; 1.0, additive; and >1.0, antagonism. The data is reported in Tables I, II and III. These results suggest that the cytotoxic effect of bicalutamide and embelin combination was dependent on the treatment schedule and cell line. When the combination of these two drugs

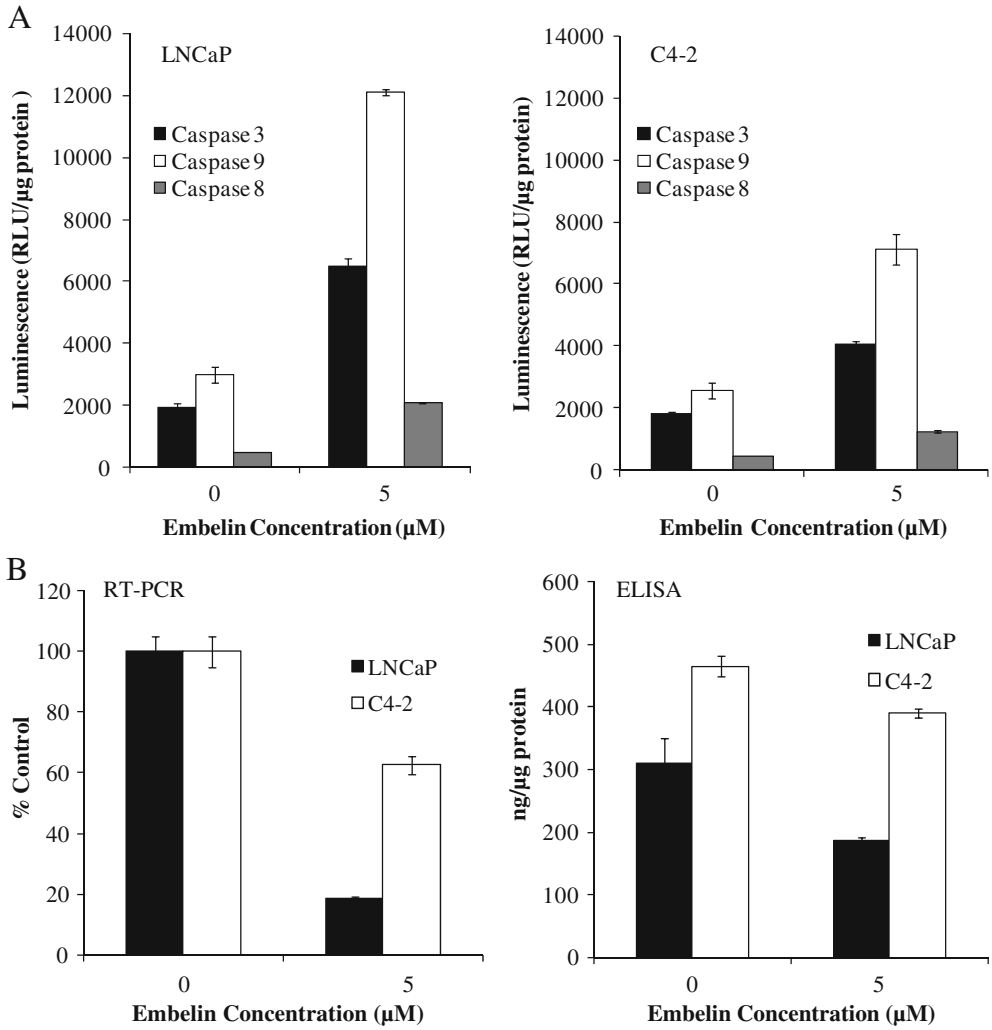

Fig. 3. Effect of embelin on caspase activation and XIAP inhibition in LNCaP and C4–2 prostate cancer cells. Embelin effectively activates caspases 3, 8 and 9 in LNCaP and C4–2 cells. Activation of caspases is higher in LNCaP cells which have comparatively lower XIAP expression. 1×10^6 LNCaP or C4–2 cells per well in six-well plates were treated with embelin for 48 h. Cells were lyzed to determine caspase 3, 8 and 9 activities in terms of relative light units (RLU) and total protein using a BCA protein assay kit. Results are presented as the mean ± SD of triplicates (**A**). XIAP expression in LNCaP and C4–2 cells using real time RT-PCR and ELISA (**B**).

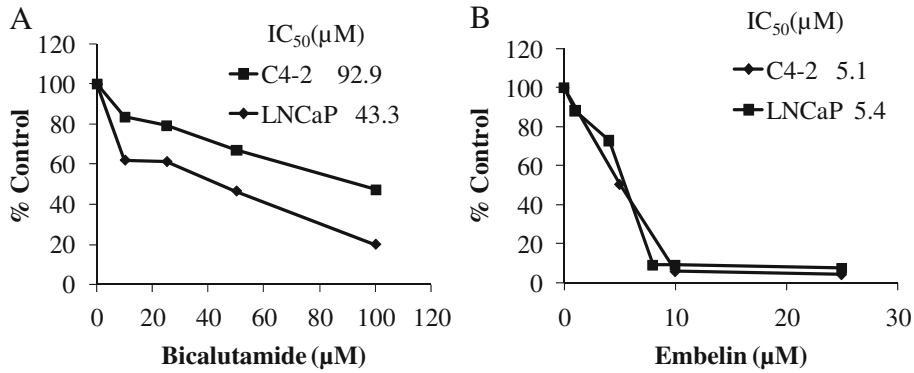

Fig. 4. Effect of drug treatment on cell viability in prostate cancer cells (C4–2 and LNCaP). **A** C4–2 and LNCaP cells treated with increasing concentrations of bicalutamide (0–100 µM) for 24 h. **B** C4–2 and LNCaP cells treated with increasing concentrations of embelin (0–25 µM) for 24 h. Results are expressed as the percentage of control.

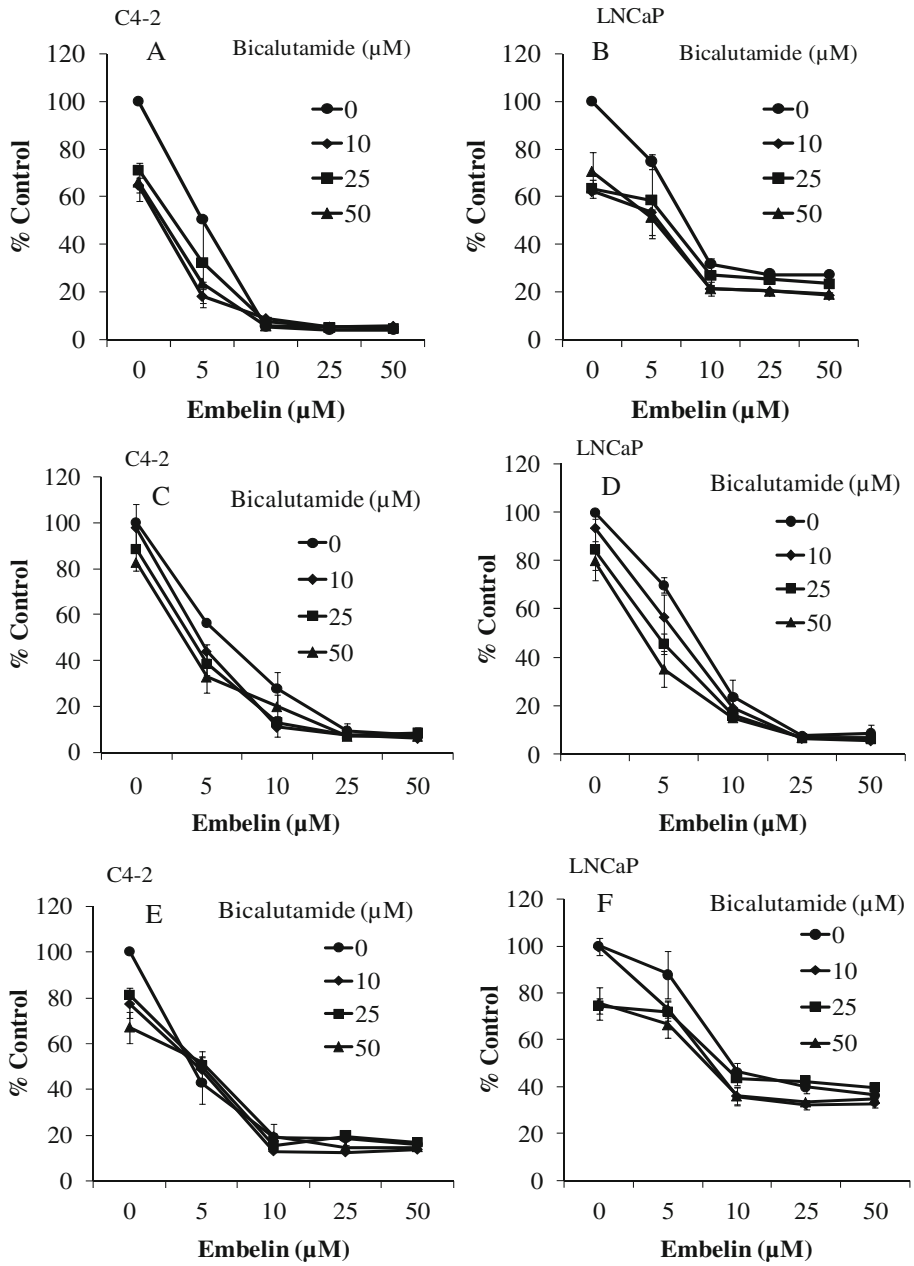

Fig. 5. Dose–response curves for bicalutamide and embelin combination in human prostate cancer cells. Simultaneous exposure (24 h) to bicalutamide and embelin in C4–2 and LNCaP cells, respectively (**A**) and (**B**). Sequential exposure (12 h incubation periods to bicalutamide followed by embelin in C4–2 and LNCaP cells, respectively (**C**) and (**D**). Sequential exposure (12 h incubation periods) to embelin followed by bicalutamide in C4–2 and LNCaP cells, respectively (**E**) and (**F**). The cell viability was measured using an MTT assay and plotted as a percentage of control.

were used, simultaneous exposure and sequential treatment of bicalutamide followed by embelin was synergistic in C4–2 cells, while additive and antagonistic effects were observed for LNCaP cells. Sequential treatment of embelin followed by bicalutamide was additive and antagonistic for both cell lines.

Characterization of Polymeric Micelles

Micelles were fabricated with polyethylene glycol-*b*-polylactic acid (PEG-PLA) di-block copolymer using the film sonication method. We determined the critical micelle concentration (CMC) using pyrene as a hydrophobic probe to observe micelle formation by monitoring polarity changes in the micellar microenvironment (28,29). Changes in the vibrational band intensity ratio (I_3/I_1) with polymer concentration was used to detect the onset of micelle formation, where I_3 at 338 nm and I_1 at 333 nm correspond to the (0,2) and (0,0) bands, respectively (30). The CMC obtained at the point of inflection of the I_3/I_1 *versus* the logarithm of polymer concentration curve was approximately 1 mg/L (data not shown). The particle size distribution of these micelles before

Table I. Synergistic Antiproliferative Activity of Bicalutamide and Embelin in Human Prostate Cancer Cells

Drug combination	Cell line	d1 (μM)	d2 (μM)	CI
Bicalutamide + Embelin	C4–2	10	1.59	0.42
	LNCaP	10	4.66	1.09
Bicalutamide → Embelin	C4–2	10	4.51	0.87
	LNCaP	10	5.90	1.05
Embelin → Bicalutamide	C4–2	10	5.65	1.22
	LNCaP	10	8.09	1.08

Combination Index (CI) of simultaneous and sequential treatment of bicalutamide and embelin in C4–2 and LNCaP cells. 5×10^3 cells were simultaneously treated with a combination of bicalutamide and embelin or sequentially [(bicalutamide followed by embelin) or (embelin followed by bicalutamide)]. Cell viability was determined by MTT assay. The combination index (CI) was calculated by the formula: $CI=(d1/D_{50}1)+(d2/D_{50}2)$, where $D_{50}1$ is the dose of bicalutamide required to produce 50% effect alone, and $d1$ is the dose of bicalutamide required to produce the same 50% effect in combination with $d2$. $D_{50}2$ is similarly the dose of embelin required to produce 50% effect alone, and $d2$ is the dose of embelin required to produce the same 50% effect in combination with d1. 10 μM bicalutamide was combined with 0, 5, 10, 25 and 50 μM embelin. The CI values are interpreted as follows: <1.0, synergism; 1.0, additive; and >1.0, antagonism. Each experiment was done in triplicate

Table III. Synergistic Antiproliferative Activity of Bicalutamide and Embelin in Human Prostate Cancer Cells

Drug combination	Cell line	d1 (μM)	d2 (μM)	CI
Bicalutamide + Embelin	C4–2	50	1.90	0.91
	LNCaP	50	4.27	1.94
Bicalutamide → Embelin	C4–2	50	3.26	1.09
	LNCaP	50	3.42	1.63
Embelin → Bicalutamide	C4–2	50	6.33	1.78
	LNCaP	50	7.71	1.96

Combination Index (CI) of simultaneous and sequential treatment of bicalutamide and embelin in C4–2 and LNCaP cells. 5×10^3 cells were simultaneously treated with a combination of bicalutamide and embelin or sequentially [(bicalutamide followed by embelin) or (embelin followed by bicalutamide)]. Cell viability was determined by MTT assay. The combination index (CI) was calculated by the formula: $CI=(d1/D_{50}1)+(d2/D_{50}2)$, where $D_{50}1$ is the dose of bicalutamide required to produce 50% effect alone, and $d1$ is the dose of bicalutamide required to produce the same 50% effect in combination with $d2$. $D_{50}2$ is similarly the dose of embelin required to produce 50% effect alone, and $d2$ is the dose of embelin required to produce the same 50% effect in combination with $d1$. 10 μM bicalutamide was combined with 0, 5, 10, 25 and 50 μM embelin. The CI values are interpreted as follows: <1.0, synergism; 1.0, additive; and >1.0, antagonism. Each experiment was done in triplicate

and after drug loading was measured by dynamic light scattering with mean particle size in the range of 30 to 50 nm.

Drug Encapsulation Efficiency and Micellar Solubility

The film sonication method was chosen for the fabrication of bicalutamide and embelin-loaded micelles since it yields micelles with higher drug loading (31). Preliminary experiments were performed to optimize formulation parameters such as sonication time, output power and the volume of water used for film hydration. This was done to obtain the highest drug loading possible. A sonication time of 7 min, output power of 25 W and hydration volume of 5 ml (*i.e.*, a micelle concentration of 4 mg/ml) proved optimal.

Table II. Synergistic Antiproliferative Activity of Bicalutamide and Embelin in Human Prostate Cancer Cells

Drug combination	Cell line	d1 (μM)	d2 (μM)	CI
Bicalutamide + Embelin	C4–2	25	2.74	0.81
	LNCaP	25	5.61	1.61
Bicalutamide → Embelin	C4–2	25	3.85	0.92
	LNCaP	25	4.47	1.20
Embelin → Bicalutamide	C4–2	25	5.80	1.41
	LNCaP	25	8.88	1.51

Combination Index (CI) of simultaneous and sequential treatment of bicalutamide and embelin in C4–2 and LNCaP cells. 5×10^3 cells were simultaneously treated with a combination of bicalutamide and embelin or sequentially [(bicalutamide followed by embelin) or (embelin followed by bicalutamide)]. Cell viability was determined by MTT assay. The combination index (CI) was calculated by the formula: $CI=(d1/D_{50}1)+(d2/D_{50}2)$, where $D_{50}1$ is the dose of bicalutamide required to produce 50% effect alone, and $d1$ is the dose of bicalutamide required to produce the same 50% effect in combination with $d2$. $D_{50}2$ is similarly the dose of embelin required to produce 50% effect alone, and $d2$ is the dose of embelin required to produce the same 50% effect in combination with $d1$; 10 μM bicalutamide was combined with 0, 5, 10, 25 and 50 μM embelin. The CI values are interpreted as follows: <1.0, synergism; 1.0, additive; and >1.0, antagonism. Each experiment was done in triplicate

To determine the maximum amount of drug that could be loaded into the micelles, the theoretical loading of bicalutamide and embelin into PEG-PLA micelles was systematically increased from 1% to 20% *w/w*. There was a linear relationship between the amount of embelin incorporated into the micelles with increasing theoretical loading. In contrast, the loading density for bicalutamide could not increase when the theoretical drug loading reached 10% or higher. At all theoretical loadings, the loading density of embelin was higher than that of bicalutamide especially at theoretical loading above 10% (Fig. 6A). From the experimental results, a theoretical loading of 5% *w/w* was chosen for all *in vitro* and *in vivo* experiments in this study since it was the optimum formulation in terms of drug loading, encapsulation efficiency, and yield.

The effect of micellar solubilization on the aqueous solubility of bicalutamide and embelin-loaded micelles was determined by shaking an excess amount of free drug or 3 mg of drug-loaded micelles in 1 ml water, respectively. Free bicalutamide and embelin exhibit very low water solubility of ~1 μg/ml, respectively. However, bicalutamide and embelin-loaded micelles resulted in a significant increase in drug solubility with increasing theoretical loading (Fig. 6B). At 10% *w/w* a 60-fold increase in water solubility was observed for a micelle concentration of 3 mg/ml. It is noteworthy that at each theoretical loading, the amount of drug brought into solution is essentially equivalent to the amount of drug successfully incorporated in the polymer.

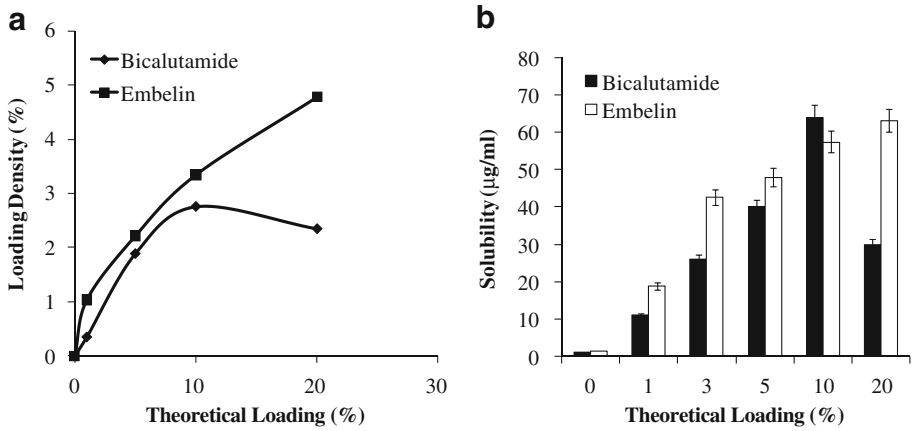

Fig. 6. Drug loading (**A**) and micellar solubilization (**B**) of bicalutamide and embelin. Water solubility of the drug was determined at 25°C. Both loading efficiency into PEG-PLA micelles and increase in aqueous solubility due to micellar solubization were higher for embelin than bicalutamide.

In vivo Efficacy Assessment of Drug-Loaded Micelles in Xenografts

Following *in vitro* characterization of bicalutamide and embelin loaded polymeric micelles in terms of particle size, micellar solubilization, drug loading and inhibitory effect on LNCaP cell proliferation, we decided to test bicalutamide-loaded micelles in mice bearing LNCaP xenografts. Xenograft flank tumors were induced in 8 week old male BALB/C nude mice by subcutaneous injection of three million LNCaP cells suspended in 1:1 media and matrigel. When tumors reached approximately 150 mm^3, mice were randomized into three groups of five mice. Each group was treated with intratumoral injection of saline, bicalutamide suspension and bicalutamide-loaded micelles at the dose of 20 mg/kg three times a week. Tumors were measured with a caliper prior to each injection, and their volumes calculated using the formula: ($width^2$ × length)/2. As shown in Fig. 7, tumor growth was effectively regressed upon treatment with bicalutamide up to 20 days post-treatment. Formulation into PEG-PLA polymeric micelles further regressed tumor growth and this effect was more significant in case of bicalulamide.

Unfortunately, these tumors became insensitive to bicalutamide at 20 days after treatment and began to grow. Since antiapoptotic proteins, including XIAP, is known to get upregulated in hormone refractory prostate cancer, we decided to treat these tumors subsequently with emblin, which is an effective XIAP inhibitor. As shown in Fig. 7, sequential treatment with embelin resulted in regression of hormone insensitive tumors.

DISCUSSION

Prostate cancer is the second leading cause of death in men in North America. Since androgens play an important role in progression of prostate cancer, androgen ablation and blockade of androgen action are the two most common modalities for treating prostate cancer. Although bicalutamide is one of the most widely used nonsteroidal antiandrogens for treating prostate cancer, it is highly hydrophobic and prolonged exposure leads to drug resistance, the occurrence of hormone refractory prostate cancer and an increased propensity for metastasis (32–35). Since hormone refractory tumors are resistant to apoptosis and overexpress XIAP, the objective of this study was to see whether small molecule XIAP inhibitor such as embelin can be used to treat bicalutamide irresponsive tumors.

Since the precise cellular mechanism by which bicalutamide induces apoptosis is still not well understood, we first measured the activity of caspases 3, 8 and 9, since caspase 9 upregulation represents mitochondrial pathway and caspase 8 upregulation represents extrinsic pathway (36). As shown in Fig. 2, there was dose dependent increase in all three caspases. However, the level was very high in the case of 3 and 9. Our results are in good agreement with the work of

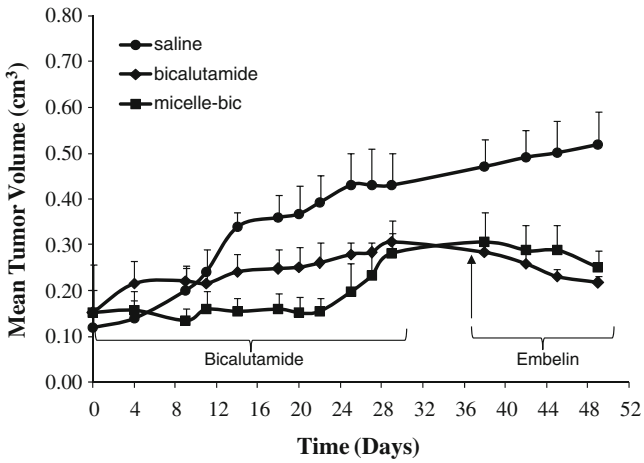

Fig. 7. Effect of bicalutamide and embelin-loaded micelles on growth of tumors derived from LNCaP prostate cancer cells in nude mice. Nude mice bearing 150-mm^3 LNCaP tumors were given an intratumoral injection of 20 mg/kg bicalutamide three times a week and tumor size was measured prior to each injection. Tumor growth regression was significantly higher for bicalutamide-loaded micelles compared to the free drug up to 20 days post-treatment. Since tumors became insensitive to bicalutamide at 20 days after treatment and began to grow, bicalutamide treatment was discontinued and embelin-loaded micelles were administered from day 28, which resulted in regression of hormone insensitive tumors. *Points* are mean tumor size (n=5); *bars*, SE.

Lee *et al.* (37), who also reported caspase 3 levels to be 5-fold higher than caspase 8 when LNCaP cells were treated with bicalutamide. Further, AR gene silencing has been reported to result in massive prostate tumor cell death through mitochondrial pathway regardless of their androgen sensitivity (38). These results suggest that bicalutamide mainly follows mitochondrial pathway.

Prolonged treatment with bicalutamide is known to convert androgen sensitive prostate cancer cells into apoptosis resistant hormone refractory cells due to overexpression of antiapoptotic genes including Bcl-2, Bcl-X_L and XIAP (39). Among them, XIAP is the most potent in inhibiting apoptosis via inhibition of effector caspases. XIAP inhibitors are known to inhibit caspases, promote mitochondrial permeability, Bcl-2 cleavage and Bak conformational change (40). Among various XIAP inhibitors, small molecule embelin is quite promising and known to inhibit caspase 9 and effector caspases (18). Therefore, we determined whether embelin can activate caspases in LNCaP and C4–2 cells (Fig. 3). We observed increased caspase 3 and 9 activity upon treatment with embelin in both cell lines. Our results are in good agreement with Nikolovska-Coleska *et al.* (18) who first showed the ability of embelin to induce caspase 3 and 9 activation in prostate cancer cells by inhibiting the activity of XIAP. While these authors studied the effect of embelin in LNCaP and other prostate cancer cells, they did not examine C4–2 cells and to the best of our knowledge no study using embelin has been done in C4–2 cells. In our study, we found caspase 3 and 9 activation to be lower in C4–2 cells compared to LNCaP cells which we attributed to higher levels of XIAP expression in C4–2 cells. ELISA and real time RT-PCR analysis on LNCaP and C4–2 cells revealed higher baseline XIAP expression in C4–2 cells and treatment with 5 μM embelin resulted in a decrease in XIAP expression in both cell lines. It is noteworthy that the decrease in XIAP expression upon treatment with embelin was more pronounced in LNCaP cells compared to C4–2 cells (Fig. 3). This outcome appears to correlate with the relative caspase 3 and 9 activation levels observed in LNCaP and C4–2 cells.

We examined the ability of bicalutamide and embelin for treating androgen dependent prostate cancer as well as hormone refractory advanced prostate cancer by observing their effect on cell proliferation. Embelin was more potent than bicalutamide in killing prostate tumor cells irrespective of their androgen status since it was effective in inhibiting the proliferation of androgen dependent LNCaP and hormone refractory C4–2 cells (Fig. 4). Isobologram analysis suggests that the simultaneous administration of bicalutamide and embelin and the sequential treatment of bicalutamide followed by embelin provide synergistic effect on the growth inhibition of hormone refractory C4–2 prostate cancer cells but additive and antagonistic effects in LNCaP cells **(**Fig. 5 and Tables I, II and III**)**. The efficacy of the above treatment schedules possibly stems from bicalutamide sensitizing the cells by androgen ablation to embelin mediated apoptosis. In contrast, the treatment schedule of embelin followed by bicalutamide was additive and antagonistic for both cell lines. However, since the definition of synergism is more stringent in the isobologram method of analysis compared to clinical synergism where drug combinations must simply produce a better tumor response than either drug alone, the observed antagonistic effects in our drug combination study may be equal or superior to that of bicalutamide or embelin alone (41).

Since bicalutamide and embelin are highly hydrophobic, their limited solubility in water can hamper their clinical use by systemic administration. Moreover, the historical use of DMSO to bring water insoluble drugs into true solution for clinical use is of great concern since DMSO is harmful to the liver and kidney and causes dose-dependent hemolysis. A potential approach to addressing these problems is to improve their aqueous solubility using polymeric micelles. Formulation of these drugs into PEG-PLA micelles significantly improved their aqueous solubility and drug loading density increased with increasing theoretical loading up to 20% for embelin and 10% for bicalutamide (Fig. 6). Embelin had higher drug loading compared to bicalutamide, possibly due to better hydrogen bonding between the carbonyl group of the PLA hydrophobic core-forming block and the hydroxyl groups of embelin. Similar observations has also been reported for quercetin which has three hydroxyl groups (42). Differences in their drug loading efficiency and micellar solubilization are also related to their different physicochemical properties as calculated using the Advanced Chemistry Development (ACD/Labs) Software V8.14 for Solaris (Ó 1994–2009 ACD/Labs): The log D (pH = 7), log P and pKa values for bicalutamide are 4.94, 9.44 and 11.49, respectively; and those of embelin are 1.20, 5.70 and 2.59, respectively. Micelle size was in the range of 30–50 nm, which is expected to allow enhanced capillary permeability and delivery to tumor and inflammatory sites. Furthermore, the small size of the micelles would facilitate the release of encapsulated drug due to the high surface area to volume ratio.

Following *in vitro* characterization, bicalutamide-loaded micelles were evaluated in mice bearing LNCaP xenografts. Tumor regression was more significant up to 20 days post-treatment with bicalutamide-loaded micelles compared to free bicalutamide. Unfortunately, tumors became insensitive to bicalutamide afterwards and began to grow. This finding is not surprising, since prostate cancer is known to become resistant to bicalutamide after prolonged treatment, leading to tumor cell proliferation. Subsequent treatment with emblin-loaded micelles resulted in regression of hormone insensitive tumors. This result clearly suggests that combination of bicalutamide with embelin has the potential to be used for treating advanced prostate tumor and metastasis. Sirotnak *et al.* have also shown synergistic effect of bicalultamide with ZD1839 (Iressa) which inhibits EGFR. However they used extremely high dose (150 mg/kg for ZD1839 and 100 mg/kg for bicalutamide) and did not measure tumor growth beyond 18 days. In our study there was significant tumor regression up to 20 days when we treated mice with bicalutamide-loaded micelles, but the tumors began to grow beyond 20 days and therefore we stopped treatment with bicalutamide on day 28 and treated mice with embelin a week later (43). Synergistic effect has also been shown in prostate cancer cell lines between bicalutamide and genistein which is an isoflavone (44).

A major goal of this study was to demonstrate proof of principle that the combination of an androgen receptor antagonist (bicalutamide) and XIAP inhibitor (embelin) was capable of regressing prostate cancer tumors. Since both bicalutamide and embelin are highly hydrophobic and the conventional use of DMSO to solubilize drugs is harmful to

the liver and kidney and causes dose-dependent hemolysis, we chose to use polymeric micelles. While the drug solubilization results are not dramatic, they were suitable for intratumoral injections for our xenograft models. For future studies involving systemic administration, we plan to optimize the selection of the hydrophobic block of our copolymer to increase the "cargo" space and enhance drug solubilization. Our laboratory is currently synthesizing polymers to address this issue and preliminary data suggests it may be able to enhance solubilization several fold compared to the poly lactic acid hydrophobic core used in this study. We are also conjugating targeting ligands to the polymeric micelles to enhance site-specific delivery after systemic administration. In conclusion, micellar delivery of antiandrogen and XIAP inhibitors has potential to treat advanced prostate cancer.

REFERENCES

1. Jemal A, Siegel R, Ward E, Hao Y, Xu J, Murray T, *et al*. Cancer statistics, 2008. CA 2008;58:71–96.
2. Huggins C, Hodges CV. Studies on prostatic cancer. I. The Effect of Castration, of Estrogen and of Androgen Injection on Serum Phosphatases in Metastatic Carcinoma of the Prostate. Cancer Res 1941;1:293–7.
3. Cunha GR, Donjacour AA, Cooke PS, Mee S, Bigsby RM, Higgind SJ, *et al*. The endocrinology and developmental biology of the prostate. Endocr Rev 1987;8:338–62. doi:10.1210/edrv-8-3-338.
4. Isaacs JT. Role of androgens in prostate cancer. Vitam Horm 1994;49:433–502. doi:10.1016/S0083-6729(08)61152-8.
5. Arnold JT, Isaacs JT. Mechanisms involved in the progression of androgen-independent prostate cnacers: it is not only the cancer cell's fault. Endocr Relat Cancer 2002;9:61–73. doi:10.1677/erc.0.0090061.
6. Miquel M, Soler A, Vaque A, Ojanguren I, Costa J, Planas R. Suspected cross-hepatotoxicity of flutamide and cyproterone acetate. Liver Int 2007;27:1144–7. doi:10.1111/j.1478-3231.2007.01549.x.
7. de Voogt HJ, Smith PH, Pavone-Macaluso M, de Pauw M, Suciu S. Cardiovascular side effects of diethylstilbestrol, cyproterone acetate, medroxyprogesterone acetate and estramustine phosphate used for the treatment of advanced prostatic cancer: results from European Organization for Research on Treatment of Cancer trials 30761 and 30762. J Urol 1986;135:303–7.
8. Blackledge G. Casodex-mechanism of action and opportunity for usage. Cancer 1993;72:3830–3. doi:10.1002/1097-0142(19931215)72:12+<3830::AID-CNCR2820721713>3.0.CO;2-D.
9. Deveraux QL, Reed JC. IAP family proteins—suppressors of apoptosis. Genes Dev 1999;13:239–52. doi:10.1101/gad.13.3.239.
10. Kasof GM, Gomes BC. Livin, a novel inhibitor of apoptosis protein family member. J Biol Chem 2001;276:3238–46. doi:10.1074/jbc.M003670200.
11. Salvesen GS, Duckett CS. IAP proteins: blocking the road to death's door. Nat Rev Mol Cell Biol 2002;3:401–10. doi:10.1038/nrm830.
12. Takahashi R, Deveraux Q, Tamm I, Welsh K, Assa-Munt N, Salvesen GS, *et al*. A single BIR domain of XIAP sufficient for inhibiting caspases. J Biol Chem 1998;273:7787–90. doi:10.1074/jbc.273.14.7787.
13. Fesik SW. Insights into programmed cell death through structural biology. Cell 2000;103:273–82. doi:10.1016/S0092-8674(00)00119-7.
14. Riedl SJ, Renatus M, Schwarzenbacher R, Zhou Q, Sun C, Fesik SW, *et al*. Structural basis for the inhibition of caspase-3 by XIAP. Cell 2001;104:791–800. doi:10.1016/S0092-8674(01)00274-4.
15. Chai J, Shiozaki E, Srinivasula SM, Wu Q, Datta P, Alnemri ES, *et al*. Structural basis of caspase-7 inhibition by XIAP. Cell 2001;104:769–80. doi:10.1016/S0092-8674(01)00272-0.
16. McEleny KR, Watson RW, Coffey RN, O'Neill AJ, Fitzpatrick JM. Inhibitors of apoptosis proteins in prostate cancer cell lines. Prostate 2002;51:133–40. doi:10.1002/pros.10061.
17. Krajewska M, Krajewski S, Banares S, Huang X, Turner B, Bubendorf L, *et al*. Elevated expression of inhibitor of apoptosis proteins in prostate cancer. Clin Cancer Res 2003;9:4914–25.
18. Nikolovska-Coleska Z, Xu L, Hu Z, Tomita Y, Li P, Roller PP, et al. Discovery of embelin as a cell-permeable, small-molecular weight inhibitor of XIAP through structure-based computational screening of a traditional herbal medicine three-dimensional structure database. J Med Chem 2004;47:2430–40. doi:10.1021/jm030420+.
19. Chitra M, Sukumar E, Suja V, Devi CS. Antitumor, anti-inflammatory and analgesic property of embelin, a plant product. Chemotherapy 1994;40:109.
20. Githui EK, Makawiti DW, Midiwo JO. Changes in the concentrations of testosterone, luteinising hormone and progesterone associated with administration of embelin. Contraception 1991;44:311–7. doi:10.1016/0010-7824(91)90020-G.
21. Ahn KS, Sethi G, Aggarwal BB. Embelin, an inhibitor of X chromosome-linked inhibitor-of-apoptosis protein, blocks nuclear factor-kappaB (NF-kappaB) signaling pathway leading to suppression of NF-kappaB-regulated antiapoptotic and metastatic gene products. Mol Pharmacol 2007;71:209–19. doi:10.1124/mol.106.028787.
22. Lavasanifar A, Samuel J, Kwon GS. Poly(ethylene oxide)-block-poly(l-amino acid) micelles for drug delivery. Adv Drug Deliv Rev 2002;54:169–90. doi:10.1016/S0169-409X(02)00015-7.
23. Yamamoto Y, Nagasaki Y, Kato Y, Sugiyama Y, Kataoka K. Long-circulating poly(ethylene glycol)-poly(D,L-lactide) block copolymer micelles with modulated surface charge. J Control Release 2001;77:27–38. doi:10.1016/S0168-3659(01)00451-5.
24. Maeda H, Wu J, Sawa T, Matsumura Y, Hori K. Tumor vasculature permeability and the EPR effect in macromolecular therapeutics: a review. J Control Release 2000;65:271–84. doi:10.1016/S0168-3659(99)00248-5.
25. Maeda H, Sawa T, Konno T. Mechanism of tumor-targeted delivery of macromolecular drugs, including the EPR effect in solid tumor and clinical overview of the prototype polymeric drug SMANCS. J Control Release 2001;74:47–61. doi:10.1016/S0168-3659(01)00309-1.
26. Mukherjee A, Kirkovsky L, Yao XT, Yates RC, Miller DD, Dalton JT. Enantioselective binding of Casodex to the androgen receptor. Xenobiotica 1996;26:117–22.
27. Steel GG, Peckham MJ. Exploitable mechanisms in combined radiotherapy-chemotherapy: the concept of additivity. Int J Radiat Oncol Biol Phys 1979;5:85–91.
28. Ananthapadmanabhan KP, Goddard ED, Turro NJ, Kuos PL. Fluorescence Probes for Critical Micelle Concentration. Langmuir 1985;1:352–5. doi:10.1021/la00063a015.
29. Ham JS. A New Electronic State in Benzene. J Chem Phys 1953;21:756–8. doi:10.1063/1.1699014.
30. Wilihelm M, Zhao CL, Wang Y, Xu R, Winnik MA. Poly (styrene-ethylene oxide) block copolymer micelle formation in water: A fluorescence probe study. Macromolecules 1991;24:1033–40. doi:10.1021/ma00005a010.
31. Blanco E, Bey EA, Dong Y, Weinberg BD, Sutton DM, Boothman DA, *et al*. b-Lapachone-containing PEG-PLA polymer micelles as novel nanotherapeutics against NQO1-overexpressing tumor cells. J Control Release 2007;122:365–74. doi:10.1016/j.jconrel.2007.04.014.
32. Grossmann ME, Huang H, Tindall DJ. Androgen receptor signaling in androgen-refractory prostate cancer. J Natl Cancer Inst 2001;93:1687–97. doi:10.1093/jnci/93.22.1687.
33. Kish JA, Bukkapatnam R, Palazzo F. The treatment challenge of hormone-refractory prostate cancer. Cancer Control 2001;8:487–95.
34. Knox JJ, Moore MJ. Treatment of hormone refractory prostate cancer. Semin Urol Oncol 2001;19:202–11.
35. Rubben H, Bex A, Otto T. Systemic treatment of hormone refractory prostate cancer. World J Urol 2001;19:99–110. doi:10.1007/s003450000186.
36. Emamaullee JA, Shapiro AM. Interventional strategies to prevent beta-cell apoptosis in islet transplantation. Diabetes 2006;55:1907–14. doi:10.2337/db05-1254.
37. Lee EC, Zhan P, Schallhom R, Packman K, Tenniswood M. Antiandrogen-induced cell death in LNCaP human prostate cancer cells. Cell Death Differ 2003;10:761–71. doi:10.1038/sj.cdd.4401228.

38. Liao X, Tang S, Thrasher JB, Griebling TL, Li B. Small-interfering RNA-induced androgen receptor silencing leads to apoptotic cell death in prostate cancer. Mol Cancer Ther 2005;4:505–15. doi:10.1158/1535-7163.MCT-04-0313.
39. Yoshida T, Kinoshita H, Segawa T, Nakamura E, Inoue T, Shimizu Y, *et al*. Antiandrogen bicalutamide promotes tumor growth in a novel androgen-dependent prostate cancer xenograft model derived from a bicalutamide-treated patient. Cancer Res 2005;65:9611–6. doi:10.1158/0008-5472.CAN-05-0817.
40. Fakler M, Loder S, Vogler M, Schneider K, Jeremias I, Debatin KM, *et al*. Small molecule XIAP inhibitors cooperate with TRAIL to induce apoptosis in childhood acute leukemia cells and overcome Bcl-2-mediated resistance. Blood 2009;113 (8):1710–22.
41. Akutsu M, Kano Y, Tsunoda S, Suzuki K, Yazawa Y, Miura Y. Schedule-dependent interaction between paclitaxel and doxorubicin in human cancer cell lines *in vitro*. Eur J Cancer 1995;31A:2341–6. doi:10.1016/0959-8049(95)00448-3.
42. Yang X, Zhu B, Dong T, Pan P, Shuai X, Inoue Y. Interactions between an anticancer drug and polymeric micelles based on biodegradable polyesters. Macromol Biosci 2008;8:1116–25. doi:10.1002/mabi.200800085.
43. Sirotnak FM, She Y, Lee F, Chen J, Scher HI. Studies with CWR22 xenografts in nude mice suggest that ZD1839 may have a role in the treatment of both androgen-dependent and androgen-independent human prostate cancer. Clin Cancer Res 2002;8:3870–6.
44. Burich RA, Holland WS, Vinall RL, Tepper C, White RW, Mack PC. Genistein combined polysaccharide enhances activity of docetaxel, bicalutamide and Src kinase inhibition in androgen-dependent and independent prostate cancer cell lines. BJU Int 2008;102:1458–66.